

PROCESSES OF CONTINENTAL
EXTENSION AS VIEWED FROM THE
DEATH VALLEY REGION, CALIFORNIA

by

Lawrence William McKenna III
S. B. Geology, Massachusetts Institute of Technology
(1984)

Submitted to the Department of Earth, Atmospheric, and
Planetary Sciences in Partial Fulfillment of the Requirements
for the Degree of

Doctor of Philosophy
at the
Massachusetts Institute of Technology
June, 1990

Signature of Author: _____
Department of Earth, Planetary, and Atmospheric Sciences
May 29, 1990

Certified by: _____
Prof. Kip V. Hodges
Thesis Supervisor

Accepted by: _____
Prof. Thomas H. Jordan
Chairman, Departmental Graduate Committee

MASSACHUSETTS INSTITUTE
OF TECHNOLOGY

JUN 05 1990

LIBRARIES

- 1 -

Lindgren

© MIT, 1990. All rights reserved.

ABSTRACT

PROCESSES OF CONTINENTAL EXTENSION AS VIEWED FROM THE DEATH VALLEY REGION, CALIFORNIA

by Lawrence William McKenna III. Submitted to the Department of Earth, Atmospheric, and Planetary Sciences in Partial Fulfillment of the Requirements for the Degree of Doctor of Philosophy at the Massachusetts Institute of Technology, May 29, 1990

CHAPTER 1

Detailed mapping of extensional structures and synextensional volcanic rocks exposed in the eastern Panamint Mountains, SE California, place new constraints on the rates and geometry of Late Miocene extension in the Death Valley area. At the eastern edge of the central Panamint Mountains, the Burro Trail and Amargosa "thrust" faults of Hunt and Mabey [1966] form sub-parallel roof and sole faults, respectively, of a kinematically related system of currently low-angle normal faults and sub-vertical strike-slip faults named here the Eastern Panamint fault system. The roof and sole faults initiated as 40-60° W-dipping normal faults in Late Miocene time and were subsequently rotated to shallow dips by later, structurally lower, normal faults. Roughly 150-160% cumulative extension can be demonstrated for Eastern Panamint structures exposed in Trail Canyon.

Late Miocene tuffs and andesites exposed in the eastern Panamint Mountains are correlative with the Sheephead Andesite and Rhodes Tuff in the southern Black Mountains. Reconstruction of these sequences indicate 25-55 km of post-10 Ma extension between the eastern Panamint and southern Black Mountains along an azimuth of N55°±3°W. This extension was dominantly accommodated by movement on the Amargosa fault system and late Neogene faults exposed along the western front of the Black Mountains. These data constrain the extension rate between the Black and Panamint Mountains to be between 6.5 and 2.5 mm/a over the past 10 Ma. Existing data on the direction and age of initiation and cessation of extension for faults in the Death Valley area show two periods of extension. The earlier period, from 15-10 Ma, has widely varying extension directions, while the later period, from 10-0 Ma is characterized by consistently NW extension directions.

CHAPTER 2

This paper reports new $^{40}\text{Ar}/^{39}\text{Ar}$ and Rb/Sr dates along a transect through the Panamint and Black Mountains of the Death Valley region, eastern California. We present step heating data from 20 samples (mineral and glass separates) collected from Proterozoic basement gneisses, Cretaceous and Cenozoic age intrusive rocks, and Cenozoic extrusive rocks that crop out within these ranges. Two concordant biotite cooling ages (10.80 ± 0.06 Ma) and two concordant K-feldspar cooling ages (10.4 ± 0.15) from dikes in the footwall of the Eastern Panamint Fault system suggest initiation of deformation along the fault near 10.5 Ma. Within the volcanic rocks in the hanging wall of the fault, a lower unit returned a biotite age of 10.3 ± 0.3 , while a glass separate from an upper unit returned an excellent plateau at 9.97 ± 0.16 Ma. These volcanic rocks were faulted by some strands of the Eastern Panamint Fault System, giving a lower bound to the time of deformation along this fault. The ages of samples from the Black Mountains, along the east side of Death

Valley, reflect the unroofing and rotation of the range in the Late Miocene. Hornblende and biotite samples from the Willow Spring Diorite give a range of ages from 10.36 to 9.96 Ma and 9.19 and 8.41 Ma respectively. The relations between the structural positions of the samples, and the relative differences in their hornblende and biotite ages suggests that the Black Mountains were rotated about a horizontal axis during their unroofing. The rotation occurred between approximately 10 and 9 Ma, with a strain rate of $4 \pm 1 \times 10^{-13} \text{ sec}^{-1}$, or approximately an order of magnitude greater than the deformation along the earlier Eastern Panamint Fault system.

CHAPTER 3

New chemical and isotopic data reported here, as well as previously published data from syn-extensional volcanic rocks from the Death Valley Region, western United States, are consistent with derivation of the volcanic rocks by mixing of two distinct mantle components with continental crust. These mantle components are equivalent to the enriched mantle and depleted mantle components identified by previous authors. The evolution of the relative contribution of the depleted versus enriched mantle sources to the syn-extensional volcanic rocks is well-explained by a lithosphere scale simple-shear model for extension within the Death Valley Extended Area. The new data reported here are from the Trail Canyon Volcanic Sequence, a 10.3 to 10.0 Ma series of basaltic andesites, andesites, dacites and rhyolites of calc-alkaline to tholeiitic composition exposed in the eastern Panamint Mountains of eastern California. Major element, trace element and isotopic data indicate that these rocks were derived by mixing of a depleted mantle-derived parental liquid and a contaminant with a crustal composition. Initial $^{87}\text{Sr}/^{86}\text{Sr}$ ratios range from 0.706 to 0.713, with corresponding variations in Rb/Sr. Lead isotope ratios vary from $^{206}\text{Pb}/^{204}\text{Pb}=18.69$ to 19.39 , $^{207}\text{Pb}/^{204}\text{Pb}=15.62$ to 15.72 , and $^{208}\text{Pb}/^{204}\text{Pb}=39.1$ to 39.74 . Finally, the three measured Nd compositions show a small range, from $^{143}\text{Nd}/^{144}\text{Nd}=0.512407$ to 0.512455 . Rare-earth element trends in the Pliocene age basalts to basaltic andesites of the nearby Nova Basin show rare-earth characteristics as the Trail Canyon samples, except that none of the Nova samples displays a Eu anomaly, and the absolute concentrations within the Nova samples are lower.

CHAPTER 4

Extension within the Basin and Range was accompanied by significant volcanism, ranging from alkalic basalts to high silica rhyolites. In this chapter, the mantle sources involved in the volcanism, and the spatial progression of the locus of volcanism, are used to test various models for active versus passive upwelling of asthenospheric material during extension. This is done by combining the existing data for the isotopic and trace element compositions of volcanic rocks within the greater Death Valley Area [Farmer et al., 1989; Ormerod et al., 1988; Walker and Coleman, submitted; McKenna, Chapter 3] with the compilations by Luedke and Smith [1978] of the age and composition of volcanic rocks within the southern Basin and Range, and placing these data on a palinspastically restored base map. In effect, this removes the apparent spatial variability in the composition of volcanic rocks caused by different amounts of post-eruption extension within the Death Valley Extended Area. With these data in hand, a number of models for the large-scale structural formation of the Basin and Range are tested, and a hybrid simple shear-active lithospheric erosion model is proposed to integrate the observations.

Thesis Supervisor: Dr. Kip V. Hodges
Associate Professor of Geology

TABLE OF CONTENTS

PROCESSES OF CONTINENTAL EXTENSION AS VIEWED FROM THE DEATH VALLEY REGION, CALIFORNIA

ABSTRACT: 3

LIST OF FIGURES: 8

LIST OF TABLES: 10

ACKNOWLEDGMENTS: 11

INTRODUCTION AND READERS' GUIDE: 14

CHAPTER 1: 17

Constraints on the Kinematics and Timing of Late Miocene-Recent Extension Between the Panamint and Black Mountains, Southeastern California

Abstract: 18

Introduction: 19

Geologic Setting: 20

Stratigraphy of Late Miocene Volcanic Rocks: 21

Structural geology of the Trail Canyon area: 22

Structural Interpretation: 24

Age of the Eastern Panamint Fault System: 25

Fault Reconstruction: 25

Significance of Volcanic Correlations: 27

Late Miocene to Recent extension in the Death Valley area: 28

Regional Significance: 29

Conclusions: 30

Acknowledgments: 31

References: 31

Figure Captions: 34

Figures: 37

CHAPTER 2: 43

Time-Temperature History of Extension in the Panamint and Black Mountains, Death Valley, California

Abstract: 44

Introduction: 45

Geologic Setting: 45

| | |
|---------------------------------------|-----------|
| Other Ar Work: | 48 |
| Procedures: | 48 |
| <i>40Ar/39Ar:</i> | <i>48</i> |
| <i>Rb/Sr:</i> | <i>51</i> |
| Data: | 51 |
| <i>Skidoo Granite:</i> | <i>52</i> |
| <i>Little Chief Stock:</i> | <i>52</i> |
| <i>Eastern Panamint Fault System:</i> | <i>53</i> |
| <i>Black Mountains:</i> | <i>54</i> |
| Discussion: | 55 |
| <i>Eastern Panamint Fault System:</i> | <i>55</i> |
| <i>Black Mountains:</i> | <i>57</i> |
| <i>Panamint Mountains:</i> | <i>61</i> |
| Conclusions: | 63 |
| Acknowledgments: | 65 |
| References: | 65 |
| Figure Captions: | 69 |
| Tables: | 72 |
| Figures: | 82 |

CHAPTER 3: 111

Geochemistry of a Miocene Volcanic Sequence and its Relation to the Scale of Mantle Heterogeneities beneath the Southern Basin and Range

| | |
|--|------------|
| Abstract: | 112 |
| Introduction: | 113 |
| Geologic Setting: | 113 |
| Analytical Techniques: | 117 |
| Previous Work: | 118 |
| Data: | 119 |
| Discussion: | 120 |
| <i>Petrogenesis: Fractional Crystallization versus Mixing:</i> | <i>120</i> |
| <i>Regional Mixing Model:</i> | <i>122</i> |
| <i>Coherence of trace element and isotopic compositions:</i> | <i>126</i> |

*Implications for the temporal variation in volcanic
sources: 128*

Conclusions: 132

References: 134

Figure Captions: 140

Tables: 144

Figures: 150

CHAPTER 4: 173

**Volcanotectonic relationships in the Death Valley and Colorado River
Extended Areas**

Abstract: 174

Models: 175

Techniques: 176

Setting: 177

Data: 178

Discussion: 180

References: 184

Figure Captions: 186

Figures: 188

BIOGRAPHICAL SKETCH: 198

LIST OF FIGURES

CHAPTER 1

- Figure 1. Tectonic Map of the Panamint Mountains: 37
Figure 2. Geology of the Death Valley Region: pocket
Figure 3. Stratigraphy of the Trail Canyon Volcanic Sequence:
pocket
Figure 4. Comparison of Trail Canyon Volcanic Sequence, Rhodes
Tuff and Sheephead Andesite: 38
Figure 5. Cross Sections, Eastern Panamint Fault System: pocket
Figure 6. Photograph of a Typical Roof-Parallel Fault: 39
Figure 7. Block Model of an Extensional Duplex: 41
Figure 8. Palinspastically Restored Regional Cross Sections: pocket
Figure 9. Direction and Timing of Extension: 42
Plate 1. pocket
Key. pocket

CHAPTER 2

- Figure 1. Location Map, Death Valley Extended Area: 82
Figure 2. Tectonic and Location Map, Panamint Mountains: 83
Figure 3. Regional Cross Section with Available Geochronology:
pocket
Figure 4.1. Release Spectra and Isochron Plots, 84-06: 84
Figure 4.2. Release Spectra and Isochron Plots, Little Chief Stock: 85
Figure 4.3. Release Spectra and Isochron Plots, Trail Canyon
Volcanic Series (2-87-24, 11-87-9, 1-87-12): 88
Figure 4.4. Release Spectra and Isochron Plots, 1-86-34: 90
Figure 4.5. Release Spectra and Isochron Plots, 1-86-36C: 92
Figure 4.6. Release Spectra and Isochron Plots, 1-86-25: 94
Figure 4.7. Release Spectra and Isochron Plots, 10-87-13A: 95
Figure 4.8. Release Spectra and Isochron Plots, 10-87-13C: 97
Figure 4.9. Release Spectra and Isochron Plots, 10-87-13D: 99
Figure 4.10. Release Spectra and Isochron Plots, 10-87-13E: 101
Figure 4.11. Release Spectra and Isochron Plots, 10-87-13A: 103
Figure 5. Summary of Willow Springs Diorite Data: 104
Figure 6. Time-Temperature Evolution of the Death Valley Area: 105

- Figure 7. Structural Model of the Eastern Panamint Fault System: 106
- Figure 8. Late Miocene Reconstruction of the Death Valley Area: 107
- Figure 9. Direction and Timing of Extension: 108

CHAPTER 3

- Figure 1. Regional Setting, Death Valley Extended Area: 150
- Figure 2. FeO*/MgO vs SiO₂, Trail Canyon Volcanic Sequence: 151
- Figure 3. Harker Diagrams, Trail Canyon Volcanic Sequence: 152
- Figure 4.1. Trace Element Variations vs SiO₂: 154
- Figure 4.2. Incompatible and Rare Earth Element Variations, Trail Canyon Volcanic Sequence and Nova Basin Volcanic Rocks: 156
- Figure 5.1. Sr Isotopic Correlations: 158
- Figure 5.2. Pb Isotopic Correlations: 159
- Figure 6. Modeled Fractional Crystallization Paths: 160
- Figure 7. Expected *versus* Observed Trace Element Variations: 162
- Figure 8. Regional Isotopic Data: 163
- Figure 9. Regional Mixing Model: 165
- Figure 10. Pb Isotopes Provenance: 167
- Figure 11. End-Member ITE Concentrations: 168
- Figure 12. Rb/Sm *versus* Sm/Nd, Regional Volcanic Rocks: 169
- Figure 13. Zr/Ba *versus* Rb/Sm and 87Rb/86Sr: 170
- Figure 14. Cartoon Depicting Lithospheric Evolution of the Death Valley Extended Area: 171

CHAPTER 4

- Figure 1. Location Map and Tectonic Setting: 188
- Figure 2. Modes of Extension: 189
- Figure 3. Inferred Mantle Source Chemistry: 190
- Figure 4A. Volcanic Rocks, >11 Ma: 191
- Figure 4B. Volcanic Rocks, 11–9 Ma: 192
- Figure 4C. Volcanic Rocks, 9–4 Ma: 193
- Figure 4D. Volcanic Rocks, 4–0 Ma: 194
- Figure 5. Location of Palinspastically restored Volcanic Rocks: 195
- Figure 6. Model of Extension within the Death Valley Area: 196

LIST OF TABLES

CHAPTER 2

Table 1. Diffusion Parameters and Closure Temperatures: 72

Table 2. Run Summary: 73

Table 3. Step Heating Release Experiment Data

Table 3.1. 10-87-13E Hornblende: 74

Table 3.2. 10-87-13D Hornblende: 74

Table 3.3. 10-87-13C Hornblende: 74

Table 3.4. 10-87-13A Hornblende: 75

Table 3.5. LCS Hornblende: 75

Table 3.6. 10-87-13E Biotite: 75

Table 3.7. 10-87-13A Biotite: 76

Table 3.8. 10-87-13C Biotite: 76

Table 3.9. 1-86-36C Biotite: 76

Table 3.10. 1-86-34 Biotite: 77

Table 3.11. 2-87-24 Biotite: 77

Table 3.12. 84-06 Biotite: 77

Table 3.13. LCS Biotite: 78

Table 3.14. 1-87-12 Biotite: 78

Table 3.15. 11-87-8 Glass: 78

Table 3.16. 1-86-34 Ksp: 79

Table 3.17. LCS Ksp: 79

Table 3.18. 1-86-25 Ksp: 79

Table 3.19. 1-86-36c Ksp: 80

Table 3.20. 10-87-9 Ksp: 80

Table 4. Sr Data: 81

CHAPTER 3

Table 1. Major Element Data: 144

Table 2. Trace Element Data: 145

Table 3. Isotopic Data: 147

Table 4. Model Characteristics: 148

Table 5. Regional Model Fits: 149

ACKNOWLEDGMENTS

Even an individual who knows me only slightly could guess that of all the parts of this thesis, this section is my favorite. Part of the fun of science is sharing the process with friends and colleagues; part of the education in science is learning from those same colleagues. Often it seems that the fun and the education have been one and the same. Those "peers and colleagues" fall naturally into three categories, with tremendous overlap, and I sincerely hope that I've covered everyone below. If I have forgotten someone, it is in word only- be sure that, in thought, I've thanked you.

Every acknowledgment I have ever read sticks the husband-wife-significant other at the end. Time to change that. In both the physical and the emotional sense, the completion of this thesis is due in large part to Elizabeth Spizman, whose help quite simply defies the depth of my vocabulary to express it. Thanks too to Elise Spizman McKenna, for reminding me of the correct balance between work and life. I am fortunate to live relatively near to most of my family, and to Jim, Anne, and my parents, thanks. I fear to think what Liz and I would have done without the trips to my mother's house in Amherst to escape Somerville! Kip, Larky and Rachel Hodges have been good friends, good cooks, and good company, for five years; the three of us will miss the three of you.

I have greatly benefitted from the support (intellectual and monetary) of a number of faculty and other professionals during the past five years. Chief among these are Prof. Stan Hart, who provided the clean lab and mass spectrometry facilities used throughout my time at MIT, and Prof. Fred Frey, who provided access to the Neutron Activation Facility for the various projects I've pursued while here. Stan also funded part of my studies, and I extend my appreciation for that. Special thanks are due to Dr. Larry Snee of the USGS for allowing me to "dirty up his flight tube" with my amphibole samples during the Ar/Ar work, and kudos too for a splendid Thanksgiving Day dinner. Prof. Doug Walker provided XRF facilities for my (ab)use, and didn't seem to mind (too much) when I broke \$600 worth of his equipment in four different screw-ups in 90 minutes.

Other individuals provided support of the intellectual kind during my tenure here. Dr. P. Ila taught me how to analyze data, bit by bit, and endlessly arranged, rearranged, and then (often) de-rearranged, the counting schedules at the INAA lab to fit my ever-changing schedules. I have greatly enjoyed my interactions with her. Prof. Tim Grove provided me with insights to petrologic problems that I hadn't, at the time, known I would run into, and thanks to him too for teaching one of the more stimulating classes I took as a graduate student. Prof. Leigh Royden continually reminded me of the elegant answers simple physics provides to geological problems, a lesson I hope to continue to use. Dr. John Grotzinger has provided me with a number of new perspectives on tectonics and sedimentation, and provided the Mac on which this thesis was written. Finally, Dr Levant Gülen introduced me to the procedures and pleasures of the isotope lab. My thesis committee, Wiki Royden, Kip Hodges, Stan Hart, Prof. Jane Selverstone, and Prof. Tom Jordan, waded through the first version of the thesis, and suggested many improvements.

The students with whom I have... studied?... lived?... with are next, and the reader will pardon me for what seems like a long list. Mike Baker, Dan Tormey, and Tanya Furman in many ways started me down the road to geochemistry, whether to their credit or my misfortune is yet to be seen. Jim Knapp, Laurence Page, Allison MacFarlane, Mary Hubbard, Liz Schermer, Tom Juster, Dave Silverberg, Peter Tilke, Barb Sheffels, Dave Dinter and Cathy Summa helped wile away the hours on the tenth floor (and other places); special thanks to Jim Knapp for late-night baseball. More recently, the new crowd, Dave McCormick, David Applegate, Julio Friedman, Deb Zervas, Eric Buchovecky, Roy Adams, Dawn Sumner and Erchie Wang have brought life back to the late shift, for which they have my gratitude. Up a floor, my thanks go out to two people who kept the isotope lab running, taught me how to turn a rock into a thesis, and who played soccer with me: Vincent Salters and Jurek Blusztajn. I have the dubious honor of owing Jurek an unbroken left leg - ask him for the details. Ro Kinzler has, for nine years (!), enlightened me unto the worlds of igneous petrology and thermodynamics; she has also kept me running for the past three years, although she probably didn't know this. Also in the gee-we've-been here-together-too-long-now category is Carolyn Ruppel, whose been a

friend since she brought fresh-baked cinnamon rolls to our Metamorphic Petrology final sometime back in 1984. Thanks to Tom Sisson for quietly showing me how much more I have to learn. Eric Hauri kindly spent the last two years sharing an office with a person who couldn't find his desk to clean it, and took messages for me at the same time!

Of course, the mess on my desk pales in comparison to the chaos in the office of Kip Hodges, my advisor. Unfortunately, I can't blame that aspect of my behavior on him. He has, however, helped to develop most other aspects of my career as a geologist, a scientist, and a baseball fan. For all three I thank him. He's also taught me how to write a better sentence, if only by correcting most of the ones I've written since 1984. I have also had the good fortune to work with and around Clark Burchfiel, who's insight and remarkable memory ("Oh, well, yea, ya know if you walk down that wash another 50 feet, there's a contact with a granite that cuts that fault and that granite's been dated at 172") have been constantly helpful for the past few years.

This final group is wide-ranging, but this is the only part my Committee doesn't get to read, so: Dr. Shelly Friedman and our colleagues for general insights, Steven Jobs and Steven Wesniack for inventing the Macintosh, and Anne McCaffery for diversionary reading.

INTRODUCTION AND READERS' GUIDE

The following four papers represent the results of my research into the processes of continental extension, as viewed from the Death Valley Area of the southwestern Basin and Range Province. Although it was not my intent when I started this project, or even when I began to describe its results, the papers represent a progressive widening in scale and scope of the subject matter. Although they are designed to "stand alone", reading them sequentially is recommended, if only because this was the order in which they were written.

Chapter 1, "Constraints on the Kinematics and Timing of Late Miocene-Recent Extension Between the Panamint and Black Mountains, Southeastern California" describes the structural geology of a particularly important, and previously misinterpreted, fault system within the Panamint Mountains. In this paper, I describe the geometry of a fault system that accommodated a significant fraction of the extension recorded in the Death Valley Area, the fault system's original orientation and dip, and finally discuss the implications of the data to the evolution of extension within the region as a whole. This chapter is now in press as one chapter in a GSA Memoir, coauthored with Kip Hodges.

Chapter 2, "Time-Temperature History of Extension in the Panamint and Black Mountains, Death Valley, California" describes the results of a $^{40}\text{Ar}/^{39}\text{Ar}$ geochronometry study of a transect across the Death Valley region. This study builds on the geometric constraints provided by the work described in Chapter 1, along with mapping completed by Kip Hodges and his students (including me) in the Panamint Mountains. It also presents an integrated model for the extension utilizing published $^{40}\text{Ar}/^{39}\text{Ar}$ and U/Pb geochronometry. This paper will be submitted to *Tectonics*.

Chapter 3, "Geochemistry of a Miocene Volcanic Sequence and its Relation to the Scale of Mantle Heterogeneities beneath the Southern Basin and Range" details the results of the chemical and isotopic research I have conducted on volcanic rocks exposed in two paleo-basins preserved within the Panamint Mountains. After discussing the chemical and isotopic results for the samples I analyzed, I describe a model for the petrogenesis of the syn-extensional volcanic rocks throughout the Death Valley Region.

This model is constructed from the data I collected, as well as most of the data on Death Valley-area basalts in the literature. The Chapter closes with the conclusion that the volcanic rocks indicate that Death Valley formed from whole-lithosphere scale simple shear. This paper will be submitted to a special volume of JGR-Solid Earth and Planets.

Chapter 4, "Volcanotectonic relationships in the Death Valley and Colorado River Extended Areas" might be subtitled "A Speculative Model". In this chapter I discuss some of the implications raised by the previous three chapters, and how they effect our perceptions of the manner in which the crust and mantle interact during extension. The primary data for this chapter are a series of maps constructed to examine the spatial distribution, and the chemical signature of, syn-extensional volcanic rocks, prepared on a palinspastically restored base. In effect, I show the position and chemical affinities of the samples discussed in Chapter 3 retro-deformed (relative to a stable Colorado Plateau) so we can examine the temporally progression of the mantle heterogeneities detailed in Chapter 3. Finally, these topics are examined in light of the polarity of extension, the movement of the locus of extension, and the movement of the locus of volcanism. This paper is designed for submission to Geology.

Because the chapters are intended to be "stand alone" papers, there are some repetitions in them, particularly in the introductions. There might appear to be a few *omissions*, too. For example, because Chapter 1 was in press before I completed the geochronologic studies discussed in Chapter 2, certain details in Chapter 1 are not compatible with data subsequently collected for Chapter 2. Whenever this occurred, I corrected these inconsistencies in the later Chapter. I greatly enjoyed writing these papers (well, at least in hindsight), and I hope you enjoy reading them.

CHAPTER 1

CONSTRAINTS ON THE KINEMATICS AND TIMING OF LATE MIOCENE-RECENT EXTENSION BETWEEN THE PANAMINT AND BLACK MOUNTAINS, SOUTHEASTERN CALIFORNIA

L.W. MCKENNA, K.V. HODGES

DEPARTMENT OF EARTH, PLANETARY, AND
ATMOSPHERIC SCIENCES, MASSACHUSETTS
INSTITUTE OF TECHNOLOGY,
CAMBRIDGE, MASSACHUSETTS, 02139

(In press, Basin and Range Extension at the Latitude of Las Vegas, ed.
B. P. Wernicke, Geological Society of America Memoir 179, 1990)

ABSTRACT

Detailed mapping of extensional structures and synextensional volcanic rocks exposed in the eastern Panamint Mountains, SE California, place new constraints on the rates and geometry of Late Miocene extension in the Death Valley area. At the eastern edge of the central Panamint Mountains, the Burro Trail and Amargosa "thrust" faults of Hunt and Mabey [1966] form sub-parallel roof and sole faults, respectively, of a kinematically related system of currently low-angle normal faults and sub-vertical strike-slip faults named here the Eastern Panamint fault system. The roof and sole faults initiated as 40-60° W-dipping normal faults in Late Miocene time and were subsequently rotated to shallow dips by later, structurally lower, normal faults. Roughly 150-160% cumulative extension can be demonstrated for Eastern Panamint structures exposed in Trail Canyon.

Late Miocene tuffs and andesites exposed in the eastern Panamint Mountains are correlative with the Sheephead Andesite and Rhodes Tuff in the southern Black Mountains. Reconstruction of these sequences indicate 25-55 km of post-10 Ma extension between the eastern Panamint and southern Black Mountains along an azimuth of $N55^{\circ}\pm 3^{\circ}W$. This extension was dominantly accommodated by movement on the Amargosa fault system and late Neogene faults exposed along the western front of the Black Mountains. These data constrain the extension rate between the Black and Panamint Mountains to be between 6.5 and 2.5 mm/a over the past 10 Ma.

Existing data on the direction and age of initiation and cessation of extension for faults in the Death Valley area show two periods of extension. The earlier period, from 15-10 Ma, has widely varying extension directions, while the later period, from 10-0 Ma is characterized by consistently NW extension directions.

INTRODUCTION

The central portion of Death Valley, SE California, constitutes one of the world's greater topographic depressions: nearly 3.5 km of relief occur between the lowest point in the valley and Telescope Peak, the highest point in the Panamint Mountains to the west (Figure 1). There is little doubt that the central Death Valley graben developed as a consequence of "pull-apart" between the NW-striking, right-lateral Furnace Creek and Southern Death Valley fault zones [Burchfiel and Stewart, 1966; Wright and Troxel, 1967], but there has been substantial debate regarding the age and amount of displacement on the normal fault systems that accommodated extension between the Panamint Mountains and the Black Mountains to the east. The fault systems involved include: 1) a group of NW-plunging, domiform, normal faults (the Death Valley "turtlebacks" of Curry [1938]) that lie along the western foot of the Black Mountains and characterize the eastern margin of the active central Death Valley basin [Otton, 1976; Wright et al., 1974; Troxel, 1986; Burchfiel et al., in preparation]; 2) a complex of low-angle normal faults in the southern Black Mountains that corresponds to the Amargosa "chaos" of Noble [1941] and Wright and Troxel [1984]; and 3) a similar normal fault complex along the eastern foot of the Panamint Mountains [Hunt and Mabey, 1966; Wright and Troxel, 1973]. Although the turtleback surfaces in the Black Mountains cut Holocene deposits and are therefore quite young [e.g., Troxel and Wright, 1987], most of the movement on the Amargosa system appears to have occurred in Late Miocene to Early Pliocene time [Wright and Troxel, 1984]. Hunt and Mabey [1966] and Stewart [1983] interpreted the chaos structures in the Black Mountains and Panamint Mountains as part of a regionally extensive fault system, and Stewart [1983] inferred that it accommodated roughly 80 km of northwestward transport of the Panamint Mountains structural block relative to the Black Mountains block. In contrast, Wright and Troxel [1967] argued that the two systems were kinematically distinct and infer substantially less relative displacement between the Panamint Mountains and the Black Mountains.

In this paper, we present the results of our detailed study of the chaos structures along the eastern foot of the Panamint Mountains, herein

referred to as the Eastern Panamint fault system. The Eastern Panamint system developed synchronously with eruption of a Late Miocene volcanic sequence exposed along the foot of the range. Besides providing constraints on the paleohorizontal during movement on the Eastern Panamint system, these volcanic rocks place important constraints on regional reconstructions because they can be correlated confidently with volcanic sequences in the southern Black Mountains.

GEOLOGIC SETTING

The Panamint Mountains occupy a central position within the Death Valley extensional corridor (Figure 1), a zone that experienced roughly 150 km of Neogene extension [Wernicke et al., 1988]. The Panamint Mountains consist of four tectonic packages [Figure 2; Hodges et al., in press]: 1) a Parautochthon, predominantly consisting of Precambrian basement gneisses; 2) a Lower Allochthon, containing upper Precambrian strata which was metamorphosed at greenschist to amphibolite facies conditions and intruded by granitoids in Mesozoic time; 3) a Middle Allochthon, including unmetamorphosed to greenschist facies upper Precambrian to upper Paleozoic strata unconformably overlain by Neogene sedimentary and volcanic units; and 4) an Upper Allochthon, consisting of displaced fragments of the Lower and Middle Allochthons as well as Latest Miocene to Pliocene extensional basin deposits. The Upper, Middle, and Lower Allochthons are separated by diachronous but uniformly top-to-the-northwest normal faults of Neogene age which collectively constitute the Tucki Mountain Detachment System. Deformation on this system of faults initiated before 10.8 Ma with movement on the Harrisburg detachment, separating the Middle and Lower Allochthons, and continued until at least 3.7 Ma [Hodges et al., in press].

The fault system that separates the Parautochthon from structurally higher tectonic packages is the focus of this paper. We will refer to it as the Eastern Panamint fault system because it is exposed along the eastern foot of the Panamint Mountains from Starvation Canyon to Blackwater Canyon (Figure 2). Structures in this system were first mapped by Hunt and Mabey [1966], who correlated the structurally lowest exposed fault with the Amargosa thrust fault of Noble [1941]. In the Panamint Mountains this

fault places upper Proterozoic to middle Paleozoic miogeoclinal strata of the Middle Allochthon on Precambrian augen gneisses of the Parautochthon. Structurally above the fault, related structures deform the miogeoclinal strata and overlying Cenozoic volcanic rocks. Although the miogeoclinal strata of the Middle Allochthon and the Precambrian basement of the Parautochthon have been described elsewhere [Hunt and Mabey, 1966], the Cenozoic sequence had not been studied specifically prior to our investigation. Because these volcanic units are crucial for palinspastic reconstructions of the Death Valley area, we describe them in some detail below.

STRATIGRAPHY OF LATE MIOCENE VOLCANIC ROCKS

Lying above the miogeoclinal rocks of the Middle Allochthon along a regional unconformity is a sequence of Cenozoic lapilli tuffs, agglomerates, and andesite flows. These units form a discontinuously exposed band along the eastern side of the Panamint Mountains and are referred to here as the Trail Canyon Volcanic Sequence. The stratigraphy of this sequence as exposed along the eastern Panamint Mountains is illustrated in Figure 3. While this stratigraphy exhibits local variations along the exposed belt, each section includes a basal breccia unit, an overlying tuff unit, and an uppermost flow/agglomerate unit.

The basal units consist of generally clast-supported ground breccia, less than 50 m thick, lying unconformably on Precambrian to Silurian miogeoclinal rocks. Conformably overlying these units are 100 to 300 m of pale green to white lapilli tuff. The tuff is poorly welded, contains approximately 10-30% clasts of pumice, crystal fragments, and rock fragments, and was deposited in at least four separate events. Locally interbedded in these tuffs are agglomerates, finely bedded tuffaceous sandstones, and oligomictic breccias of Ordovician units (Ely Spring Dolomite and Eureka Quartzite); these clastic sequences are each less than 5 m thick.

On the ridges immediately south and north of Trail Canyon, the lapilli tuffs are conformably overlain by a sequence of basaltic-andesite flows and agglomerates totalling 110 m thick. The agglomerates contain clasts of

intermediate volcanic rocks up to 2 m x 2 m x 1 m in size, surrounded by a fine-grained, locally altered, matrix. At all other exposures of the volcanic sequence, the tuff is overlain by perlite and rhyolite flows. These flows are conformable on the tuff in the central Panamint Mountains (Figure 3), but lie unconformably on the tuff at the extreme southern and northern exposures of the sequence. The three northern exposures of the sequence (see Figure 1 for locations) are capped by basalt, which appears to be temporally equivalent to the basalts of the Funeral Formation [Cemen et al., 1985].

As reported in McKenna [Chapter 2], these flows have been dated by $^{40}\text{Ar}/^{39}\text{Ar}$ and Rb/Sr techniques at 10.3 to 9.98 Ma. This range is somewhat older than that suggested by previously obtained K-Ar data [Wes Hildreth unpublished], which indicated an age of 9.4-8.6 Ma for the tuff and overlying basaltic andesites. As noted by Wright et al. [1984b], the Trail Canyon Volcanic Sequence is similar to the Rhodes Tuff and the Sheephead Andesite, exposed at Salsberry Pass and elsewhere in the southern Black Mountains (Figure 2). Potassium-argon ages for biotites from the Rhodes Tuff range from 10.8 to 10.4 Ma [L. Wright, pers. comm., 1989], in good agreement with the $^{40}\text{Ar}/^{39}\text{Ar}$ results of McKenna [Chapter 2]. Composite sections for the Rhodes Tuff, Sheephead Andesite [from Wright et al., 1984] and the Trail Canyon Volcanic Sequence [this report] are shown in Figure 4, along with available geochronologic constraints. The correlation of these units is excellent: thicknesses, lithology, stratigraphy and age of both the tuffs and the andesites are very similar. The ground breccias within the Trail Canyon Volcanic Sequence occur only locally, and their absence in the Salsberry Pass outcrops does not weaken the correlation. We conclude, as Wright et al. [1984] hypothesized, that the Trail Canyon Volcanic Sequence and the Rhodes Tuff and Sheephead Andesite are correlative units.

STRUCTURAL GEOLOGY OF THE TRAIL CANYON AREA

A geologic map and interpretive cross sections of the Trail Canyon area are shown on Plates 1 and Figure 5 respectively. The structural architecture of the area is dominated by the Eastern Panamint fault system. Faults within the system can be divided into three classes based on

their orientation and structural relationships: lower-angle faults, higher-angle faults, and E-W-striking faults.

The lower-angle faults are characterized by present-day dips of 5-30°W, bedding-fault angles of ~70°, brecciated contacts 0.1 to 10 m wide and stratigraphic displacements of 300-1400 m. These features are well-illustrated on Figure 6, which shows the contact at Location A (Plate I), looking N. Here the zone of fault gouge varies from 4 to over 8 m thick, and consists of brecciated Ordovician Eureka Quartzite and Ely Spring Dolomite. Breccias of the two lithologies are separated by diffuse contacts (less than a few decimeters) and form lenses a few meters thick and 10-15 wide (see right side of Figure 6 photograph). At this outcrop, Ely Spring Dolomite and Eureka Quartzite overlie, along the brecciated contact, the older Pogonip Dolomite. This relation and the lensoidal morphology suggest normal displacement along this lower-angle fault. Similar younger-on-older relations are seen on the other lower-angle faults, also suggesting normal displacement. Along the extreme eastern edge of the map area, lower-angle faults cut units of the Trail Canyon Volcanic Sequence, juxtaposing them with Cambrian Nopah and Bonanza King lithologies.

In contrast to the lower-angle faults, the higher-angle faults have steep present-day dips (60-75°E), low fault-to-bedding angles (0-10°), sharp, unbrecciated contacts, and stratigraphic displacements of less than a few hundred meters. These relationships are well-displayed at Location B on Plate 1, where a higher-angle fault at ~10° to bedding juxtaposes footwall Nopah Formation against hanging wall Pogonip Limestone. The higher-angle faults cut units of the Trail Canyon Volcanic Sequence, but both truncate and are truncated by the E-W striking faults.

The third type of faults exposed in the lower Trail Canyon area are sub-vertical, E-W-striking faults with displacements of less than 100 – 200m. These faults are non-planar, displaying macroscopic warps with height to width ratios of ~1, as exhibited at Location C on Plate 1. E-W striking faults can truncate (Location D) or splay out of (Location E) the lower-angle faults. In the latter case, the lower-angle faults form a continuous surface that is

not offset by W-E striking faults. Like the other fault types, the E-W-striking faults cut units of the Trail Canyon Volcanic Sequence.

STRUCTURAL INTERPRETATION

The structurally highest, lower-angle fault in the Eastern Panamint fault system corresponds to the Burro Trail fault of Hunt and Mabey [1966]. The Burro Trail fault serves as an upper structural bound for the Eastern Panamint system (Plate I). The base of the system is buried beneath the alluvium of Death Valley in the Trail Canyon area, but it is well exposed to the south in the vicinity of Chuckwalla Canyon (Figure 1). Here the basal fault corresponds to the Amargosa "thrust" of Hunt and Mabey [1966]; to avoid confusion with the Amargosa Chaos of the Black Mountains, we refer to the structure near Chuckwalla Canyon as the Chuckwalla fault. The Chuckwalla fault places Precambrian Stirling Quartzite on basement gneisses at Chuckwalla Canyon. Below the fault, the gneisses exhibit Type I S-C mylonitic fabrics [Lister and Snoke, 1984] indicating hanging wall down-to-the-west (normal) displacement. The degree of mylonitization increases toward the Chuckwalla fault, and we infer that the mylonitic fabric is related to displacement on the fault.

The geometry of the Eastern Panamint system can be considered an extensional duplex [cf., Gibbs, 1984; Burchfiel et al., submitted]. Following the original definition of a duplex [Dahlstrom, 1970], we use the term extensional duplex in a purely geometric sense, without kinematic significance, because we can envision several distinctive scenarios in which different fault timing relationships could lead to the same duplex geometry. The Eastern Panamint duplex contains four types of faults, shown schematically on Figure 7. Subparallel, *roof and sole normal faults* (the Burro Trail and Chuckwalla faults, respectively) form bounding surfaces between which *roof-parallel* and *oblique normal faults* have extended the rocks within the duplex, and *transfer faults* separate differentially extended domains. Within the Trail Canyon area, the roof-parallel, oblique, and transfer faults appear as the lower-angle, higher-angle, and E-W-striking faults respectively.

AGE OF THE EASTERN PANAMINT FAULT SYSTEM

Many extensional fault systems in the Basin and Range Province exhibit tectonites that developed in a variety of deformational regimes, from high-temperature plasticity to cataclastic flow [e.g., Wernicke, 1981]. In most cases, the oldest tectonites are mylonites developed at intermediate structural levels [e.g., Davis et al., 1983; Hodges et al., 1987]. Consequently, we might expect the mylonitic fabrics developed below the Chuckwalla fault to be the oldest structural features of the Eastern Panamint system. Unfortunately, the age of this mylonitization is poorly constrained. Conventional K-Ar ages for biotites from the mylonitic gneiss of 14 ± 1.5 and 11 ± 1 Ma were reported by Stern et al. [1966; recalculated using the decay constants of Steiger and Jäger, 1977], but these ages probably reflect cooling of the gneiss through the biotite closure temperature after the intrusion of abundant felsic dikes (dated at 15 ± 1.5 Ma by Stern et al. [1966]), rather than the age of mylonitization.

McKenna [Chapter 2] reports $^{40}\text{Ar}/^{39}\text{Ar}$ results for a K-feldspar from the gneiss; the spectrum is disturbed and no age information can be extracted from it. Argon data for biotites and K-feldspars from the granitic dikes in the gneiss give good isochron ages at 10.65 – 10.8 and 10.4 Ma respectively. We interpret these dates to represent the age at which the footwall of the Eastern Panamint Fault System cooled through the biotite and K-feldspar closure temperatures by structural unroofing along the fault system, suggesting a Late Miocene age for the faulting. This conclusion is strengthened by the observation that faults within the Eastern Panamint Fault System have cut and rotated some units of the Trail Canyon Volcanic Sequence. Older volcanic units in the sequence have been tilted to a greater extent than younger units, and the youngest units unconformably overlie some of the westernmost faults of the duplex. Consequently, we assign a Late Miocene age (10.5 to 10.0 Ma) to the Eastern Panamint system.

FAULT RECONSTRUCTION

Deformation along the Eastern Panamint fault system can be restored assuming an original, approximately horizontal, attitude of the basal units

of the Trail Canyon volcanic sequence. The lowest units within the sequence (Figure 3) include ground breccias, fluviually reworked tuffs and oligomictic breccias of Ordovician Eureka Quartzite and Ely Spring Dolomite. All are sub-parallel with each other and the basal eruptive units. The fluviually reworked tuffs are laminated on scales of millimeters to centimeters, were deposited in a low-energy environment, and were arguably originally horizontal. Thus, we infer that the basal unconformity below the Trail Canyon Volcanic Sequence, and the basal units of the sequence itself, were originally subhorizontal.

With these constraints, a restored version of Section AA' is shown on Figure 5e. Extension within the exposed portion of the Eastern Panamint fault system is approximately 150-160%, although this represents a minimum estimate for the total extension within the duplex. A maximum estimate for extension within the duplex can be made using the observation that the Eastern Panamint fault system juxtaposes Siluro-Devonian units with the basement gneisses exposed at Chuckwalla Canyon — the upper limit of extension would then be equivalent to the stratigraphic thicknesses of pre-Silurian units. This would indicate a displacement along the Eastern Panamint fault system of a minimum of 7 km. This estimate of stratigraphic thicknesses has an uncertainty of a few kilometers, and should be viewed as an approximate limit only.

The reconstruction shown in Figure 5e also demonstrates that deformation in the Eastern Panamint fault system initiated at shallow depths, with moderate dips of 40-60°W. The present shallow dips of the roof and sole faults are due to syn- to post-deformational rotation of the entire duplex. This rotation is probably the same as that which folded the entire Panamint Mountains into a shallowly NNW-plunging anticline (the F₆ deformation of Hodges et al. [1987], see Figure 8 of this report), with an axial trace that is approximately coincident with the crest of the range. The timing, cause and nature of this folding are all somewhat controversial. Labotka et al. [1980] concluded that the NNW-trending anticline formed between 80 Ma and the intrusion of the Little Chief Stock at 10.8 Ma, while Wright et al. [1981] considered the Panamint Mountains to be a Mesozoic anticlinorium. On the contrary, we suggest that most of the folding

associated with the NNW-trending anticline post-dates Middle Miocene intrusion of the Little Chief Stock for the following reasons. Units in all exposures of the Trail Canyon Volcanic Sequence along the eastern limb of the Panamint Mountains currently dip 20-40° E, suggesting that 20-40° of tilting along an approximately N-S trending axis has occurred since deposition of the sequence at 10.5-10.0 Ma. The Harrisburg fault (see Figure 1), which formed prior to the intrusion of the Little Chief Stock, is also folded around this N-S axis. Near Telescope Peak, the Harrisburg fault dips approximately 10° E, while some 15 km northeast of Telescope Peak the fault dips 55°E, recording at least 45° of post-faulting folding. These data suggest that roughly 5-25° of rotation on the east side of the range occurred before 10.5-10.0 Ma and after formation of the Harrisburg fault. The amount of rotation increases eastward from the crest of the range, in a manner incompatible with simple block rotation of the range.

Labotka et al. [1980] suggested that some of the deformation associated with the folding of the range is accommodated by N-S striking, sub-vertical faults common throughout the central Panamint Mountains. Both Labotka et al. [1980] and Harding [1986] suggested that the deformation on some these faults was Precambrian in age, but most apparently had Tertiary offset. Reconnaissance mapping in upper Trail Canyon [McKenna and Hodges, unpub. data] shows that these steeply-east dipping normal faults cut the Miocene Harrisburg fault. We interpret these faults to represent the brittle accommodation of reverse drag along structurally lower, west-dipping listric normal faults [Hamblin, 1965]. These conclusions do not exclude the possibility of Mesozoic folding within the Panamint Mountains, but do indicate that the majority of folding took place after 10.8 Ma.

SIGNIFICANCE OF VOLCANIC CORRELATIONS

Correlation of the Trail Canyon Volcanic Sequence with the Rhodes Tuff and Sheephead Andesite allows constraints to be put on the timing and geometry of post-Oligocene extension between the Black and Panamint Mountains. The Rhodes Tuff and Sheephead Andesite are exposed in a WNW-trending belt at the southern terminus of the Black Mountains, where they lie unconformably on the Johnnie and Stirling Formations [Wright et al., 1984b]. Outcrops of the Sheephead Andesite, as shown on

Figure 2, are preserved only along two narrow belts within a wider area underlain by the Rhodes Tuff. Similarly, the basaltic-andesite of the Trail Canyon Volcanic Sequence is restricted to an area 5 km wide astride Trail Canyon. Figure 8 shows a cross section of the palinspastically restored Death Valley area, with controls provided by matching outcrops of the Sheephead Andesite and its Trail Canyon Volcanic Sequence equivalent. The apparent azimuth of extension is N55W°, in excellent agreement with the common assumption that Death Valley opened parallel to the N55°W strike of the Furnace Creek fault zone [e.g., Burchfiel and Stewart, 1966]. A maximum estimate for the extension between the Panamint and Black Mountains after 10.0 Ma is approximately 45 km.

Our estimate of the amount of extension would be decreased by the presence of Trail Canyon Volcanic Sequence under the alluvium of Death Valley, and would be increased by restoring the rotations and extension of the Rhodes Tuff within the Black Mountains. In the former case, a minimum estimate of approximately 25 km of post-10.0 Ma extension can be made by assuming that the entire width of Death Valley is underlain by units equivalent to the Trail Canyon Volcanic Sequence. Restoration of the extension within the Black Mountains is fraught with uncertainty, but we feel that at most only 10 km of extension could be added by this mechanism. Given these uncertainties, the total extension is 45^{+10}_{-25} km, and the average rate of extension between the Black and Panamint Mountains is 4.5 - 2.5 mm/a over the past 10 Ma.

LATE MIOCENE TO RECENT EXTENSION IN THE DEATH VALLEY AREA

Our interpretation of the the post-Late Miocene extensional development of the Death Valley area is shown by the cross sections in Figure 8. At present (Figure 8a), the Trail Canyon and Rhodes Tuff - Sheephead Andesite sequences are separated by two major Neogene normal fault systems: the Amargosa fault system and the frontal faults of the Black Mountains (including the Death Valley "turtlebacks"). We infer that 25-55 km of extension between the correlative volcanic sequences was largely accommodated by movement on these fault systems. Removal of this deformation results in the geometry shown in Figure 8b for Late Miocene

time, subsequent to movement on the Eastern Panamint fault system. The reconstruction shown indicates that the Eastern Panamint system developed immediately west of the modern, western foot of the Black Mountains. We suggest that the Trail Canyon Volcanic Sequence in the footwall of the Amargosa system now lies buried beneath Death Valley. Restoration of displacement along the Eastern Panamint fault system is constrained by the presence of gneisses in its footwall, and their inferred correlation to the gneisses exposed in the central Panamint Mountains [Labotka et al., 1980]. The implied Middle Miocene reconstruction (Figure 8c) restores the Harrisburg detachment and Panamint thrust such that they project above the present erosional level in the Black Mountains.

REGIONAL SIGNIFICANCE

Wernicke et al. [1988] suggested that the likely correlation of the Panamint thrust fault in the Panamint Mountains with the Chicago Pass thrust in the Nopah Range (Figure 2) implies roughly 90 km of extension over the past 15 million years. They inferred, using the data of Wright et al. [1984], that extension rates over the past 10 million years were less than half the rates between 15 and 10 Ma. The reconstructions shown in Figure 8 suggest that at least 25-55 km of the total 90 km of extension occurred after 10.0 Ma, even if we assume no extension between the Black Mountains and the Nopah Range between 10.0 Ma and the present. A *minimum* estimate for the average extension rate for the last 10 m.y. between the Nopah Range and the Panamint Mountains is thus 6.5 - 2.5 mm/a, while a *maximum* estimate for the extension rate between 15-10 Ma is 13-7 mm/a. Within the precision of the available data, there is no clear distinction between extension rates in the Nopah - Panamint transect before and after 10 Ma.

Our results contribute to the growing quantitative database on extension in the Death Valley corridor. Figure 9 illustrates currently available constraints on the ages, movement directions, and displacement rates of major detachment systems within the corridor plotted as a function of approximate paleolongitude. Although only two of the well-studied structures initiated prior to Late Miocene time, the available data suggest that extension directions in the Death Valley corridor may have been variable prior to approximately 10 Ma, at which time an overall

northwesterly extension direction became firmly established. Although there was a general tendency for extension to have initiated and ceased westward with time across the corridor [Wright et al., 1984a], this generalization breaks down in the area between the Black Mountains and the Owens Valley over the Late Miocene - Recent interval.

CONCLUSIONS

The Eastern Panamint fault system constitutes an extensional duplex which developed in Late Miocene time. The initial dip of the system was moderately westward, and the total stratigraphic displacement across the system was between 3 and 7 kilometers. Correlation of the Trail Canyon Volcanic Sequence with the Rhodes Tuff and Sheephead Andesite in the Black Mountains supports the hypothesis of Stewart [1983] that large-scale extension occurred between the Black Mountains and Panamint Mountains, but our results contradict Stewart's suggestion that this extension was accommodated by a detachment system which included the Amargosa Chaos in the Black Mountains and the Eastern Panamint duplex. Specifically, the Eastern Panamint and Amargosa systems initiated with different geometries (moderate vs. shallow westward dips) at different times (during vs. after Late Miocene eruption of the Trail Canyon - Sheephead - Rhodes volcanic sequence). The available data indicate that horizontal and vertical displacements of the Panamint Mountains relative to the Black Mountains were basically decoupled: most of the 25 to 55 kilometers of horizontal displacement was accommodated by the Amargosa system and more recent faults along the western front of the Black Mountains, while most of the uplift of the Black Mountains relative to the Panamint Mountains (> 5 km; Figure 8c) occurred by movement on the Eastern Panamint system.

ACKNOWLEDGMENTS

Assistance in the field was provided by Jim Cureton and Elizabeth Spizman; Liz Schermer, Joan Fryxell and Jim Knapp made useful observations and comments on the ideas presented herein. Lauren Wright and Terry Pavlis made thorough reviews of an earlier version of the manuscript; L. Wright made many excellent comments on the map and cross-sections. Finally, thanks to Stan Hart for access to the geoalchemy labs. Support for this research was provided by National Science Foundation grants EAR-8319768 and EAR-8512283 to KVH, and EAR- to SRH.

REFERENCES

- Bachman, S.B., Pliocene-Pleistocene break-up of the Sierra Nevada- White-Inyo Mountains block and formation of Owens Valley, *6*, 461-463, 1978.
- Burchfiel, B.C. and Stewart, J.H., "Pull-Apart" origin of the central segment of Death Valley, California, *Geol. Soc. Amer. Bull.*, *77*, 439-442, 1966.
- Cemen, I., Drake, R. and Wright, L.A., Cenozoic sedimentation and sequence of deformational events at the southeastern end of the Furnace Creek strike-slip fault zone, Death Valley region, California, *in, Strike-slip Deformation, Basin Formation, and Sedimentation*, Biddle, K. T., and Christie-Blick, N., eds., *Soc. Econ. Paleon. Min. Spec. Pub.*, *37*, 127-141, 1985.
- Curry, H.D., "Turtleback" fault surfaces in Death Valley, California [abs], *Geol. Soc. Amer. Bull.*, *49*, 1875., 1938.
- Dahlstrom, C.D.A., Structural Geology in the eastern margin of the Canadian Rocky Mountains, *Bull. Can. Pet. Geol.*, *18*, 332-406, 1970.
- Davis, G.H., Shear-zone model of the origin of metamorphic core complexes, *Geology*, *11*, 342-347, 1983.

- Gibbs, A.D., Structural evolution of extensional basin margins., *J. Geol. Soc. Lond.*, 141, 609-620, 1984.
- Hamblin, W.K., Origin of "reverse drag" on the downthrown side of normal faults, *Geol. Soc. Amer. Bull.*, 76, 1145-1164, 1965.
- Harding, M., Structural evolution of the Wildrose Peak area, Death Valley, California,
- Hodges, K.V., Walker, J.D. and Wernicke, B.P., Footwall structural evolution of the Tucki Mountain detachment system, Death Valley region, southeastern California, in *Continental Extensional Tectonics*, edited by Coward, M.P., Dewey, J.F. and Hancock, P.L., pp. 393-408, Geological Society of London, Oxford, 1987.
- Hunt, C.B. and Mabey, D.R., Stratigraphy and structure, Death Valley, California, *U. S. Geol. Surv. Prof. Pap.*, 494-A, 162 pp, 1966.
- Labotka, T.C., Albee, A.L., Lanphere, M.A. and McDowell, S.D., Stratigraphy, structure, and metamorphism in the central Panamint Mountains (Telescope Peak Quadrangle), Death Valley area, California, *Geol. Soc. Amer. Bull.*, 91, pt. I 125-129; pt II. 843-933, 1980.
- Lister, G.S. and Snoke, A.W., S-C mylonites, *J. Struct. Geol.*, 6, 617-638, 1984.
- Minster, J.B. and Jordan, T.H., Vector constraints on western U.S. deformation from space geodesy, neotectonics, and plate motions, *J. Geophys. Res.*, 92, 4798-4804, 1987.
- Noble, L.F., Structural features of the Virgin Spring area, Death Valley, California, *Geol. Soc. Am. Bull.*, 52, 941-1000, 1941.
- Otton, J.K., Geologic features of the Central Black Mountains, Death Valley, California, in *Geologic features, Death Valley, California*, edited by Troxel, B.W. and Wright, L.A., pp. 45-50, 1976.

- Steiger, R.H. and Jäger, E., Subcommittee on geochronology: Convention on the use of decay constants in geo- and cosmochronology, *Earth Planet. Sci. Lett.*, 36, 359-362, 1977.
- Stern, T.W., Newall, M.F. and Hunt, C.B., Uranium-Lead and potassium-argon ages of parts of the Amargosa Thrust complex, Death Valley, California, *USGS Prof. Pap. 550-B*, B142-B147, 1966.
- Stewart, J.H., Extensional tectonics in the Death Valley area, California: Transport of the Panamint Range structural block 80 km northwestward., *Geology*, 11, 153-157, 1983.
- Troxel, B.W., Significance of Quaternary fault patterns, west side of the Mormon Point turtleback, southern Death Valley, California: A model of listric normal faults, in *Quaternary tectonics of southern Death Valley, California*, edited by Troxel, B.W., pp. 37-40, Friends of the Pleistocene, Shoshone, California, 1986.
- Troxel, B.W. and Wright, L.A., Tertiary extensional features, Death Valley region, eastern California, in *Centennial Field Guide*, edited by Hill, M.L., pp. 121-132, Cordilleran Section of the Geological Society of America, Boulder, Colorado, 1987.
- Wernicke, B., Axen, G.J. and Snow, J.K., Basin and Range extensional tectonics at the latitude of Las Vegas, Nevada, *Geol. Soc. Amer. Bull.*, 100, 1738-1757, 1988.
- Wernicke, B.P., Low-angle faults in the Basin and Range Province—Nappe tectonics in an extending orogen, *Nature*, 291, 645-648, 1981.
- Wright, L.A., Drake, R.E. and Troxel, B.W., Evidence for the westward migration of severe Cenozoic extension, southeastern Great Basin, California, *Geol. Soc. Amer. Abs. with Prog.*, 16, 701, 1984.
- Wright, L.A., Kraemer, J.H., Thornton, C.P. and Troxel, B.W., Type sections of two newly-named volcanic units of the central Death Valley volcanic field, eastern California, in *Geology of the northern one-half*

Confidence Hills 15' Quadrangle, Inyo County, California, pp. California Division of Mines and Geology, 1984.

Wright, L.A. and Troxel, B.W., Limitations on right-lateral, strike-slip displacement, Death Valley and Furnace Creek Faults zones, California, *Geol. Soc. Amer. Bull.*, 78, 933-958, 1967.

Wright, L.A. and Troxel, B.W., Shallow-fault interpretation of Basin and Range structure, southwestern Great Basin, in *Gravity and Tectonics*, edited by de Jong, K.A. and Scholten, R., pp. 397-407, Wiley and Sons, New York, 1973.

Wright, L.A. and Troxel, B.W., Geology of the northern half of the Confidence Hills 15' Quadrangle, Death Valley region, eastern California: The area of the Amargosa chaos, *Calif. Div. Mines Geol. Map Sheet*, 34, 1984.

Wright, L.A., Troxel, B.W., Burchfiel, B.C., Chapman, R.H. and Labotka, T.C., *Geologic cross section from the Sierra Nevada to the Las Vegas Valley, eastern California to southern Nevada*, pp. 1981.

FIGURE CAPTIONS

Figure 1. Tectonic map of the northern and central Panamint Range. See Figure 2 for location, structural packages (shown in key) are separated by normal faults shown by heavy black lines. Abbreviations are: AP, Aguerberry Point; BTF, Burro Trail fault; BWW, Black Water Wash, CW, Chuckwalla Canyon; EF, Emigrant fault; HCP, Hall Canyon Pluton; HF, Harrisburg fault; LCS, Little Chief Stock; PT, location of Panamint Thrust; SG, Skidoo Granite; TC, Trail Canyon; TM, Tucki Mountain; TP, Telescope Peak. The study area is indicated by the box labeled "Plate 1".

Figure 2. Simplified geology and general location map for the Death Valley area. Large box shows area of Figure 1; line shows cross section trace of Figure 8. Faults are shown by heavy lines (teeth on upper plate of thrust faults, barbs on hanging wall of normal faults); contacts are shown by thinner lines. Rock types are identified by numbered key: 1,

Recent alluvial fill; 2, older (Pliocene to Recent) fanglomerate; 3, Trail Canyon Volcanic Sequence and correlative Rhodes Tuff and Sheephead Andesite; 4, Cenozoic volcanic rocks; 5, Cenozoic intrusive rocks; 6, Mesozoic intrusive rocks; 7, Miogeoclinal sedimentary rocks; 8, Metamorphosed Miogeoclinal sedimentary rocks; 9, Amphibolite grade metamorphic rocks and basement crystalline rocks. Abbreviations are: AF, Amargosa Fault; EPFS, Eastern Panamint Fault System; FCFZ, Furnace Creek fault zone; HF, Harrisburg Fault; GWR, Greenwater Range; LCS, Little Chief Stock; NR, Nopah Range; RSR, Resting Spring Range.

Figure 3. Stratigraphy of the Trail Canyon Volcanic Sequence (in pocket).

Figure 4. Generalized stratigraphic columns for the Trail Canyon Volcanic Sequence [this report] and the Rhodes Tuff and Sheephead Andesite [Wright et al., 1984b]. Geochronological constraints are from: Wright et al. [1984b, Rhodes Tuff and Sheephead Andesite], and McKenna [Chapter 2].

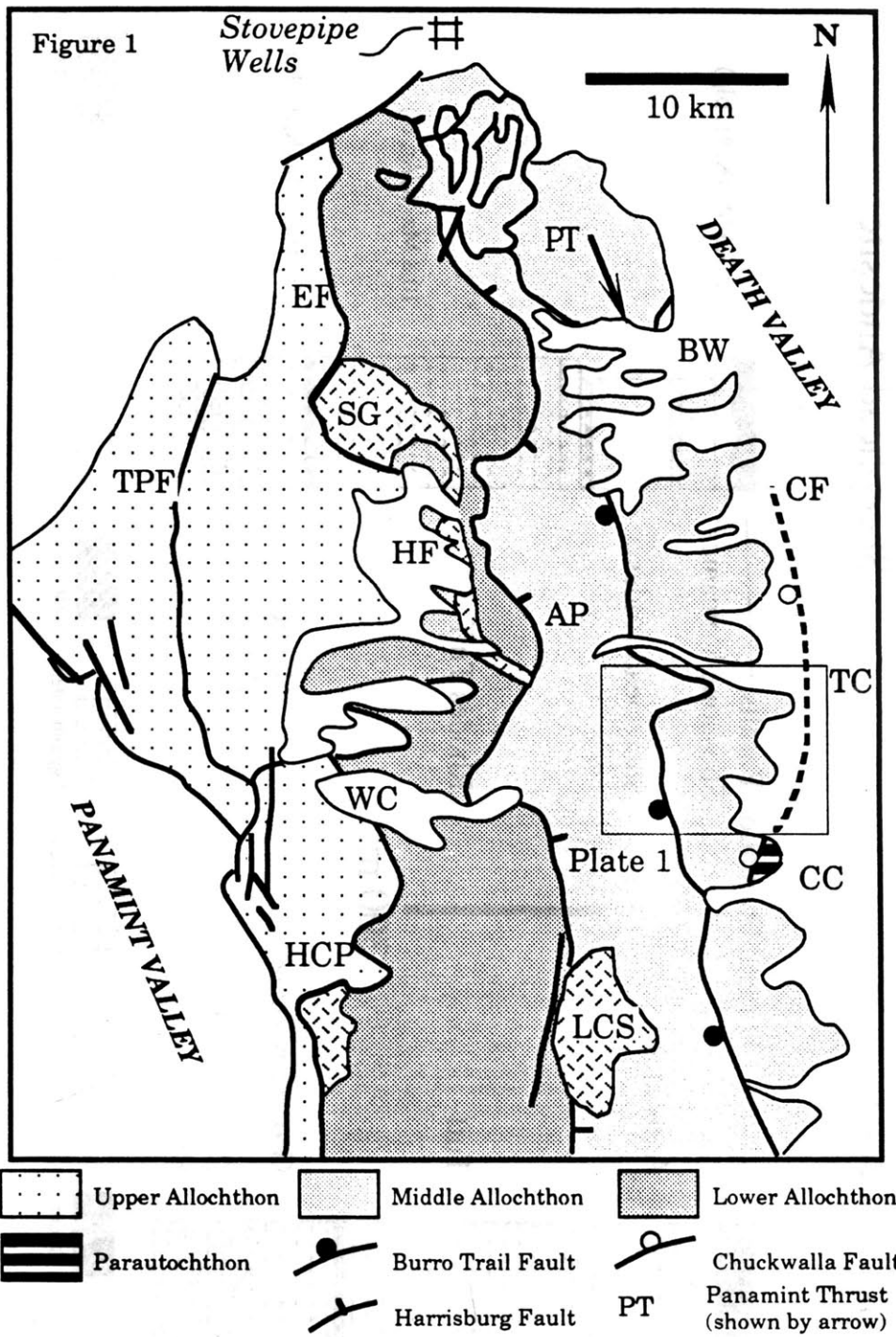
Figure 5. Cross sections of the Trail Canyon Area; section lines are shown on Plate 1. A-D: Interpretive cross sections. E: Restored version of section AA', rotated to paleohorizontal with controls provided by volcanic units. Unit Tvu is undifferentiated volcanic rocks; individual units are omitted for clarity. (In pocket).

Figure 6. Photograph and interpretive line drawing of a typical lower-angle fault, exposed at Location A (see Plate 1), looking N10°E; note 2m scale on right edge of line drawing. Intensely brecciated Ordovician Ely Spring Dolomite (Tboes) and Ordovician Eureka Quartzite (Tboe) separate unbrecciated units of Ely Spring, Eureka Quartzite (in the hanging wall; the Eureka is out of view on the left) and Ordovician Pogonip Group (Op, footwall). The brecciated zone is 4 to 8 m thick and is formed by overlapping, lensoidal lens of individual units with diffuse (decimeter-wide) contacts. Displacement along the fault zone was in a normal sense with the hanging wall to the west, or left; the displacement appears to be up dip due to post-displacement rotation of the eastern Panamint Mountains. (In pocket).

Figure 7. Block model for an extensional duplex, courtesy of Prof. J. D. Walker, University of Kansas. The subparallel roof and sole faults bound a volume extended by additional normal faults (black lines with ball symbols). Intrasheet transfer faults (gray lines) separate domains of differential extension within the duplex. These two fault types are equivalent to the lower-angle and W-E striking faults within the Trail Canyon area.

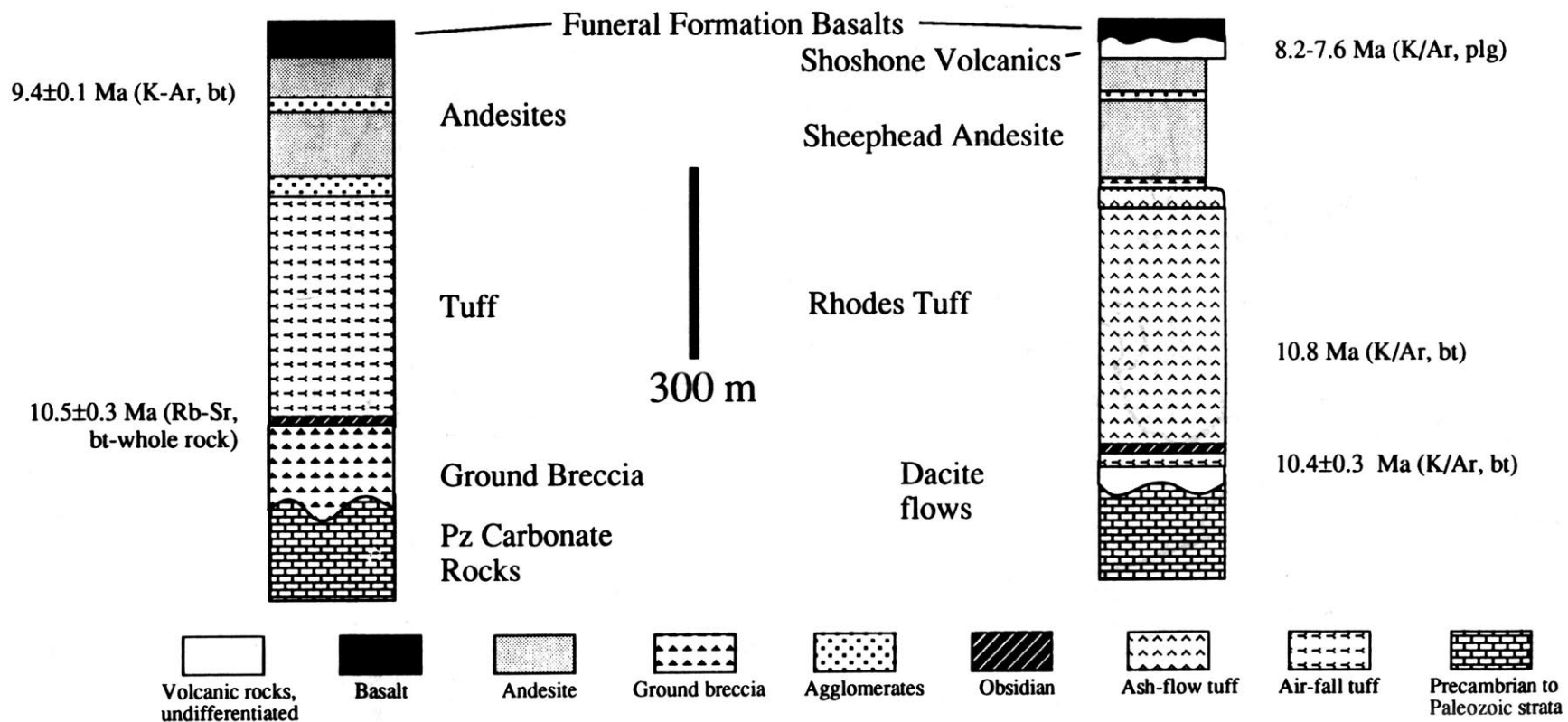
Figure 8. Palinspastic reconstruction of the Panamint Valley-Death Valley-Black Mountains (see Figure 2 for location). AFS, Amargosa Fault System; EF, Emigrant fault; EPFS, Eastern Panamint Fault System; HF, Harrisburg Fault; LCS, Little Chief Stock; PT, Panamint Thrust; PVFZ, Panamint Valley Fault Zone; Tail Canyon Volcanic Sequence, Trail Canyon Volcanic Series; RT/SA, Rhodes Tuff and Sheephead Andesite; j/st, contact between Precambrian Johnnie and Sterling Formations; gn/pcs, contact between gneissic basement rocks and Precambrian sedimentary rocks. Tectonic packages are shaded as in Figure 1, except for the parautochthon, which is unpatterned.

Figure 9. Synoptic graph of time of extension versus the approximate longitude of the extensional fault for the Death Valley Area. Location of faults are shown on Figure 2, abbreviations used (and sources for data) are: AF, Amargosa and Death Valley faults [this report]; EF, Emigrant fault [Hodges et al., 1989]; EP Eastern Panamint fault system [this report]; HF, Harrisburg fault [Hodges et al., 1987]; KR, Kingston Range Detachment [Burchfiel et al., in preparation]; OV, Owens Valley and Independence faults [Bachman, 1978]; PV, Panamint Valley; TP, Towne Pass fault. Wedges give the direction (with its uncertainty) and the rate (mm/a, rates given adjacent to the wedges). The wedges are oriented with north vertical. Also given are the Holocene extension rate [Minster and Jordan, 1987] and a possible net extension vector for post-20 Ma extension [Wernicke et al., 1988]. While the age of initiation of extension generally youngs to the west, both rates and direction of extension vary widely over time and space.



Trail Canyon Volcanic Sequence

Rhodes Tuff Sheephead Andesite



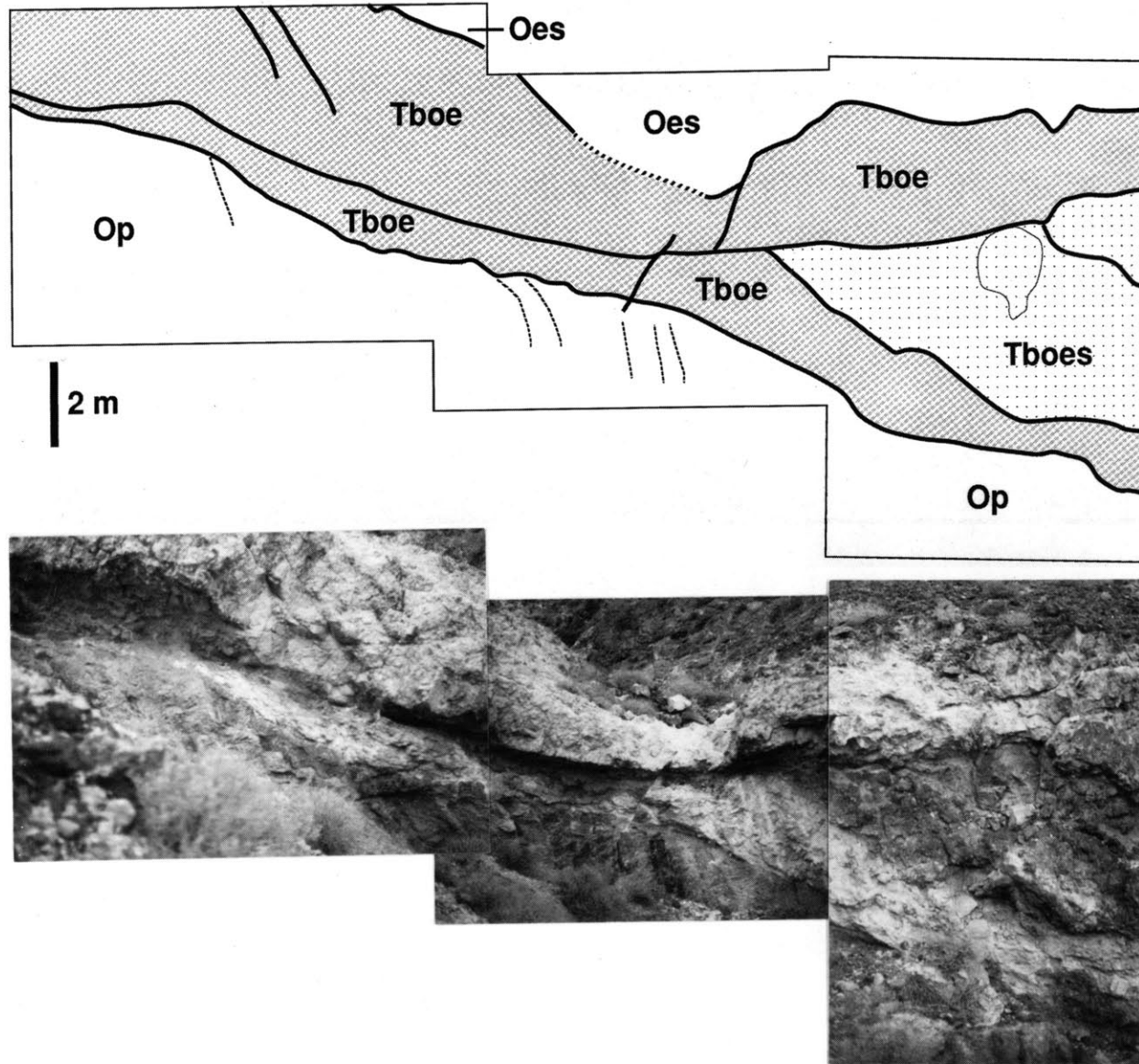


Figure 7

Block Model for an Extensional Duplex

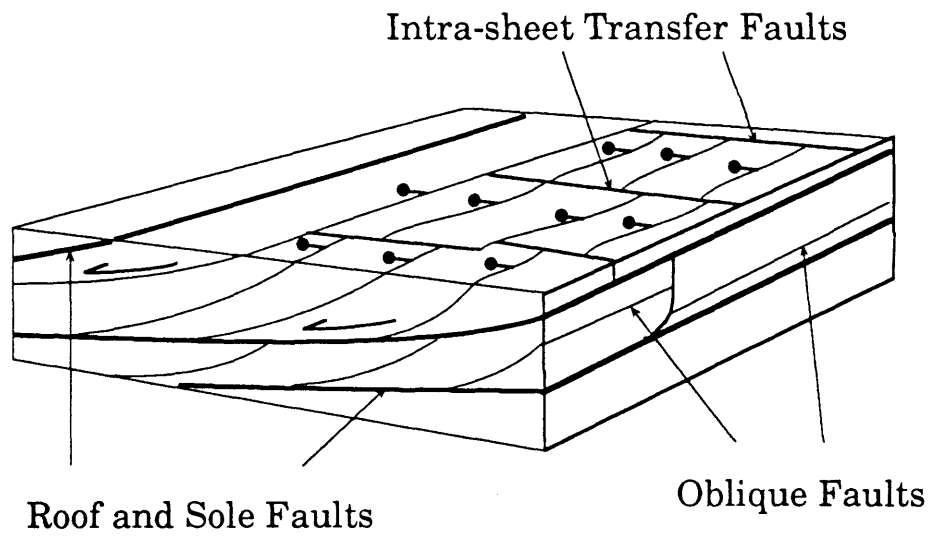
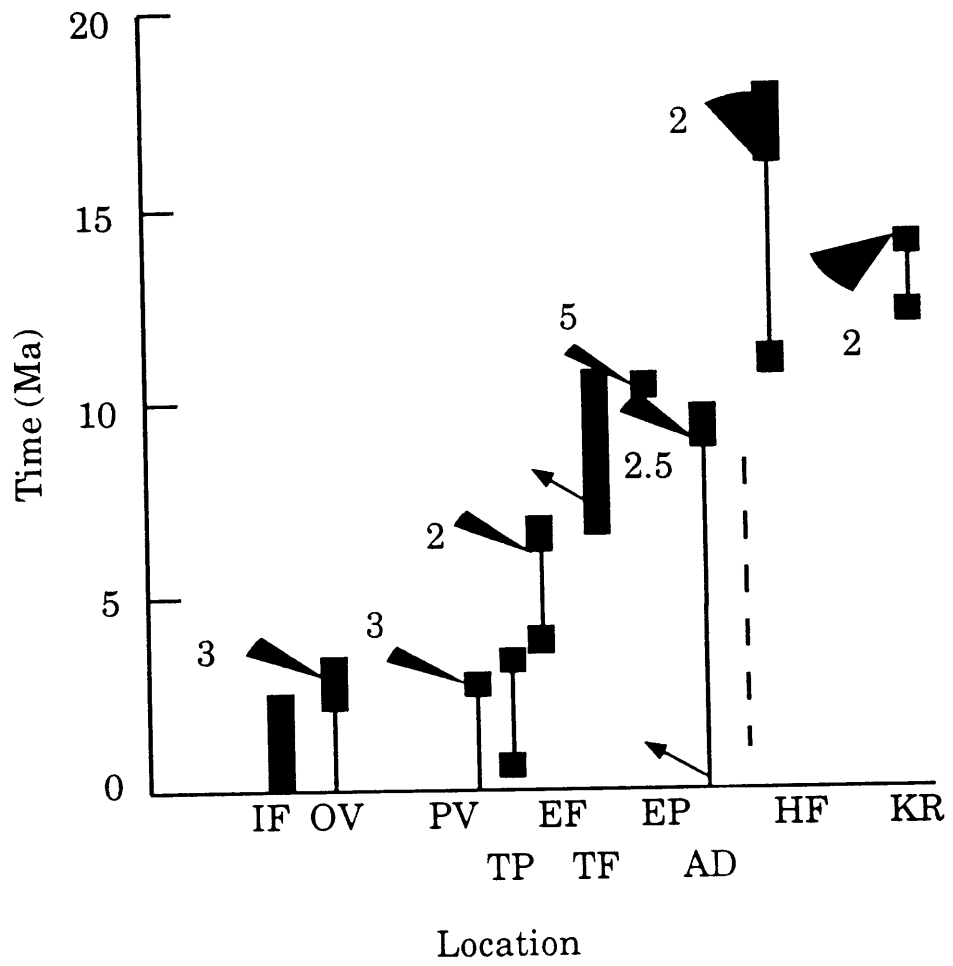


Figure 9



CHAPTER 2

TIME-TEMPERATURE HISTORY OF
EXTENSION IN THE PANAMINT AND
BLACK MOUNTAINS, DEATH VALLEY,
CALIFORNIA

ABSTRACT

This paper reports new $^{40}\text{Ar}/^{39}\text{Ar}$ and Rb/Sr dates along a transect through the Panamint and Black Mountains of the Death Valley region, eastern California. We present step heating data from 20 samples (mineral and glass separates) collected from Proterozoic basement gneisses, Cretaceous and Cenozoic age intrusive rocks, and Cenozoic extrusive rocks that crop out within these ranges. Two concordant biotite cooling ages (10.80 ± 0.06 Ma) and two concordant K-feldspar cooling ages (10.4 ± 0.15) from dikes in the footwall of the Eastern Panamint Fault system suggest initiation of deformation along the fault near 10.5 Ma. Within the volcanic rocks in the hanging wall of the fault, a lower unit returned a biotite age of 10.3 ± 0.3 , while a glass separate from an upper unit returned an excellent plateau at 9.97 ± 0.16 Ma. These volcanic rocks were faulted by some strands of the Eastern Panamint Fault System, giving a lower bound to the time of deformation along this fault.

The ages of samples from the Black Mountains, along the east side of Death Valley, reflect the unroofing and rotation of the range in the Late Miocene. Hornblende and biotite samples from the Willow Spring Diorite give a range of ages from 10.36 to 9.96 Ma and 9.19 and 8.41 Ma respectively. The relations between the structural positions of the samples, and the relative differences in their hornblende and biotite ages suggests that the Black Mountains were rotated about a horizontal axis during their unroofing. The rotation occurred between approximately 10 and 9 Ma, with a strain rate of $4\pm 1 \times 10^{-13} \text{ sec}^{-1}$, or approximately an order of magnitude greater than the deformation along the earlier Eastern Panamint Fault system.

INTRODUCTION

Although an area of active study for a century, relatively few detailed kinematic analyses have been made within the Basin and Range. A complete understanding of the forces which drive the extension within the Basin and Range requires detailed information on the geometry, timing, and location of structures which have accommodated the extension. In addition, time-temperature information is necessary to understand strain rates and unroofing rates associated with extension. The Death Valley area is one transect in the Basin and Range for which good regional [Wernicke et al., 1988] and detailed local constraints are available for the geometry of the surfaces which accommodated extension. In this contribution, we integrate existing structural constraints on the geometry of extension in the Death Valley area with time-temperature data provided by $^{40}\text{Ar}/^{39}\text{Ar}$ and Rb/Sr geochronology to form a kinematic model of the strain and evaluate strain rates during Neogene extension in the area. The geochronometry we report here constrains the timing of displacement on the major fault structures active during the extension, while geometric constraints (some reported previously in McKenna and Hodges [in press], and Hodges et al. [in press]) provide information on the kinematic evolution of a 100 km-scale extensional system within the Basin and Range Province.

GEOLOGIC SETTING

Death Valley occupies the central section of an extensional system that stretches from the Sierra Nevada in the west to the Spring Mountains in the east (Figure 1). Estimates for the total post-Sevier age extension in this system range from less than 100 [Stewart, 1983] to over 250 km [Wernicke et al., 1988]. Neogene extension within the central portion of this area, based upon the reconstructions of Wernicke et al. [1988], is approximately 150 km. Currently, extension in the Basin and Range is proceeding at a rate of 10 ± 2 mm/yr along a $N60^\circ W \pm 20^\circ$ azimuth [Minster and Jordan, 1987].

The study area consists of the mountain ranges which bound central Death Valley: the Black Mountains to the east and the Panamint Mountains to the west. The Black Mountains consist of basement gneisses,

amphibolite facies to unmetamorphosed miogeoclinal sediments, abundant Cenozoic age siliceous to intermediate composition intrusive rocks, and Tertiary volcanic and clastic rocks [Drewes, 1966; Otton, 1977]. The Cenozoic volcanic rocks rest with slight unconformity over the miogeoclinal sediments, and this package as a whole currently dips steeply eastward [Holm and Wernicke, 1989]. Much of the western part of the Black Mountains is supported by the Willow Spring Diorite, a Miocene hornblende diorite that is variably metamorphosed [Asmerom et al., 1990]. The diorite is intruded by granite to quartz monzonite stocks [Otton, 1977]. Two major fault systems are present in the Black Mountains: a system of low-angle normal faults in the southern Black Mountains that corresponds to the Amargosa "chaos" of Noble [1941] and Wright and Troxel [1984], and a group of NW-plunging, domiformal, normal faults (the Death Valley "turtlebacks" of Curry [1938]) that lie along the western foot of the Black Mountains and characterize the eastern margin of the active central Death Valley basin [Otton, 1976; Troxel, 1986; Wright et al., 1974; Burchfiel et al., in press]. Mapping by Burchfiel et al. [in press] indicates that these faults dipped 17° to the northwest when they were active.

The tectonic framework of the study area is shown in Figures 1 and 2. The Panamint Mountains consist of four tectonic packages [Hodges et al., in press]: 1) a Parautochthon, consisting predominantly of Precambrian basement gneisses intruded by younger granitic and intermediate composition dikes [Hunt and Mabey, 1966; Stern and Newall, 1966], 2) a Lower Allochthon, consisting of amphibolite grade basement gneisses and Precambrian to Paleozoic lower amphibolite facies metasedimentary rocks, 3) a Middle Allochthon, including unmetamorphosed to greenschist facies upper Precambrian to upper Paleozoic strata unconformably overlain by Neogene sedimentary and volcanic units, and 4) an Upper Allochthon, consisting of displaced fragments of the Lower and Middle Allochthons as well as Latest Miocene to Pliocene fan conglomerates and volcanic flows. Two large granitoid plutons are present within the Panamint Mountains. The contact between the Lower and Middle Allochthon is intruded by the Little Chief Stock, a hornblende+biotite-granite porphyry intruded into the central Panamint Mountains. The petrology and mineralogy of the stock are discussed in detail by McDowell [1974, 1978]. McDowell suggested that it

was intruded at high levels within the crust, and may have vented to the surface. The Skidoo Granite is a 101 ± 8 Ma sill-like body which is intruded into the Lower Allochthon in the north-central Panamint Mountains [Hodges et al., in press].

The Upper, Middle, and Lower Allochthons are separated by a diachronous but uniformly top to the north-west collection of normal faults which together constitute the Tucki Mountain Detachment system. The Harrisburg Fault, along which deformation ceased prior to 10.8 Ma [Hodges et al., in press], is the oldest fault in the system, and separates the Lower and Middle Allochthons. The Eastern Panamint Fault system separates the Parautochthon from structurally higher tectonic packages; its geometry was described by McKenna and Hodges [in press, Chapter 1] as an extensional duplex [Gibbs, 1984]. The duplex is framed by shallowly west-dipping normal faults which acted as roof and sole faults, which bound a volume dissected by steeply east-dipping, bedding parallel normal faults. In the northern Panamint Mountains, the duplex has a thickness of a few kilometers. At the southern end of the Panamint Mountains, the roof and sole faults apparently converge to a single fault surface [Hunt and Mabey, 1966]. The Emigrant Fault separates the Upper and Middle Allochthons, and was apparently active between 6.5 and 3.7 Ma [Hodges et al., 1988]. The Emigrant Fault cuts segments of the Harrisburg fault, and displaced sections of the Harrisburg Fault can be found in the hanging wall of the Emigrant Fault [Harding, 1986; Hodges et al., in press].

There has been substantial debate regarding the age, sequence, and amount of displacement on the normal fault systems that accommodated extension within the Death Valley Extended Area. Although the turtleback surfaces in the Black Mountains cut Holocene deposits and are therefore quite young [Troxel and Wright, 1987], most of the movement on the Amargosa system appears to have occurred in Late Miocene to Early Pliocene time [Wright and Troxel, 1984]. The Amargosa fault is currently a west dipping to flat structure which truncates Miocene volcanic rocks [Wright and Troxel, 1984] within the southern Black Mountains. This fault was imaged by the Death Valley COCORP line, and was thought by Serpa et al. [1988] to lie approximately midway between the Panamint and Black

Mountains, and to dip approximately 30°W. The Eastern Panamint Fault System was inferred by Hunt and Mabey [1966] to be correlative with the Amargosa Fault, but McKenna and Hodges [in press] have shown that the Eastern Panamint system initiated at high angle (60°W) and was not correlative with the Amargosa Fault. The samples analyzed for this study were chosen to constrain the absolute and relative ages of deformation and unroofing along these faults.

OTHER AR WORK

Previous $^{40}\text{Ar}/^{39}\text{Ar}$ studies in the area have been carried out by Labotka et al. [1985] in the Panamint Mountains, Asmerom et al. [1990] in the Black Mountains, and DeWitt et al. [1988] in the Funeral Mountains. Labotka et al. [1985] analyzed mineral separates from a variety of igneous and metamorphic units in the western Panamint Mountains. The results formed two groups; an older age group with biotite and muscovite cooling ages of 150 Ma, and a younger group with latest Cretaceous muscovite and biotite cooling ages. Asmerom et al. [1990] reported $^{40}\text{Ar}/^{39}\text{Ar}$ data for two splits of hornblende from a single sample of diorite from the Black Mountains that returned plateau and isochron dates of 10.1 ± 0.8 Ma and 9.9 ± 0.2 Ma respectively. The results of DeWitt et al. [1988] are "complex"; excess Ar in the Funeral Mountains is pervasive and highly variable over short distances, and few of the samples returned usable plateau or isochron dates. In general, the data suggest two thermal events of early and late Cretaceous Age. The results of Labotka et al. [1985] and Asmerom et al. [1990] are discussed further below.

PROCEDURES

$^{40}\text{Ar}/^{39}\text{Ar}$

Mineral separates of 60 to 120 mesh size (250 to 125 microns) were prepared by standard heavy liquid, magnetic separator, and paper shaking methods, cleaned with reagent grade acetone and deionized water in an ultrasonic bath, and finally air dried. These separates were then picked by hand to greater than 99% purity. Individual samples, ranging from 17 to 400 mg in mass, were wrapped in aluminium foil boats and sealed in glass vials along with the monitor minerals prior to irradiation.

All samples were irradiated simultaneously for 30 total hours at the 1 MW Triga reactor at the U.S.G.S. in Denver, Colorado. The argon isotopic composition of the samples were measured in static mode on a Mass Analyzer Products 215 Rare Gas mass spectrometer with a sensitivity of 9.736×10^{-13} moles/V (The use of trade names is not an endorsement and is for identification purposes only). Analyses were corrected for mass fractionation using a measured atmospheric ratio of 298.9. Corrections for irradiation-produced ^{40}Ar (from K) and ^{39}Ar (from Ca) were determined from production rates measured on pure K_2SO_4 and CaF_2 salts irradiated with the samples, while corrections for Cl-derived ^{37}Ar were made using the method of Roddick [1983]. Measured values of ^{37}Ar and ^{39}Ar were corrected for post-irradiation decay. Detailed description of the equations for these corrections can be found in Snee and Chesley [in press].

J values for the analyses were calculated using the irradiation monitor MMhb-1 (1.555 weight percent K_2O), with an accepted K-Ar age of 519.4 Ma [Alexander et al., 1978; Dalrymple et al., 1981]. Imprecisions in J were calculated from the reproducibility of split gas fractions for each monitor, and are typically in the range of 0.15 to 0.35% (1σ). J values for each sample are interpolated from surrounding monitors, and have uncertainties similar to those of the monitors. Note that these uncertainties are not considered in determining the presence of a plateau in a sample. Uncertainties in date calculations for individual steps were assigned using the equations of Dalrymple et al. [1981]. All isotopic abundances and decay constants used here were those of Steiger and Jäger [1977].

The ability to extract multiple geochronologically relevant dates from a single sample produces an assortment of terms describing the meaning and geological relevance of the $^{39}\text{Ar}/^{40}\text{Ar}$ data. Within this paper, we use the term "date" to refer to an analytically determined number, whereas "age" refers to a date interpreted as having geologic significance. We utilize several different types of ages in this paper. A plateau age (t_p) is defined as the mean age from three or more contiguous, concordant release steps in a sample, where concordancy is defined at the 2σ level [Dalrymple and Lanphere, 1969]. The preferred age (t_A) is defined as the age which

best estimates the age of contiguous steps which do not define a plateau; in short, it is a poor person's plateau.

We also utilize inverse isochron, or isotope correlation, ages (t_I), determined through the inverse isochron method of Turner [1971]. The isochron approach is often helpful in elucidating the presence of non-atmospheric initial Ar and in determining dates for samples, particularly K-feldspars, with excess Ar superimposed upon the *in situ* signal. In this technique [Dalrymple et al., 1988; Roddick, 1978], a sample has a date inversely proportional to the $^{39}\text{Ar}/^{40}\text{Ar}$ intercept on a $^{36}\text{Ar}/^{40}\text{Ar}$ vs. $^{39}\text{Ar}/^{40}\text{Ar}$ plot. Because the date of a sample is inversely proportional to the "x"-intercept of the regression, the uncertainties in the date are not symmetrically distributed about the resulting date. The degree of asymmetry is proportional to the magnitude of the "x" intercept, and so will be greater for younger samples. Despite this, the precision of the analyses presented here are sufficiently good that this asymmetry is small, and the mean uncertainty is given instead. These uncertainties include all sources of error, including those in production ratios, isotope abundances, and J values.

Blank values were *not* subtracted from the measured isotope abundances prior to isochron analysis for the following reasons. Firstly, the blank abundances are clearly a function of temperature, with lower temperature steps having a smaller absolute blank than higher temperature steps. This results in over-correction for the lower temperature (and often low abundance) heating steps. Secondly, blank levels during sample analysis were very low compared to sample signals (often less than 0.1%), and can be safely ignored. Finally, as pointed out by Roddick et al. [1980], non-atmospheric blank ratios require correction because of their potential affect on ^{36}Ar abundances. During the time of the analyses, blank ratios were consistently less than 1000, or approximately 3 times atmospheric levels, thus reducing the effect of this problem. The correctness of this procedure can be judged by comparing isochron results to age spectrum results for samples with good plateaux. A least-cubes regression [York 1969] was used to evaluate the isotopic ratio data. Goodness of fit was measured via the MSWD; samples with an $\text{MSWD} \leq 2.5$

were considered to define an isochron. For samples with an $MSWD \geq 2.5$, the scatter of data about a regression line is greater than could be expected from experimental error, and these samples are considered to define "errorchrons".

Typically $^{39}\text{Ar}/^{40}\text{Ar}$ dates are interpreted as recording the age at which a system closed to the diffusion of Ar. Closure temperatures (T_C) are a weak function of cooling rate, and for geologically relevant cooling rates, closure temperatures for hornblende and biotite are 850-750 K [Harrison, 1981] and 570-530 K [Harrison et al., 1985] respectively. Because the closure temperature of K-feldspar is determined by the structural state of the crystal, Arrhenius plots were made for the samples analyzed here, and closure temperatures were calculated directly [Harrison and McDougall, 1981]. Low temperature steps were generally used in these calculations; the derived diffusion parameters and resulting closure temperatures are given in Table 1. One volcanic glass sample was analyzed in this study: correspondingly the age of this sample refers to the time of its eruption and quenching. Although the Arrhenius plot for this sample shows systematic non-linearity at high temperatures, estimates of its diffusion parameters and T_C are given in Table 1.

Rb/Sr

Isotope ratios and concentrations were determined through isotope dilution techniques [Hart and Brooks, 1977]. Strontium and rubidium data were collected at MIT on a nine inch, 60° mass spectrometer. Strontium data are reported relative to Elmer & Anders SrCO_3 standard $^{87}\text{Sr}/^{86}\text{Sr} = 0.70800$, and are normalized relative to $^{86}\text{Sr}/^{88}\text{Sr} = 0.1194$. Precisions are 0.1% for Rb, 0.03% for Sr and $<0.008\%$ for $^{87}\text{Sr}/^{86}\text{Sr}$. Strontium and rubidium blank levels are insignificant for the analyses reported. Closure temperatures for Rb diffusion in biotite are given by Harrison et al. [1979] as 600 K.

DATA

Twenty samples were analyzed for the study; data are summarized in Table 2, presented in Table 3 and illustrated in Figures 4.1–4.11. The samples included hornblendes, biotites and an orthoclase from the Black

Mountains, biotites and orthoclases from granites and gneisses of the Eastern Panamint Fault System footwall; a biotite and glass separate from the Trail Canyon Volcanic Sequence; hornblende, biotite and orthoclase from the Little Chief Stock; and a biotite from the Skidoo granite. In addition, Rb-Sr mineral ages were determined on some of these units to constrain their crystallization age. These data are shown in Table 4 and 5.

Below we briefly describe the $^{40}\text{Ar}/^{39}\text{Ar}$ and Rb/Sr data for the samples, from west to east. The majority of the $^{40}\text{Ar}/^{39}\text{Ar}$ spectra are relatively uncomplicated, generally yielding good plateaux or, in the case of orthoclase, shallow saddle-shaped spectra. Such patterns reflect the relatively simple thermal history of the samples, while the small age range in the sample set reflects the regional-scale rapidity with which all the samples cooled below their respective closure temperatures. The location of each sample is shown on Figures 2 and 3.

Skidoo Granite

Biotite from the Skidoo granite has a broad Ar loss profile with a minimum date of 17 Ma and a maximum of 76 Ma (Figure 4.1). The last 70% of the gas shows a range of dates between 70 and 76 Ma. Because of the small range in $^{39}\text{Ar}/^{40}\text{Ar}$, the t_{I} for the sample is poorly constrained, although the radiogenic nature of the gas results in a poorly constrained date of 74 ± 1.4 Ma. The granite has a crystallization age, from a whole rock Rb-Sr isochron, of 101 ± 8 Ma [Hodges et al., in press].

Little Chief Stock

Hornblende, biotite and orthoclase separates were analyzed by $^{40}\text{Ar}/^{39}\text{Ar}$; these and a plagioclase separate were also analyzed for Rb/Sr. As shown on Figure 4.2A, the hornblende shows a classic excess argon profile in the early steps, with a minimum at 11.2 ± 0.25 Ma, and then rises again to high values. Isochron analysis (Figure 4.2B) suggests an approximate date of 12.6 ± 2.3 Ma with a distinctly non-atmospheric $^{40}\text{Ar}/^{39}\text{Ar}$ of 329 ± 8 . The biotite gives a good plateau with some 78% of the gas at a date of 11.21 ± 0.08 (2σ) Ma. The orthoclase sample gave a broad loss or slow cooling profile with a minimum date of 11.02 Ma and a well-constrained isochron date of 11.09 ± 0.11 Ma. Rubidium-strontium data for

mineral separates [Hodges et al., in press] indicate closure of the system to Rb diffusion in biotite at 10.8 ± 0.6 Ma (2σ).

Eastern Panamint Fault System

One volcanic glass sample and one biotite sample from the Trail Canyon Volcanic Sequence were analyzed using $^{40}\text{Ar}/^{39}\text{Ar}$. The glass sample 11-87-8, from the uppermost exposed flow of the sequence, gave an exceptionally well-behaved plateau (nearly 95% of the gas) with a date of 9.97 ± 0.16 Ma (Figure 4.3 A). A concordant isochron date of 9.98 ± 0.1 Ma illustrates the nearly complete closure of this glass to Ar diffusion since cooling (figure 4.3D). A biotite from a lower unit in the sequence (2-87-24) also displayed a plateau, with 61% of the gas giving a date of 10.26 ± 0.3 Ma (Figure 4.3 A). Again, the isochron age was concordant, at 10.22 ± 0.06 Ma (Figure 4.3 B). These data agree relatively well with an unpublished conventional K-Ar date determined on these units by Wes Hildreth of 9.9 Ma (personal communication).

Units in the footwall of the Eastern Panamint Fault System consist primarily of augen gneisses and granitic to andesitic dikes intruding the gneisses [McKenna, unpublished mapping; Hunt and Mabey, 1966; Stern et al., 1966]. We analyzed six samples from the footwall: two orthoclases and two biotites from granite porphyry dikes, one orthoclase from the augen gneiss and one biotite from an andesitic dike. The orthoclase separates show nearly identical spectra consisting of very shallow saddle-shaped spectra with minima at 10.21 and 10.33 Ma (Figures 4.4 A and 4.5 A). The utility of isochron analysis is illustrated well by these samples, which both give errorchron dates of 10.37 ± 0.19 and 10.36 ± 0.10 Ma (figures 4.4 C and 4.5 C). It is interesting to note that despite the widely different D_0 values for the samples, they have very similar release spectra. Biotite separates from the granites did not yield plateaux (Figures 4.4 A and 4.5 A), but gave errorchron dates of 10.80 ± 0.06 and 10.65 ± 0.05 Ma (Figures 4.4 B and 4.5 B). An orthoclase sample from the augen gneiss failed to give an interpretable age spectrum or isochron plot (Figure 4.6). The sample is characterized by a minimum date of approximately 20 Ma in a deep saddle-shaped spectra. Finally, a biotite sample from an andesitic dike within the footwall produced a good plateau with 92% of the gas giving a date of 11.10 ± 0.36 Ma

(Figure 4.3 A). A less well defined, but still concordant, isochron date of 10.88 ± 0.65 Ma is indicated by the data (Figure 4.5 B).

Black Mountains

The final set of samples is from two units within the Black Mountains to the east of Death Valley. Four hornblendes, three biotites and a orthoclase were analyzed to evaluate the time of unroofing of the central Black Mountains. The hornblendes and biotites were taken from the Willow Spring Diorite, while the orthoclase was extracted from a granitic stock which intrudes the diorite. All samples from the diorite were taken along a 2 km traverse northwest of Gold Valley (Figure 5). The four hornblendes all display plateaux, with 50-72% of the gas on plateau. Dates ranged from 9.98 ± 0.12 for samples C to 10.42 ± 0.32 Ma for sample A, taken at the most easterly station of the transect (Figures 4.7 A – 4.10 A). Isochron dates for the samples tended to be somewhat less than, but concordant within error, to the plateau dates (Figures 4.7 B– 4.10 B). At the 2σ level, the date range of the hornblendes is significant.

The biotite separates were extracted from the same hand samples used for the hornblende samples, and while they show a greater variation in ages than the hornblendes, it is biotite C which has the oldest date, with a preferred date of 9.08 ± 0.06 Ma with 46.8% of the gas in two steps (Figure 4.8 A). The corresponding isochron date is 9.19 ± 0.09 Ma (Figure 4.8 C). Biotites A and E were similar to one another with plateaux of 8.49 ± 0.08 and 8.39 ± 0.08 containing 62 and 60% of the gas (Figure 4.7 A and 4.10 A). The orthoclase sample, from a granitic stock which intrudes the diorite, displays a highly structured trend on the isotope correlation plot (Figure 4.11 B), with $^{39}\text{Ar}/^{40}\text{Ar}$ increasing systematically from the first to the sixth step, and then decreasing again towards zero. Isochron dates for steps 1-6 and 7-17 are significantly different: the early steps give 7.03 ± 0.02 Ma with an initial $^{40}\text{Ar}/^{36}\text{Ar}$ of 307, while the latter steps have a date of 6.86 ± 0.29 Ma with an initial $^{40}\text{Ar}/^{36}\text{Ar}$ of 372. Because the MSWD of the early steps is much lower than that of the high temperature steps, and because the initial ratio for the early steps is more nearly atmospheric, we accept the older of the dates as the appropriate one for this sample. It is possible that the dates

are from two distinct reservoirs within the sample. We think this unlikely because the higher temperature steps have the younger date.

DISCUSSION

The $^{39}\text{Ar}/^{40}\text{Ar}$ and Rb/Sr dates presented above place excellent constraints on the timing and rates of extension along the major fault systems within the Death Valley area. In this section, we discuss these constraints, infer strain rates for displacements along these faults, and finally consider the results in the regional context.

Eastern Panamint Fault System

The timing and duration of movement along the Eastern Panamint Fault System is bounded by the ages of the Trail Canyon Volcanic Sequence and the $^{39}\text{Ar}/^{40}\text{Ar}$ ages for rocks within its footwall. The geochronometry of the Trail Canyon Volcanic Sequence establishes its extrusion during a 0.2 Ma period from 10.2 Ma to 9.98 Ma. Granitic dikes in the footwall have $^{39}\text{Ar}/^{40}\text{Ar}$ cooling ages of 10.36 Ma (orthoclase), 10.80 Ma (biotite) and Rb/Sr cooling ages, from biotite-mineral model ages of 11.3 ± 0.3 Ma. An intermediate composition dike intruded into the Ordovician section of the duplex zone (and cut by the duplex faults) has an older $^{39}\text{Ar}/^{40}\text{Ar}$ biotite age of 11.10 Ma. Structural observations [McKenna and Hodges, in press; Chapter 1] suggests that some units of the Trail Canyon Volcanic Sequence are cut by faults within the Eastern Panamint Fault System, while the entire sequence was rotated during deposition by movement along the Eastern Panamint Fault System.

These observations are consistent with extension along the Eastern Panamint Fault System occurring approximately concurrently with extrusion of the Trail Canyon Volcanic Sequence, at 10.2 to 10.0 Ma. In this model, the rapid cooling of samples 1-86-36c and 1-86-34 through the biotite (both Rb/Sr and $^{40}\text{Ar}/^{39}\text{Ar}$) and orthoclase ($^{40}\text{Ar}/^{39}\text{Ar}$) closure temperatures (Figure 6) could be due to either rapid exhumation and cooling of the footwall after intrusion of the dikes, or to quenching of the dikes following intrusion into cold, previously exhumed gneisses. We prefer the former explanation for the following reasons. The Trail Canyon Volcanic Sequence was deposited in a basin formed by the Eastern Panamint Fault

System [McKenna and Hodges, in press; Chapter 1], with the oldest units now filling the basin as much as 1 m.y. younger than the crystallization age for the dikes within the footwall. This discordancy suggests that intrusion of the dikes pre-dated formation of the Trail Canyon Volcanic Sequence basin, and hence initiation of the Eastern Panamint Fault System. Secondly, the characteristic cooling time of a thin (less than a few meters half-thickness) is very short. For half-widths of less than 10 m (larger than that for the dikes sampled here), the center of the dike will cool to ambient temperatures on time scales of years [Turcotte and Schubert, 1982, p. 176]. We infer from this that samples 1-86-36c and 1-86 34 were emplaced into relatively warm country rock at 11.3 Ma, cooled rapidly to ambient footwall temperatures, and then tracked the thermal evolution of the footwall.

Strain rates of this deformation can be estimated from the information presented above along with a simple geometric analysis. The simplified geometry of the Eastern Panamint Fault System is shown in Figure 7. In our model, we make the following simplifying assumptions: 1) rotation of the Trail Canyon Volcanic Sequence, as shown by consistent variations in the dip of the units, was due to syndepositional rotation along structurally lower, listric normal faults; 2) all movement along the fault occurred during the interval 10.3 to 10.0 Ma; 3) Further rotation of the Trail Canyon Volcanic Sequence and the Eastern Panamint Fault System as a whole, as evidenced by the contemporary dip of the uppermost units of the sequence (20°E, [McKenna and Hodges, in press; Chapter 1]) was accommodated on faults structurally below the Eastern Panamint Fault System; and 4) strain was partitioned homogeneously throughout the width of the duplex zone. With these assumptions, we have from Figure 7

$$\frac{L}{R} = \frac{L'}{R'} \quad (1a)$$

$$R' = \frac{L'}{L} R \quad (1b).$$

To a first approximation after extension:

$$A-A' = L' \quad (2),$$

while prior to extension,

$$A-A' = (L')^2 + (R')^2 - 2L'R' \cos(\alpha) \quad (3).$$

Field relations from McKenna and Hodges [in press; Chapter 1], provide $R = 1.1 \pm 0.3$ km and $L = 1.8 \pm .5$ km. The probable width of the deformed zone, L' , is difficult to quantify precisely; McKenna and Hodges [in press; Chapter 1] argued for a value of 5 to 10 km. With these values and from (1b), the value for R' , the down slip throw along the fault system is,

$$R' = \frac{(7.5 \pm 2.5)}{1.8} 1.1 = 5 \pm 2 \text{ km}$$

The initial dip of the Trail Canyon Volcanic Sequence is well constrained at $60^\circ W$, which suggests some 2.5 ± 1 km of horizontal and 4.2 ± 2 km vertical displacement along the fault system. These values are in reasonably good agreement with estimates for the displacement estimated by stratigraphic offset along the fault, about 7 km.

The strain ϵ and strain rate $\dot{\epsilon}$ of this deformation can also be calculated from the chronological data and the geometric model. We have, from (1a) and (3) a strain

$$\epsilon = \frac{\Delta l}{l} = \left(1 + \frac{R}{L} - 2 \frac{R}{L} \cos \alpha\right)^{1/2} - 1 = 0.3 \pm 0.1 \quad (4)$$

for the values of R and L above. Strain rates, assuming the deformation occurred over the time span recorded by the age difference within the Trail Canyon Volcanic Sequence of 0.30 Ma, are thus $3 \pm 1 \times 10^{-14} \text{ sec}^{-1}$. The strain and strain rates are more precise than the value for R' because the uncertainty in L' is canceled in the calculations.

Black Mountains

The eight samples from the Black Mountains demonstrate the uplift and rotation of the range in late Miocene time. When combined with the data discussed above, they clearly demonstrate the eastward younging of cooling ages across the greater Death Valley area, and by inference the age of the extension which unroofed them.

The transect across the Willow Spring Diorite was designed to examine the variations in the time-temperature history of the diorite during uplift. The crystallization age (U-Pb zircon) of the Willow Spring Diorite was determined by Asmerom et al. [1990] as 11.6 ± 0.2 Ma. They also published two hornblende $^{40}\text{Ar}/^{39}\text{Ar}$ dates of 10.13 ± 0.82 (t_P) and 9.9 ± 0.2 Ma (t_I) from two splits of the same sample of diorite.

Figure 5 and Table 6 give the location and current elevation of the Willow Spring Diorite samples, and their location projected onto a plane parallel to the local extension direction, N55°W. The position of the sample from Asmerom et al. [1990] is also tabulated in Table 6. The hornblende and biotite closure dates have two distinctive features: one is the similarity in hornblende dates for samples C, D, and E at 10.05 ± 0.05 Ma, with A giving a much older date of 10.4 ± 0.32 Ma. The other is the larger range in biotite ages, with C the oldest at a t_I of 9.19 ± 0.09 , A at a t_I of $8.70 \pm (0.07)$ Ma and E the youngest at $8.41 \pm (0.05)$ Ma.

The range in ages within the Willow Spring Diorite could be due to a number of causes, including: a) T_C differences between the hornblendes in different samples, b) local variations in temperature of the Willow Spring Diorite due to fluid circulation or other local perturbations, c) variations in temperature due to geothermal gradients within the diorite.

The distance between the samples suggests that local, non-equilibrium temperature variations are not the cause of the age differences in the samples. Characteristic times for conduction of thermal anomalies through the diorite, over a scale length of 1000 m would be on the order of 3×10^4 to 3×10^5 years, assuming a κ (thermal diffusivity) of 10^{-6} to 10^{-7} m^2/sec [Turcotte and Schubert, 1982]. While the hornblende age differences are on the order of this upper limit, biotite age differences are considerably larger than this upper limit. Circulation of fluids through the pluton and its accompanying advection of heat would tend to homogenize the temperature within the pluton at rates as fast or faster than those calculated for conduction. We conclude that the age differences in the biotites and the hornblendes within the Willow Spring Diorite are not due to local-scale temperature heterogeneities within the pluton.

One other method of producing age variations within the Willow Spring Diorite is by unroofing and cooling the pluton. The age differences would then reflect the combined effects of the unroofing of the pluton and the local geothermal gradient. Local unroofing rates can be estimated from the observation of Holm and Wernicke [1989] that the Willow Spring Diorite was intruded at a depth of greater than 10 km (and perhaps as great as 35 km); the lack of a significant contact aureole around the pluton, suggesting that it was in approximate thermal equilibrium with the surrounding country rock; the crystallization age of the Willow Spring Diorite [Asmerom et al., 1990] of 11.6 Ma; and subsequent exposure of the diorite at the surface prior to 5 Ma [Asmerom et al., 1990]. Assuming an original emplacement depth of 20 ± 10 km, the Willow Spring Diorite was unroofed at a rate of 2-6 km/Ma. Solidus temperatures for amphibole-bearing melts of andesitic to basaltic composition in the pressure range of 3 to 10 kb are in the range of 1030-930 K [Gilbert et al., 1982]. Assuming that the country rock was thermally equilibrated with the pluton, the geothermal gradient at the time of intrusion would have been 25 K to 75 K/km.

With this model, the age of hornblende 13A at 10.36 and the others at 9.96 – 10.11 Ma would be due to the different age at which they were unroofed through the hornblende closure temperature, 850 – 750 K. Sample A is older because it passed through the isotherm first, with the remaining samples passing through the closure temperature at a later time, all approximately synchronously. This scenario requires either large horizontal thermal gradients in the geotherm or rotation of the Willow Spring Diorite, and hence the Black Mountains, since its intrusion. The biotite samples have an age distribution which suggests that they passed through the biotite closure temperature in their current topographic sequence: C, followed by A, followed by E. We tentatively interpret this pattern to reflect the rotation of the Black Mountains into its current position sometime between the $^{40}\text{Ar}/^{39}\text{Ar}$ age of the younger hornblendes and the oldest biotite age, or between 10.05 and 9.2 Ma. Clearly more work should be done on the diorite to constrain this hypothesis further. Holm and Wernicke [1989] and Asmerom et al. [1990] have suggested that the Black Mountains rotated some time after the intrusion of the Willow Spring

Diorite and extrusion of the Rhodes Tuff and Sheephead Andesite. These timing constraints agree quite well with the scenario presented here.

This rotation appears to have been completed between 10.05 and 9.2 Ma. The amount of rotation, assessed through the contemporary dips of Paleozoic units within the Black Mountains and the dips of the Rhodes Tuff, is approximately 30-70° of top to the east rotation. Clearly this is not enough rotation to restore the geometry of the transect, based upon the plane defined by samples C, D, and E. It may be that some amount of rotation occurred prior to eruption of the Rhodes Tuff and Sheephead Andesite; that is prior to the closure of hornblendes C, D, and E. If the rotation were faster than the time scale of conductive relaxation, local rotation of the isotherms would not be recorded by the hornblendes. Regardless of the mechanism, restoring the geometry of the diorite to would require additional rotation for a total of over 90° top to the west counter-rotation. Strain rates for this deformation are

$$\dot{\epsilon} = \frac{2\Delta\Theta}{\Delta t} = \frac{3\pm 1 \text{ rad}}{0.8 \times 10^{13} \text{ sec}} = 4\pm 1 \times 10^{-13} \text{ sec}^{-1} \quad (5)$$

or approximately an order of magnitude greater than the strain rate for deformation along the Eastern Panamint Fault System.

The difference in the timing of unroofing of the Eastern Panamint Fault System footwall and the Willow Spring Diorite (Figure 6) is most likely due to the difference in initiation of movement along the faults which exposed these once deep-seated sections of crust. The reconstructed position of the Eastern Panamint Fault System and its relationship to the Black Mountains is shown in Figure 8. Rocks from the footwall of the Eastern Panamint Fault System clearly demonstrate movement along the fault at 10.5 to 10.0 Ma. Because this fault system was absent above the Willow Spring Diorite, or present at very shallow structural levels at 10.0 Ma, the amount of unroofing accomplished by the faulting, and hence the amount of cooling in the Black Mountains due to this deformation was fairly small. This is reflected (Figure 6) in the temperature of the Eastern Panamint Fault System footwall at 10.0 Ma (≈ 510 K from orthoclase ages) and Willow

Spring Diorite temperatures at the same time ($\approx 850 - 750$ K from hornblende ages).

Unroofing and cooling (but not the rotation) of the Willow Spring Diorite was due to a fault or faults between the Eastern Panamint Fault System and the present exposures of the Willow Spring Diorite. The Death Valley Fault (the "turtleback" faults) on the west side of the Black Mountains and the Amargosa Fault [Hunt and Mabey, 1966; Noble, 1941; Wright and Troxel, 1984], present at the surface in the southern Death Valley and inferred to be present in the subsurface in Death Valley from COCORP data, are the faults primarily responsible for this unroofing. The timing of cooling of the Willow Spring Diorite indicates that the cooling took place at a much slower rate than that of the Eastern Panamint Fault System footwall. This may be due in part to the very different dips of the faults accommodating the extension: the Eastern Panamint Fault System at 60° and the Amargosa and Death Valley Faults at much shallower dips of 20° , which could result in much slower footwall unroofing along the shallower faults.

Panamint Mountains

The release spectrum of the biotite from the Skidoo pluton shows a wide zone of Ar loss superimposed on a poorly defined "plateau" which averages 72 Ma, concordant with the t_I of 74 ± 1.4 Ma. We interpret these dates to represent closure of the biotite at approximately 72 Ma, followed by a loss of Ar due to either slow cooling or a brief reheating, followed by quenching at 17 Ma. The Skidoo Pluton has a whole-rock Rb/Sr date of 100 ± 8 Ma [Hodges et al., in press], suggesting a cooling rate of 130 K/Ma, about the same as seen in the Willow Spring Diorite. This sample of the Skidoo was taken from a small satellite body of the granite (see Figure 2) which lies less than 200 m from the Harrisburg Fault. This fault separates the Middle and Lower allochthons shown in Figure 2; the Little Chief Stock cuts this fault, providing a lower age constraint for the fault of 10.8 ± 0.6 Ma.

The result for the Skidoo Pluton is consistent with the $^{40}\text{Ar}/^{39}\text{Ar}$ results of Labotka et al., 1985, who found two distinct age groups in their $^{40}\text{Ar}/^{39}\text{Ar}$ work in the western Panamint Mountains. The younger group (samples

PML 193, PML 179, PML 181, and PML 250c of Labotka et al. [1985]) have biotite and muscovite t_{AS} of 55 to 66 Ma, with PML 193 giving a biotite t_p of 80 and a hornblende t_A of 144 Ma, all with uncertainties of 2 to 10 Ma. In contrast, the other samples (PML 167c, PML 140c, CP 474e, and CP 503) have t_{AS} for biotite and muscovite of 150 to 160 Ma. A poorly defined hornblende t_p of 180 ± 15 was recovered from PML 167c. All of the older samples were taken from Paleozoic sediments; samples in the younger group were taken from stratigraphically similar Paleozoic sediments and from a granitic pluton in the western part of the Panamint Mountains (the Hall Canyon Pluton). Labotka et al. [1985] interpreted these data as representing the effects of a spatially variable retrogradational metamorphism within the Panamint Mountains, with the younger Late Cretaceous dates corresponding to the age of the retrogradation.

In contrast, we interpret this pattern as being due to the juxtaposition of two terrains (the Middle and Lower Allochthons) with distinct thermal histories by the Harrisburg Fault. The older group of samples from Labotka et al. [1985] were all taken from the Middle Allochthon, whereas samples in the younger groups were taken from the Lower Allochthon, as shown in Figure 2. At the southern end of Wildrose Canyon (Figure 2), the Harrisburg Fault is parallel to bedding, and separates the Precambrian Johnnie and Kingston Peak Formations; it is straightforward to place the samples of Labotka et al. [1985] into the tectonic framework of the range. Note that whereas more recent faulting has displaced a fragment of the Harrisburg Fault westward from the crest of the range (Figure 2), the sample taken from the hanging wall of the Harrisburg Fault is similar in age to other Middle Allochthon samples. This interpretation is also visible in the cross-sectional view in Figure 3. The time of exposure of the Middle and Lower Allochthons at the earth's surface is constrained by two indirect lines of evidence. The Little Chief Stock, which intrudes both the Middle and Lower Allochthons, was emplaced within a few kilometers of the surface [McDowell, 1974], and indicates that at 10.8 Ma these terrains were also within a few kilometers of the surface. Also, clasts of both the Middle and Lower Allochthons are present in the Early Pliocene fanglomerates of the Upper Allochthon [Hodges et al., in press].

These data are permissive of a wide range of ages for deformation along the Harrisburg Fault. It is possible that the Harrisburg Fault was responsible for the unroofing and cooling of the Lower Allochthon, and that the fault is Cretaceous in age [Walker, personal communication, 1990]. The Harrisburg Fault could also be Late Tertiary in age, in which case the Cretaceous mica ages in the Lower Allochthon would be unrelated to the unroofing of the allochthon along the fault. The cooling history of the Middle and Lower Allochthons were different at least until after parts of the Lower Allochthon cooled below mica closure temperatures. This provides the upper age constraint for their juxtaposition, 80 Ma. The lower age constraint remains that suggested by Hodges et al. [in press], 10.8 Ma from the crystallization age of the Little Chief Stock. More data, in particular the low temperature-time history of the Lower Allochthon, are needed to further constrain the timing of this deformation.

The data also make more precise the pattern noted by McKenna and Hodges [in press; Chapter 1], in which the locus of extensional faults within the Death Valley Extended Area does not monotonically progress westward with time, but in fact migrates locally eastward and westward simultaneously (Figure 9). On the largest scale, that of the entire extensional system, it is clear that the western limit of faulting does progress monotonically westward with time. However, there are two clear examples of eastward migration of extension within the area: the Harrisburg- Kingston Range Detachment, and Eastern Panamint Fault System-Amargosa Fault-Death Valley Fault sequences.

CONCLUSIONS

Deformation along the Eastern Panamint Fault System was accompanied by the eruption of andesitic to rhyolitic volcanic flows and rhyolite tuffs. Extension and volcanism were short lived beginning at 10.5 Ma and ending by 10.0 Ma. Geometrical relationships between the volcanic rocks and the fault system suggest a strain rate across the fault system during deformation of $3 \pm 1 \times 10^{-14} \text{ sec}^{-1}$. Total extensional strain within the fault system was is 0.3 ± 0.1 .

The samples from the Black Mountains demonstrate the uplift and rotation of the range in the late Miocene. Strain rates during the deformation were approximately $4 \pm 1 \times 10^{-13} \text{ sec}^{-1}$ or approximately an order of magnitude greater than the strain rate for deformation along the Eastern Panamint Fault System. The difference in the timing of unroofing of the Eastern Panamint Fault System footwall and the Willow Spring Diorite (Figure 6) is most likely due to the difference in initiation of movement along the faults which exposed these crustal sections.

The Amargosa and Death Valley Faults, exposed in the western Black Mountains, were active after deformation along the Eastern Panamint Fault System had ceased. Within the resolution of our data, we can not distinguish between unroofing of the Black Mountains along the Amargosa and Death Valley Faults. We can demonstrate that the unroofing of the Black Mountain along some combination of these faults occurred between 10.4 and 7.5 Ma. By 5 Ma, the core of the Black Mountains had been exposed at the surface.

On a regional scale, the deformation rates determined here add to a growing set of estimates of the strain rates associated with extension within the Basin and Range Province. The rates derived here (of the order $10^{-13} \text{ sec}^{-1}$), can be compared to the rates estimated for contemporary extension (of the order $6 \times 10^{-16} \text{ sec}^{-1}$) [Minster and Jordan, 1987], and the rate averaged over the history of extension at this latitude [Wernicke et al., 1989] of order $4 \times 10^{-16} \text{ sec}^{-1}$.

ACKNOWLEDGMENTS

Thanks to the Ar lab at the USGS, including Larry Snee, Shahid Baig, Gary Davidson, and Ross Black, for sharing their Ar expertise with me in the latter part of 1989. Thanks too to Larry Snee for a great Thanksgiving Dinner. This research was sponsored by the National Science Foundation (EAR-8319768 and EAR-8512283), to K.V. Hodges.

REFERENCES

- Alexander, E.C.J., Mickelson, G.M. and Lanphere, M.A., MMhb-1: A new ^{40}Ar - ^{39}Ar dating standard, *U.S. Geol. Surv. Open-File Rept.*, 78-701, 6-8, 1978.
- Asmerom, Y., Snow, J.K., Holm, D.K., Jacobsen, S.B., Wernicke, B.P. and Lux, D.R., Rapid uplift and crustal growth in extensional environments: An isotopic study from the Death Valley Region, California, *Geology*, 18, 223-226, 1990.
- Burchfiel, Black Mountain stuff, in press.
- Burchfiel, B.C., Hodges, K.V. and Walker, J.D., Geology of the Kingston Range Detachment, in preparation.
- Curry, H.D., "Turtleback" fault surfaces in Death Valley, California [abs], *Geol. Soc. Amer. Bull.*, 49, 1875., 1938.
- Dalrymple, G.B., Alexander, E.C.J., Lanphere, M.A. and Kraker, G.P., Irradiation of samples for $^{40}\text{Ar}/^{39}\text{Ar}$ dating using the Geological Survey TRIGA reactor, *U.S. Geol. Surv., Prof. Pap.*, 1176, 1981.
- Dalrymple, G.B. and Lanphere, M.A., *Potassium-argon dating*, pp. Freeman, San Francisco, 1969.
- Dalrymple, G.B., Lanphere, M.A. and Pringle, M.S., Correlation diagrams in ^{40}Ar - ^{39}Ar dating: Is there a correct choice?, *Geophys. Res. Lett.*, 15, 589-591, 1988.

- DeWitt, E., Sutter, J.F., Wright, L.A. and Troxel, B.W., Ar-Ar chronology of Early Cretaceous regional metamorphism, Funeral Mountains, California--A case study of excess argon, *Geol. Soc. Amer. Abs. w. Prog.*, 20, A16-A17, 1988.
- Gibbs, A.D., Structural evolution of extensional basin margins., *J. Geol. Soc. Lond.*, 141, 609-620, 1984.
- Harrison, T.M., Diffusion of ^{40}Ar in hornblende, *Contrib. Mineral. Petrol.*, 78, 324-331, 1981.
- Harrison, T.M., Duncan, I. and McDougall, I., Diffusion of ^{40}Ar in biotite: Temperature, pressure and compositional effects, *Geochim. Cosmochim. Acta*, 49, 2461-2468, 1985.
- Harrison, T.M. and McDougall, I., Excess ^{40}Ar in metamorphic rocks from Broken Hill, New South Wales: implications for $^{40}\text{Ar}/^{39}\text{Ar}$ age spectra and the thermal history of the region, *Earth Planet. Sci. Lett.*, 55, 123-149, 1981.
- Hart, S.R. and Brooks, The geochemistry and evolution of early Precambrian mantle, *Contrib. Mineral. Petrol.*, 61, 109-128, 1977.
- Hodges, K.V., McKenna, L.W. and Harding, M.B., Structural unroofing of the central Panamint Mountains, Death Valley region, SE California, in *Extensional Tectonics at the Latitude of Las Vegas, NV*, edited by Wernicke, B.P., pp. Geological Society of America, Boulder, CO, in press.
- Hodges, K.V. and Walker, J.D., Thermobarometric constraints on the unroofing history of the Funeral Mountains, SE California, *J. Geophys. Res.*, in press.
- Holm, D.K. and Wernicke, B., Are the Black Mountains, Death Valley, CA, a 15-30 km crustal section?, *Geol. Soc. Amer. Abstr. w. Prog.*, 21, A353, 1989.
- Hunt, C.B. and Mabey, D.R., Stratigraphy and structure, Death Valley, California, *U. S. Geol. Surv. Prof. Pap.*, 494-A, 162 pp, 1966.

- Labotka, T.C., Warasila, R.L. and Spangler, R.R., Polymetamorphism in the Panamint Mountains, California — A ^{40}Ar - ^{39}Ar study, *J. Geophys. Res.*, *90*, 10359-10371, 1985.
- McDowell, S.D., Emplacement of the Little Chief Stock, Panamint Range, California, *Geol. Soc. Amer. Bull.*, *85*, 1535-1546, 1974.
- McDowell, S.D., Little Chief Granite Porphyry: Felspar Crystallization History, *Geol. Soc. Amer. Bull.*, *89*, 33-49, 1978.
- McKenna, L.W., and Hodges, K. V., Constraints on the Kinematics and Timing of Late Miocene-Recent Extension Between the Panamint and Black Mountains, Southeastern California, in press, *Extension at the Latitude of Las Vegas*, edited by Wernicke, B. P., Geological Society of America Memoir.
- Minster, J.B. and Jordan, T.H., Vector constraints on western U.S. deformation from space geodesy, neotectonics, and plate motions, *J. Geophys. Res.*, *92*, 4798-4804, 1987.
- Noble, L.F., Structural features of the Virgin Spring area, Death Valley, California, *Geol. Soc. Am. Bull.*, *52*, 941-1000, 1941.
- Otton, J.K., Geologic features of the Central Black Mountains, Death Valley, California, in *Geologic features, Death Valley, California*, edited by Troxel, B.W. and Wright, L.A., pp. 45-50, 1976.
- Roddick, J.C., The application of isochron diagrams in ^{40}Ar - ^{39}Ar dating: A discussion, *Earth Planet. Sci. Lett.*, *41*, 233-244, 1978.
- Roddick, J.C., High precision intercalibration of ^{40}Ar - ^{39}Ar standards, *Geochim. Cosmochim. Acta*, *47*, 887-898, 1983.
- Roddick, J.C., Cliff, R.A. and Rex, D.C., The evolution of excess argon in alpine biotites — a ^{40}Ar - ^{39}Ar analysis, *Earth Planet. Sci. Lett.*, *48*, 185-208, 1980.

- Steiger, R.H. and Jäger, E., Subcommittee on geochronology: Convention on the use of decay constants in geo- and cosmochronology, *Earth Planet. Sci. Lett.*, 36, 359-362, 1977.
- Stern, T.W., Newall, M.F. and Hunt, C.B., Uranium-Lead and potassium-argon ages of parts of the Amargosa Thrust complex, Death Valley, California, *USGS Prof. Pap. 550-B*, B142-B147, 1966.
- Stewart, J.H., Extensional tectonics in the Death Valley area, California: Transport of the Panamint Range structural block 80 km northwestward., *Geology*, 11, 153-157, 1983.
- Troxel, B.W., Significance of Quaternary fault patterns, west side of the Mormon Point turtleback, southern Death Valley, California: A model of listric normal faults, in *Quaternary tectonics of southern Death Valley, California*, edited by Troxel, B.W., pp. 37-40, Friends of the Pleistocene, Shoshone, California, 1986.
- Troxel, B.W. and Wright, L.A., Tertiary extensional features, Death Valley region, eastern California, in *Centennial Field Guide*, edited by Hill, M.L., pp. 121-132, Cordilleran Section of the Geological Society of America, Boulder, Colorado, 1987.
- Turcotte, D.L. and Schubert, G., *Geodynamics*, pp. 450, John Wiley & Sons, New York, 1982.
- Turner, G., ^{40}Ar - ^{39}Ar ages from the lunar maria, *Earth Planet. Sci. Letter*, 11, 169-191, 1971.
- Wernicke, B., Axen, G.J. and Snow, J.K., Basin and Range extensional tectonics at the latitude of Las Vegas, Nevada, *Geol. Soc. Amer. Bull.*, 100, 1738-1757, 1988.
- Wright, L.A., Otton, J.K. and Troxel, B.W., Turtleback surfaces of Death Valley viewed as phenomena of extension, *Geology*, 2, 53-54, 1974.
- Wright, L.A. and Troxel, B.W., Shallow-fault interpretation of Basin and Range structure, southwestern Great Basin, in *Gravity and Tectonics*,

edited by deJong, K.A. and Scholten, R., pp. 397-407, Wiley and Sons, New York, 1973.

Wright, L.A. and Troxel, B.W., Geology of the northern half of the Confidence Hills 15' Quadrangle, Death Valley region, eastern California: The area of the Amargosa chaos, *Calif. Div. Mines Geol. Map Sheet 34*, 1984.

Wright, L.A., Troxel, B.W., Williams, E.G. and Roberts, M.T., Precambrian sedimentary environments of the Death Valley region, eastern California, in *Geological Society of America Cordilleran Section Field Trip Guidebook*, pp. 27-35, Death Valley Publishing Company, Shoshone, CA, 1974.

York, D., Least squares fitting of a straight line with correlated errors, *Earth Planet. Sci. Lett.*, 5, 320-324, 1969.

FIGURE CAPTIONS

Figure 1. Regional map showing location of the Death Valley area in relation to the southwestern Basin and Range Province. The area of Figure 2 is boxed. Thicker lines show trace of major normal faults (unadorned) and strike slip faults (arrowed). Faults which define the Death Valley Extended Area are shown in black, other faults are greyed. The location of the cross section shown in Figure 3 is also shown.

Figure 2. Tectonic sketch map of the Panamint Mountains, showing locations of samples for the study (black squares), and those of Labotka et al. [1985] (empty and diagonally ruled squares). The Panamint Mountains consist of four structural packages, separated by normal faults: a parautochthon overlain structurally by the Lower, Middle and Upper Allochthons. The location of the cross section shown in Figure 3 is also shown.

Figure 3. Interpretive cross section of the Panamint-Black Mountain transect, with available geochronometric measurements from this and

other studies. Key identifies symbols used on diagram, patterns for the tectonic units of the Panamint Mountains as on Figure 2, except that the Parautochthon is unpatterned. The parautochthon is equivalent to the footwall of the Eastern Panamint Fault System. Sources of data not determined in this study: Asmerom et al. [1990], Hodges et al. [in press], Labotka et al. [1985], L. A. Wright [pers. communication, 1988]. See text for details.

Figure 4. Step heating release spectra (apparent age in Ma versus fraction of $^{39}\text{Ar}_K$ released), $^{39}\text{Ar}/^{37}\text{Ar}$ versus fraction of $^{39}\text{Ar}_K$ released (for hornblende samples only) and inverse isochron diagrams ($^{36}\text{Ar}/^{40}\text{Ar}$ versus $^{39}\text{Ar}/^{40}\text{Ar}$) for the samples measured in this study. If multiple phases for a given sample were analyzed, the release spectra are shown together; for this reason the order of the figures does not parallel the sample list in Tables 2 or 4. Uncertainties in both diagrams are at the 1σ level. Note the expanded scales for samples from the Little Chief Stock and the Skidoo granite (84-06).

Figure 5. Sketch map (lower), and projected cross section (upper) of the Gold Valley area of the Black Mountains (see Figure 1 for location). Localities for samples 10-87-13 A, C, D and E are shown in the map; the location of samples YA-1 [Asmerom et al., 1990] is also shown. Sample 10-87-9 is from a Tertiary granitoid which intrudes the Willow Spring Diorite. Upper diagram shows the elevations and locations of the samples projected onto a $\text{N}55^\circ\text{W}$ plane, parallel to the local mean extension direction. The $^{39}\text{Ar}/^{40}\text{Ar}$ ages (Ma) of the hornblende and biotite separates for each station is shown in italics adjacent to the station. Numbers in parenthesis are the uncertainties, in least significant digits, of the $^{39}\text{Ar}/^{40}\text{Ar}$ isochron ages.

Figure 6. Time-temperature graphs for the study area. A. Cooling history for the parautochthon (Eastern Panamint Fault System Footwall), the Little Chief Stock (LCS) and the Willow Spring Diorite (Black Mountains). Data from this study, Asmerom et al. [1990], and Hodges et al. [in press]. Note the large time differential between cooling of the Black Mountains and the Eastern Panamint Fault System, indicating the time lag between significant unroofing between these two areas. B.

Cooling history for the Lower and Middle Allochthons in the Panamint Mountains (Figures 2 and 3), using the data of this study (small square with error bars) and the reinterpreted data of Labotka et al. [1985]. Note the very different history for the two terrains, particularly during the period of significant granitoid intrusion into the Middle Allochthon (indicated by double-headed arrow).

Figure 7. A. Schematic sketch section of the geology of the Eastern Panamint Fault System, showing rotation of volcanic units (the sub-horizontal lines), onlapping nature of volcanic rocks over the fault strands (heavier, west-dipping lines). B. Geometric model, based on Figure 7A, used to estimate strain and strain rates across the fault system. See text for details.

Figure 8. Late Miocene (10.0 Ma) reconstruction of Figure 3. From McKenna and Hodges [in press; Chapter 1].

Figure 9. Synoptic graph of time of extension versus the approximate longitude of the extensional fault for the Death Valley Area. Location of faults are shown on Figure 2, abbreviations used are: AF, Amargosa and Death Valley faults ; EF, Emigrant fault; EP Eastern Panamint fault system; HF, Harrisburg fault; KR, Kingston Range Detachment; OV, Owens Valley and Independence faults; PV, Panamint Valley; TP, Towner Pass fault. Wedges give the direction (with its uncertainty) and the rate (mm/a, rates given adjacent to the wedges). The wedges are oriented with north vertical. Also given are the Holocene extension rate [Minster and Jordan, 1987] and a possible net extension vector for post-20 Ma extension [Wernicke et al., 1988]. While the age of initiation of extension generally youngs to the west, both rates and direction of extension vary widely over time and space. (See Chapter 1 for data sources).

Table 1. Diffusion Parameters and Closure Temperatures, K-Feldpars

| Sample | 1-86-34 | 1-86-36C | 10-87-9 | LCS | 1-86-25 | 11-87-8 |
|--|-------------------------|----------|---------|--------|----------|---------|
| E_a (10^5 J mol $^{-1}$ K $^{-1}$) | 1.49(6) | 1.61(6) | 1.7(1) | 3.3(2) | 1.70(4) | 1.52(7) |
| $\ln(D_0/l^2)$ (sec $^{-1}$) | 3.7(6) | 7(2) | 8(3) | 34(20) | 9.1(1.5) | 12(2) |
| Cooling Rate (K/Ma) | Closure Temperature (K) | | | | | |
| 10 | 480 | 480 | 490 | 600 | 480 | 410 |
| 100 | 510 | 510 | 520 | 620 | 510 | 430 |
| 1000 | 540 | 540 | 550 | 640 | 540 | 450 |

Notes: All uncertainties are 1σ . Values for E_a and $\ln(D_0/l^2)$ were derived from the low temperature release steps of the indicated samples. Closure temperatures are rounded to the nearest 10 K.

Table 2: Run Summary

| Analysis Number | Sample Number | Phase | Mass (mg) | J [†] | T _p (Ma) | ±2s (Ma) | % of ³⁹ Ar on plateau | number of steps | T ₁ (Ma) | ±2s (Ma) | MSWD | number of steps | ³⁶ Ar/ ⁴⁰ Ar _i | ±2s |
|-----------------|---------------|-------|-----------|----------------|---------------------|-------------------|----------------------------------|-----------------|---------------------|----------|------|-----------------|---|------|
| 1 | 10-87-13E | Hbl | 384.5 | 0.007495 | 9.98 | 0.12 | 69.5 | 3 | 10.09 | 0.09 | 1.4 | 11 | 280 | 11.5 |
| 2 | 10-87-13D | Hbl | 506.5 | 0.007530 | 10.06 | 0.05 | 50.8 | 3 | 10.11 | 0.06 | 1.8 | 13 | 300 | 7.0 |
| 3 | 10-87-13C | Hbl | 466.0 | 0.007523 | 10.0 | 0.20 | 71.8 | 6 | 9.96 | 0.05 | 2.5 | 17 | 296 | 1.9 |
| 4 | 10-87-13A | Hbl | 102.9 | 0.007503 | 10.4 | 0.32 | 54.6 | 3 | 10.36 | 0.09 | 0.6 | 14 | 299 | 2.3 |
| 5 | LCS | Hbl | 118.9 | 0.007490 | | | | | 12.60 | 2.25 | 9.5 | 15 | 329 | 8.0 |
| 6 | 10-87-13E | Bt | 78.9 | 0.007465 | 8.39 | 0.08 | 61.7 | 4 | 8.41 | 0.06 | 1.3 | 13 | 290 | 5.5 |
| 7 | 10-87-13A | Bt | 106.7 | 0.007480 | 8.49 | 0.08 | 59.7 | 4 | 8.70 | 0.14 | 2.6 | 12 | 277 | 5.5 |
| 8 | 10-87-13C | Bt | 120.5 | 0.007530 | 9.08 _‡ | 0.06 _‡ | 46.8 _‡ | 2 | 9.19 | 0.16 | 2.4 | 10 | 292 | 5.0 |
| 9 | 1-86-36C | Bt | 106.3 | 0.007530 | 10.65 _‡ | 0.10 _‡ | 43.4 _‡ | 2 | 10.65 | 0.05 | 4.0 | 13 | 273 | 6.0 |
| 10 | 1-86-34 | Bt | 101.5 | 0.007455 | | | | | 10.83 | 0.06 | 3.2 | 13 | 292 | 7.0 |
| 11 | 2-87-24 | Bt | 17.2 | 0.007555 | 10.30 | 0.28 | 60.6 | 4 | 10.22 | 0.06 | 1.6 | 11 | 297 | 2.8 |
| 12 | 84-06 | Bt | 104.0 | 0.007555 | 72 _‡ | 0.80 _‡ | 76 _‡ | 10 | 74 | 1.4 | 40 | 10 | 252 | 170 |
| 13 | LCS | Bt | 106.7 | 0.007465 | 11.21 | 0.08 | 78.3 | 6 | 11.28 | 0.03 | 1.8 | 11 | 292 | 0.9 |
| 14 | 1-87-12 | Bt | 41.6 | 0.007560 | 11.1 | 0.36 | 92.4 | 9 | 11.00 | 0.04 | 2.0 | 13 | 302 | 1.8 |
| 15 | 11-87-8 | Glass | 157.5 | 0.007520 | 9.97 | 0.16 | 94.8 | 9 | 9.98 | 0.06 | 1.4 | 15 | 297 | 2.4 |
| 16 | 1-86-34 | Ksp | 204.4 | 0.007530 | | | | | 10.4 | 0.36 | 9.8 | 19 | 300 | 1.7 |
| 17 | LCS | Ksp | 115.6 | 0.007485 | | | | | 11.1 | 0.11 | 3.6 | 19 | 298 | 1.6 |
| 18 | 1-86-25 | Ksp | 127.8 | 0.007550 | | | | | | | | | | |
| 19 | 1-86-36c | Ksp | 120.8 | 0.007460 | | | | | 10.4 | 0.20 | 3.2 | 19 | 297 | 1.1 |
| 20 | 10-87-9 | Ksp | 119.1 | 0.007490 | | | | | 7.03 | 0.04 | 1.3 | #1-6 | 307 | 1.2 |

Notes: This Table summarizes the results of the step heating experiments found in Table 3. † J values calculated from MMhb-1; typical uncertainties are 0.25%, and all are <0.35%.
‡ Date given is a preferred age (t_A), not a plateau age (t_p).

Table 2.1
10-87-13E

| Temp (°C) | Rad'ogenic ⁴⁰ Ar (V) | K-derived ³⁹ Ar (V) | F ratio | Radiogenic Yield (%) | Fraction of ³⁹ Ar Total (%) | Apparent Age (Ma) | Uncertainty (1 s) (Ma) | ³⁹ Ar/ ⁴⁰ Ar | ³⁶ Ar/ ⁴⁰ Ar |
|--------------|---------------------------------------|--------------------------------------|---------|----------------------------|--|-------------------------|------------------------------|------------------------------------|------------------------------------|
| 500 | 0.02239 | 0.00675 | 3.318 | 3.0 | 0.1 | 44.3 | 7.9 | 0.00911(2) | 0.00328(2) |
| 600 | 0.02531 | 0.01566 | 1.616 | 16.6 | 0.3 | 21.7 | 2.7 | 0.1028(1) | 0.00282(9) |
| 650 | 0.03429 | 0.02258 | 1.518 | 5.8 | 0.4 | 20.4 | 3.2 | 0.03802(3) | 0.00318(3) |
| 700 | 0.02933 | 0.02969 | 0.988 | 32.3 | 0.5 | 13.3 | 1.1 | 0.3283(3) | 0.00228(8) |
| 800 | 0.04212 | 0.06529 | 0.645 | 31.1 | 1.1 | 8.71 | 0.44 | 0.4842(7) | 0.00232(7) |
| 900 | 0.06789 | 0.10181 | 0.667 | 40.8 | 1.6 | 8.99 | 0.39 | 0.6145(4) | 0.00200(7) |
| 950 | 0.10669 | 0.14716 | 0.725 | 56.4 | 2.4 | 9.78 | 0.40 | 0.7829(8) | 0.00147(8) |
| 1000 | 0.76462 | 1.03923 | 0.736 | 72.9 | 16.7 | 9.92 | 0.06 | 1.00(1) | 0.00091(2) |
| 1050 | 1.99780 | 2.69071 | 0.742 | 85.3 | 43.3 | 10.01 | 0.03 | 1.161(2) | 0.000488(4) |
| 1100 | 0.43086 | 0.58376 | 0.738 | 82.3 | 9.4 | 9.95 | 0.08 | 1.126(2) | 0.00059(2) |
| 1125 | 0.47346 | 0.62619 | 0.756 | 83.0 | 10.1 | 10.19 | 0.05 | 1.108(1) | 0.00057(1) |
| 1175 | 0.51812 | 0.67336 | 0.769 | 83.7 | 10.8 | 10.37 | 0.06 | 1.099(1) | 0.00054(2) |
| 1225 | 0.04918 | 0.07447 | 0.660 | 56.8 | 1.2 | 8.91 | 0.25 | 0.866(1) | 0.00146(7) |
| 1275 | 0.05805 | 0.07234 | 0.802 | 67.9 | 1.2 | 10.82 | 0.69 | 0.853(1) | 0.0010(1) |
| 1450 | 0.0423 | 0.0589 | 0.718 | 32.8 | 0.9 | 9.68 | 0.49 | 0.4553(6) | 0.00228(6) |
| Total Gas | | | 0.751 | | 100 | 10.13 | 0.09 | | |

Table 3.2
10-87-13D

| Temp (°C) | Radiogenic ⁴⁰ Ar (V) | K-derived ³⁹ Ar (V) | F ratio | Radiogenic Yield (%) | Fraction of ³⁹ Ar Total (%) | Apparent Age (Ma) | Uncertainty (1 s) (Ma) | ³⁹ Ar/ ⁴⁰ Ar | ³⁶ Ar/ ⁴⁰ Ar |
|--------------|---------------------------------------|--------------------------------------|---------|----------------------------|--|-------------------------|------------------------------|------------------------------------|------------------------------------|
| 500 | 0.02049 | 0.01366 | 1.500 | 2.8 | 0.2 | 20.3 | 3.2 | 0.01867(4) | 0.00328(2) |
| 600 | 0.04252 | 0.03440 | 1.236 | 34.9 | 0.5 | 16.7 | 1.9 | 0.2830(3) | 0.0022(2) |
| 700 | 0.05125 | 0.06278 | 0.816 | 6.7 | 0.9 | 11.06 | 0.58 | 0.08207(3) | 0.00315(1) |
| 800 | 0.05875 | 0.08893 | 0.661 | 41.2 | 1.3 | 9.0 | 1.0 | 0.6266(4) | 0.0019(2) |
| 900 | 0.09758 | 0.15441 | 0.632 | 46.7 | 2.3 | 8.56 | 0.34 | 0.7438(6) | 0.00180(5) |
| 950 | 0.17167 | 0.22092 | 0.777 | 56.0 | 3.2 | 10.52 | 0.36 | 0.7252(6) | 0.00149(7) |
| 975 | 0.27492 | 0.34515 | 0.797 | 60.4 | 5.1 | 10.79 | 0.11 | 0.763(1) | 0.00134(2) |
| 1000 | 0.80547 | 1.07843 | 0.747 | 65.2 | 15.8 | 10.12 | 0.07 | 0.8793(8) | 0.00118(2) |
| 1025 | 1.17534 | 1.57803 | 0.745 | 77.2 | 23.1 | 10.09 | 0.05 | 1.046(2) | 0.00076(2) |
| 1050 | 0.59263 | 0.81101 | 0.731 | 80.4 | 11.9 | 9.90 | 0.09 | 1.111(2) | 0.00065(2) |
| 1075 | 0.33831 | 0.43756 | 0.773 | 77.2 | 6.4 | 10.47 | 0.08 | 1.008(1) | 0.00076(2) |
| 1100 | 0.38198 | 0.49665 | 0.769 | 75.3 | 7.3 | 10.42 | 0.15 | 0.988(1) | 0.00083(4) |
| 1150 | 0.55463 | 0.70751 | 0.784 | 74.9 | 10.4 | 10.62 | 0.05 | 0.964(1) | 0.00084(1) |
| 1200 | 0.31838 | 0.41288 | 0.771 | 75.3 | 6.0 | 10.44 | 0.17 | 0.984(1) | 0.00083(4) |
| 1350 | 0.29629 | 0.38780 | 0.764 | 73.1 | 5.7 | 10.33 | 0.16 | 0.965(1) | 0.00090(4) |
| Total Gas | | | 0.758 | | 100.1 | 10.27 | 0.13 | | |

Table 3.3
10-87-13C

| Temp (°C) | Radiogenic ⁴⁰ Ar (V) | K-derived ³⁹ Ar (V) | F ratio | Radiogenic Yield (%) | Fraction of ³⁹ Ar Total (%) | Apparent Age (Ma) | Uncertainty (1 s) (Ma) | ³⁹ Ar/ ⁴⁰ Ar | ³⁶ Ar/ ⁴⁰ Ar |
|--------------|---------------------------------------|--------------------------------------|---------|----------------------------|--|-------------------------|------------------------------|------------------------------------|------------------------------------|
| 500 | 0.01296 | 0.01434 | 0.903 | 0.4 | 0.2 | 12.2 | 6.5 | 0.00470(2) | 0.003370(8) |
| 600 | 0.03090 | 0.02553 | 1.211 | 5.5 | 0.4 | 16.4 | 2.4 | 0.04508(6) | 0.00320(3) |
| 650 | 0.02390 | 0.02843 | 0.841 | 3.4 | 0.4 | 11.4 | 2.3 | 0.04029(4) | 0.00327(2) |
| 700 | 0.04054 | 0.04356 | 0.931 | 18.2 | 0.6 | 12.6 | 1.2 | 0.1959(1) | 0.00276(5) |
| 800 | 0.05654 | 0.09008 | 0.628 | 17.4 | 1.3 | 8.50 | 0.76 | 0.2774(1) | 0.00279(5) |
| 850 | 0.05635 | 0.07087 | 0.795 | 35.1 | 1.0 | 10.76 | 0.58 | 0.4434(3) | 0.00219(7) |
| 900 | 0.06983 | 0.11972 | 0.583 | 27.0 | 1.7 | 7.90 | 0.74 | 0.4657(2) | 0.00247(7) |
| 950 | 0.15409 | 0.21664 | 0.711 | 34.7 | 3.1 | 9.63 | 0.09 | 0.4898(3) | 0.00221(1) |
| 975 | 0.21317 | 0.28786 | 0.741 | 46.0 | 4.2 | 10.02 | 0.19 | 0.6245(5) | 0.00183(3) |
| 1000 | 1.37115 | 1.86302 | 0.736 | 68.5 | 27.0 | 9.96 | 0.04 | 0.9382(7) | 0.001066(7) |
| 1025 | 1.04447 | 1.41876 | 0.736 | 70.2 | 20.6 | 9.96 | 0.03 | 0.961(1) | 0.001007(5) |
| 1050 | 0.28518 | 0.37821 | 0.754 | 57.0 | 5.5 | 10.20 | 0.12 | 0.760(1) | 0.00145(3) |
| 1075 | 0.35814 | 0.48340 | 0.741 | 62.7 | 7.0 | 10.03 | 0.15 | 0.8530(8) | 0.00126(3) |
| 1100 | 0.38492 | 0.52089 | 0.739 | 61.9 | 7.6 | 10.00 | 0.10 | 0.843(1) | 0.00129(3) |
| 1150 | 0.69367 | 0.92230 | 0.752 | 68.0 | 13.4 | 10.18 | 0.03 | 0.9120(9) | 0.001081(6) |
| 1200 | 0.15340 | 0.19552 | 0.785 | 38.8 | 2.8 | 10.62 | 0.28 | 0.4972(4) | 0.002074(3) |
| 1450 | 0.18158 | 0.21643 | 0.839 | 23.3 | 3.1 | 11.35 | 0.29 | 0.2787(1) | 0.002598(2) |
| Total Gas | | | 0.744 | | 99.9 | 10.07 | 0.13 | | |

Table 3.4

| 10-87-13A | | Hornblende | | Mass (mg): 298.9 | | J: 0.007503 | | | | |
|--------------|---------------------------------------|--------------------------------------|---------|----------------------------|--|-------------------------|------------------------------|------------------------------------|------------------------------------|--|
| Temp (°C) | Radiogenic ⁴⁰ Ar (V) | K-derived ³⁹ Ar (V) | F ratio | Radiogenic Yield (%) | Fraction of ³⁹ Ar Total (%) | Apparent Age (Ma) | Uncertainty (1 s) (Ma) | ³⁹ Ar/ ⁴⁰ Ar | ³⁶ Ar/ ⁴⁰ Ar | |
| 500 | 0.01458 | 0.01001 | 1.456 | 3.2 | 0.6 | 19.6 | 7.9 | 0.02231(4) | 0.00327(4) | |
| 600 | 0.01385 | 0.01920 | 0.721 | 6.6 | 1.2 | 9.7 | 2.1 | 0.0916(2) | 0.00316(7) | |
| 650 | 0.01150 | 0.01475 | 0.780 | 3.4 | 0.9 | 10.5 | 2.7 | 0.0440(1) | 0.00326(3) | |
| 700 | 0.01313 | 0.01795 | 0.731 | 8.5 | 1.1 | 9.9 | 4.5 | 0.1164(2) | 0.0031(1) | |
| 800 | 0.02236 | 0.02846 | 0.786 | 12.2 | 1.8 | 10.6 | 2.9 | 0.1551(1) | 0.0029(1) | |
| 900 | 0.02957 | 0.04050 | 0.730 | 20.1 | 2.6 | 9.9 | 2.0 | 0.2761(3) | 0.0027(1) | |
| 950 | 0.05037 | 0.06264 | 0.804 | 39.5 | 4.0 | 10.9 | 2.0 | 0.4935(5) | 0.0020(3) | |
| 1000 | 0.25789 | 0.33156 | 0.778 | 64.9 | 21.1 | 10.50 | 0.03 | 0.8407(9) | 0.001187(2) | |
| 1025 | 0.25891 | 0.33360 | 0.776 | 75.2 | 21.3 | 10.47 | 0.25 | 0.977(1) | 0.00083(6) | |
| 1050 | 0.14473 | 0.19199 | 0.754 | 71.6 | 12.2 | 10.17 | 0.22 | 0.957(1) | 0.00095(6) | |
| 1100 | 0.14272 | 0.17768 | 0.803 | 68.9 | 11.3 | 10.84 | 0.23 | 0.864(1) | 0.00105(5) | |
| 1175 | 0.21091 | 0.27187 | 0.776 | 59.6 | 17.3 | 10.47 | 0.3 | 0.7733(6) | 0.00137(7) | |
| 1250 | 0.03389 | 0.03492 | 0.971 | 25.7 | 2.2 | 13.1 | 1.2 | 0.2657(2) | 0.00251(8) | |
| 1400 | 0.03409 | 0.03399 | 1.003 | 17.9 | 2.2 | 13.5 | 1.2 | 0.1790(2) | 0.00277(5) | |
| Total Gas | | | 0.789 | | 99.8 | 10.65 | 0.52 | | | |

Table 3.5

| LCS | | Hornblende | | Mass (mg): 118.9 | | J: 0.007490 | | | | |
|--------------|---------------------------------------|--------------------------------------|---------|----------------------------|--|-------------------------|------------------------------|------------------------------------|------------------------------------|--|
| Temp (°C) | Radiogenic ⁴⁰ Ar (V) | K-derived ³⁹ Ar (V) | F ratio | Radiogenic Yield (%) | Fraction of ³⁹ Ar Total (%) | Apparent Age (Ma) | Uncertainty (1 s) (Ma) | ³⁹ Ar/ ⁴⁰ Ar | ³⁶ Ar/ ⁴⁰ Ar | |
| 400 | 0.04806 | 0.00346 | 13.900 | 10.8 | 0.2 | 178 | 24 | 0.00774(6) | 0.00302(5) | |
| 500 | 0.05271 | 0.00348 | 15.126 | 20.1 | 0.2 | 193 | 31 | 0.01326(4) | 0.0027(1) | |
| 600 | 0.02968 | 0.00440 | 6.744 | 5.7 | 0.3 | 88.9 | 9.6 | 0.0084(1) | 0.00319(2) | |
| 700 | 0.02709 | 0.00941 | 2.878 | 11.3 | 0.6 | 38.5 | 7.1 | 0.0394(7) | 0.00300(8) | |
| 800 | 0.04478 | 0.01552 | 2.886 | 21.0 | 0.9 | 38.6 | 4.7 | 0.0728(1) | 0.00267(8) | |
| 900 | 0.07592 | 0.02621 | 2.897 | 27.8 | 1.6 | 38.72 | 0.36 | 0.0096(1) | 0.002442(8) | |
| 950 | 0.06267 | 0.04647 | 1.349 | 27.2 | 2.8 | 18.1 | 2.0 | 0.2022(2) | 0.0024(1) | |
| 975 | 0.05624 | 0.04670 | 1.204 | 27.2 | 2.8 | 16.2 | 2.9 | 0.2266(3) | 0.0024(2) | |
| 1000 | 0.09222 | 0.09302 | 0.991 | 31.8 | 5.6 | 13.35 | 0.82 | 0.3217(2) | 0.00231(5) | |
| 1025 | 0.31486 | 0.35110 | 0.897 | 40.7 | 21.1 | 12.08 | 0.10 | 0.4551(3) | 0.002012(9) | |
| 1050 | 0.26213 | 0.31632 | 0.829 | 40.6 | 19.0 | 11.16 | 0.13 | 0.4921(3) | 0.00201(2) | |
| 1100 | 0.17872 | 0.15702 | 1.138 | 46.2 | 9.4 | 15.31 | 0.23 | 0.4071(2) | 0.00182(3) | |
| 1150 | 0.32984 | 0.26155 | 1.261 | 55.0 | 15.7 | 16.96 | 0.11 | 0.4380(2) | 0.00151(1) | |
| 1250 | 0.46152 | 0.25111 | 1.838 | 50.2 | 15.1 | 24.66 | 0.39 | 0.2737(1) | 0.00168(3) | |
| 1400 | 0.19961 | 0.07906 | 2.525 | 12.2 | 4.7 | 33.80 | 0.29 | 0.04823(2) | 0.00297(4) | |
| Total Gas | | | 1.343 | | | 18.06 | 0.43 | | | |

Table 3.6

| 10-87-13E | | Biotite | | Mass (mg): 106.3 | | J: 0.007465 | | | | |
|--------------|---------------------------------------|--------------------------------------|---------|----------------------------|--|-------------------------|------------------------------|------------------------------------|------------------------------------|--|
| Temp (°C) | Radiogenic ⁴⁰ Ar (V) | K-derived ³⁹ Ar (V) | F ratio | Radiogenic Yield (%) | Fraction of ³⁹ Ar Total (%) | Apparent Age (Ma) | Uncertainty (1 s) (Ma) | ³⁹ Ar/ ⁴⁰ Ar | ³⁶ Ar/ ⁴⁰ Ar | |
| 500 | 0.00860 | 0.02729 | 0.315 | 4.7 | 0.2 | 4.2 | 1.5 | 0.1490(2) | 0.00322(6) | |
| 600 | 0.08752 | 0.16564 | 0.528 | 25.4 | 1.4 | 7.00 | 0.47 | 0.4830(4) | 0.00252(5) | |
| 700 | 0.62187 | 0.96644 | 0.643 | 54.0 | 8.4 | 8.64 | 0.10 | 0.8457(5) | 0.00154(2) | |
| 750 | 0.55298 | 0.88682 | 0.635 | 79.3 | 7.7 | 8.53 | 0.05 | 1.263(1) | 0.00067(1) | |
| 800 | 0.39139 | 0.62210 | 0.629 | 72.4 | 5.4 | 8.45 | 0.13 | 1.162(1) | 0.00091(3) | |
| 850 | 0.32756 | 0.50762 | 0.645 | 73.7 | 4.4 | 8.67 | 0.11 | 1.154(1) | 0.00086(3) | |
| 900 | 0.44046 | 0.71617 | 0.615 | 67.2 | 6.2 | 8.26 | 0.03 | 1.104(1) | 0.001087(6) | |
| 950 | 0.75949 | 1.21040 | 0.627 | 70.6 | 10.6 | 8.43 | 0.06 | 1.137(2) | 0.00097(1) | |
| 1000 | 0.98017 | 0.55686 | 0.630 | 81.9 | 13.6 | 8.45 | 0.04 | 1.316(2) | 0.000583(9) | |
| 1050 | 1.39209 | 2.24059 | 0.621 | 86.0 | 19.5 | 8.35 | 0.03 | 1.402(2) | 0.000437(7) | |
| 1000 | 1.28993 | 2.07423 | 0.622 | 89.1 | 18.1 | 8.36 | 0.04 | 1.451(2) | 0.00033(1) | |
| 1150 | 0.27436 | 0.43925 | 0.625 | 78.7 | 3.8 | 8.39 | 0.23 | 1.274(1) | 0.00069(7) | |
| 1300 | 0.03359 | 0.05616 | 0.598 | 18.4 | 0.5 | 8.0 | 1.5 | 0.3007(1) | 0.0027(1) | |
| Total Gas | | | 0.625 | | 99.8 | 8.4 | 0.08 | | | |

Table 3.7

| 10-87-13A | | Biotite | | Mass (mg): 106.7 | J: 0.007480 | | | | |
|--------------|---------------------------------------|--------------------------------------|---------|----------------------------|--|-------------------------|------------------------------|------------------------------------|------------------------------------|
| Temp (°C) | Radiogenic ⁴⁰ Ar (V) | K-derived ³⁹ Ar (V) | F ratio | Radiogenic Yield (%) | Fraction of ³⁹ Ar Total (%) | Apparent Age (Ma) | Uncertainty (1 s) (Ma) | ³⁹ Ar/ ⁴⁰ Ar | ³⁶ Ar/ ⁴⁰ Ar |
| 500 | 0.01671 | 0.06169 | 0.271 | 6.7 | 0.4 | 3.7 | 1.2 | 0.2484(3) | 0.00315(7) |
| 600 | 0.23002 | 0.46521 | 0.494 | 23.6 | 2.9 | 6.66 | 0.08 | 0.4783(2) | 0.002584(9) |
| 700 | 1.04308 | 1.64454 | 0.634 | 51.3 | 10.3 | 8.54 | 0.06 | 0.8142(6) | 0.00163(1) |
| 750 | 0.83741 | 1.29030 | 0.649 | 75.5 | 8.1 | 8.74 | 0.05 | 1.175(1) | 0.00080(1) |
| 800 | 0.56121 | 0.87647 | 0.640 | 70.4 | 5.5 | 8.62 | 0.06 | 1.1102(8) | 0.00098(2) |
| 850 | 0.39517 | 0.62587 | 0.631 | 64.3 | 3.9 | 8.50 | 0.05 | 1.0274(7) | 0.00119(1) |
| 900 | 0.56774 | 0.91222 | 0.622 | 58.6 | 5.7 | 8.38 | 0.05 | 0.9499(8) | 0.001385(9) |
| 950 | 1.00265 | 1.58249 | 0.634 | 59.7 | 9.9 | 8.53 | 0.04 | 0.9498(8) | 0.001349(8) |
| 1000 | 1.51071 | 2.38548 | 0.633 | 69.8 | 15.0 | 8.53 | 0.05 | 1.113(1) | 0.000999(8) |
| 1050 | 1.90615 | 3.04356 | 0.626 | 75.4 | 19.1 | 8.43 | 0.03 | 1.217(1) | 0.000805(7) |
| 1100 | 1.56754 | 2.48303 | 0.631 | 80.8 | 15.6 | 8.50 | 0.03 | 1.294(1) | 0.000620(5) |
| 1150 | 0.31832 | 0.49873 | 0.638 | 73.7 | 3.1 | 8.59 | 0.15 | 1.166(1) | 0.00088(4) |
| 1300 | 0.03346 | 0.03696 | 0.905 | 11.7 | 0.2 | 12.2 | 2.3 | 0.1295(2) | 0.00298(7) |
| Total Gas | | | 0.628 | | 99.7 | 8.46 | 0.06 | | |

Table 3.8

| 10-87-13C | | Biotite | | Mass (mg): 120.6 | J: 0.007530 | | | | |
|--------------|---------------------------------------|--------------------------------------|---------|----------------------------|--|-------------------------|------------------------------|------------------------------------|------------------------------------|
| Temp (°C) | Radiogenic ⁴⁰ Ar (V) | K-derived ³⁹ Ar (V) | F ratio | Radiogenic Yield (%) | Fraction of ³⁹ Ar Total (%) | Apparent Age (Ma) | Uncertainty (1 s) (Ma) | ³⁹ Ar/ ⁴⁰ Ar | ³⁶ Ar/ ⁴⁰ Ar |
| 500 | 0.01559 | 0.04933 | 0.316 | 4.9 | 0.4 | 4.29 | 0.78 | 0.15446(7) | 0.0032(3) |
| 600 | 0.06805 | 0.21399 | 0.318 | 12.9 | 1.8 | 4.31 | 0.84 | 0.4066(2) | 0.0029(8) |
| 700 | 0.52029 | 0.73418 | 0.709 | 44.3 | 6.2 | 9.60 | 0.18 | 0.6289(3) | 0.0018(3) |
| 750 | 0.68866 | 0.98628 | 0.696 | 78.2 | 8.3 | 9.43 | 0.06 | 1.134(1) | 0.0007(1) |
| 800 | 0.53899 | 0.77791 | 0.693 | 77.1 | 6.8 | 9.39 | 0.06 | 1.1236(8) | 0.0007(1) |
| 850 | 0.42079 | 0.62208 | 0.676 | 69.1 | 5.2 | 9.17 | 0.12 | 1.0309(7) | 0.0010(4) |
| 900 | 0.39930 | 0.57823 | 0.691 | 61.1 | 4.9 | 9.36 | 0.27 | 0.8924(6) | 0.0013(4) |
| 950 | 0.53546 | 0.78965 | 0.678 | 61.2 | 6.7 | 9.19 | 0.05 | 0.7607(5) | 0.0016(1) |
| 1000 | 0.90613 | 1.31501 | 0.691 | 65.1 | 11.1 | 9.36 | 0.04 | 0.9515(7) | 0.00116(8) |
| 1050 | 1.21301 | 1.82000 | 0.665 | 74.6 | 15.4 | 9.03 | 0.04 | 1.131(1) | 0.00083(6) |
| 1150 | 2.50244 | 3.72560 | 0.672 | 82.9 | 31.4 | 9.10 | 0.03 | 1.246(1) | 0.00055(6) |
| 1300 | 0.17012 | 0.22413 | 0.705 | 29.6 | 2.0 | 9.56 | 0.23 | 0.4214(2) | 0.0023(2) |
| Total Gas | | | 0.673 | | 100.2 | 9.12 | 0.10 | | |

Table 3.9

| 1-86-36C | | Biotite | | Mass (mg): 106.3 | J: 0.007530 | | | | |
|--------------|---------------------------------------|--------------------------------------|---------|----------------------------|--|-------------------------|------------------------------|------------------------------------|------------------------------------|
| Temp (°C) | Radiogenic ⁴⁰ Ar (V) | K-derived ³⁹ Ar (V) | F ratio | Radiogenic Yield (%) | Fraction of ³⁹ Ar Total (%) | Apparent Age (Ma) | Uncertainty (1 s) (Ma) | ³⁹ Ar/ ⁴⁰ Ar | ³⁶ Ar/ ⁴⁰ Ar |
| 500 | 0.02285 | 0.12216 | 0.187 | 3.9 | 0.9 | 2.54 | 0.25 | 0.21042(9) | 0.00325(2) |
| 600 | 0.06071 | 0.14092 | 0.431 | 12.6 | 1.0 | 5.84 | 0.47 | 0.2935(1) | 0.00295(3) |
| 700 | 0.55733 | 0.71719 | 0.777 | 37.1 | 5.0 | 10.53 | 0.09 | 0.4797(6) | 0.00212(1) |
| 750 | 1.01867 | 1.30511 | 0.781 | 74.9 | 9.1 | 10.57 | 0.04 | 0.9684(8) | 0.000827(7) |
| 800 | 1.34282 | 1.71748 | 0.782 | 85.9 | 12.0 | 10.59 | 0.03 | 1.1092(9) | 0.000450(3) |
| 850 | 1.07499 | 1.36985 | 0.785 | 88.5 | 9.6 | 10.63 | 0.04 | 1.138(1) | 0.000360(8) |
| 900 | 0.93414 | 1.14859 | 0.813 | 84.9 | 8.0 | 11.01 | 0.05 | 1.0541(8) | 0.00048(1) |
| 950 | 1.06942 | 1.31152 | 0.815 | 81.6 | 9.2 | 11.04 | 0.07 | 1.0098(8) | 0.00059(1) |
| 1000 | 1.86490 | 2.36410 | 0.789 | 85.7 | 16.6 | 10.68 | 0.04 | 1.0972(9) | 0.000456(6) |
| 1050 | 2.16089 | 2.75824 | 0.783 | 85.3 | 19.3 | 10.61 | 0.04 | 1.1003(9) | 0.000468(6) |
| 1100 | 0.85173 | 1.08045 | 0.788 | 83.4 | 7.6 | 10.68 | 0.09 | 1.067(1) | 0.00053(3) |
| 1150 | 0.13826 | 0.17802 | 0.777 | 56.4 | 1.2 | 10.52 | 0.05 | 0.7304(5) | 0.001466(8) |
| 1300 | 0.05597 | 0.06400 | 0.875 | 33.3 | 0.4 | 11.84 | 0.98 | | |
| Total Gas | | | 0.781 | | 99.9 | 10.58 | 0.06 | | |

Table 3.10
1-86-34

| Biotite | | Mass (mg): 101.5 | | J: 0.007455 | | | | | | |
|--------------|---------------------------------------|--------------------------------------|---------|----------------------------|--|-------------------------|------------------------------|------------------------------------|------------------------------------|--|
| Temp (°C) | Radiogenic ⁴⁰ Ar (V) | K-derived ³⁹ Ar (V) | F ratio | Radiogenic Yield (%) | Fraction of ³⁹ Ar Total (%) | Apparent Age (Ma) | Uncertainty (1 s) (Ma) | ³⁹ Ar/ ⁴⁰ Ar | ³⁶ Ar/ ⁴⁰ Ar | |
| 500 | 0.02202 | 0.09971 | 0.221 | 3.6 | 0.7 | 2.97 | 0.69 | 0.16440(9) | 0.00326(3) | |
| 600 | 0.06466 | 0.09258 | 0.698 | 15.9 | 0.7 | 9.37 | 0.80 | 0.2281(3) | 0.00284(5) | |
| 700 | 0.46792 | 0.55586 | 0.842 | 42.9 | 4.0 | 11.29 | 0.13 | 0.5115(6) | 0.00192(2) | |
| 750 | 0.83639 | 1.04179 | 0.803 | 78.5 | 7.5 | 10.77 | 0.09 | 0.986(1) | 0.00070(2) | |
| 800 | 1.00913 | 1.24774 | 0.809 | 86.3 | 9.0 | 10.84 | 0.06 | 1.077(1) | 0.00043(2) | |
| 850 | 0.87054 | 1.06846 | 0.815 | 87.1 | 7.7 | 10.92 | 0.07 | 1.0791(9) | 0.00041(2) | |
| 900 | 0.90526 | 1.12750 | 0.803 | 83.3 | 8.1 | 10.77 | 0.05 | 1.0471(9) | 0.00054(1) | |
| 950 | 1.02851 | 1.23799 | 0.831 | 81.5 | 8.9 | 11.14 | 0.06 | 0.9899(9) | 0.00060(1) | |
| 1000 | 1.77380 | 2.20546 | 0.804 | 87.9 | 15.9 | 10.78 | 0.04 | 1.103(1) | 0.000382(7) | |
| 1050 | 2.90925 | 3.68081 | 0.790 | 89.1 | 26.6 | 10.60 | 0.04 | 1.139(1) | 0.000338(9) | |
| 1100 | 0.98557 | 1.22609 | 0.804 | 88.3 | 8.9 | 10.78 | 0.05 | 1.109(1) | 0.00036(1) | |
| 1150 | 0.13056 | 0.16767 | 0.779 | 52.7 | 1.2 | 10.44 | 0.39 | 0.6807(4) | 0.00159(7) | |
| 1300 | 0.08120 | 0.09110 | 0.891 | 36.3 | 0.7 | 11.95 | 0.70 | 0.4091(4) | 0.00215(8) | |
| Total Gas | | | 0.801 | | 99.9 | 10.74 | 0.08 | | | |

Table 3.11
2-87-24

| Biotite | | Mass (mg): 17.2 | | J: 0.007555 | | | | | | |
|--------------|---------------------------------------|--------------------------------------|---------|----------------------------|--|-------------------------|------------------------------|------------------------------------|------------------------------------|--|
| Temp (°C) | Radiogenic ⁴⁰ Ar (V) | K-derived ³⁹ Ar (V) | F ratio | Radiogenic Yield (%) | Fraction of ³⁹ Ar Total (%) | Apparent Age (Ma) | Uncertainty (1 s) (Ma) | ³⁹ Ar/ ⁴⁰ Ar | ³⁶ Ar/ ⁴⁰ Ar | |
| 500 | 0.00908 | 0.02112 | 0.430 | 7.4 | 0.9 | 5.9 | 2.1 | 0.1726(3) | 0.00313(0) | |
| 600 | 0.02733 | 0.04481 | 0.610 | 19.9 | 1.9 | 8.29 | 0.80 | 0.3271(2) | 0.00270(6) | |
| 700 | 0.05987 | 0.07336 | 0.816 | 16.9 | 3.1 | 11.09 | 0.53 | 0.2069(1) | 0.00281(2) | |
| 800 | 0.11942 | 0.15575 | 0.767 | 57.6 | 6.7 | 10.42 | 0.32 | 0.7561(4) | 0.00142(6) | |
| 850 | 0.17583 | 0.23421 | 0.751 | 68.3 | 10.0 | 10.20 | 0.26 | 0.9172(7) | 0.00105(6) | |
| 900 | 0.23495 | 0.32440 | 0.724 | 71.8 | 13.9 | 9.84 | 0.31 | 1.0006(7) | 0.00093(8) | |
| 950 | 0.28388 | 0.37719 | 0.753 | 73.9 | 16.1 | 10.23 | 0.10 | 0.9907(9) | 0.00086(2) | |
| 1000 | 0.27054 | 0.35068 | 0.771 | 76.0 | 15.0 | 10.48 | 0.13 | 0.993(1) | 0.00079(3) | |
| 1050 | 0.31069 | 0.41558 | 0.748 | 77.1 | 17.8 | 10.16 | 0.20 | 1.041(1) | 0.00075(5) | |
| 1100 | 0.20356 | 0.27163 | 0.749 | 74.8 | 11.6 | 10.18 | 0.14 | 1.0068(8) | 0.00083(3) | |
| 1150 | 0.05575 | 0.06520 | 0.855 | 55.4 | 2.8 | 11.62 | 0.54 | 0.6512(7) | 0.00150(8) | |
| 1300 | 0.00580 | 0.00212 | 2.670 | 5.9 | 0.1 | 36. | 29. | 0.0022(1) | 0.0031(2) | |
| Total Gas | | | 0.737 | | 99.9 | 10.22 | 0.27 | | | |

Table 3.12
84-06

| Biotite | | Mass (g): 104.0 | | J: 0.007555 | | | | | | |
|--------------|---------------------------------------|--------------------------------------|---------|----------------------------|--|-------------------------|------------------------------|------------------------------------|------------------------------------|--|
| Temp (°C) | Radiogenic ⁴⁰ Ar (V) | K-derived ³⁹ Ar (V) | F ratio | Radiogenic Yield (%) | Fraction of ³⁹ Ar Total (%) | Apparent Age (Ma) | Uncertainty (1 s) (Ma) | ³⁹ Ar/ ⁴⁰ Ar | ³⁶ Ar/ ⁴⁰ Ar | |
| 500 | 0.19675 | 0.15763 | 1.248 | 27.0 | 1.1 | 16.93 | 0.66 | 0.2165(3) | 0.00247(2) | |
| 600 | 4.13427 | 1.51568 | 2.728 | 64.7 | 10.3 | 36.80 | 0.20 | 0.23781(7) | 0.001189(2) | |
| 650 | 8.30712 | 1.87175 | 4.438 | 82.4 | 12.7 | 59.50 | 0.32 | 0.18593(9) | 0.000591(2) | |
| 700 | 12.07916 | 2.29068 | 5.273 | 91.9 | 15.5 | 70.47 | 0.38 | 0.1746(1) | 0.0002678(6) | |
| 750 | 8.19456 | 1.50035 | 5.462 | 93.8 | 10.2 | 72.94 | 0.40 | 0.1719(1) | 0.0002054(9) | |
| 800 | 4.80041 | 0.84601 | 5.674 | 93.8 | 5.7 | 75.72 | 0.42 | 0.16554(7) | 0.0002055(9) | |
| 850 | 5.22345 | 0.93222 | 5.603 | 92.6 | 6.3 | 74.80 | 0.40 | 0.16549(4) | 0.000246(2) | |
| 900 | 5.69204 | 1.06933 | 5.323 | 90.1 | 7.3 | 71.13 | 0.38 | 0.16953(8) | 0.000330(2) | |
| 950 | 7.36826 | 1.40477 | 5.245 | 90.6 | 9.5 | 70.11 | 0.38 | 0.1730(1) | 0.000313(3) | |
| 1000 | 8.84409 | 1.62368 | 5.447 | 93.2 | 11.0 | 72.75 | 0.40 | 0.1714(1) | 0.000224(1) | |
| 1050 | 5.33317 | 0.96436 | 5.530 | 94.2 | 6.5 | 73.84 | 0.40 | 0.1706(1) | 0.000189(2) | |
| 1150 | 2.67964 | 0.48570 | 5.517 | 93.6 | 3.3 | 73.67 | 0.40 | 0.16994(6) | 0.000211(2) | |
| 1300 | 0.44868 | 0.08468 | 5.298 | 75.1 | 0.6 | 70.80 | 0.64 | 0.14187(7) | 0.000840(8) | |
| Total Gas | | | 4.971 | | 100.0 | 66.50 | 0.38 | | | |

Table 3.13

| LCS | | Biotite | | Mass (mg): 106.6 | | J: 0.007465 | | | | |
|--------------|---------------------------------------|--------------------------------------|---------|----------------------------|--|-------------------------|------------------------------|------------------------------------|------------------------------------|--|
| Temp (°C) | Radiogenic ⁴⁰ Ar (V) | K-derived ³⁹ Ar (V) | F ratio | Radiogenic Yield (%) | Fraction of ³⁹ Ar Total (%) | Apparent Age (Ma) | Uncertainty (1 s) (Ma) | ³⁹ Ar/ ⁴⁰ Ar | ³⁶ Ar/ ⁴⁰ Ar | |
| 500 | 0.00872 | 0.04064 | 0.214 | 2.8 | 0.2 | 2.89 | 0.86 | | | |
| 600 | 0.05990 | 0.10940 | 0.548 | 7.4 | 0.7 | 7.36 | 0.86 | 0.12946(8) | 0.00329(3) | |
| 700 | 0.39482 | 0.49081 | 0.804 | 21.7 | 2.9 | 10.80 | 0.10 | 0.1350(1) | 0.00313(3) | |
| 750 | 0.72099 | 0.84995 | 0.849 | 47.2 | 5.1 | 11.39 | 0.16 | 0.2702(2) | 0.002649(7) | |
| 800 | 0.79577 | 0.93941 | 0.847 | 56.3 | 5.6 | 11.37 | 0.10 | 0.5588(2) | 0.00178(2) | |
| 850 | 1.01081 | 1.19760 | 0.844 | 60.3 | 7.2 | 11.33 | 0.05 | 0.6687(4) | 0.00146(2) | |
| 900 | 0.70418 | 0.84477 | 0.834 | 58.5 | 5.0 | 11.19 | 0.05 | 0.7192(4) | 0.001330(8) | |
| 950 | 1.08602 | 1.30230 | 0.834 | 57.9 | 7.8 | 11.20 | 0.03 | 0.7058(5) | 0.001394(6) | |
| 1000 | 1.79260 | 2.14799 | 0.835 | 64.5 | 12.8 | 11.20 | 0.03 | 0.6985(4) | 0.001414(4) | |
| 1100 | 3.70728 | 4.44425 | 0.834 | 71.1 | 26.6 | 11.20 | 0.04 | 0.7779(5) | 0.001188(4) | |
| 1150 | 2.41013 | 2.87854 | 0.837 | 75.9 | 17.2 | 11.24 | 0.04 | 0.8593(6) | 0.000591(4) | |
| 1300 | 1.24397 | 1.48692 | 0.837 | 66.4 | 8.9 | 11.23 | 0.04 | 0.9143(7) | 0.000794(7) | |
| Total Gas | | | 0.833 | | 100 | 11.18 | 0.06 | | | |

Table 3.14

| 1-87-12 | | Biotite | | Mass (mg): 41.6 | | J: 0.007560 | | | | |
|--------------|---------------------------------------|--------------------------------------|---------|----------------------------|--|-------------------------|------------------------------|------------------------------------|------------------------------------|--|
| Temp (°C) | Radiogenic ⁴⁰ Ar (V) | K-derived ³⁹ Ar (V) | F ratio | Radiogenic Yield (%) | Fraction of ³⁹ Ar Total (%) | Apparent Age (Ma) | Uncertainty (1 s) (Ma) | ³⁹ Ar/ ⁴⁰ Ar | ³⁶ Ar/ ⁴⁰ Ar | |
| 500 | 0.04397 | 0.06118 | 0.719 | 12.1 | 1.1 | 9.8 | 1.1 | 0.1686(4) | 0.00297(5) | |
| 600 | 0.07329 | 0.08872 | 0.826 | 20.5 | 1.6 | 11.23 | 0.46 | 0.2483(2) | 0.00269(3) | |
| 700 | 0.20250 | 0.23026 | 0.879 | 29.2 | 4.3 | 11.95 | 0.21 | 0.3331(2) | 0.00239(2) | |
| 750 | 0.21360 | 0.25876 | 0.825 | 65.6 | 4.8 | 11.22 | 0.21 | 0.7983(6) | 0.00115(4) | |
| 800 | 0.28252 | 0.35330 | 0.800 | 73.0 | 6.5 | 10.87 | 0.13 | 0.9199(7) | 0.00089(3) | |
| 850 | 0.34754 | 0.43109 | 0.806 | 78.2 | 8.0 | 10.96 | 0.23 | 0.9788(7) | 0.00071(6) | |
| 900 | 0.45594 | 0.56813 | 0.803 | 80.6 | 10.6 | 10.91 | 0.13 | 1.103(1) | 0.00063(3) | |
| 950 | 0.52519 | 0.64155 | 0.819 | 85.6 | 11.8 | 11.13 | 0.11 | 1.055(1) | 0.00046(2) | |
| 1000 | 0.63522 | 0.77841 | 0.816 | 84.8 | 14.4 | 11.10 | 0.12 | 1.049(1) | 0.00048(3) | |
| 1050 | 0.87828 | 1.08274 | 0.811 | 83.3 | 20.0 | 11.03 | 0.06 | 1.036(1) | 0.00054(1) | |
| 1100 | 0.58748 | 0.72300 | 0.813 | 88.1 | 13.4 | 11.05 | 0.11 | 1.0056(8) | 0.00062(3) | |
| 1150 | 0.15566 | 0.16366 | 0.951 | 72.4 | 3.0 | 12.93 | 0.48 | 0.7662(5) | 0.00091(9) | |
| 1300 | 0.03816 | 0.03311 | 1.153 | 27.2 | 0.6 | 15.7 | 2.5 | 0.2363(3) | 0.0024(1) | |
| Total Gas | | | 0.82 | | 100.1 | 11.15 | 0.16 | | | |

Table 3.15

| 11-87-8 | | Glass | | Mass (mg): 157.2 | | J: 0.007520 | | | | |
|--------------|---------------------------------------|--------------------------------------|---------|----------------------------|--|-------------------------|------------------------------|------------------------------------|------------------------------------|--|
| Temp (°C) | Radiogenic ⁴⁰ Ar (V) | K-derived ³⁹ Ar (V) | F ratio | Radiogenic Yield (%) | Fraction of ³⁹ Ar Total (%) | Apparent Age (Ma) | Uncertainty (1 s) (Ma) | ³⁹ Ar/ ⁴⁰ Ar | ³⁶ Ar/ ⁴⁰ Ar | |
| 300 | 0.01096 | 0.00285 | 3.840 | 12.9 | 0.0 | 51. | 15. | 0.0033(3) | 0.0022(1) | |
| 350 | 0.04223 | 0.06289 | 0.671 | 13.1 | 0.5 | 9.08 | 0.83 | 0.1952(1) | 0.00294(4) | |
| 400 | 0.14784 | 0.19573 | 0.755 | 40.5 | 1.5 | 10.22 | 0.25 | 0.5393(5) | 0.00200(3) | |
| 450 | 0.31061 | 0.42544 | 0.730 | 62.5 | 3.3 | 9.88 | 0.12 | 0.8634(7) | 0.00125(2) | |
| 500 | 0.59431 | 0.81399 | 0.730 | 81.2 | 6.4 | 9.88 | 0.08 | 1.1239(9) | 0.00060(2) | |
| 550 | 0.96591 | 1.31761 | 0.733 | 88.7 | 10.4 | 9.92 | 0.05 | 1.223(1) | 0.00035(1) | |
| 600 | 1.24445 | 1.68443 | 0.739 | 91.2 | 13.2 | 9.99 | 0.06 | 1.256(1) | 0.00024(1) | |
| 650 | 1.54166 | 2.08281 | 0.740 | 74.5 | 16.4 | 10.01 | 0.04 | 1.0164(9) | 0.000839(7) | |
| 700 | 1.74369 | 2.36928 | 0.736 | 93.7 | 18.6 | 9.96 | 0.06 | 1.288(1) | 0.00017(2) | |
| 750 | 1.46808 | 1.98608 | 0.739 | 93.6 | 15.6 | 10.00 | 0.03 | 1.280(1) | 0.000181(7) | |
| 800 | 0.7546 | 1.01536 | 0.743 | 89.3 | 8.0 | 10.05 | 0.11 | 1.214(1) | 0.00033(4) | |
| 850 | 0.27451 | 0.37416 | 0.734 | 73.8 | 2.9 | 9.93 | 0.19 | 1.0154(8) | 0.00086(5) | |
| 950 | 0.16749 | 0.21557 | 0.777 | 61.6 | 1.7 | 10.51 | 0.21 | 0.7998(5) | 0.00128(4) | |
| 1050 | 0.09257 | 0.12882 | 0.719 | 70.1 | 1.0 | 9.72 | 0.86 | 0.9842(9) | 0.0009(2) | |
| 1300 | 0.02388 | 0.05003 | 0.477 | 20.4 | 0.4 | 6.5 | 2.0 | 0.4284(3) | 0.0026(2) | |
| Total Gas | | | 0.737 | | 99.9 | 9.98 | 0.09 | | | |

Table 3.16

| 1-86-34 | | Ksp | Mass (mg): 204.4 | | J: 0.007530 | | | | | |
|--------------|---------------------------------------|--------------------------------------|------------------|----------------------------|--|-------------------------|------------------------------|------------------------------------|------------------------------------|--|
| Temp (°C) | Radiogenic ⁴⁰ Ar (V) | K-derived ³⁹ Ar (V) | F ratio | Radiogenic Yield (%) | Fraction of ³⁹ Ar Total (%) | Apparent Age (Ma) | Uncertainty (1 s) (Ma) | ³⁹ Ar/ ⁴⁰ Ar | ³⁶ Ar/ ⁴⁰ Ar | |
| 400 | 0.04801 | 0.01915 | 2.507 | 0.9 | 0.1 | 33.7 | 3.1 | 0.00356(1) | 0.003354(4) | |
| 500 | 0.06068 | 0.04016 | 1.511 | 2.0 | 0.2 | 20.4 | 1.7 | 0.01326(2) | 0.003316(6) | |
| 550 | 0.07077 | 0.07000 | 1.011 | 4.1 | 0.3 | 13.68 | 0.81 | 0.04007(3) | 0.00324(1) | |
| 600 | 0.15221 | 0.17362 | 0.877 | 4.7 | 0.7 | 11.87 | 0.17 | 0.05339(1) | 0.003226(3) | |
| 700 | 0.33403 | 0.37773 | 0.884 | 9.1 | 1.5 | 11.97 | 0.20 | 0.10264(2) | 0.003077(5) | |
| 750 | 0.42497 | 0.55217 | 0.770 | 21.1 | 2.2 | 10.42 | 0.08 | 0.27543(8) | 0.002667(7) | |
| 800 | 0.51046 | 0.66845 | 0.764 | 32.8 | 2.7 | 10.34 | 0.05 | 0.4309(4) | 0.002271(5) | |
| 850 | 0.52408 | 0.66140 | 0.792 | 29.6 | 2.7 | 10.73 | 0.16 | 0.3753(2) | 0.00237(2) | |
| 900 | 0.46873 | 0.59914 | 0.782 | 27.0 | 2.4 | 10.60 | 0.05 | 0.3462(2) | 0.002468(6) | |
| 950 | 0.43485 | 0.55276 | 0.787 | 26.5 | 2.2 | 10.65 | 0.26 | 0.3374(2) | 0.00248(2) | |
| 1000 | 0.51935 | 0.67185 | 0.773 | 22.4 | 2.7 | 10.47 | 0.09 | 0.2910(1) | 0.002623(7) | |
| 1050 | 0.94571 | 1.20279 | 0.786 | 21.4 | 4.9 | 10.65 | 0.03 | 0.2724(4) | 0.002660(3) | |
| 1100 | 2.11999 | 2.78094 | 0.762 | 24.8 | 11.2 | 10.33 | 0.04 | 0.3260(2) | 0.002543(2) | |
| 1125 | 2.8308 | 3.65505 | 0.774 | 27.0 | 14.8 | 10.49 | 0.04 | 0.3497(1) | 0.002468(3) | |
| 1150 | 7.35878 | 9.27211 | 0.794 | 31.1 | 37.5 | 10.75 | 0.03 | 0.3926(3) | 0.002330(1) | |
| 1175 | 1.49461 | 1.82395 | 0.819 | 28.4 | 7.4 | 11.10 | 0.04 | 0.3481(2) | 0.002419(3) | |
| 1200 | 0.43124 | 0.51541 | 0.837 | 22.9 | 2.1 | 11.33 | 0.15 | 0.2742(2) | 0.00260(1) | |
| 1250 | 0.70496 | 0.81344 | 0.867 | 20.4 | 3.3 | 11.73 | 0.14 | 0.2356(2) | 0.002693(8) | |
| 1400 | 0.27407 | 0.29068 | 0.943 | 17.2 | 1.2 | 12.76 | 0.05 | 0.18262(7) | 0.002802(2) | |
| Total Gas | | | 0.797 | | 100.1 | 10.79 | 0.05 | | | |

Table 3.17

| LCS | | Ksp | Mass (mg): 115.6 | | J: 0.007485 | | | | | |
|--------------|---------------------------------------|--------------------------------------|------------------|----------------------------|--|-------------------------|------------------------------|------------------------------------|------------------------------------|--|
| Temp (°C) | Radiogenic ⁴⁰ Ar (V) | K-derived ³⁹ Ar (V) | F ratio | Radiogenic Yield (%) | Fraction of ³⁹ Ar Total (%) | Apparent Age (Ma) | Uncertainty (1 s) (Ma) | ³⁹ Ar/ ⁴⁰ Ar | ³⁶ Ar/ ⁴⁰ Ar | |
| 400 | 0.02756 | 0.03551 | 0.776 | 1.3 | 0.2 | 10.5 | 1.3 | 0.01736(3) | 0.00333(1) | |
| 500 | 0.07476 | 0.07583 | 0.986 | 14.2 | 0.5 | 13.26 | 0.80 | 0.1441(2) | 0.00290(3) | |
| 550 | 0.40548 | 0.50735 | 0.799 | 43.7 | 3.1 | 10.76 | 0.22 | 0.5501(3) | 0.00189(3) | |
| 600 | 1.28485 | 1.54573 | 0.831 | 57.0 | 9.4 | 11.19 | 0.06 | 0.6902(4) | 0.001443(9) | |
| 700 | 0.94971 | 1.16009 | 0.819 | 79.9 | 7.0 | 11.02 | 0.05 | 0.9849(7) | 0.00065(1) | |
| 750 | 0.36520 | 0.44289 | 0.825 | 79.5 | 2.7 | 11.10 | 0.11 | 0.9726(8) | 0.00067(3) | |
| 800 | 0.57210 | 0.68912 | 0.830 | 72.8 | 4.2 | 11.18 | 0.11 | 0.883(1) | 0.00090(2) | |
| 850 | 0.60029 | 0.72794 | 0.825 | 61.0 | 4.4 | 11.10 | 0.04 | 0.7446(9) | 0.001307(7) | |
| 900 | 0.59912 | 0.72272 | 0.829 | 44.5 | 4.4 | 11.16 | 0.11 | 0.5393(3) | 0.00187(2) | |
| 950 | 0.74551 | 0.87824 | 0.849 | 30.8 | 5.3 | 11.43 | 0.12 | 0.3635(2) | 0.002340(9) | |
| 1000 | 1.04368 | 1.25608 | 0.831 | 26.1 | 7.6 | 11.18 | 0.06 | 0.3144(2) | 0.002500(5) | |
| 1025 | 0.96469 | 1.15665 | 0.834 | 27.5 | 7.0 | 11.23 | 0.05 | 0.3301(2) | 0.002453(5) | |
| 1050 | 1.17232 | 1.43234 | 0.818 | 29.3 | 8.7 | 11.02 | 0.10 | 0.3594(2) | 0.002389(7) | |
| 1075 | 1.53897 | 1.86473 | 0.825 | 30.6 | 11.3 | 11.11 | 0.03 | 0.3725(2) | 0.002344(3) | |
| 1100 | 1.33818 | 1.57123 | 0.852 | 33.2 | 9.5 | 11.46 | 0.04 | 0.3913(2) | 0.002257(3) | |
| 1125 | 1.16354 | 1.34863 | 0.863 | 34.4 | 8.2 | 11.61 | 0.06 | 0.3999(2) | 0.002217(5) | |
| 1150 | 0.46658 | 0.53460 | 0.873 | 30.5 | 3.2 | 11.75 | 0.16 | 0.3501(1) | 0.00235(1) | |
| 1250 | 0.23022 | 0.24704 | 0.932 | 32.3 | 1.5 | 12.54 | 0.39 | 0.3473(2) | 0.00228(4) | |
| 1400 | 0.24924 | 0.27349 | 0.912 | 32.5 | 1.7 | 12.27 | 0.12 | 0.3575(2) | 0.00228(1) | |
| Total Gas | | | 0.837 | | 99.9 | 11.27 | 0.08 | | | |

Table 3.18

| 1-86-25 | | Ksp | Mass (mg): 127.8 | | J: 0.007550 | | | | | |
|--------------|---------------------------------------|--------------------------------------|------------------|----------------------------|--|-------------------------|------------------------------|------------------------------------|------------------------------------|--|
| Temp (°C) | Radiogenic ⁴⁰ Ar (V) | K-derived ³⁹ Ar (V) | F ratio | Radiogenic Yield (%) | Fraction of ³⁹ Ar Total (%) | Apparent Age (Ma) | Uncertainty (1 s) (Ma) | ³⁹ Ar/ ⁴⁰ Ar | ³⁶ Ar/ ⁴⁰ Ar | |
| 400 | 1.11533 | 0.02660 | 41.928 | 35.5 | 0.1 | 496.1 | 2.3 | 0.00847(2) | 0.00218(5) | |
| 500 | 5.36725 | 0.16587 | 32.358 | 80.6 | 0.6 | 394.3 | 1.0 | 0.02491(2) | 0.00065(3) | |
| 600 | 9.27821 | 0.76539 | 12.122 | 78.9 | 2.7 | 157.98 | 0.42 | 0.06508(2) | 0.00071(1) | |
| 650 | 4.30704 | 0.84573 | 5.093 | 73.7 | 3.0 | 68.06 | 0.19 | 0.14488(5) | 0.00088(2) | |
| 700 | 3.79773 | 0.78531 | 4.836 | 78.7 | 2.8 | 64.69 | 0.18 | 0.16295(9) | 0.00071(4) | |
| 750 | 4.09347 | 0.86878 | 4.712 | 79.4 | 3.1 | 63.06 | 0.20 | 0.1688(1) | 0.00069(5) | |
| 800 | 2.13778 | 0.66087 | 3.325 | 76.9 | 2.3 | 43.53 | 0.12 | 0.2381(1) | 0.00077(4) | |
| 850 | 1.21679 | 0.6793 | 1.791 | 72.6 | 2.4 | 24.23 | 0.08 | 0.4067(4) | 0.00091(5) | |
| 900 | 1.2519 | 0.78324 | 1.598 | 68.9 | 2.8 | 21.64 | 0.11 | 0.4328(2) | 0.00104(9) | |
| 950 | 2.28237 | 1.04719 | 2.18 | 66.7 | 3.7 | 29.44 | 0.11 | 0.3067(2) | 0.00122(6) | |
| 1000 | 7.4742 | 2.08387 | 3.587 | 70.6 | 7.3 | 48.20 | 0.13 | 0.19716(7) | 0.000991(9) | |
| 1025 | 5.78793 | 1.60233 | 3.612 | 72.4 | 5.6 | 48.54 | 0.13 | 0.20079(9) | 0.00093(1) | |
| 1075 | 27.96347 | 5.07877 | 5.506 | 83.0 | 17.8 | 73.48 | 0.20 | 0.15097(7) | 0.000571(7) | |
| 1125 | 48.37285 | 7.60500 | 6.361 | 88.1 | 26.7 | 84.62 | 0.23 | 0.1386(1) | 0.000399(4) | |
| 1225 | 28.33813 | 4.78500 | 5.922 | 87.7 | 16.8 | 78.91 | 0.21 | 0.14834(4) | 0.000411(7) | |
| 1400 | 5.10511 | 0.68232 | 7.482 | 86.0 | 2.4 | 99.13 | 0.28 | 0.11501(7) | 0.00047(5) | |
| Total Gas | | | 5.547 | | 100.1 | 74.01 | 0.21 | | | |

Table 3.19
1-86-36c

| Temp | Radiogenic ⁴⁰ Ar | K-derived ³⁹ Ar | F ratio | Radiogenic Yield | Fraction of ³⁹ Ar Total | Apparent Age | Uncertainty | ³⁹ Ar/ ⁴⁰ Ar | ³⁶ Ar/ ⁴⁰ Ar |
|-----------|-----------------------------|----------------------------|---------|------------------|------------------------------------|--------------|-------------|------------------------------------|------------------------------------|
| (°C) | (V) | (V) | | (%) | (%) | (Ma) | (1 s) | | |
| 400 | 0.03303 | 0.01376 | 2.401 | 1.0 | 0.1 | 32.0 | 3.9 | 0.00428(1) | 0.003349(7) |
| 500 | 0.08606 | 0.06991 | 1.231 | 2.4 | 0.4 | 16.49 | 0.82 | 0.01954(2) | 0.003303(6) |
| 600 | 0.30556 | 0.34824 | 0.877 | 6.8 | 1.9 | 11.77 | 0.20 | 0.07777(4) | 0.003153(5) |
| 700 | 0.60076 | 0.73161 | 0.821 | 14.3 | 4.0 | 11.02 | 0.14 | 0.1746(1) | 0.002899(6) |
| 750 | 0.44785 | 0.58030 | 0.772 | 40.3 | 3.2 | 10.36 | 0.06 | 0.525(1) | 0.00201(1) |
| 800 | 0.40687 | 0.52514 | 0.775 | 31.8 | 2.9 | 10.40 | 0.08 | 0.4118(6) | 0.00230(1) |
| 850 | 0.40669 | 0.52223 | 0.779 | 29.3 | 2.9 | 10.45 | 0.14 | 0.3773(4) | 0.00239(2) |
| 900 | 0.46427 | 0.59442 | 0.781 | 30.0 | 3.3 | 10.48 | 0.07 | 0.3851(2) | 0.002366(6) |
| 950 | 0.63861 | 0.82768 | 0.772 | 26.3 | 4.6 | 10.35 | 0.03 | 0.3425(4) | 0.002490(4) |
| 1000 | 0.89601 | 1.14905 | 0.780 | 24.1 | 6.3 | 10.46 | 0.05 | 0.3097(4) | 0.002567(6) |
| 1025 | 0.76237 | 0.97798 | 0.780 | 24.9 | 5.4 | 10.46 | 0.06 | 0.3206(2) | 0.002539(5) |
| 1050 | 0.98073 | 1.28924 | 0.761 | 25.7 | 7.1 | 10.21 | 0.07 | 0.3385(2) | 0.002513(6) |
| 1075 | 1.65032 | 2.14494 | 0.769 | 28.9 | 11.8 | 10.32 | 0.04 | 0.3774(3) | 0.002402(5) |
| 1100 | 1.9399 | 2.44848 | 0.792 | 32.3 | 13.5 | 10.63 | 0.05 | 0.4090(2) | 0.002288(4) |
| 1125 | 2.49868 | 3.16844 | 0.789 | 34.9 | 17.4 | 10.58 | 0.03 | 0.4440(2) | 0.002199(2) |
| 1150 | 1.37482 | 1.71205 | 0.803 | 33.1 | 9.4 | 10.77 | 0.05 | 0.4142(5) | 0.002259(7) |
| 1200 | 0.41067 | 0.49216 | 0.834 | 29.1 | 2.7 | 11.19 | 0.12 | 0.3496(2) | 0.00239(1) |
| 1250 | 0.16503 | 0.20416 | 0.806 | 26.2 | 1.1 | 10.82 | 0.52 | 0.3256(6) | 0.00249(5) |
| 1400 | 0.33192 | 0.3812 | 0.871 | 27.5 | 2.1 | 11.68 | 0.19 | 0.3171(2) | 0.00245(2) |
| Total Gas | | | 0.792 | | 100.1 | 10.63 | 0.07 | | |

Table 3.20
10-87-9

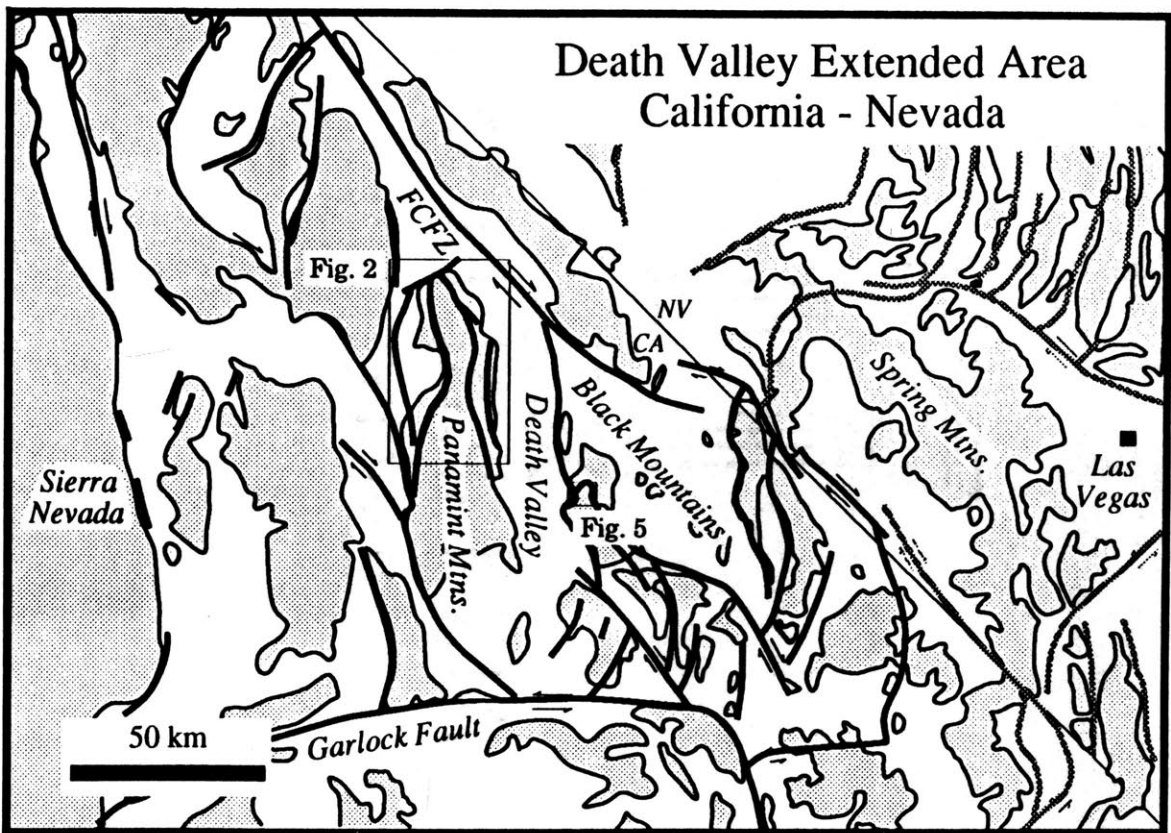
| Temp | Radiogenic ⁴⁰ Ar | K-derived ³⁹ Ar | F ratio | Radiogenic Yield | Fraction of ³⁹ Ar Total | Apparent Age | Uncertainty | ³⁹ Ar/ ⁴⁰ Ar | ³⁶ Ar/ ⁴⁰ Ar |
|-----------|-----------------------------|----------------------------|---------|------------------|------------------------------------|--------------|-------------|------------------------------------|------------------------------------|
| (°C) | (V) | (V) | | (%) | (%) | (Ma) | (1 s) | | |
| 400 | 0.05765 | 0.03282 | 1.757 | 5.4 | 0.1 | 23.6 | 1.7 | 0.03668(2) | 0.00320(1) |
| 500 | 0.03990 | 0.06408 | 0.623 | 16.2 | 0.3 | 8.4 | 1.2 | 0.2606(2) | 0.00283(8) |
| 600 | 0.21983 | 0.38314 | 0.574 | 42.1 | 1.7 | 7.74 | 0.21 | 0.7381(7) | 0.00195(4) |
| 700 | 0.65631 | 1.23398 | 0.532 | 54.6 | 5.5 | 7.17 | 0.05 | 1.0363(9) | 0.00152(1) |
| 750 | 0.53992 | 1.02553 | 0.526 | 82.3 | 4.6 | 7.10 | 0.03 | 1.586(2) | 0.000559(8) |
| 800 | 0.51540 | 0.97282 | 0.530 | 81.8 | 4.3 | 7.14 | 0.05 | 1.565(2) | 0.00057(2) |
| 850 | 0.40541 | 0.76504 | 0.530 | 77.3 | 3.4 | 7.15 | 0.08 | 1.479(2) | 0.00073(2) |
| 950 | 0.79689 | 1.45050 | 0.549 | 70.8 | 6.5 | 7.41 | 0.06 | 1.304(1) | 0.00096(2) |
| 1000 | 0.69247 | 1.22102 | 0.567 | 65.8 | 5.4 | 7.65 | 0.12 | 1.172(1) | 0.00113(3) |
| 1025 | 0.62196 | 1.05980 | 0.587 | 63.9 | 4.7 | 7.91 | 0.05 | 1.099(1) | 0.00120(1) |
| 1075 | 1.20937 | 2.00184 | 0.599 | 59.3 | 9.0 | 8.08 | 0.03 | 0.9989(9) | 0.001360(6) |
| 1100 | 1.00252 | 1.65339 | 0.606 | 58.8 | 7.4 | 8.17 | 0.04 | 0.9783(9) | 0.001378(7) |
| 1125 | 1.43938 | 2.33170 | 0.617 | 61.6 | 10.4 | 8.32 | 0.03 | 1.006(1) | 0.001283(4) |
| 1150 | 2.90219 | 4.69516 | 0.618 | 60.1 | 20.9 | 8.33 | 0.02 | 0.961(1) | 0.001333(2) |
| 1200 | 1.83553 | 2.92236 | 0.628 | 55.1 | 13.0 | 8.47 | 0.03 | 0.8843(8) | 0.001505(6) |
| 1250 | 0.25706 | 0.38948 | 0.660 | 46.9 | 1.7 | 8.90 | 0.16 | 0.7158(5) | 0.00178(3) |
| 1400 | 0.15067 | 0.22047 | 0.683 | 43.6 | 1.0 | 9.21 | 0.26 | 0.6420(8) | 0.00190(4) |
| Total Gas | | | 0.595 | 61.9 | 99.9 | 8.02 | 0.05 | | |

Table 4: Sr isotopic Data

| | 1-86-36c | | |
|---------------------------------|------------|-------------|-----------|
| | K-feldspar | plagioclase | biotite |
| Rb | --- | 51(1) | 734(7) |
| Sr | 80.3(8) | 595(6) | 8.9(1) |
| $^{87}\text{Rb}/^{86}\text{Sr}$ | --- | 0.248(2) | 240(2) |
| $^{87}\text{Sr}/^{86}\text{Sr}$ | 0.71160(4) | 0.70990(4) | 0.7508(8) |

Notes: Analysis of mineral separates at the MIT Center for Geoalchemy. All concentrations in ppm. Uncertainties (2σ) in the last place are given in ().

Figure 1



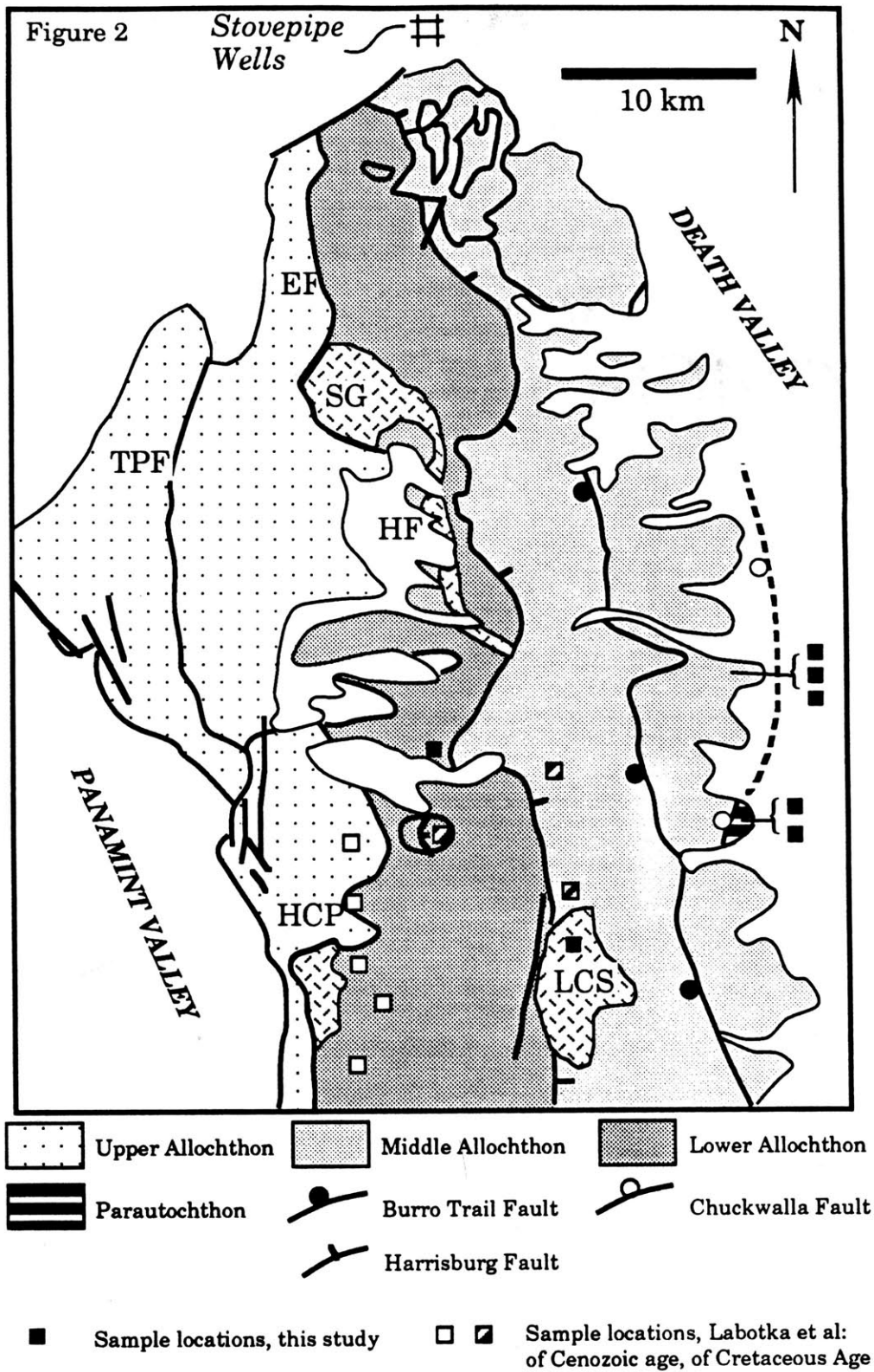


Figure 4.1 A, B

84-06
(Skiddo Granite)
biotite

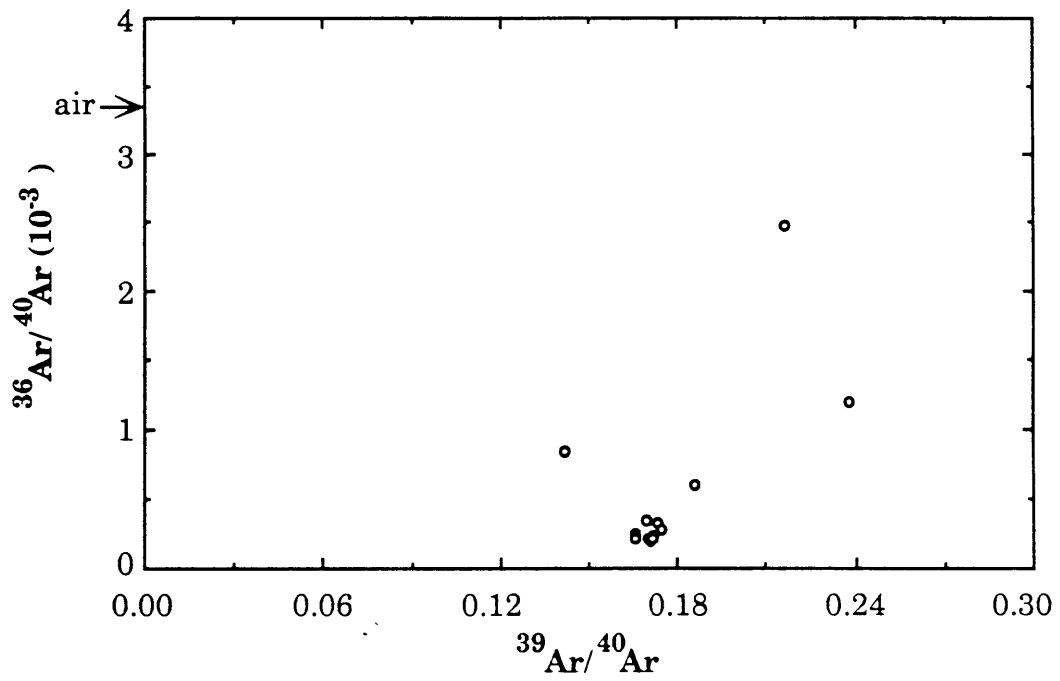
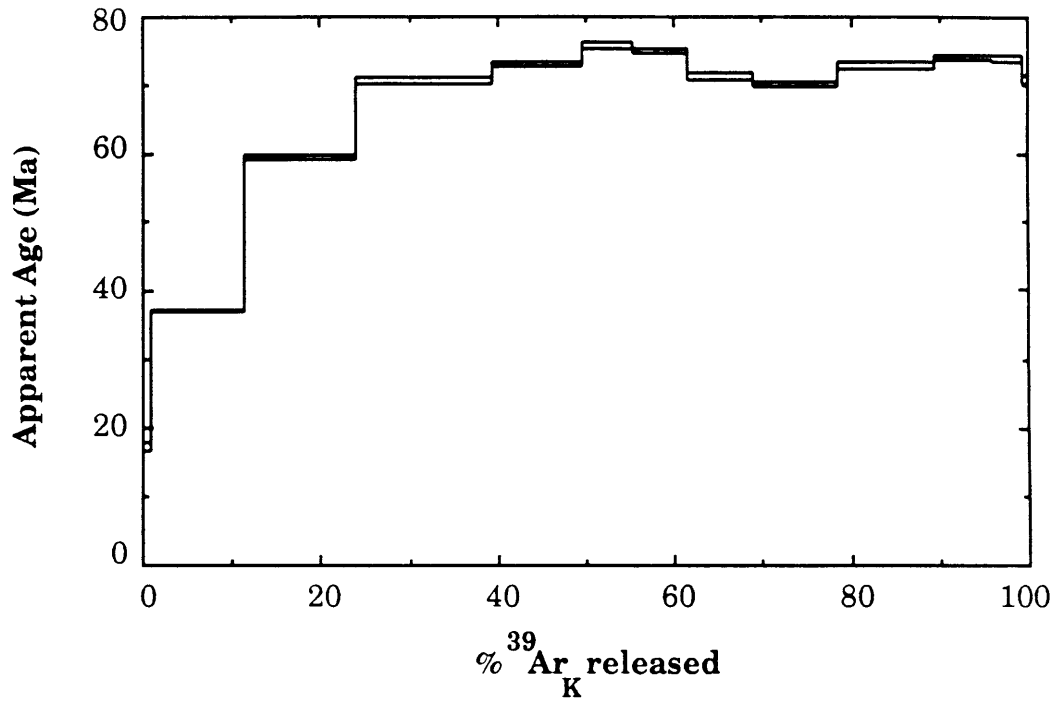


Figure 4.2 A

**Little Chief Stock
(Granite Porphyry)
hornblende, biotite, K-feldspar**

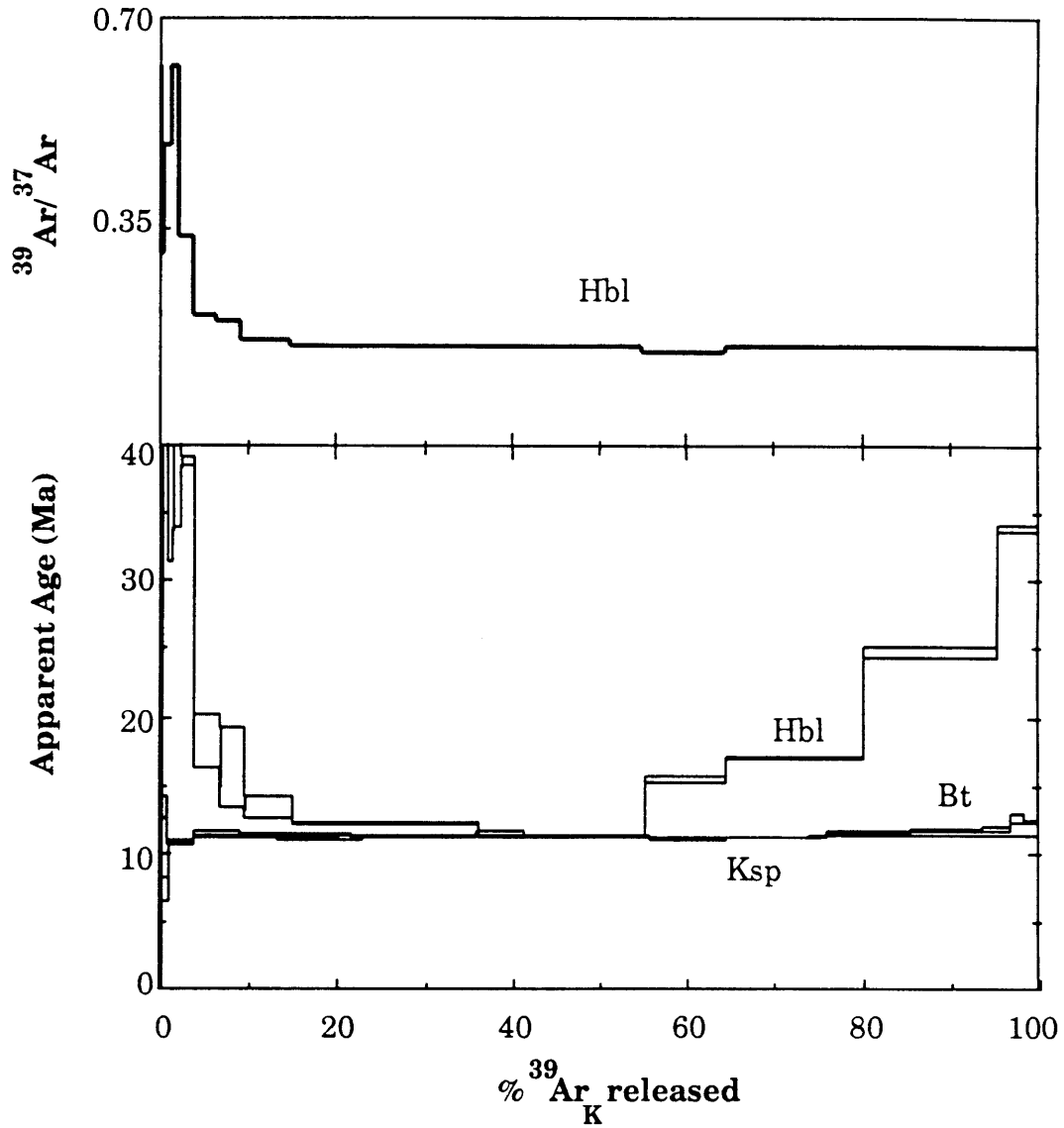


Figure 4.2 B, C

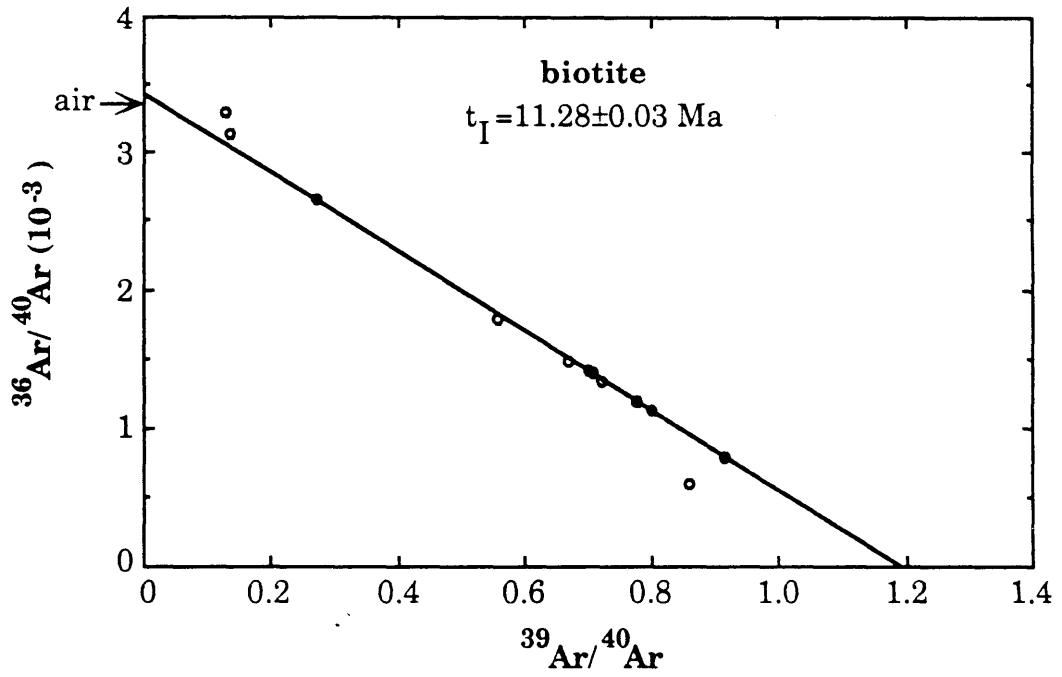
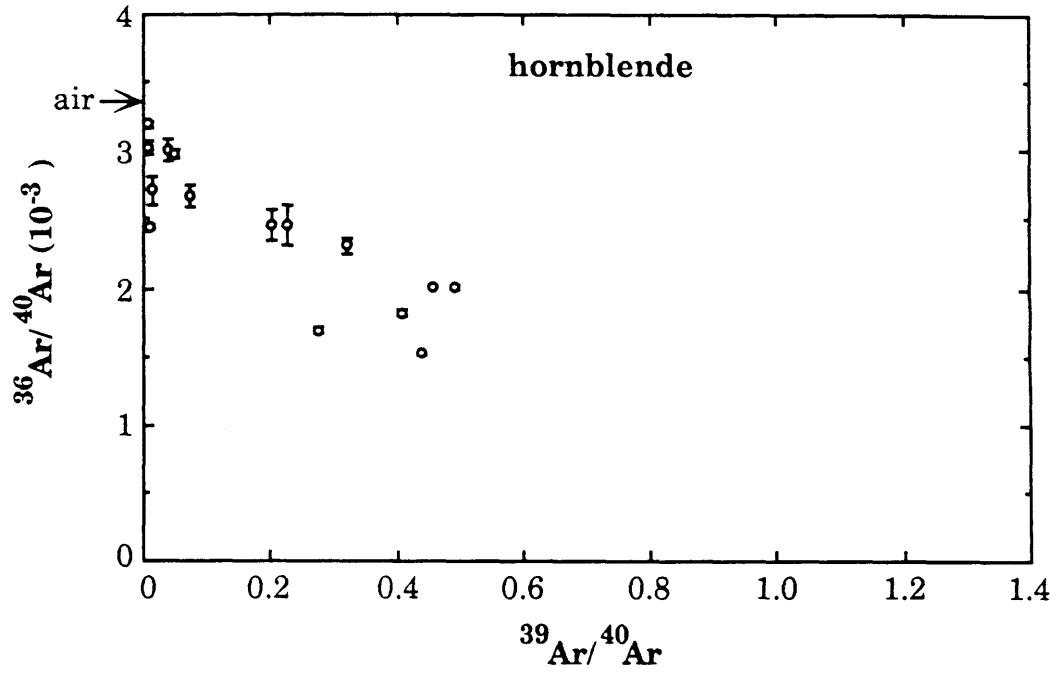


Figure 4.2 D

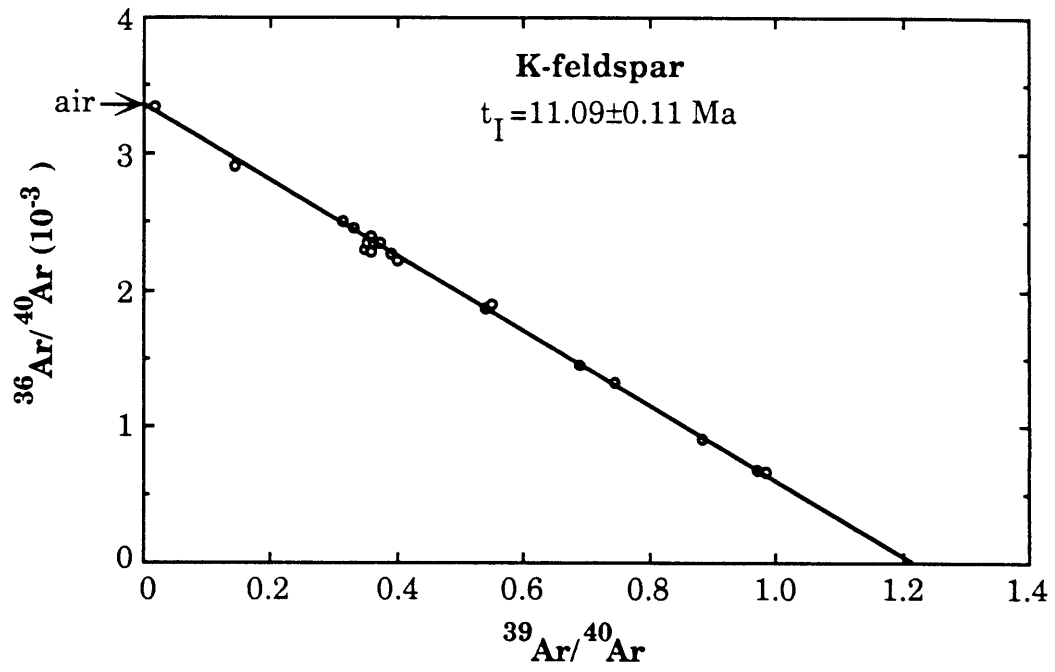


Figure 4.3 A, B

**2-87-24, 11-87-9, 1-87-12
(Trail Canyon Volcanic Sequence)
biotite, glass**

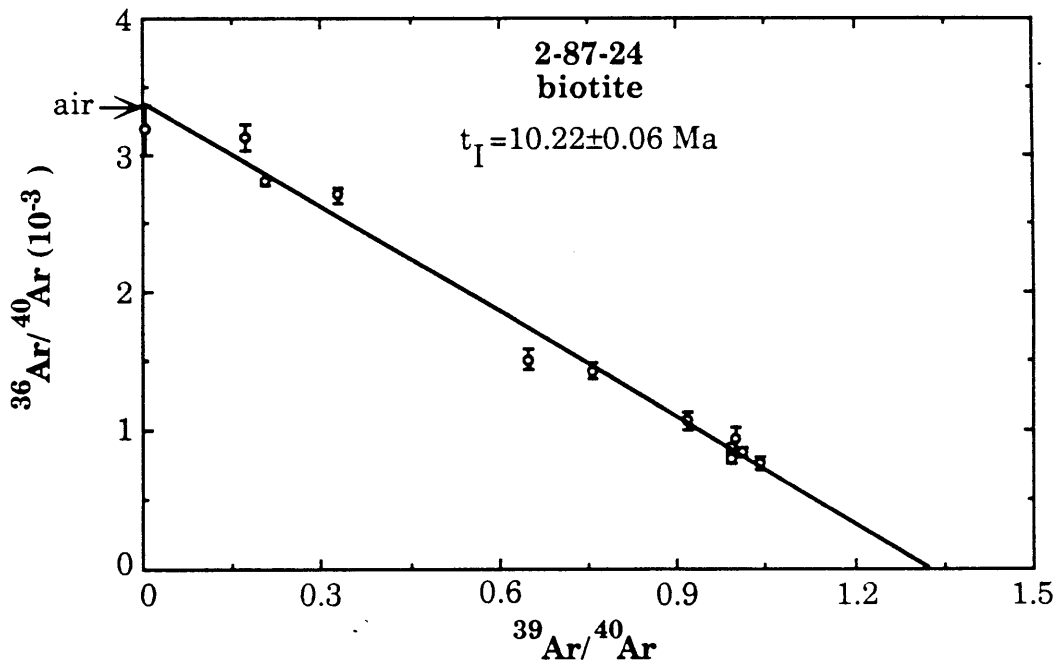
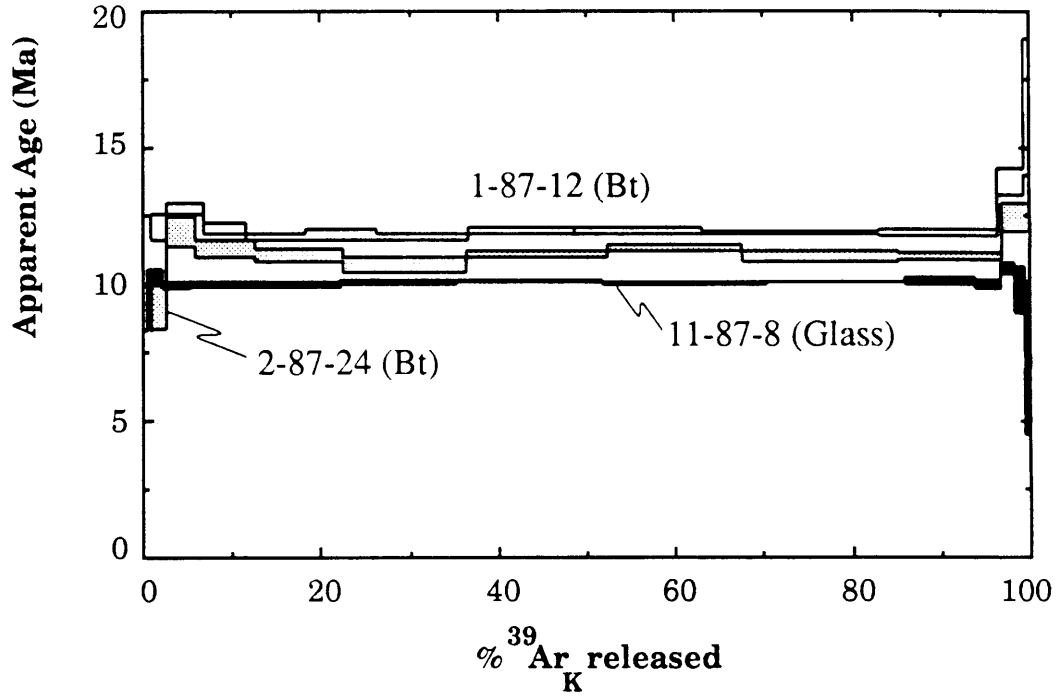


Figure 4.3 C, D

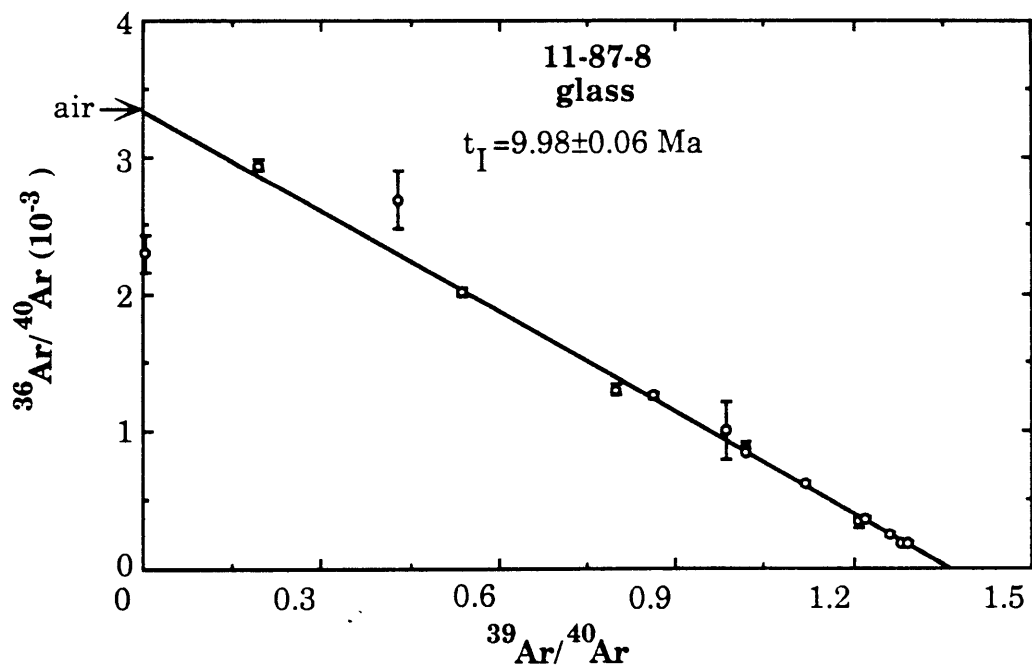
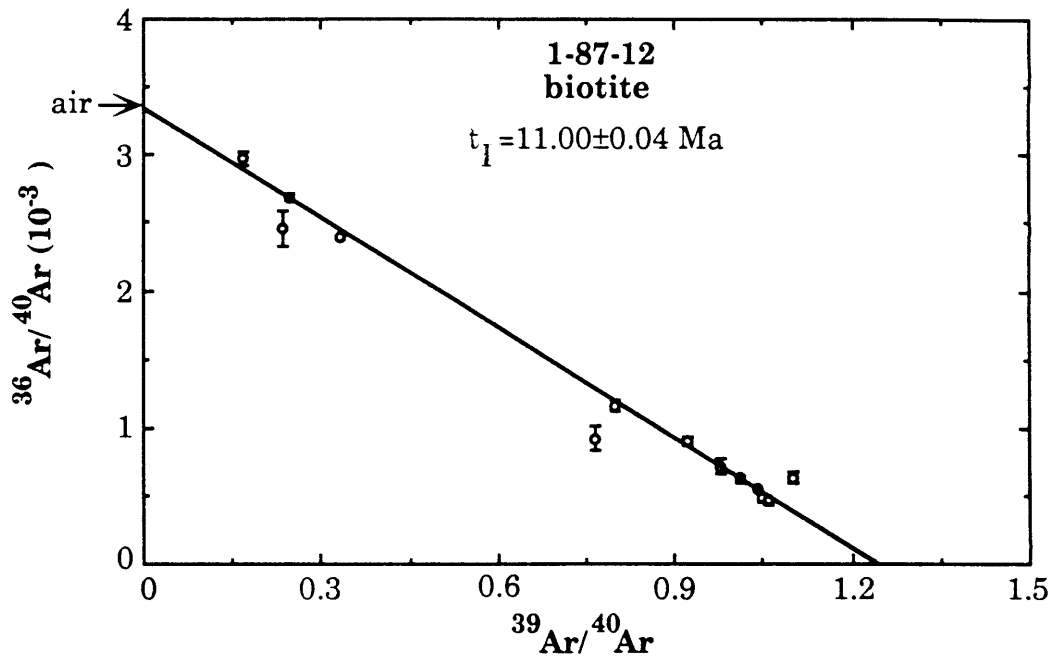


Figure 4.4 A, B

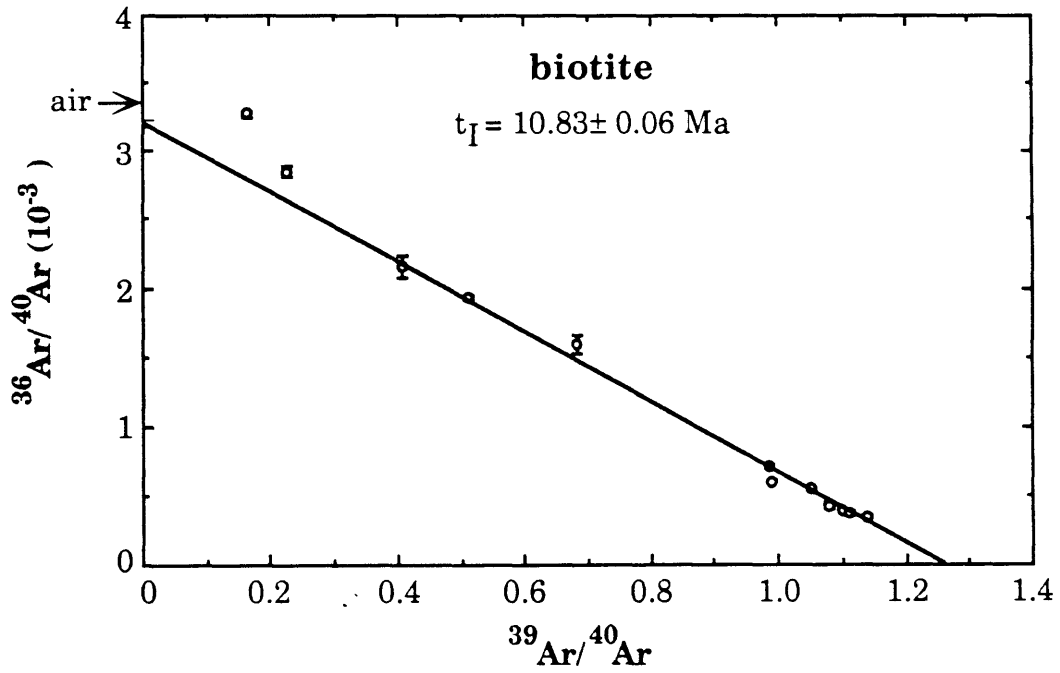
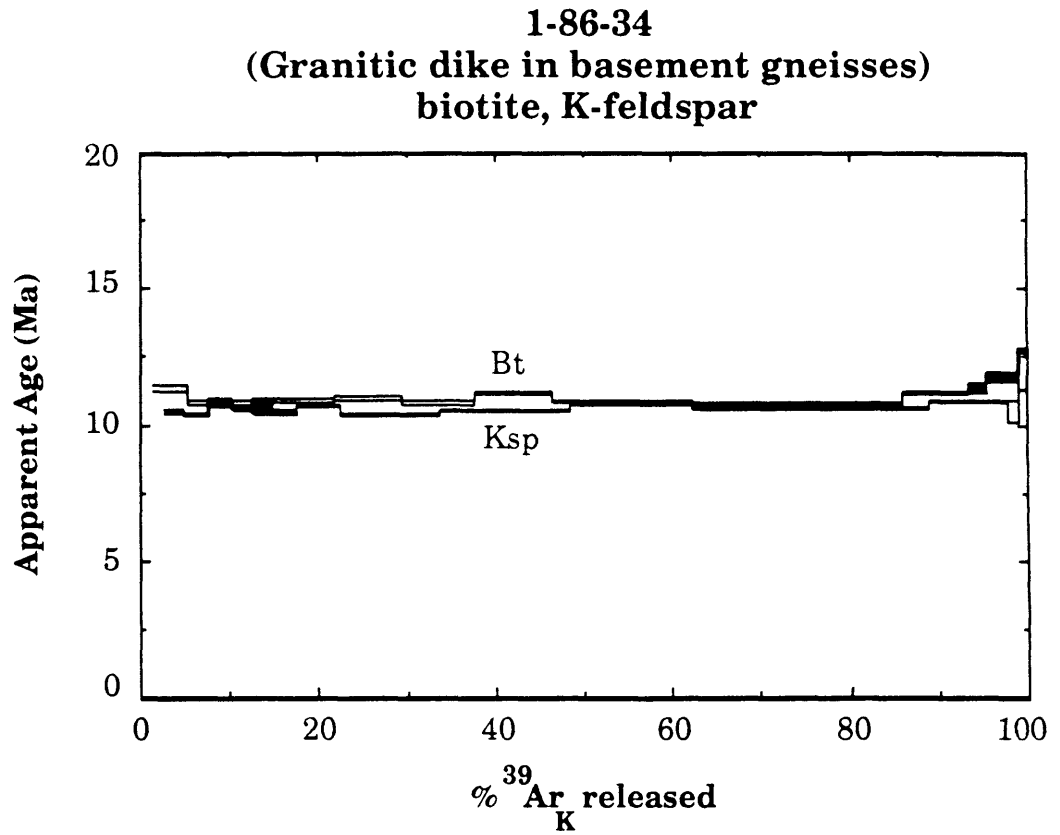


Figure 4.4 C

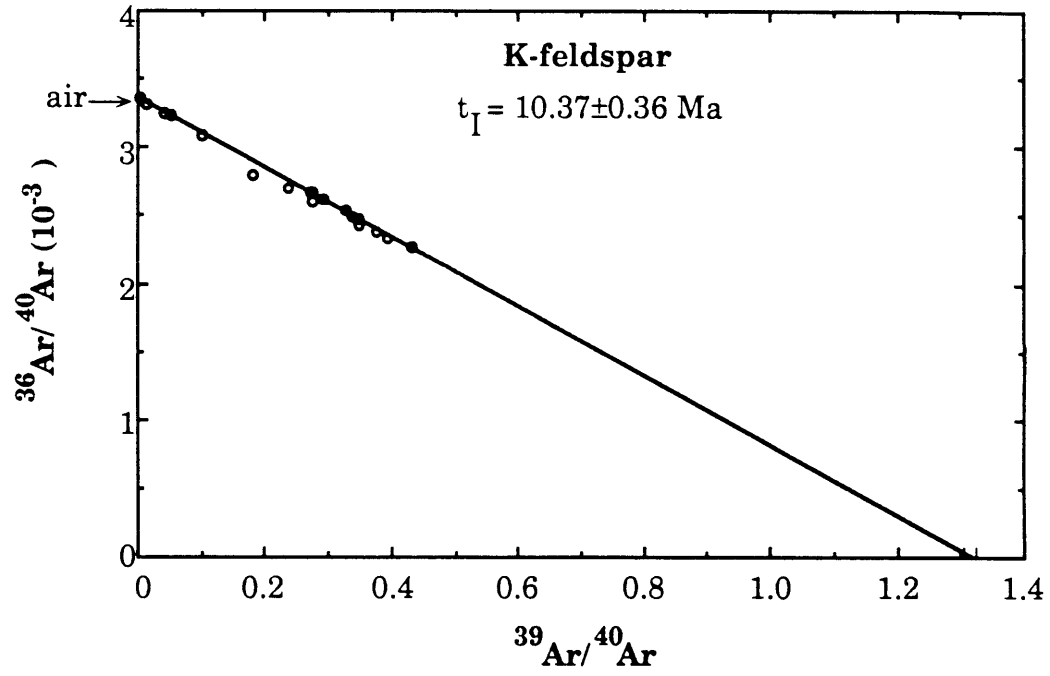


Figure 4.5 A, B

1-86-36C
(granitic dikes in basement gneisses)
biotite, K-feldspar

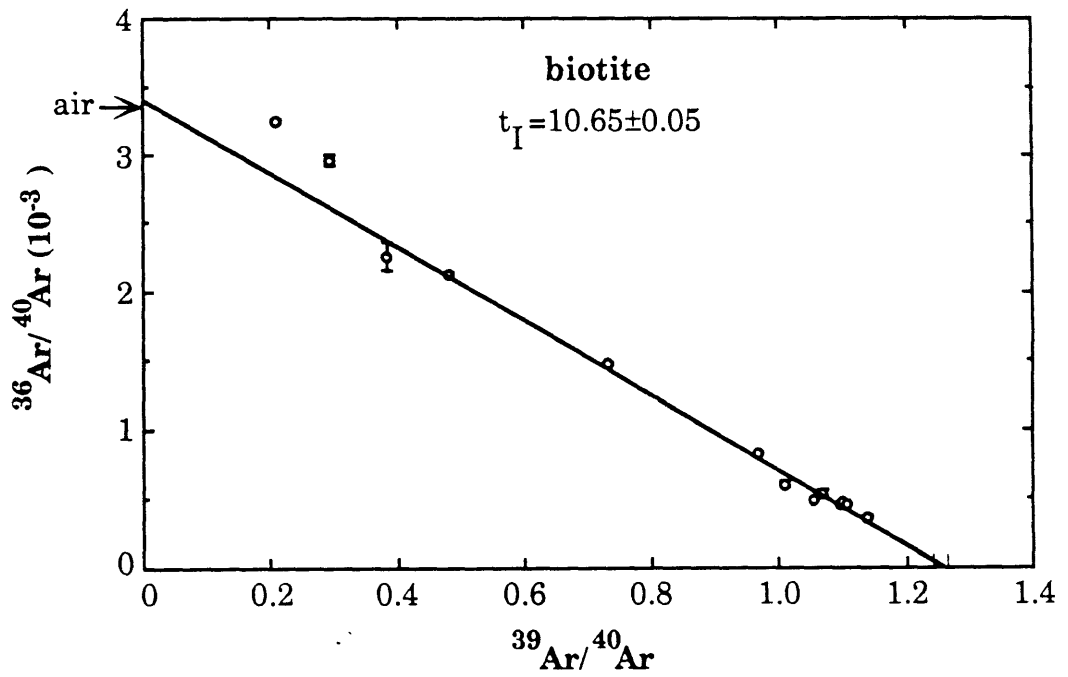
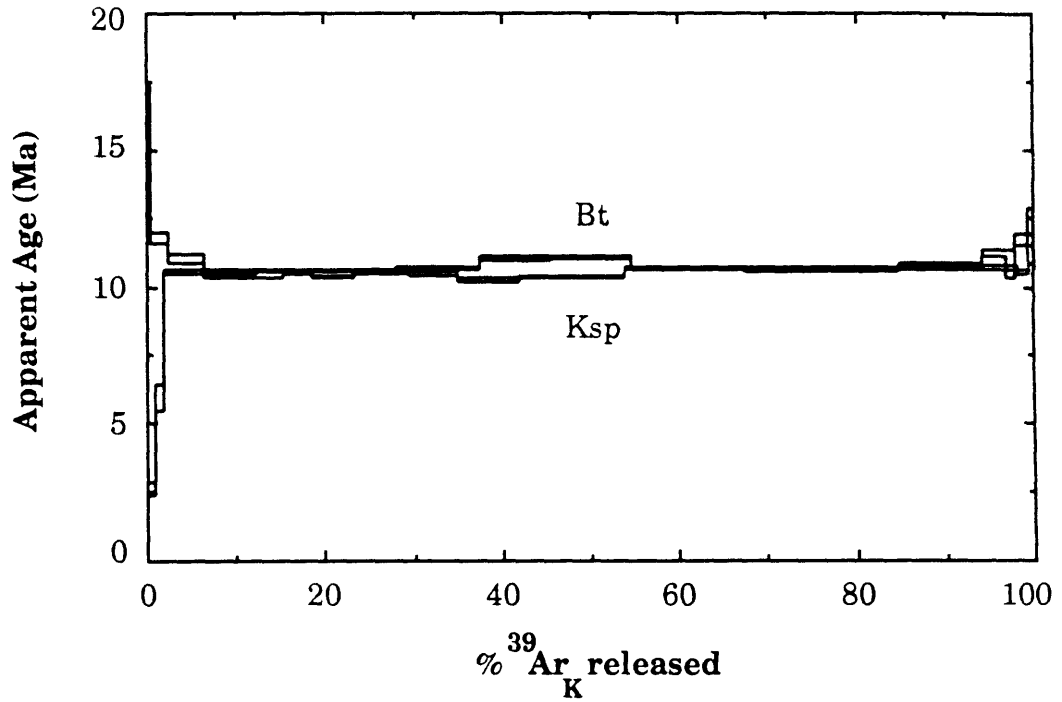


Figure 4.5 C

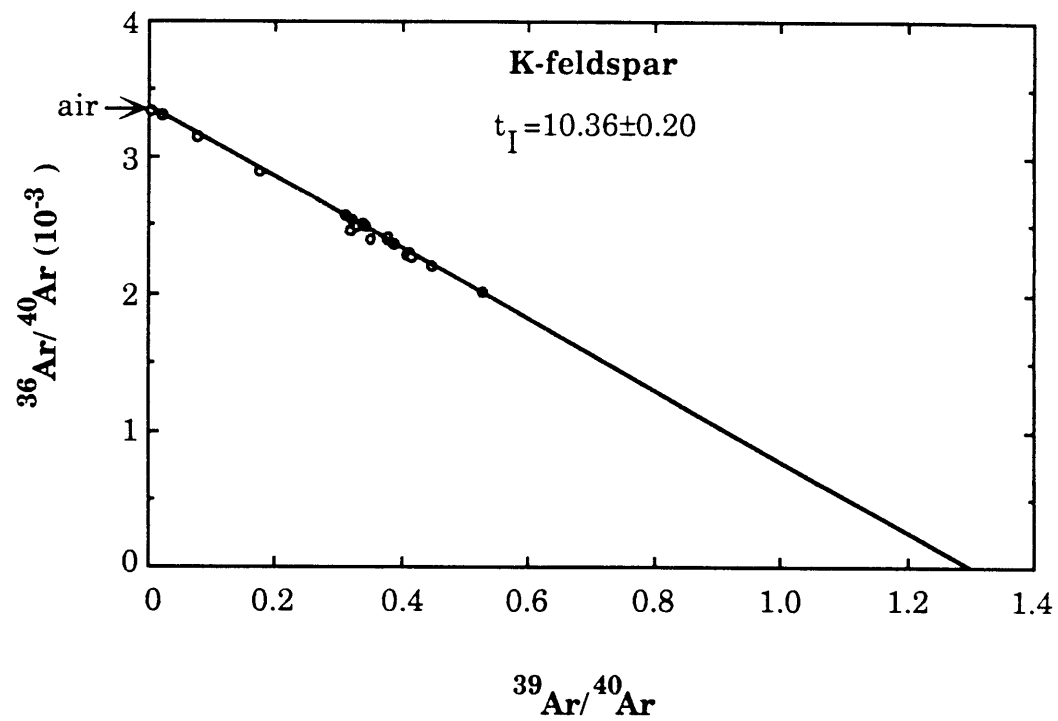


Figure 4.6 A, B

1-86-25
(Basement augen-gneiss)
K-feldspar

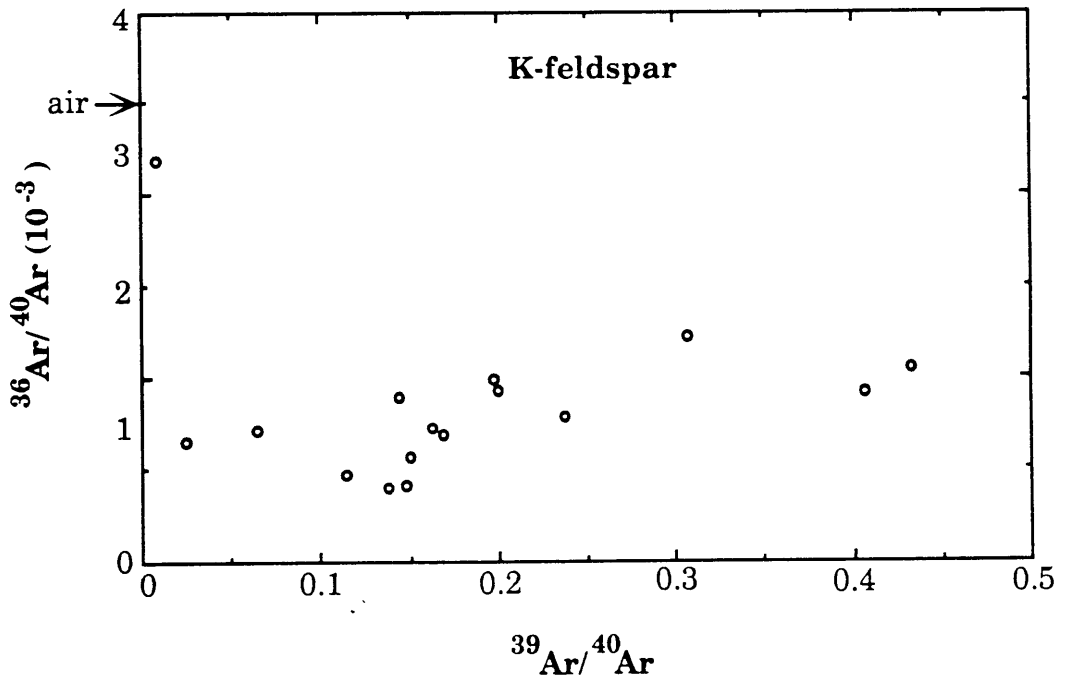
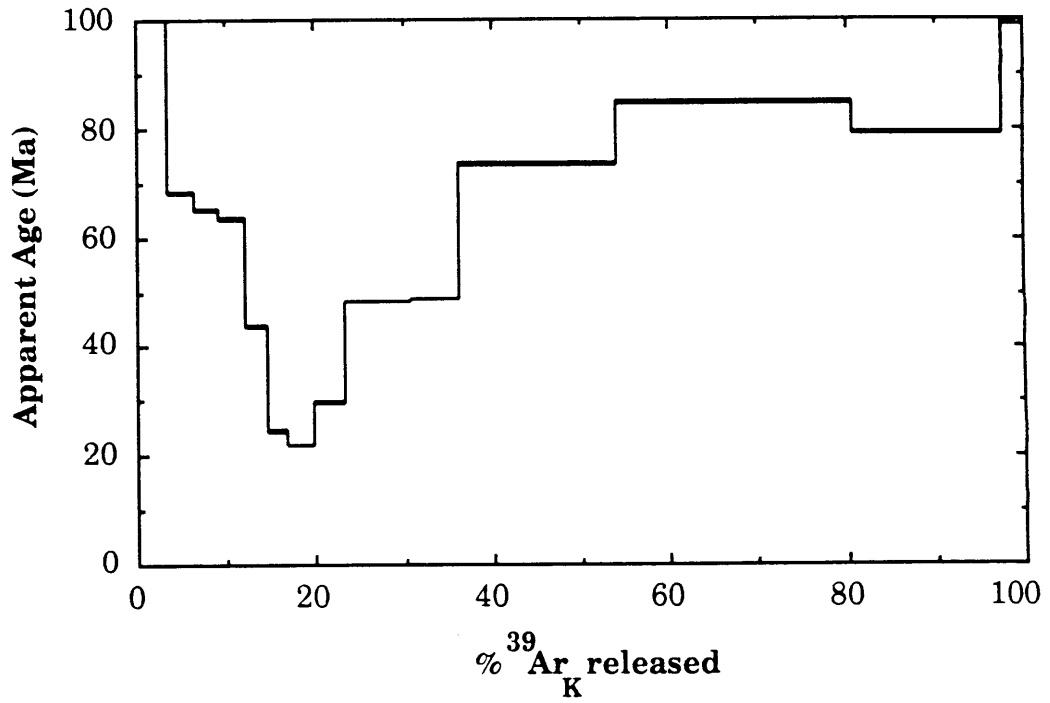


Figure 4.7 A

10-87-13A
(Willow Spring Diorite)
hornblende, biotite

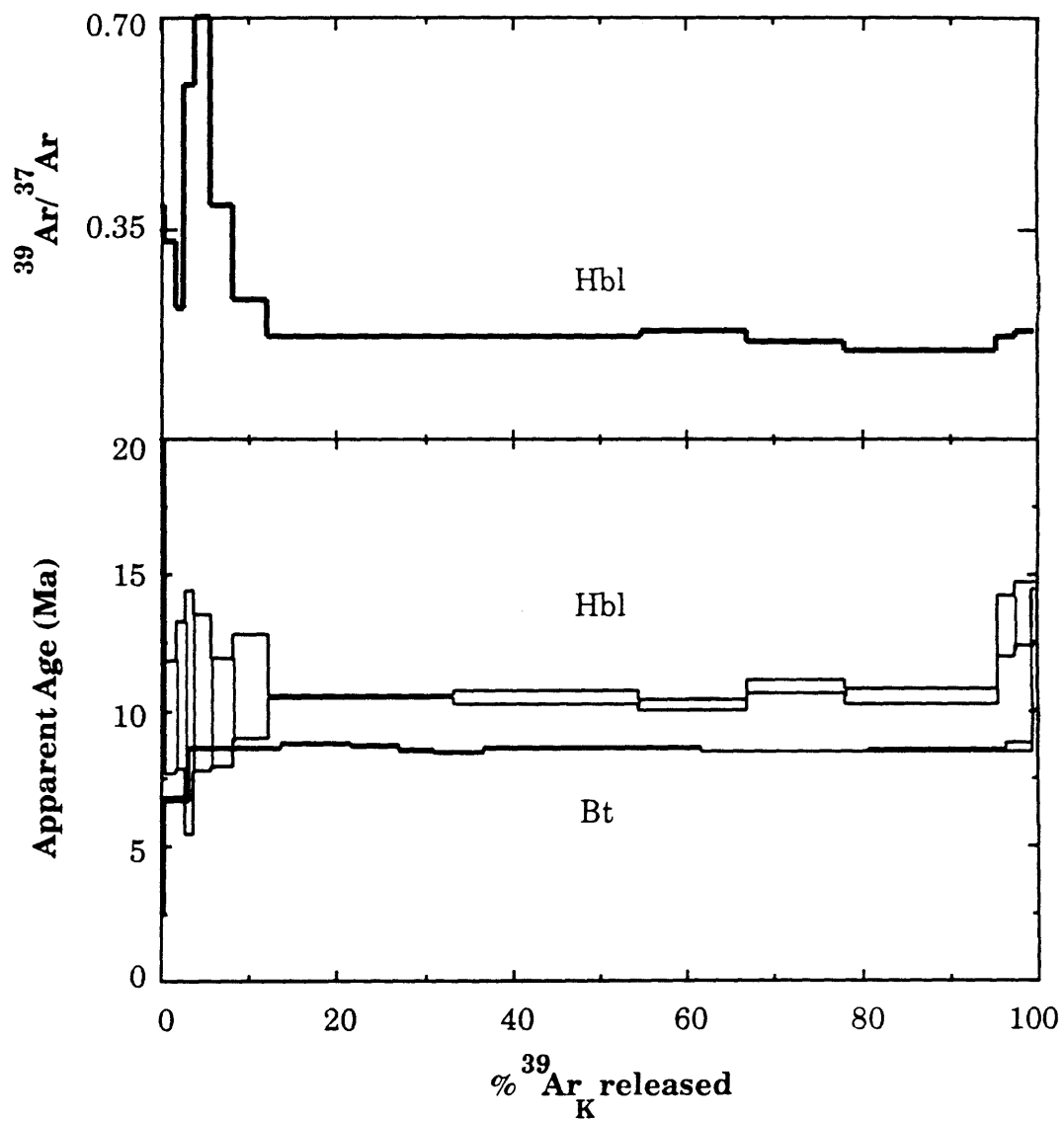


Figure 4.7 B, C

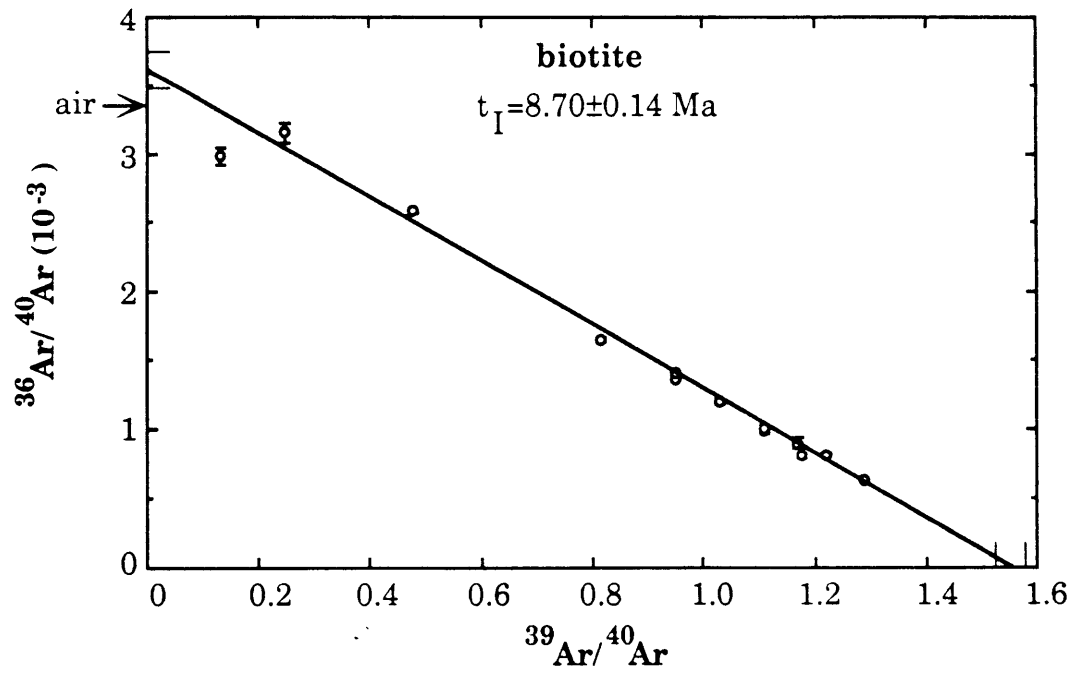
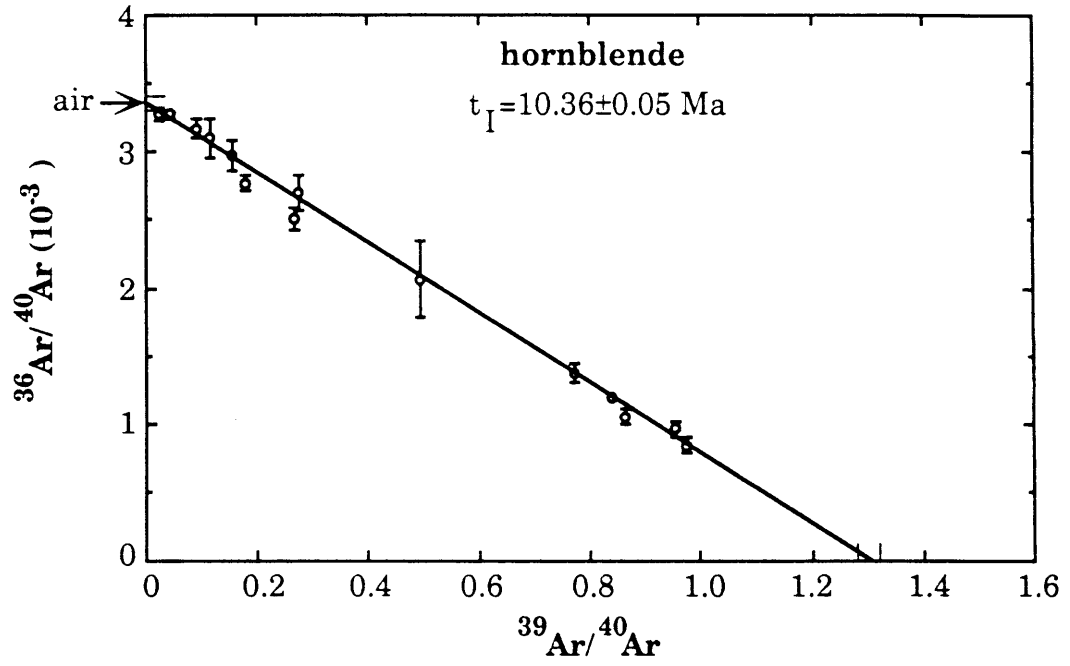


Figure 4.8 A

10-87-13C
(Willow Spring Diorite)
hornblende, biotite

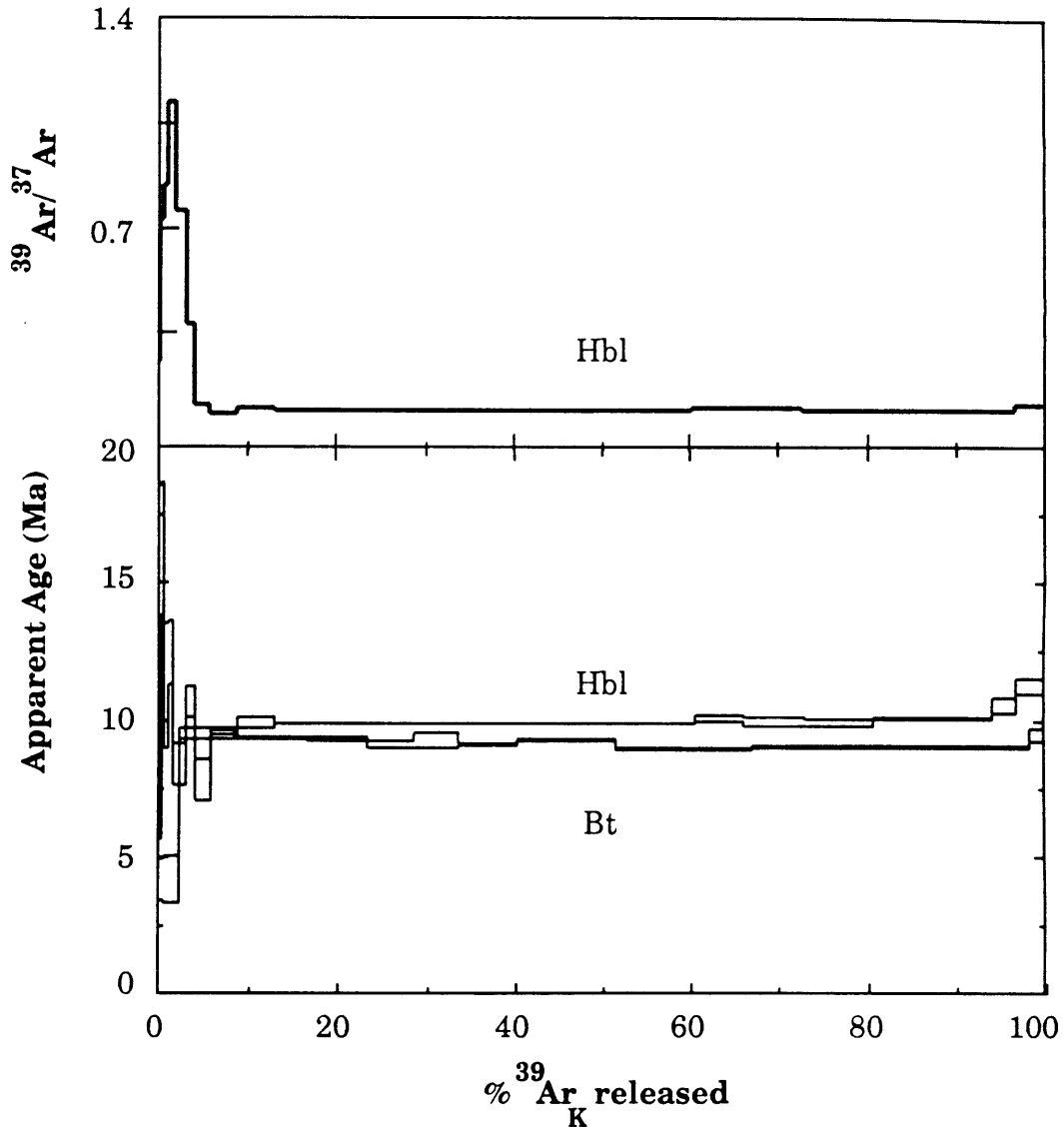


Figure 4.8 B, C

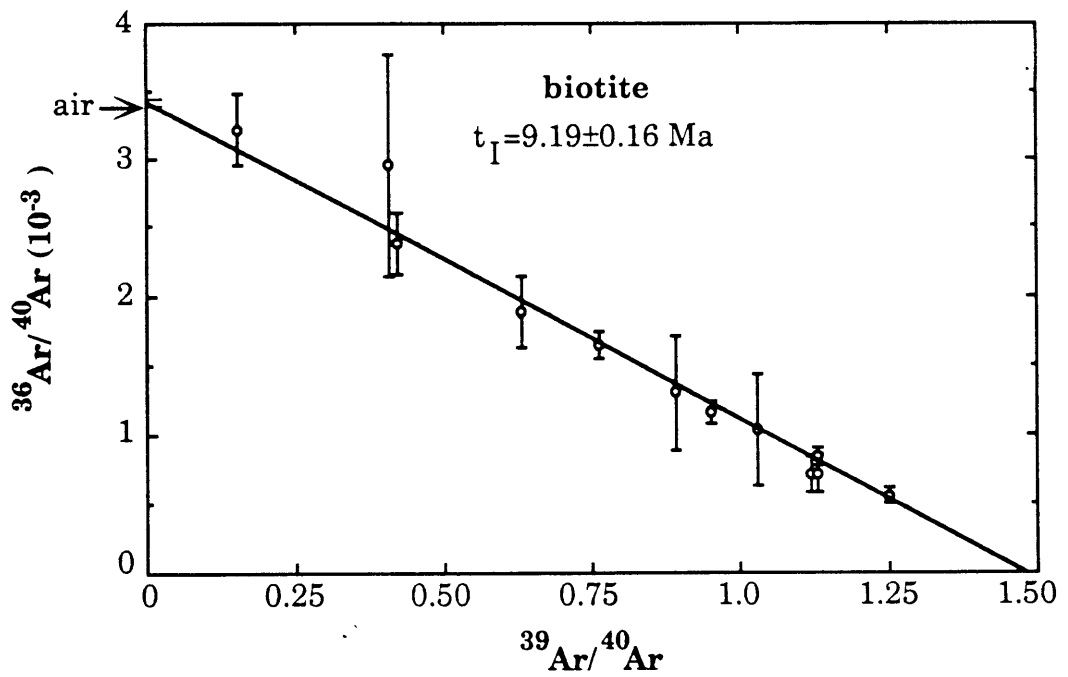
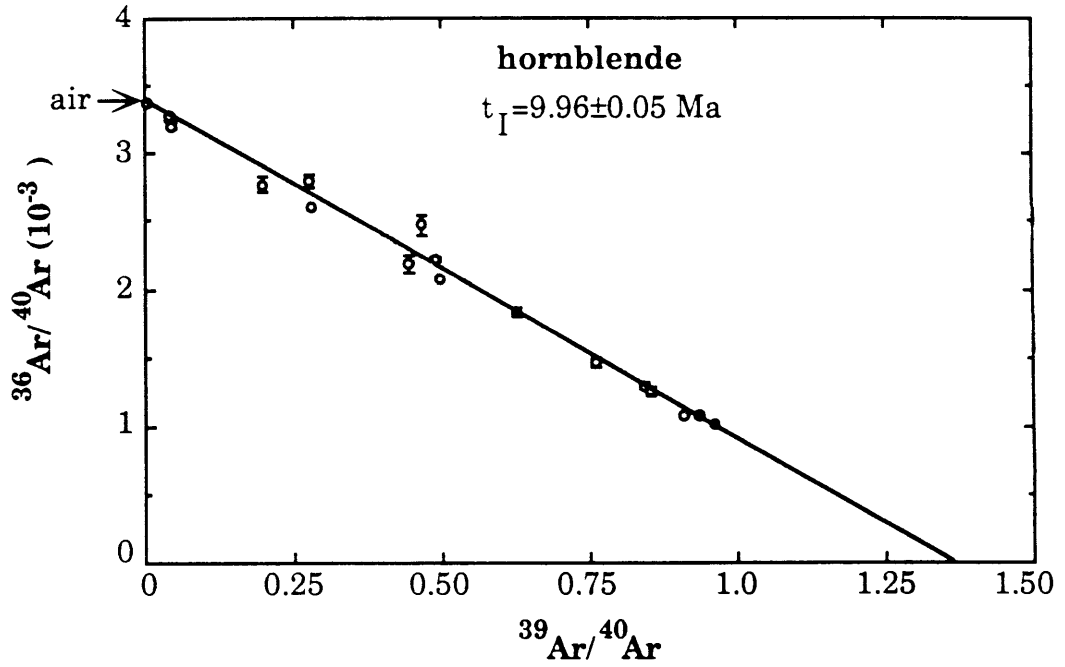


Figure 4.9 A

**10-87-13D
(Willow Spring Diorite)
hornblende**

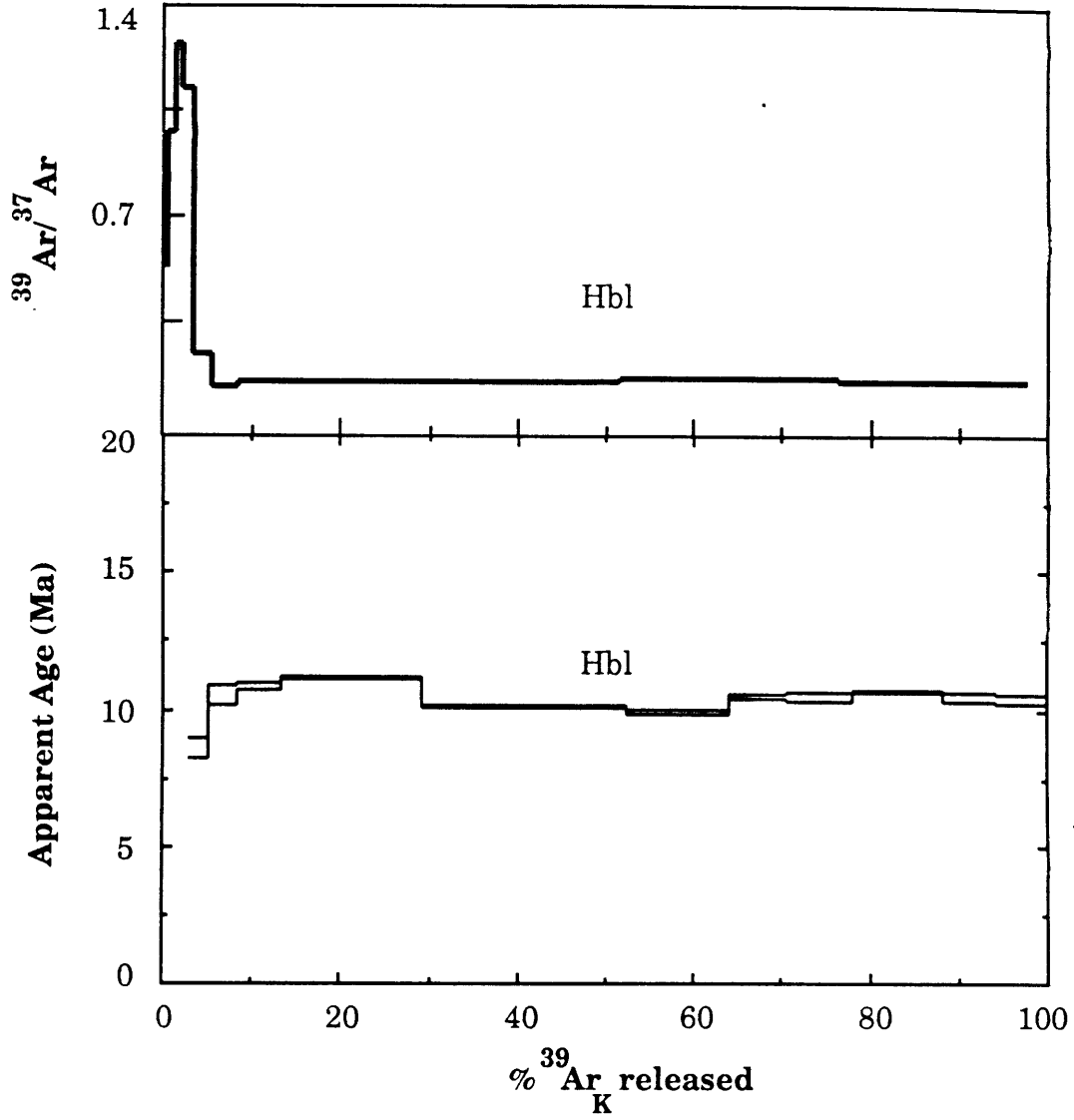


Figure 4.9 B

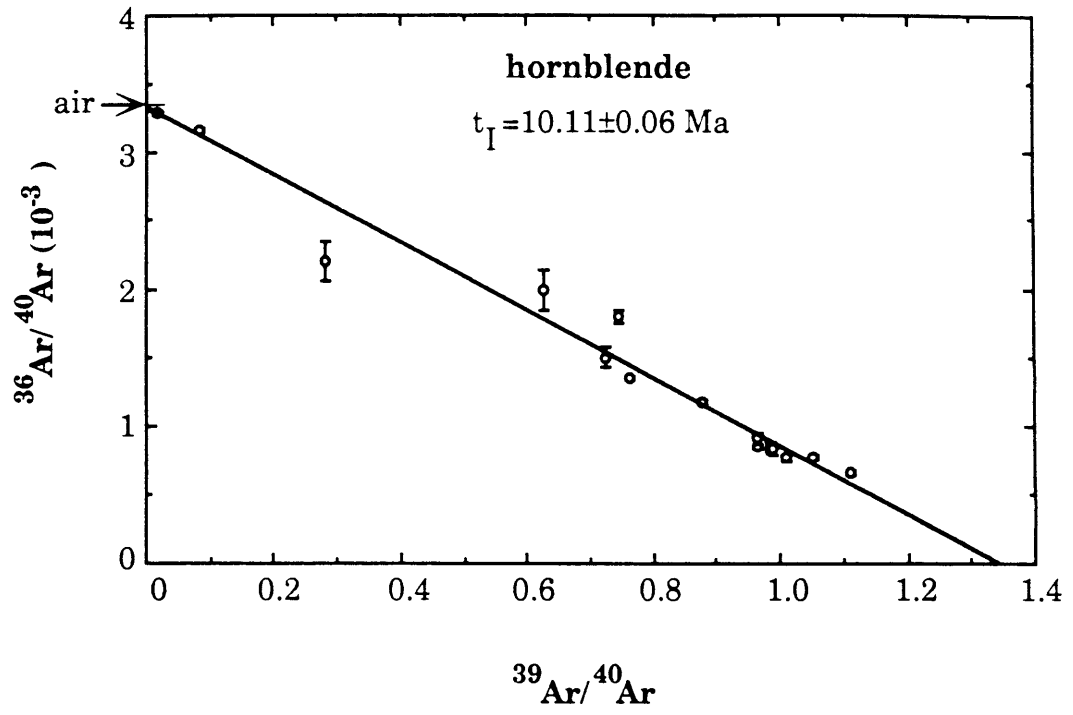


Figure 4.10 A

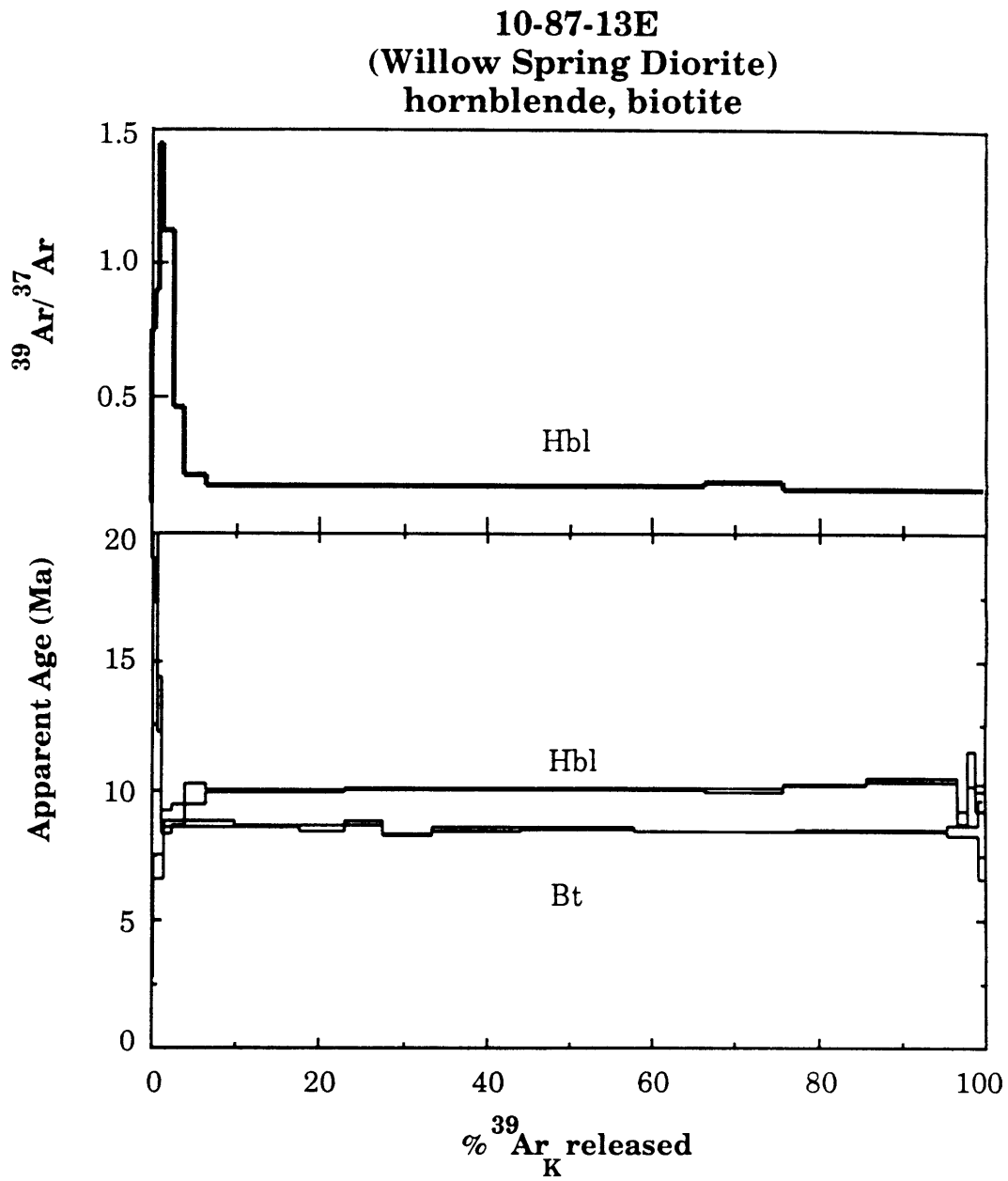


Figure 4.10 B, C

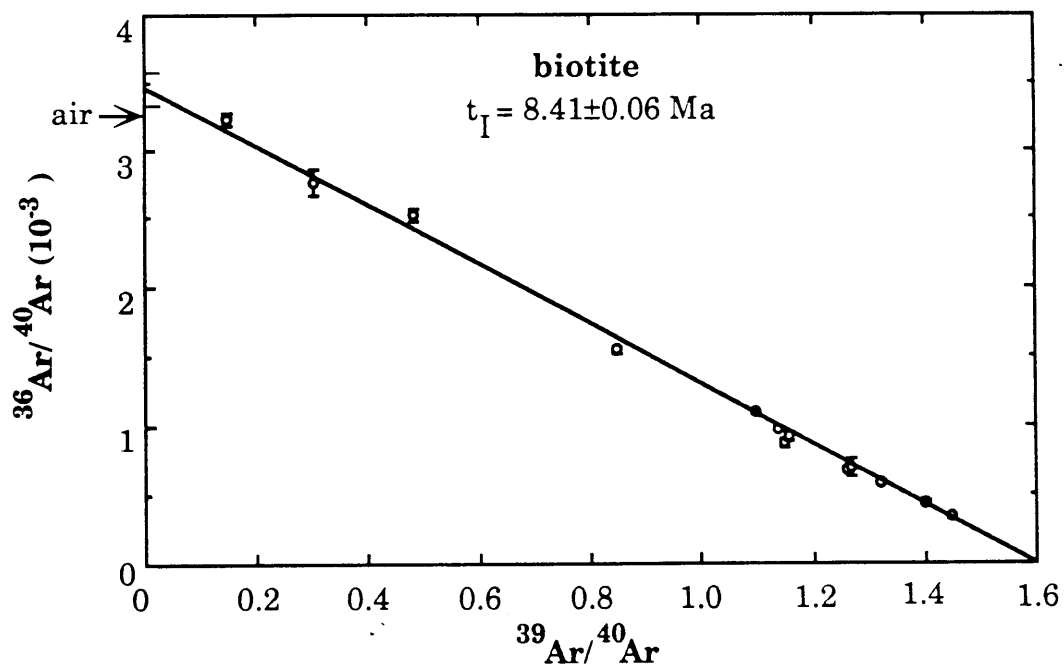
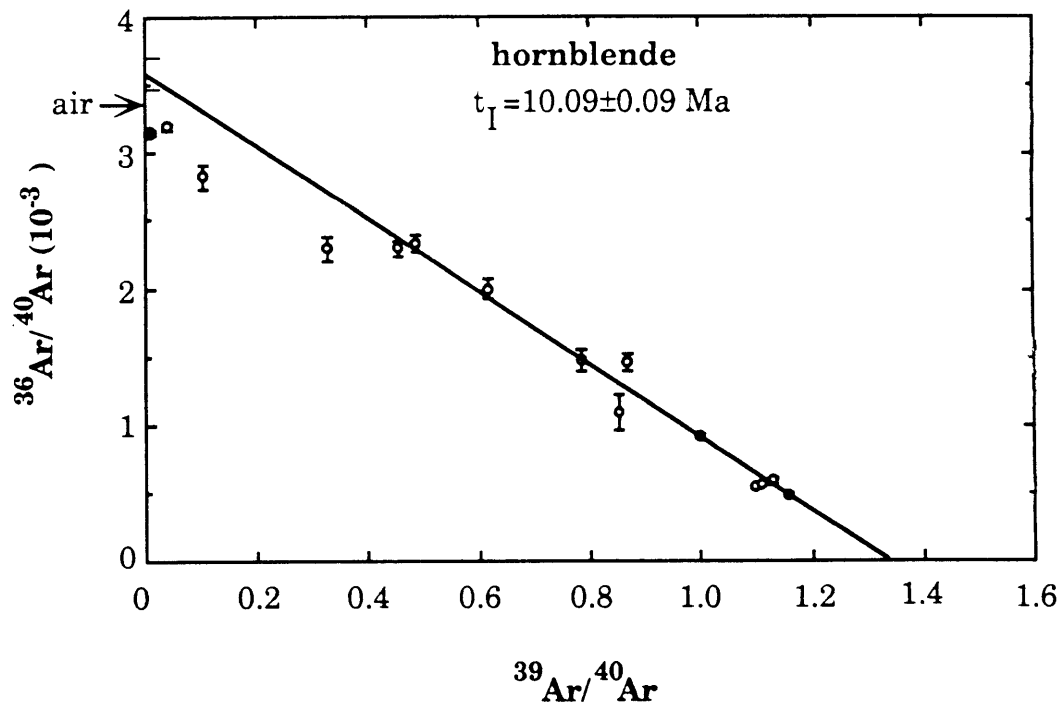


Figure 4.11 A, B

**10-87-9
(Granite Porphyry)
K-feldspar**

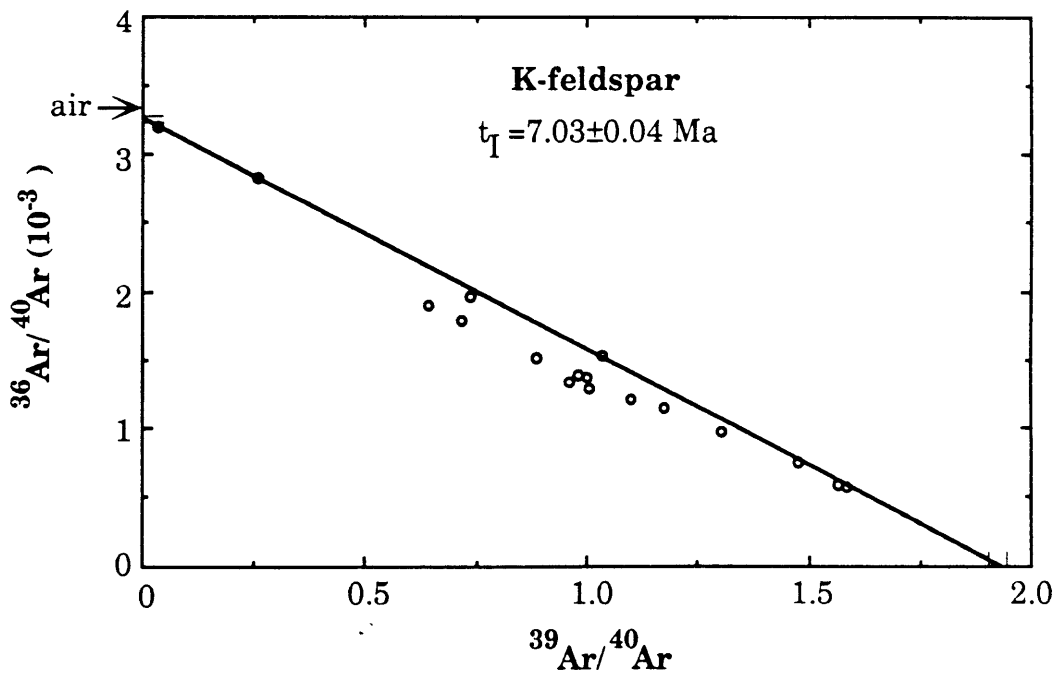
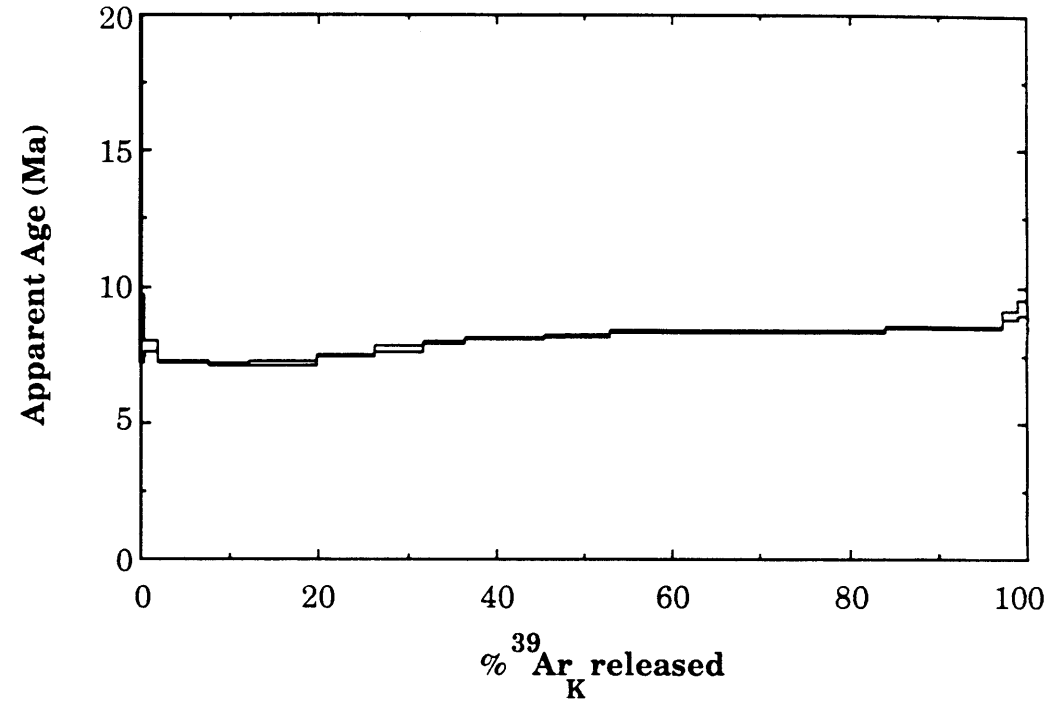
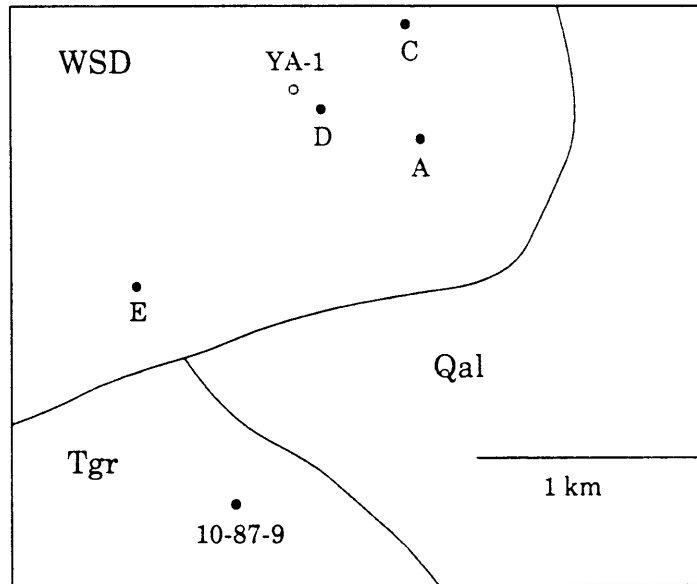
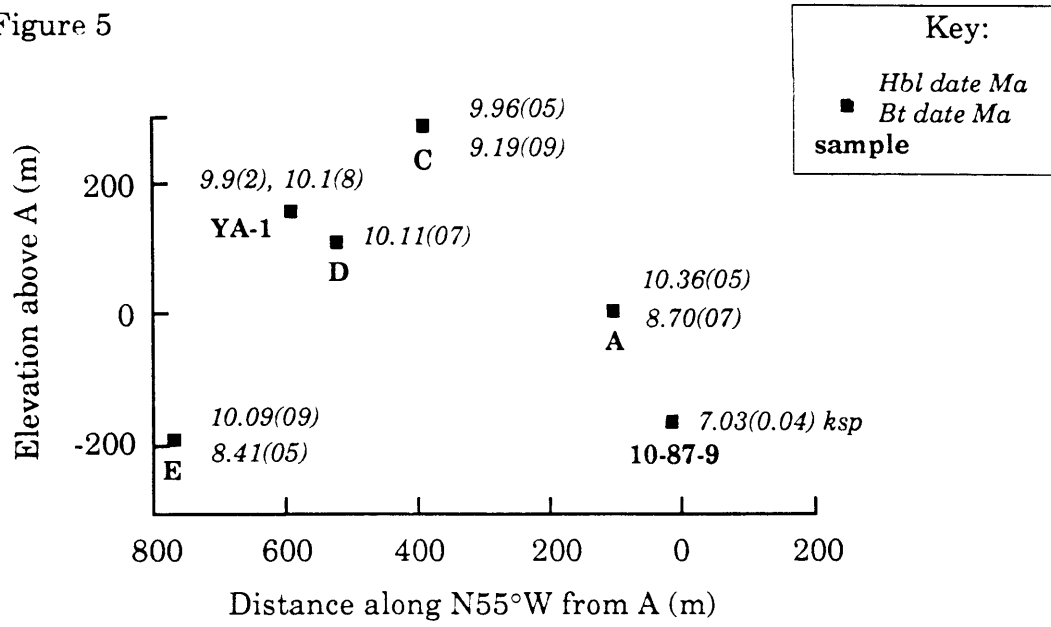


Figure 5



Sketch map of sample localities from the Willow Spring Diorite, Gold Valley, Black Mountains, California

Figure 6

Time Temperature Evolution

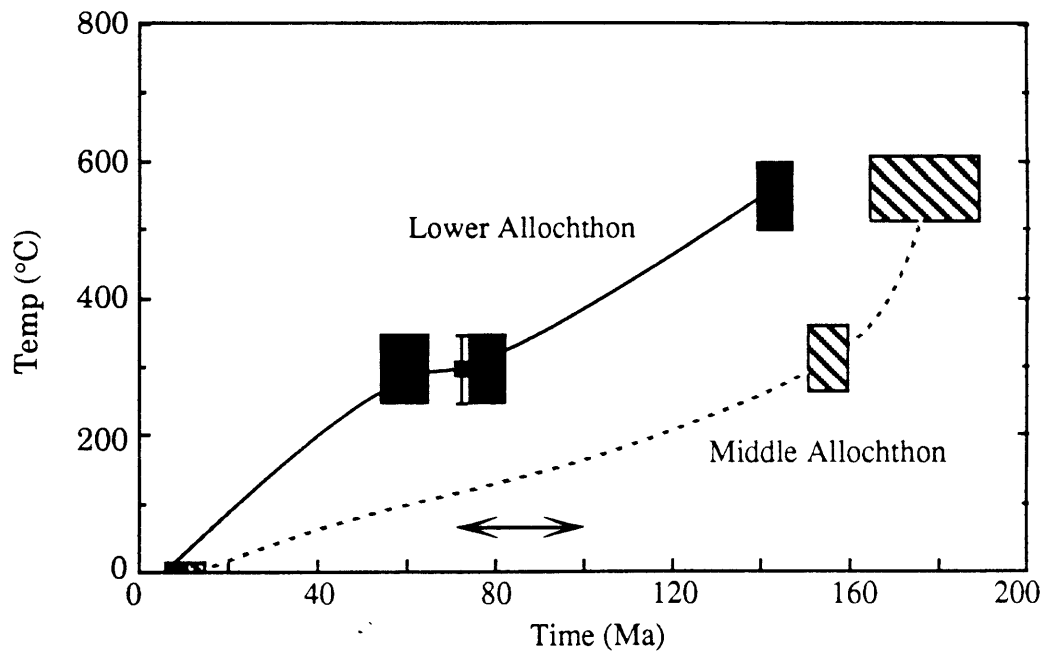
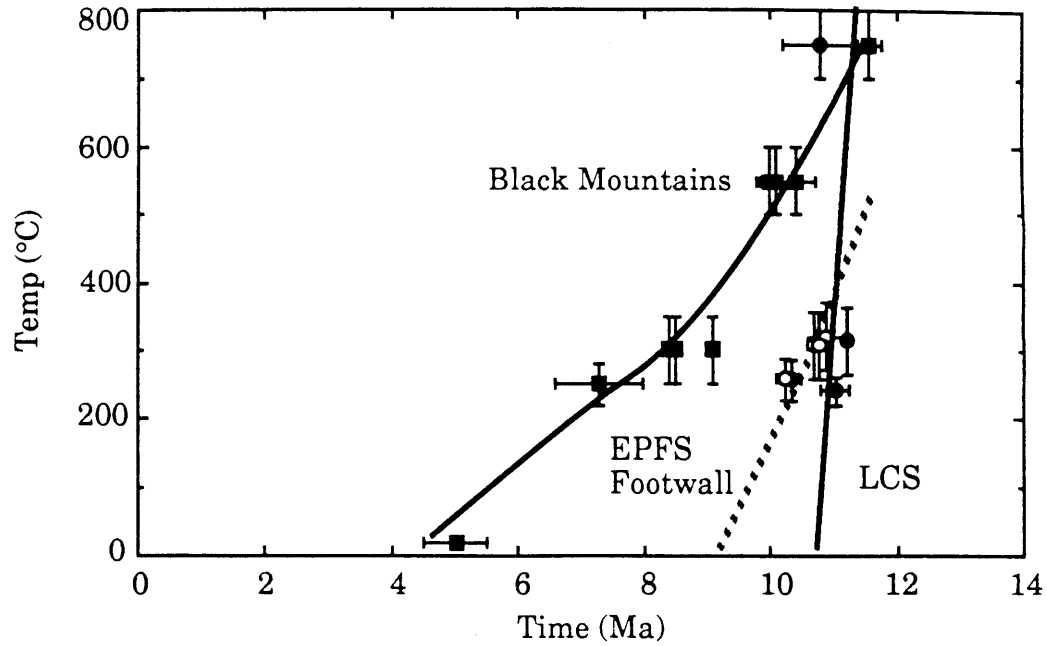
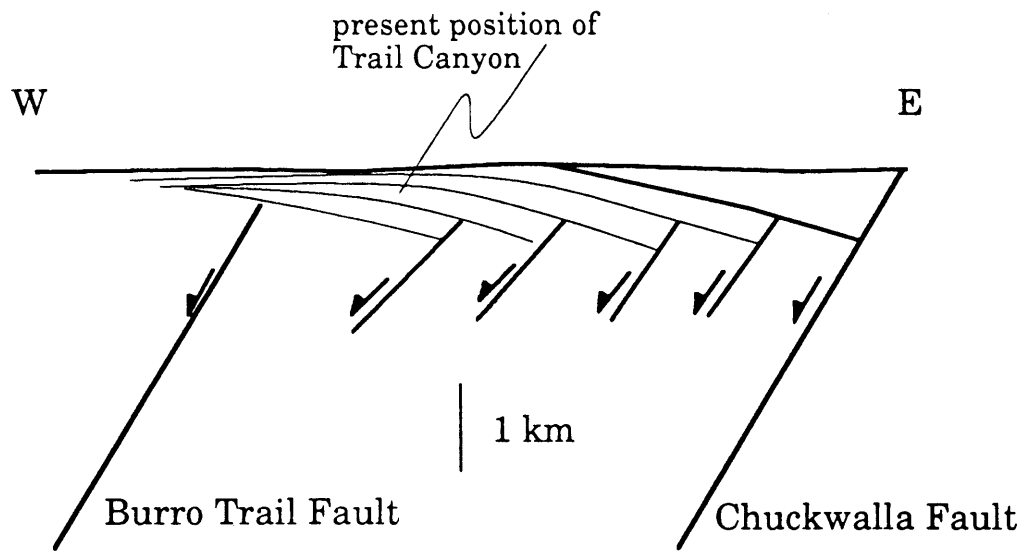
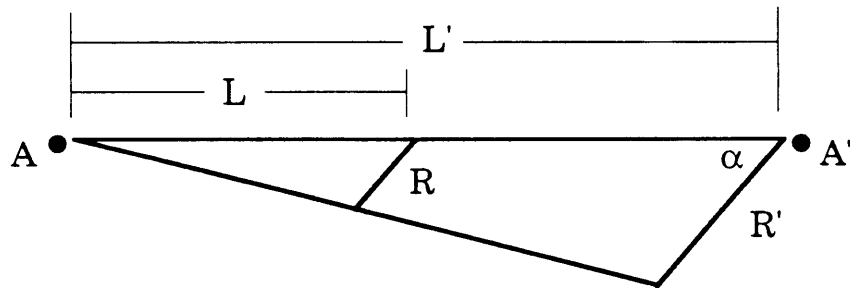


Figure 7

The Geology:



The Model:



Late Miocene

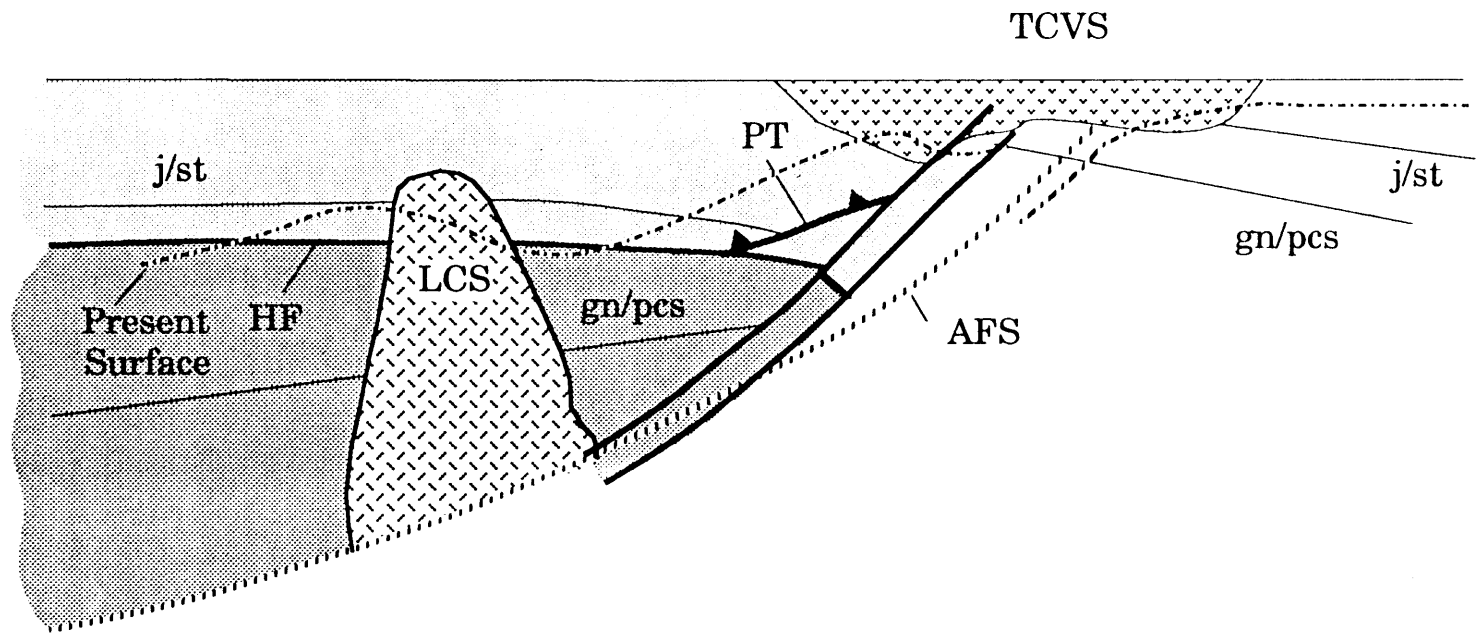
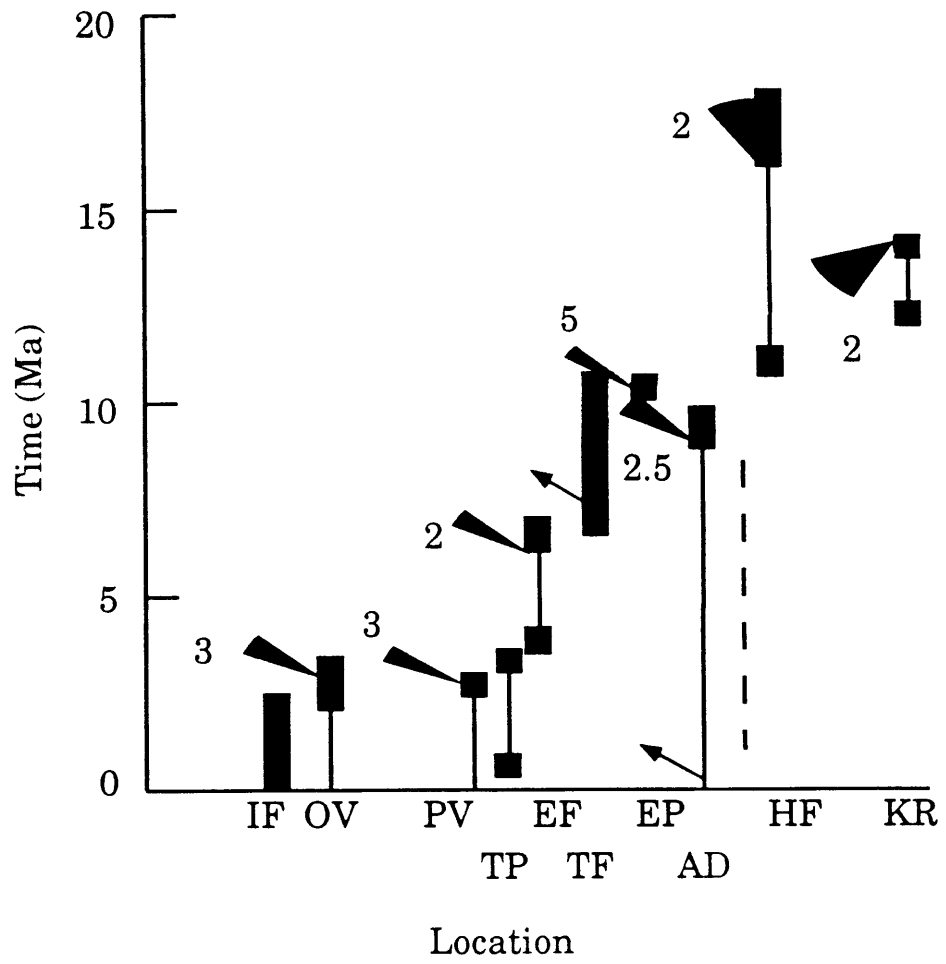


Figure 9



CHAPTER 3

GEOCHEMISTRY OF A MIOCENE VOLCANIC SEQUENCE AND ITS RELATION TO THE SCALE OF MANTLE HETEROGENEITIES BENEATH THE SOUTHERN BASIN AND RANGE

ABSTRACT

New chemical and isotopic data reported here, as well as previously published data from syn-extensional volcanic rocks from the Death Valley Region, western United States, are consistent with derivation of the volcanic rocks by mixing of two distinct mantle components with continental crust. These mantle components are equivalent to the enriched mantle and depleted mantle components identified by previous authors. The evolution of the relative contribution of the depleted versus enriched mantle sources to the syn-extensional volcanic rocks is well-explained by a lithosphere scale simple-shear model for extension within the Death Valley Extended Area.

The new data reported here are from the Trail Canyon Volcanic Sequence, a 10.3 to 10.0 Ma series of basaltic andesites, andesites, dacites and rhyolites of calc-alkaline to tholeiitic composition exposed in the eastern Panamint Mountains of eastern California. Major element, trace element and isotopic data indicate that these rocks were derived by mixing of a depleted mantle-derived parental liquid and a contaminant with a crustal composition. Initial $^{87}\text{Sr}/^{86}\text{Sr}$ ratios range from 0.706 to 0.713, with corresponding variations in Rb/Sr. Lead isotope ratios vary from $^{206}\text{Pb}/^{204}\text{Pb}=18.69$ to 19.39, $^{207}\text{Pb}/^{204}\text{Pb}=15.62$ to 15.72, and $^{208}\text{Pb}/^{204}\text{Pb}=39.1$ to 39.74. Finally, the three measured Nd compositions show a small range, from $^{143}\text{Nd}/^{144}\text{Nd}=0.512407$ to 0.512455. Rare-earth element trends in the Pliocene age basalts to basaltic andesites of the nearby Nova Basin show rare-earth characteristics as the Trail Canyon samples, except that none of the Nova samples displays a Eu anomaly, and the absolute concentrations within the Nova samples are lower.

INTRODUCTION

The Basin and Range province of the western United States is a pervasively extended area of the earth's crust that is remarkably well exposed. Unlike other large areas which have suffered extensional strains on the order of $\beta=2-3$ (200% to 300%), the Basin and Range is accessible to both detailed mapping and to detailed, directed field sampling. These characteristics make the area an ideal natural laboratory for investigating the relationships between continental extension and volcanism.

Three aspects of this problem have dominated the literature in the past few years. The studies of Carlson et al. [1981] and Menzies et al. [1983], among others, have established the isotopic and chemical heterogeneity of the sub-Basin and Range mantle. Debate on the scale and secular variation of these mantle heterogeneities is accompanied by a debate on the temporal variability of mantle sources for syn-extensional basalts, specifically the sequence source areas (as identified chemically) are tapped during volcanism. Finally, both of the previous topics have been examined in light of the possibility that these apparent heterogeneities may have been caused by either bulk or selective contamination of "mantle" signals by continental crust [Watson, 1982]. Here we report the results of our study of Late Miocene to Pliocene volcanic rocks from the Death Valley area, in the southwest section of the Basin and Range province, and the implication that these results have for understanding each of the three topics discussed above. The major element, trace element, and isotopic (Sr, Pb and some Nd) compositions of the Miocene age Trail Canyon Volcanic Sequence are given, as well as new trace element contents of samples from the Mio-Pliocene age Nova Basin. The Trail Canyon Volcanic Sequence represents the oldest volcanic rocks analyzed in detail from the Death Valley Extended Area, and these analyses establish a longer time span than previously available for studying the evolution of magmatic sources during extension.

GEOLOGIC SETTING

Located on the western edge of both the Basin and Range province and the North American continent, the crust and mantle of the Death Valley

area have experienced a complex and lengthy history of deformation [Burchfiel and Davis, 1975]. After continental rifting in Middle to Late Proterozoic time, the western margin of North America acted as a passive margin through the Paleozoic until Permian time. Following Permian truncation [Walker, 1988], the margin of the continent was dominated by arc volcanism and eastward-directed subduction [Busby-Spera, 1988] for much of the Mesozoic. Some disagreement exists as to the geometry of the Late Cretaceous – Early Cenozoic phase of subduction: Bird [1988] has suggested, on the basis of numerical modelling, that the Farallon plate was subducted at zero angle below North America, while others [Farmer and De Paolo, 1983; Farmer et al., 1989] have suggested a more steeply dipping subduction zone.

Extensional tectonism has dominated the Cenozoic history of the Basin and Range province. Following subduction of the Farallon/Kula plate beneath North America, the plate margin was transformed into a zone of right lateral shear as the nascent San Andreas Fault migrated northward along the edge of the North American/Pacific plates. Stock and Molnar [1988] suggest through global plate reconstructions that this transition would have occurred at the latitude of the Death Valley region between 20 and 10 Ma. The onset of extension within the Western North America was diachronous, with extension initiating in the northern and southern ends of the Basin and Range, migrating toward the center with time [Sonder et al., 1987]. Within the southern Basin and Range, extension probably initiated at approximately 18-15 Ma [Bohannon, 1984; Burchfiel et al., in preparation but see Dokka and Travis, 1990 for an opposing view] and continues to the present.

As might be expected from the diachroneity of extension, variations in the deformational history and total extensional strain are common within the Basin and Range Province. A fundamental division in the character, timing, and extent of extension between the "northern" and "southern" Basin and Range, with a border near the latitude of Las Vegas has been known for some time [Eaton, 1982]. More recent work has further refined estimates of the scale of strain heterogeneities, allowing the definition of domains which appear to act as coherent systems undergoing diachronous

extension in uniform directions [Bohannon, 1984; Burchfiel et al., in preparation; Howard and John, 1987].

The Death Valley area is a particularly well-studied extensional domain which lies along the western edge of the Basin and Range, bounded by the Sierra Nevada to the west, the Furnace Creek fault zone to the north, the Spring Mountains to the east, and the Garlock Fault to the south (Figure 1). The earliest extension within the Death Valley Extended Area began at approximately 24 Ma within the Funeral Mountains [Cemen et al., 1985], although the scale and relationship of this early extension to the "Basin and Range" episode is unclear. The main episode of Cenozoic extension initiated at the Kingston Range Detachment between 14.5 and 12.5 Ma [Burchfiel et al., in preparation], and migrated, in a general sense, to the west with time [McKenna and Hodges, in press Chapter 1; Wright et al., 1984]. The active loci of extension are located along the Death Valley, Panamint Valley and Owens Valley fault systems. Although the geometries and kinematic histories of the faults which accommodated extension varied somewhat, the Death Valley area has generally extended along a N55°W direction along shallowly to moderately westward-dipping normal faults since prior to the Miocene [McKenna and Hodges, in press, Chapter 1; Wernicke et al., 1988]. Total extension within this section of the Basin and Range was estimated by Wernicke et al. [1988] as approximately 250 km, suggesting a total stretching of $\beta=2-3$.

Despite this stretching, both refraction and reflection seismic data clearly indicate the presence of a continuous Moho beneath the Death Valley area at 30-35 km depth [Serpa et al., 1988; de Voogd et al., 1988]. Reconciling the large extension seen in the upper levels of the crust with the absence of Moho disruptions is a continuing topic of investigation [Block and Royden, in press; Gans, 1987; Serpa et al., 1988]. Gans [1987] has argued that this geometry is due to uniform (pure shear) stretching of the lithosphere and subsequent underplating or injection of mantle-derived melts to the crust. Block and Royden [in press] argued that the geometry of highly extended areas within the Basin and Range required significant lateral flow of lower crust from less extended areas to more highly extended areas, thus eliminating the "need" for injection of mantle material into the

crust. Simple-shear models of extension can explain the Moho observations by shallow intersection angles and rapid re-establishment of the Moho through syn-extensional magmatism.

All of these models predict a direct coupling between crustal extension and thermal, physical and chemical changes within the lower crust, mantle lithosphere and asthenosphere. These changes should be reflected in the composition of syn-extensional magmas erupted within the extended area. Leeman [1970, 1982], Farmer et al. [1989], Ormerod et al. [1988] and Bacon et al. [1984], among others, have utilized this coupling to examine the relationships between extension and magmatism within the Death Valley Extended Area. Although the results of these studies are in some disagreement, it is clear that the isotopic and chemical composition of volcanic rocks within the Basin and Range can be used to examine the interaction of crust, lithosphere and asthenosphere during extension.

Samples analyzed in this study are from two Mio-Pliocene basins now stranded in the Panamint Mountains of central Death Valley (Figure 1): the Eastern Panamint and Nova Basins. The older flows fill the Eastern Panamint Basin and are part of the the Trail Canyon Volcanic Sequence, which crops out along the eastern foot of the Panamint Mountains and the Central Black Mountains. Biotite and glass separates from the Trail Canyon Volcanic Sequence yield $^{40}\text{Ar}/^{39}\text{Ar}$ ages indicating that the Trail Canyon Volcanic Sequence was extruded during a 0.3 Ma period from 10.3 to 10.0 Ma [McKenna, submitted; Chapter 2]. The basalts through basaltic andesites from the Nova Basin are between 6 and 3.6 Ma old [see Hodges et al., 1988 for references] The major element and isotopic chemistry of the volcanic rocks from the Nova Basin been described by Coleman and Walker [in press] and Walker and Coleman [submitted] respectively; they concluded that the composition of the flows was due to a combination of fractional crystallization and crustal contamination. In this paper we present two sets of data: major element, trace element, and isotopic contents of the Trail Canyon Volcanic Sequence flows, and trace element contents of the Nova Basin flows.

ANALYTICAL PROCEDURES

Locations for samples from the Trail Canyon Volcanic Sequence are given in Appendix 1; Coleman and Walker [in press] give sample locations for the Nova Basin samples. Fresh, unaltered samples were cleaned by boiling in deionized water, ultrasounded, and finally crushed in a silica shatterbox. Major and trace elements were determined by X-ray fluorescence on a fully automated Rigaku X-ray spectrometer at the University of Kansas. Uncertainties, based on repeated analyses of standards, are 0.5-1% of the measurement for major elements, 1-2% of the measurement for trace elements with concentrations greater than 50 ppm, and 5-10% of the measurement for trace elements with concentrations less than 50 ppm.

Isotope ratios and concentrations were determined through standard isotope dilution techniques: Hart and Brooks [1977] for Sr; Zindler et al. [1979] for Nd; and Pegram [1986] for Pb. Strontium, Rb, Nd and Pb data were collected at MIT on a nine-inch, 60° spectrometer (NIMA-B); some Nd and Pb data were collected at the University of Kansas (VG Sector). Strontium data are reported relative to Eimer & Amend standard SrCO₃ $^{87}\text{Sr}/^{86}\text{Sr}=0.7080$, and are normalized relative to $^{86}\text{Sr}/^{88}\text{Sr}=0.1194$. In-run precisions on $^{87}\text{Sr}/^{86}\text{Sr}$ were <0.01% (2 σ) and generally better than 0.006% (2 σ). Neodymium ratios are reported relative to BCR-1=0.512622, and are normalized to $^{146}\text{Nd}/^{144}\text{Nd}=0.7219$. In-run precisions are better than 0.01% (2 σ). All Pb samples are fractionation-corrected by a factor of $0.1\pm 0.05\%$ /amu as determined by repeated analyses of NBS 982 common Pb standard, and are normalized to NBS 982 ($^{206}\text{Pb}/^{204}\text{Pb}=16.9388$, $^{207}\text{Pb}/^{204}\text{Pb}=15.4941$, $^{208}\text{Pb}/^{204}\text{Pb}=36.7115$). Precisions for Rb, Sr, and Nd concentrations determined through isotope dilution are better than 1%; blank levels for all isotopes are insignificant for the analyses reported.

Instrumental neutron activation analysis (INAA) was carried out at MIT; procedures and analysis techniques are reported by Ila and Frey [1984] and Lindstrom and Korotev [1982]. Reproducibilities of the analyses are approximately 1-5%; the precision for many elements is significantly better than the reproducibility. Data shown in Table 1 are quoted with

precision errors only except for samples 3-87-19 and 2-87-16, where the uncertainties reflect the results of two separate analyses.

PREVIOUS WORK

The Basin and Range Province has been an active research area for geochemists for decades; Leeman [1970, 1986] and Hedge and Noble [1971] report some of the earlier work on the isotopic composition of syn-extensional volcanic rocks in the Basin and Range. As noted by Farmer et al. [1989], despite this long history of study, relatively few workers have measured the Sr, Pb and Nd isotopic composition, as well as the trace element contents, of each of the rocks they have studied. Despite this, a regional data base for volcanic rocks exposed in the Death Valley Extended Area is available and growing. As work on the isotopic chemistry of oceanic rocks has illustrated, multi-isotopic data are necessary in order to fully explore the complexity of source heterogeneity.

Farmer et al. [1989] studied a series of Late Miocene to recent basalts along a transect from Crater Flat, Nevada (Figure 1) to Cima Dome. They concluded that the source areas of basalts from the Death Valley portion of the transect were distinct from source areas in other parts of the Basin and Range. They suggested that the source of the atypical Death Valley basalts was probably old (2.0-2.3 Ga) mantle lithosphere preserved within the Death Valley area. On the basis of Sr and trace element data on a suite of rocks exposed throughout the Basin and Range, Ormerod et al. [1988] argued that no lithosphere of 2.0-2.3 Ga age is present in the southern Basin and Range, and that the source for the syn-extensional magmas resides within the asthenosphere.

Walker and Coleman [in press] and Coleman and Walker [submitted] examined the major element contents and Sr, Pb and Nd isotopic composition of basalts and andesites exposed in the Nova Basin of the Panamint Mountains, and concluded that three sources were needed to explain the variation of the data: an asthenospheric source similar to that suggested by Farmer et al. [1989], an upper crustal "contaminant", and a previously unrecognized felsic component they correlated with sub-Sierra Nevada crust. Bacon et al. [1984] and Novak and Bacon [1986] examined the

major element chemistry and Pb and Sr isotopic chemistry of basalts through andesites exposed in the Coso Range (Figure 1). They too concluded that the chemical data could be explained by assimilation of a crustal component with a mafic parental liquid. In the remainder of this paper, we test the model of Walker and Coleman [submitted] by utilizing both the new measurements reported here, and the results of the workers above.

DATA

Major and trace element results are reported in Tables 1 and 2, while isotopic results are presented in Table 3. The Trail Canyon Volcanic Sequence consists of basaltic andesites, dacites and rhyolites, as shown on Figure 2. We are not sure if the compositional gaps in the series (at 57-62% SiO₂ and 68-72% SiO₂) are real or due to sampling bias.

The rocks are calc-alkaline in character, although their FeO*/MgO characteristics (Figure 2) classify them as weakly calc-alkaline to tholeiitic. Oxide variation diagrams (Figure 3) show roughly linear trends, with noticeable inflections of most oxides at 73% SiO₂ and, for alumina, at 62% SiO₂. Most of the samples analyzed for the study are aphyric to 20-30% phyrlic, and some of the scatter on the oxide diagrams may be due to the presence of phenocrysts in the samples.

Minor and trace element concentrations for the Trail Canyon Volcanic Sequence are reported in Table 2, and show wide variations, often correlated with SiO₂ (Figure 4.1). Concentrations of highly incompatible trace elements (Th, Ba, Rb) are high for the lower silica samples, ranging from 4, 825 and 87 to 19.5, 2040, and 158 ppm respectively. Rare earth element (REE) and incompatible trace element (ITE) plots are shown in Figure 4.2. Samples from the Trail Canyon Volcanic Sequence (Figure 4.2 A and C) show moderately HREE depleted, concave-up REE variations, with (La/Yb)_{cn} ratios of 10-15. A subset of the samples have pronounced negative Eu anomalies. Samples from the Nova Basin (figure 4.2 B and D) display similar REE variations, with concave-up patterns and slightly lower (La/Yb)_{cn} ratios of 4-10. Only one of the Nova Basin samples, a pyroxene-phyric tuff, displays a (negative) Eu anomaly.

The range in isotopic compositions measured in the Trail Canyon Volcanic Sequence parallels the variation in bulk composition. Initial $^{87}\text{Sr}/^{86}\text{Sr}$ ratios are plotted versus Rb/Sr ratios in Figure 5a (corrections are calculated using an age of 10.25 Ma [McKenna, submitted; Chapter 2]) The data show a wide range of initial ratios from 0.706 to 0.713, with corresponding variations in Rb/Sr. Lead isotope variations are shown in Figure 5B, and range from $^{206}\text{Pb}/^{204}\text{Pb}=18.69$ to 19.39, $^{207}\text{Pb}/^{204}\text{Pb}=15.62$ to 15.72, and $^{208}\text{Pb}/^{204}\text{Pb}=39.1$ to 39.74. Finally, the three measured Nd compositions show a small range, from $^{143}\text{Nd}/^{144}\text{Nd}=0.512407$ to 0.512455. Correlation of the various isotope ratios with each other are discussed in the regional context below.

DISCUSSION

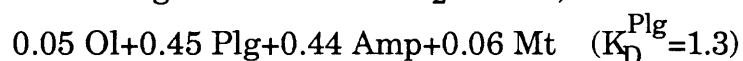
Petrogenesis: Crystallization versus Mixing

Both fractional crystallization of a parental basalt and mixing of basaltic and rhyolitic magmas have been invoked as the source of calc-alkaline series liquids [Gill, 1981; Grove and Donnelly-Nolan, 1986]. We test these competing models in this section of the paper, by comparing the results of fractional crystallization models with simple mixing models. We conclude that although the major element variations can be adequately explained by fractionation of plagioclase + amphibole + magnetite \pm olivine \pm biotite (Plg+Amf+Mt \pm Ol \pm Bt), trace element considerations suggests that magma mixing was the primary agent responsible for the chemical evolution of these flows.

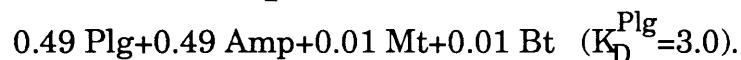
Because the Trail Canyon Volcanic Sequence contains hornblende and biotite phenocrysts, we modeled the major element variations of the series by a fractional crystallization model which included olivine, plagioclase, K-amphibole, K-biotite, and magnetite. In this model, the composition of solid phases was determined through equilibrium partition coefficients (Fe-Mg for Ol, Amp and Bt; Na-Ca for Plg [Grove, 1982]) between the crystallizing solids and the liquid. Small fractions of solid (0.05 weight fraction of the liquid remaining at any given step) were removed at each increment, with the result that F, the fraction of liquid remaining at step n, is equal to 0.95^n . The equilibrium constant ($K_D=[\text{Fe}_x] [\text{Mg}_l]/[\text{Fe}_l] [\text{Mg}_x]$) for Ol was set at 0.38,

and Plg K_D 's varied from 1.3 at the early steps to 3.0 at $\text{SiO}_2 > 64\%$ [Baker, 1988]. Amphibole and biotite K_D 's were set at 0.5 for all SiO_2 values (T. Sisson, unpub data). We chose sample 2-87-19, the sample with the lowest SiO_2 and highest MgO, FeO, and Al_2O_3 , as the assumed parental liquid. Although other, more primitive (and hypothetical) compositions could have been used, this procedure results in a model with many fewer free parameters. The proportion of phases removed at any step was chosen to give the best fit to the data. Results of the best fit model are shown on Figure 6.

The trend of the data is fit well by two sequential fractionation assemblages. For $54\% \leq \text{SiO}_2 \leq 60.5\%$,



and for $60.5 \leq \text{SiO}_2 \leq 71.5\%$



The primary misfit is in Al_2O_3 , which is consistently low for the entire model. This could be due to a low estimate for the initial Al_2O_3 composition of the parental liquid, but no attempt was made to "bump" the composition of the parental liquid to achieve a better fit. Other oxides are well-modeled until $\text{SiO}_2 = 72\%$, at which point a clear inflection in the Al_2O_3 , CaO and Na_2O trends indicate the disappearance of Mt, and the arrival of sanidine, on the liquidus.

At the end of the model described above, F had been reduced to 0.25. The success of the fractional crystallization model can be tested by examining the ratio of incompatible trace elements in the parental and residual liquids. For totally incompatible elements, this ratio should approach $1/F$. The ratios of Th, Nb, La, and Ba between the assumed parental liquid (2-87-19) and the remaining samples are shown in Figure 7, and illustrate the incompatibility of the data with a simple fractional crystallization model. While F and the concentration ratios are well-correlated, the ratios do not follow the expected $1/F$ relationship. Rather, the ratio of sample/assumed parental liquid defines a straight line with shallow slope, converging at the high- SiO_2 (low F) end of the array to 2 to 4 times parental concentrations.

This is the behavior expected from a system in which concentrations are controlled by simple mixing.

Two additional observations are consistent with petrogenesis of the Tail Canyon Volcanic Sequence by binary mixing. The fractional crystallization model predicts a total of approximately 40% (by weight) plagioclase fractionation in the interval $\text{SiO}_2=54$ to 71%. Such a large amount of plagioclase fractionation should produce a large, negative Eu anomaly in the liquid, a trend which is not observed (Figure 4.2 C, horizontally lined field). Additionally, the oxide plots in Figure 3 indicate that the scatter about a mixing line from the most mafic samples to the samples at $\text{SiO}_2=71$ wt % is about the same as for the fractionation model. This is clearly not a sufficient argument for mixing, but is necessary. Clearly the trend at $\text{SiO}_2>71\%$ can not be explained by mixing with the assumed parental liquid used above, due to the sharp inflection in Al_2O_3 , CaO and other oxides. We infer from the presence of sanidine phenocrysts in these liquids that this trend is controlled by fractionation of plagioclase and an alkali feldspar. Figure 4.2 C (vertically ruled field) shows the more substantial negative Eu anomaly for the samples with $\text{SiO}_2 > 71$ wt %, due to the fractionation of plagioclase. While the high silica end of the line of descent is at least partially controlled by fractionation, the arguments above indicate that binary mixing was the primary agent controlling the evolution of the Tail Canyon Volcanic Sequence. In the next section of the paper, we show that the mixing hypothesis is consistent with the trace element and isotopic data from both the Nova and Trail Canyon Volcanic Sequence flows, as well as with the regional data set.

Regional Mixing Model

The result above, that the major element evolution of the Trail Canyon Volcanic Sequence was controlled primarily by magma mixing, could be expected from previous studies of Basin and Range volcanic rocks. Bacon et al. [1984], Coleman and Walker [in press], and Gans et al. [1988] all report the importance of mixing in generating the syn-extensional rocks they studied within the Basin and Range Province. The ubiquity of the process in both time and space suggests that it could be examined on a regional scale. In this section we utilize isotopic results from this report and others

to semi-quantitatively assess the degree and relative contributions of crustal and mantle sources in the genesis of syn-extensional volcanic rocks within the Death Valley Extended Area. In a latter section, we demonstrate the coherence of the isotopic and trace element composition of the end-members, and then discuss the implication of these results for the physical and chemical structure of the sub-Basin and Range lithosphere.

Figure 8 shows the variation in Sr, Pb and Nd isotopic ratios for four data sets within the Death Valley Extended Area: the Death Valley-Pancake Range transect of Farmer et al. [1989], the Coso Range [Novack and Bacon, 1986], the Nova Basin [Walker and Coleman, submitted] and the Trail Canyon Volcanic Sequence [this report]. In each of the two-isotope variation diagrams, the data form a non-linear field with the Trail Canyon Volcanic Sequence aligned toward one end, and samples from the Coso Range and DVPR transect at the other. The samples from the Nova Basin tend to lie between the apices defined by the other data sets. The general trend of the regional isotopic data set is suggestive of three component mixing. We tested this hypothesis by modeling the trend of the isotopic data as due to the mixing of three chemically distinct reservoirs.

In the general case of isotopic ratio diagrams with different normalization isotopes, a mixture of components will follow a hyperbolic trajectory [Langmuir et al., 1978]. Although analytical solutions to the three component mixing problem can be derived, they are cumbersome and not particularly revealing. Instead we calculated the ratio of a mixture of three components using simple mass balance:

$$R_m = \frac{\sum_{i=1}^n R_i C_i X_i}{\sum_{i=1}^n C_i X_i} \quad (1)$$

where R_m is the isotopic ratio in the mixture, R_i is the same ratio in reservoir i , C_i is the concentration of the element in reservoir i , X_i is the weight fraction of reservoir i in the mixture, the subscript i refers to the reservoirs, and n is the number of reservoirs. Variables involved in the calculations below include six parameters for each of the three reservoirs:

the concentrations C and isotopic ratios R of each of the three elements (Sr, Nd and Pb in this study) being modeled. The isotopic compositions of the reservoirs were set equal to the extreme isotopic compositions of the data shown in Figure 8. As we show below, these isotopic ratios are compatible with those of sub-Basin and Range reservoirs suggested by previous studies [Menzies et al., 1983; Novack and Bacon, 1986; Walker and Coleman, submitted]. While better fits of the model to the data could be made by choosing different isotopic compositions, the technique we use is a more conservative approach. Concentrations of Sr, Nd, and Pb for the reservoirs were chosen based on typical concentrations for these elements in mantle and crustal reservoirs [Farmer et al., 1989; Ormerod et al., 1988], and then modified to give acceptable fits to the data. The resulting model parameters are given in Table 4.

The resulting mixing model is shown in Figure 9, with contours (at 0, 33, 66 and 100 wt % for each component) overlaid on the regional data set. For the 0 and 100% cases, the three component model is a simple binary model, and these curves demonstrate the inability of two component mixing to explain the data trends. The concavity of the mixing lines are sensitive to the ratio of concentrations and isotopic ratios in each reservoir: for this model, the greatest sensitivity in the position of a mixing line are in the A-B and A-C lines on the Pb-Sr plot. Other lines are reasonably stable with respect to small changes in concentration and isotope ratios. In the three 2-isotope variation diagrams, the model reproduces most, although not all, of the variation seen in the regional data set.

We interpret the reservoirs to represent three distinct chemical (and perhaps physical) reservoirs: the continental crust (reservoir A), an enriched mantle (reservoir B), and a depleted mantle (reservoir C). The crustal assignment is straightforward: the siliceous nature of the Trail Canyon Volcanic Sequence, and radiogenic Sr, Nd and Pb values all suggest crustal compositions. The Pb data for the dacitic and rhyolitic Trail Canyon Volcanic Sequence, as well as the Coso Range data, plot within the Pb field of Great Basin miogeoclinal sediments as defined by Zartman [1974] (Figure 10, his Area II Pb measurements), suggesting that a large component of the Pb was scavenged from sources within the upper crust.

The component with $^{87}\text{Sr}/^{86}\text{Sr}=0.703$, $\epsilon\text{Nd}=+10$, and $^{208}\text{Pb}/^{204}\text{Pb}=38.7$ (reservoir C) is identified with a mantle source similar in composition to the source for MORBs. Following Menzies et al., [1983], Farmer et al. [1989] and Ormerod et al. [1988], we label this source as "depleted mantle" (DM). Finally, the reservoir with $^{87}\text{Sr}/^{86}\text{Sr}=0.707$, $\epsilon\text{Nd}=-10$, and $^{208}\text{Pb}/^{204}\text{Pb}=38.3$ is correlated with "enriched mantle", or EM [Farmer et al. , 1989; Ormerod et al., 1988].

The model presented above is successful in a) reproducing the projected 2-element isotope variations of the data and (b) doing so with reservoirs which are chemically plausible and recognizable from previous work. Given this success, we used the model to predict the relative contribution of each reservoir in a sample to its isotopic composition. Each sample in the Death Valley Extended Area for which Sr, Nd and Pb data were available (a subset of the data shown in Figure 8, see Table 5) was fit to the isotope mixing model determined above, by calculating the mixture of components which best approximated the isotopic composition of the sample. This provided a unique (for each sample) weight fraction of each component in the sample. Because we do not have an analytical form of the mixing surface, the samples were fit using a simplex procedure [Press, 1986; pg. 289], with a least squares loss function of the form

$$\text{Loss} = \sum \left[\left(\frac{{}^{87}\text{Sr}/{}^{86}\text{Sr}_d - {}^{87}\text{Sr}/{}^{86}\text{Sr}_m}{s_{\text{Sr}}} \right)^2 + \left(\frac{\epsilon\text{Nd}_d - \epsilon\text{Nd}_m}{s_{\text{Nd}}} \right)^2 + \left(\frac{{}^{208}\text{Pb}/{}^{204}\text{Pb}_d - {}^{208}\text{Pb}/{}^{204}\text{Pb}_m}{s_{\text{Pb}}} \right)^2 \right] \quad (2).$$

Where the d subscript refer to a datum from the regional data set, the m subscript refers to the model, and the σ to the normalization errors for each isotope. These were set equal to 2.5% of the total range of the data, or 0.0003 for Sr, 0.5 ϵ units for Nd, and 0.05 for Pb. For Pb and Nd, theses weights are approximately equal to the measurement uncertainty for the isotope ratio; for Sr the s utilized is approximately an order of magnitude greater than the typical measurement uncertainty. These weights were chosen because they represent equal portions of the data range, but decreasing the Sr uncertainty to 0.00008 (about two times the typical uncertainty) does not

materially affect our results. The sensitivity of the derived component weights to small changes in composition is linear, and can be gauged by comparing the derived weights for samples with similar isotopic compositions. The fit is fairly robust because the loss function is generally steep, allowing good determination of fit.

The results of the model, including the χ^2 residuals of the fits, is given in Table 5. A point can be considered to fit "acceptably" if the χ^2 residuals is less than about 2. Overall, the samples fit the model reasonably well, as would be expected from the projected models shown above. A few samples clearly fit very poorly: two from the Coso Range, and two from the Nova Basin, all with residuals of greater than 45. Sample PP-8 from the Nova Basin is a pyroxene-phyric air-fall tuff, and appears to be unusual both isotopically and chemically (see below). The other Nova Basin outlier has no unique characteristics to suggest its high residual. Samples PP-41, -48, and -49, with residuals on the order of 5-10, contain small amounts of alteration products (calcite or iddingsite) and may have suffered some post-emplacement alteration.

Coherence of trace element and isotopic compositions

The coherence between the isotopic and trace element compositions of the two mantle reservoirs can be obscured both by crustal contamination and by fractionation (via crystallization) of the mantle-derived liquid during ascent, processes which would tend to modify the original trace element composition of the melt. In this section we compare the REE and ITE variations of the regional data set, and identify correlations between the isotopic and trace element contents of the reservoirs. We use the results of the previous section to identify those samples with particularly high components of each of the reservoirs, and infer the effect of crustal contamination on the REE and ITE signals of the syn-extensional volcanic rocks.

Lum et al. [1989] and Ormerod et al. [1988] have discussed the trace element nature of the EM and DM, pointing out the High Field Strength Element (HFSE)/Large Ion Lithophile (LIL) fractionation between these reservoirs. Ormerod et al. [1988] utilized the Zr/Ba of their samples to

differentiate these EM and DM components, and we do the same for the Nova Basin and Trail Canyon Volcanic Sequence sequence in Figure 13 B, plotted versus $^{87}\text{Sr}/^{86}\text{Sr}$. The data from the Panamint Range fields form a triangular shaped area, reaching high Zr/Ba at low $^{87}\text{Sr}/^{86}\text{Sr}$, and low Zr/Ba (<0.2) over a range of $^{87}\text{Sr}/^{86}\text{Sr}$ of 0.706 to 0.710. Ormerod et al interpreted samples with Zr/Ba <0.20 to represent melts derived from an "EM" component, while samples with Zr/Ba >0.20 represented melts derived from "DM" sources. The effect of high level fractionation and crustal contamination can be assessed by the trend of the siliceous Trail Canyon Volcanic Sequence-samples toward high $^{87}\text{Sr}/^{86}\text{Sr}$ and low Zr/Ba, reflecting perhaps the removal of HFSE by magnetite fractionation.

Comparing the relative reservoir contributions to the samples in Table 5 to the trace element profiles shown in Figure 4.2 suggested other criteria that could be used to distinguish the chemical profiles of the EM, DM and crustal reservoirs. Figure 11 shows the ITE plots for samples from Table 5 which have high percentages of each component. The diagram indicates that two criteria can be used to distinguish the "end-members": LREE fractionation (eg, Sm/Nd) easily distinguishes the DM from EM, while a strong Rb/Sm fractionation separates the crustal reservoir from both EM and DM. In Figure 12a, we plot these provenance indicators for the samples from Table 5 for which analyses are available. This diagram was contoured by weights of the DM, EM and crustal reservoirs calculated through the isotopic mixing model, by transferring the results tabulated in Table 5 on to the figure, and then separating points which had >40 and $>60\%$ of the EM and DM components. The results are very consistent, with the plot clearly separating the three reservoirs. One sample does not follow the trend defined by the others (shown as a circle on Figure 12 A, from the DVPR set of Farmer et al. [1989]), and was omitted from the set defining the contours. The reasons for the misfit are not known, but indicate the need for more data to test the correctness of this procedure.

We use this calibration set to examine the much larger set of Death Valley Extended Area samples for which trace elements, but not isotopic data, are available in Figure 12 B. In this figure, trace element data for all samples from the regional data set are superimposed on the contours

defined in Figure 12 A. They demonstrate, as suggested by other techniques, that the variation of Sm/Nd at low Rb/Sm is apparently not due to contamination by continental crust, but reflects real source (intra-mantle) variations. This is indicated by the wide variation in Sm/Nd for samples with low degrees of Rb/Sm enrichment. While the effect of crustal contamination can be quite strong, the Rb/Sm index accounts for this component directly, demonstrating the source heterogeneity. The Rb/Sm ratio distinguishes the components well, as can be seen by comparing the Zr/Ba vs. Rb/Sm plot in Figure 13 A to the Zr/Ba vs. $^{87}\text{Sr}/^{86}\text{Sr}$ in Figure 13 B. Again the EM-DM division of Ormerod et al. [1988] is shown for reference. One additional benefit of the plot shown in Figure 12 is that all the necessary concentration ratios for determining the samples provenance can be determined from isotope dilution methods, a relatively standard procedure when measuring isotopic compositions for a sample.

Implications for the temporal variation in volcanic sources

The isotopic mixing model, the Rb/Sm vs Sm/Nd plot, and the Zr/Ba vs $^{87}\text{Sr}/^{86}\text{Sr}$ plot all indicate that the Trail Canyon Volcanic Sequence has a strong component of DM. We interpret this trend to indicate the presence of a DM component in the Trail Canyon Volcanic Sequence samples. Because the Trail Canyon Volcanic Sequence is a syn-early extension sequence [McKenna, Chapter 2], it appears that the earliest large episode of volcanism in the Death Valley Extended Area was sourced by mantle with a strong DM composition. In contrast, all these indicators of provenance suggests that the Nova Basin samples, as noted by Walker and Coleman [1987, 1989], contain significant contributions from both the EM and DM components, as well as continental crust. We discuss the implications of these observations in the following sections.

The existence of chemically identifiable mantle reservoirs beneath the Basin and Range Province is by now well established. The physical disposition of these reservoirs is not agreed upon, and remains controversial. Menzies [1989] described two enriched mantle reservoirs beneath the Western United States, and correlated the EM described in this paper to Archean age mantle lithosphere (his EM1), and the DM component with a "sub-Proterozoic [age crust] lithospheric wedge" (his

DMM). Farmer et al. [1989] also identified an EM and DM component in their study of the DVPR samples. They too correlated the EM component with lithospheric mantle, but considered it to be Proterozoic age lithosphere preserved beneath the area of their transect. Finally, Ormerod et al. [1988] delineated both lithosphere and asthenosphere-resident sources in their study, and argued that the distinctive asthenospheric melts (equivalent in composition to our DM component) reached the surface only after 2-3 Ma. One key to determining the physical disposition of these chemical reservoirs is understanding the time history of their presence in syn-extensional volcanic rocks, and the length of time since formation of the reservoir.

Within the volcanic fields of the Panamint Mountains, evidence from Figures 8, 9, 10, 12b, and 13 all argue for the presence of the DM component, and the relative absence of the EM component, in the Trail Canyon Volcanic Sequence flows. A DM component is present in the older southern DVPR samples studied by Farmer et al. [1989]; in addition they noted that an EM signature appeared in their younger (<3 Ma) southern Death Valley samples. This trend is similar to that seen in the flows from the Panamint Mountains. The Nova Basin flows (4-6 Ma) clearly indicate the strong presence of an EM component, as well as DM, in their formation. This sequence of DM followed by EM is opposite to that seen by Ormerod et al. [1988], even though the area they sampled included, judging from their Figure 1, flows from the Nova Basin. It is only through the use of a longer time base (that is, the Late Miocene-age Trail Canyon Volcanic Sequence and older DVPR samples) that this DM-EM progression is resolved.

Two hypotheses can explain the observation that, within the Death Valley Extended Area, DM signatures dominate the early volcanism, and are joined by an EM component sometime between 6 and 3 Ma depending upon location. In the first, the onset of EM is due to the tapping by melts of a source with long-term enrichment. In the second, the appearance of an EM signal is due to tapping of newly enriched reservoir. In the latter case, this enrichment would have been of regional scale, accomplished perhaps by the movement of metasomatic fluids through the mantle at some time after 10 Ma. The metasomatism model however does not account for the

coherence between the isotopic and trace element contents discussed above. This correlation suggests to us that no recent enrichment has taken place, in that enrichments that are only a few millions of years old would simply not have sufficient time to produce the isotopic differences shown in Figure 8.

Therefore we assume that the presence of EM within the Nova Basin samples reflects the tapping of a long-lived, enriched mantle source following significant and regional melting of a DM source. The DM component was most likely exposed under the Panamint Mountain area by the long-term history of abundant, large-scale intrusions into the lithosphere under the Death Valley Extended Area. It is important to remember at this juncture that, at 10.0 Ma, the Basin and Range Province in the Death Valley Area was significantly narrower than it is today, and was probably on the order of 200 km wide. At 10.0 Ma, post-Jurassic plutons which had been emplaced into the middle to upper crust form a significant fraction (perhaps 10%) of the currently exposed outcrop of the Death Valley Extended Area. It appears likely that the lithosphere of the Death Valley Extended Area had been regionally heated and locally eroded prior to the initiation of significant extension at 14.5 to 12.5 Ma.

Despite the pervasive plutonism within the sub-Death Valley Extended Area lithosphere, the EM reservoir was clearly not destroyed during the process, nor was it mixed homogeneously within the thermally perturbed mantle. As noted by Perry et al. [1987], it is difficult to call on a simple "marble-cake" mantle model to explain these observations, because one would expect the more fertile EM layers in the cake to melt before the already depleted DM layers. More likely, one must invoke a process which increased the availability of EM component to the source area with time under the eastern Death Valley Extended Area area, but provided a source of DM melts early in the extension. A successful model should also explain the observations of Ormerod et al. [1988], that the DM component reappears in the western Great Basin after 5 Ma. We show in Figure 14 a model which integrates these observations.

In Figure 14 A we show the disposition of crust, EM and DM reservoirs at an early stage of extension. The mantle lithosphere is shown as

consisting "primarily" of EM component, and the asthenosphere as "primarily" DM component, in recognition of the probable "marble-cake" structure of the reservoirs. The position of the Colorado Plateau and the Sierra Nevada arc are inferred from Wernicke et al. [1988] and Levy and Christie-Blick [1989], whereas the lithospheric keel below the Colorado Plateau is taken from Menzies [1989]. At 9-11 Ma, extension in the eastern edge of the nascent Basin and Range Province had extended the area east of both the Trail Canyon Volcanic Sequence and the DVPR samples. The lithosphere below the area that would become the Death Valley Extended Area had, by 9 Ma, suffered multiple large scale intrusions, some of which appear to have been derived from a DM source). However, east of the Death Valley Extended Area, in the "amagmatic corridor" of Eaton [1982], the lack of any significant intrusions prevented the rise of the DM component into the lithosphere, resulting in either the absence of volcanism or the lack of a DM signal.

Over the period 4-9 Ma, extension within the Death Valley Extended Area migrated both westward and eastward from its locus at 11-9 Ma [Wernicke et al., 1988]. As lithosphere-scale simple shear continued, the mantle lithosphere was thinned below the location of the Death Valley Extended Area, allowing asthenospheric melts to rise, and perhaps thermally eroding the EM layer [Perry et al., 1988]. The extension brought the Death Valley Extended Area off the area of large scale DM intrusions, and exposed to an EM reservoir heated by upwelling, perhaps partially melted, DM, producing the EM enriched Nova Basin and younger DVPR of Farmer [1989]. Finally, Figure 14 C shows the latest development of the system, as continued extension brought the asthenosphere into contact with a thermally (and perhaps mechanically eroded) mantle lithosphere. This upwelling contributed to a late pulse of DM derived melts, and explains the transition from EM to DM dominated basalts observed by Ormerod et al. [1988]. This model could be tested directly by determining the isotopic composition (and hence source provenance) of the earliest volcanic rocks from within the Death Valley Extended Area, such as those exposed in the Kingston and McCulloch Ranges of California and Nevada.

CONCLUSIONS

This paper reports the major, trace and isotopic compositions of the 10.3 to 10.0 Ma Trail Canyon Volcanic Sequence, presently exposed in the Panamint Mountains of eastern California. The flows consist of basaltic andesite through rhyolite, and are calc-alkaline to tholeiitic in character. The major, trace and isotopic data clearly indicate that this series formed through mixing of a silicic endmember (of crustal composition) and a more mafic, mantle-derived parental liquid.

The isotopic compositions (Sr, Nd, and Pb) of Miocene-Recent volcanic rocks from the Death Valley Extended Area can be explained by mixing of three distinct components: a crustal source with $^{87}\text{Sr}/^{86}\text{Sr}=0.715$, $\epsilon\text{Nd}=-15$, and $^{208}\text{Pb}/^{204}\text{Pb}=40$; a depleted mantle source with $^{87}\text{Sr}/^{86}\text{Sr}=0.703$, $\epsilon\text{Nd}=+10$, and $^{208}\text{Pb}/^{204}\text{Pb}=38.7$; and an enriched mantle source with $^{87}\text{Sr}/^{86}\text{Sr}=0.707$, $\epsilon\text{Nd}=-10$, and $^{208}\text{Pb}/^{204}\text{Pb}=38.3$. The contribution of these components to different flows within a single field can vary enormously, indicating the need to consider many samples from a field before labeling a field as "enriched" or depleted. Rare earth and incompatible trace element contents of the reservoirs are distinct, and well correlated with the isotopic depletions and enrichments of the reservoirs, indicating that the chemical enrichments are not due to fluxing from recent metasomatic or partial melt liquids.

Consideration of the regional isotopic and trace element contents of volcanic rocks from the Death Valley Extended Area suggests that extension here has been accommodated via simple shear. The trends in the sources of the volcanic rocks are compatible with upwelling of asthenospheric melts of depleted composition dominating the early extensional magmatism. This plume of depleted mantle is in effect left behind by extension in the overlying lithosphere, exposing unaltered enriched mantle underneath the extending crust, and allowing enriched melts to reach the surface. Continued extension and thermal erosion have removed the enriched mantle lithosphere from below the area of currently active extension, exposing the westernmost areas of the Death Valley Extended Area to asthenosphere-derived melts. Further refinement and

testing of these models depends upon the identification and analysis of pre-extensional and very early syn-extensional volcanic rocks.

REFERENCES

- Asmerom, Y., Snow, J.K., Holm, D.K., Jacobsen, S.B., Wernicke, B.P. and Lux, D.R., Rapid uplift and crustal growth in extensional environments: An isotopic study from the Death Valley Region, California, *Geology*, 18, 223-226, 1990.
- Bacon, C.R., Kurasawa, H., Delevaux, M.H., Kistler, R.W. and Doe, B.R., Lead and strontium isotopic evidence for crustal interaction and compositional zonation in the source regions of Pleistocene basaltic and rhyolitic magmas of the Coso volcanic field, California, *Contrib. Mineral. Petrol.*, 85, 366-375, 1984.
- Baker, M.B., Evolution of lavas at Mt. Shasta volcano, N. California: An experimental and petrologic study,
- Bird, P., Formation of the Rocky Mountains: a continuum computer model, *Science*, 239, 1988.
- Block, M.A. and Royden, L.H., Core complex geometry and large-scale flow of the lower crust, *Tectonics*, in press.
- Bohannon, R.G., *Nonmarine sedimentary rocks of Tertiary Age in the Lake Meade region, southeastern Nevada and northwestern Arizona*, pp. 72, 1984.
- Burchfiel, B.C. and Davis, G.A., Nature and controls of Cordilleran orogenesis, extensions of an earlier synthesis, *Am. J. Sci.*, 275-A, 363-396, 1975.
- Burchfiel, B.C., Hodges, K.V. and Walker, J.D., Geology of the Kingston Range Detachment, in preparation.
- Busby-Spera, C.J., Speculative tectonic model for the early Mesozoic arc of the southwest Cordilleran United States, *Geology*, 16, 1121-1125, 1988.

- Carlson, R.W., Lugmair, G.W. and Macdougall, J.D., Columbia River volcanism: The question of mantle heterogeneity or crustal contamination, *Geochim. Cosmochim. Acta*, **45**, 2483-2499, 1981.
- Cemen, I., Drake, R. and Wright, L.A., Cenozoic sedimentation and sequence of deformational events at the southeastern end of the Furnace Creek strike-slip fault zone, Death Valley region, California, in, *Strike-slip Deformation, Basin Formation, and Sedimentation*, Biddle, K. T., and Christie-Blick, N., eds., *Soc. Econ. Paleon. Min. Spec. Pub.*, **37**, 127-141, 1985.
- Coleman, D.S. and Walker, J.D., Geochemistry of Mio-Pliocene volcanic rocks from around Panamint Valley, Death Valley area, California, in *Basin and Range Extension Tectonics at the Latitude of Las Vegas*, edited by Wernicke, B.P., pp. Geological Society of America, Boulder, Colorado, in press.
- Dokka, R.K. and Travis, C.J., Late Cenozoic strike-slip faulting in the Mojave Desert, California, *Tectonics*, **9**, 311-340, 1990.
- Eaton, G.P., The Basin and Range Province: origin and tectonic significance, *Ann. Rev. E. Planet. Sci.*, **10**, 409-440, 1982.
- Farmer, G.L. and De Paolo, D.J., Origin of Mesozoic and Tertiary granite in the western United States and implications for pre-Mesozoic crustal structure, 1, Nd and Sr isotopic studies in the geocline of the northern Great Basin, *J. Geophys. Res.*, **88**, 3379-3401, 1983.
- Farmer, G.L., Perry, F.V., Semken, S., Crowe, B., Curtis, D. and De Paolo, D.J., Isotopic evidence on the structure and origin of subcontinental lithospheric mantle in southern Nevada, *J. Geophys. Res.*, **94**, 7885-7898, 1989.
- Gans, P.B., An open system, two-layer crustal stretching model for the eastern Great Basin, *Tectonics*, **6**, 1-12, 1987.

- Gans, P.B., Mahood, G.A. and Schermer, E., *Synextensional magmatism in the Basin and Range Province: a case study from the eastern Great Basin*, pp. 53, Geological Society of America, Boulder, Colorado, 1988.
- Gill, J.B., *Orogenic Andesites and Plate Tectonics*,. Spring Verlag, New York, 1981.
- Grove, T.L. and Donnelly-Nolan, J.M., The evolution of young silicic lavas at Medicine Lake Volcano, California: Implications for the origin of compositional gaps in calc-alkaline series lavas, *Contrib. Mineral. Petrol.*, 92, 281-302, 1986.
- Grove, T.L., Gerlach, D.C. and Sando, T.W., Origin of calc-alkaline series lavas at Medicine Lake volcano by fractionation, assimilation, and mixing, *Contrib. Mineral. Petrol.*, 80, 160-182, 1982.
- Hart, S.R. and Brooks, The geochemistry and evolution of early Precambrian mantle, *Contrib. Mineral. Petrol.*, 61, 109-128, 1977.
- Hedge, C.E. and Noble, D.C., Upper Cenozoic basalts with high Sr87/Sr86 and Sr/Rb ratios, southern Great Basin, western United States, *Geol. Soc. Amer. Bull.*, 82, 3503-3510, 1971.
- Hodges, K.V., McKenna, L.W., Stock, J.M., Knapp, J.K., Page, L., Silverberg, D.S. and Walker, J.D., Evolution of extensional basins and Basin and Range topography west of Death Valley, SE California, *Tectonics*, 8, 453-467, 1988.
- Hopper, R.H., Geologic section from the Sierra Nevada to Death Valley, California, *Geol. Soc. Amer. Bull.*, 58, 393-423, 1947.
- Howard, K.A. and John, B.E., Crustal extension along a rooted system of imbricate low angle faults: Colorado River extensional corridor, California and Arizona, in *Continental Extension Tectonics*, pp. 299-311, Geological Society of London, London, 1987.
- Ila, P. and Frey, F., Utilization of neutron activation analysis in the study of geologic materials, *44th supplement*, 710-716, 1984.

- Kuno, H., Petrology of Hakone volcano and the adjacent areas, Japan, *Geol. Soc. Amer. Bull.*, 61, 957-1019, 1950.
- Langmuir, C.H., Vocke, R.B., Hanson, G. and Hart, S.R., A general mixing equation with applications to Icelandic basalts, *Earth Planet. Sci. Lett.*, 37, 380-392, 1978.
- Leeman, W.P., The isotopic composition of strontium in late-Cenozoic basalts from the Basin-Range province, western United States, *Geochim. Cosmochim. Acta*, 34, 857-872, 1970.
- Leeman, W.P., Tectonic and magmatic significance of strontium isotopic variations in Cenozoic volcanic rocks from the western United States, *Geol. Soc. Amer. Bull.*, 93, 857-872, 1982.
- Lindstrom, D.J. and R.L. Korotev, TEABAGS: computer programs for instrumental neutron activation analysis, *J. Radioanal. Chem.*, 70, 439-458, 1982.
- Lum, C.C., Leeman, W.P., Foland, K.A., Kargel, J.A. and Fitton, J.G., Isotopic variations in continental basaltic lavas as indicators of mantle heterogeneity: examples from the western U. S. cordillera, *J. Geophys. Res.*, 94, 7871-7884, 1989.
- McKenna, L.W., and Hodges, K. V., Constraints on the Kinematics and Timing of Late Miocene-Recent Extension Between the Panamint and Black Mountains, Southeastern California, in press, *Extension at the Latitude of Las Vegas*, edited by Wernicke, B. P., Geological Society of America Memoir.
- McKenna, L.W., Snee, L. and Hodges, K.V., Time-Temperature History of Extension in the Panamint and Black Mountains, Death Valley, California.
- Menzies, M.A., Cratonic, circumcratonic and oceanic mantle domains beneath the Western United States, *J. Geophys. Res.*, 94, 7899-7915, 1989.

- Menzies, M.A., Leeman, W.P. and Hawkesworth, C.J., Isotope geochemistry of Cenozoic volcanic rocks reveals mantle heterogeneity below western United States, *Nature*, 303, 205-209, 1983.
- Miyashiro, A., Volcanic rock series in island arcs and active continental margins, *Am. Jour. Sci.*, 274, 321-355, 1974.
- Novack, S.W. and Bacon, C.R., *Pliocene Volcanic Rocks of the Coso Range, Inyo County, California*, pp. U. S. Government Printing Office, Washington, D. C., 1986.
- Ormerod, D.S., Hawkesworth, C.J., Rogers, N.W., Leeman, W.P. and Menzies, M.A., Tectonic and magmatic transitions in the Western Great Basin, USA, *Nature*, 333, 349-353, 1988.
- Pegram, W.J., Geochemical processes in the sub-continental mantle and the nature of crust-mantle interaction: Evidence from the Mesozoic Appalachian Tholeiite Province, Ph. D Thesis, MIT, Cambridge, Massachusetts.
- Perry, F.V., Baldrige, W.S. and De Paolo, D.J., Role of asthenosphere and lithosphere in the genesis of Late Cenozoic basaltic rocks from the Rio Grande Rift and adjacent regions of the Southwestern United States, *J. Geophys. Res.*, 92, 9193-9213, 1987.
- Press, W.H., Flannery, B.P., Teukolsky, S.A. and Vetterling, W.T., *Numerical Recipes*, pp. 818, Cambridge University Press, New York, 1986.
- Serpa, L., de Voogd, B., Wright, L., Wilemin, J., Oliver, J., Hauser, E. and Troxel, B., Structure of the central Death Valley pull-apart basin from COCORP profiles in the southern Great Basin, *Geol. Soc. Amer. Bull.*, 100, 1437-1450, 1988.
- Sonder, L.J., England, P.C., Wernicke, B.P. and Christiansen, R.L., A physical model for Cenozoic extension of western North America., in *Continental Extensional Tectonics*, edited by Coward, M.P., Dewey, J.F.

- and Hancock, P.L., pp. 187-201, Geological Society of London, Oxford, 1987.
- Stock, J.M. and Molnar, P., Uncertainties and implications of the Late Cretaceous and Tertiary position of North America relative to the Farallon, Kula and Pacific plates, *Tectonics*, 7, 1339-1384, 1988.
- Taylor, S.R. and McClelland, S.M., *The Continental Crust: its Composition and Evolution*, pp. 312, Blackwell Scientific Publications, Oxford, 1985.
- de Voogd, B.L., Serpa, L. and Brown, L., Crustal extension and magmatic processes: COCORP profiles from Death Valley and Rio Grande rift, *Geol. Soc. Amer. Bull.*, 100, 1550-1567, 1988.
- Walker, J.D., Permian and Triassic rocks of the Mojave Desert and their implications for timing and mechanisms of continental truncation, *Tectonics*, 7, 685-709, 1988.
- Walker, J.D. and Coleman, D.S., Crustal-scale kinematics of extensional deformation in the Death Valley extended area revealed by geochemistry of volcanic rocks, *Geology*, submitted.
- Watson, E.B., Basalt contamination by continental crust, *Contrib. Mineral. Petrol.*, 80, 73-87, 1982.
- Wernicke, B., Axen, G.J. and Snow, J.K., Basin and Range extensional tectonics at the latitude of Las Vegas, Nevada, *Geol. Soc. Amer. Bull.*, 100, 1738-1757, 1988.
- Wright, L.A., Drake, R.E. and Troxel, B.W., Evidence for the westward migration of severe Cenozoic extension, southeastern Great Basin, California, *Geol. Soc. Amer. Abs. with Prog.*, 16, 701, 1984.
- Wright, L.A., Kraemer, J.H., Thornton, C.P. and Troxel, B.W., Type sections of two newly-named volcanic units of the central Death Valley volcanic field, eastern California, in *Geology of the northern one-half Confidence Hills 15' Quadrangle, Inyo County, California*, pp. California Division of Mines and Geology, 1984.

Zartman, R.E., Lead isotope provinces in the Cordillera of the western United States and their geological significance, *Econ. Geol.*, 69, 792-805, 1974.

Zindler, A., Hart, S.R., Frey, F.A. and Jakobsson, S.P., Nd and Sr isotope ratios and rare earth element abundances in Rekjanes Peninsula basalts: evidence for mantle heterogeneity beneath Iceland, *Earth Planet. Sci. Lett.*, 45, 1979.

FIGURE CAPTIONS

Figure 1. Location map and regional tectonic setting. The Trail Canyon Volcanic Sequence and Nova Basin volcanics are shown by the dark stipple labeled TC and NB respectively. Other volcanic rocks discussed in this report are indicated: filled squares, Coso Range [Bacon et al, 1984]; unfilled diamonds, Death Valley-Pancake Range Transect [Farmer et al, 1989]; x's, samples from Ormerod et al [1988]. Heavy black lines are faults with normal offset if unadorned, strike slip if arrowed. Basins are unpatterned, ranges are stippled.

Figure 2. FeO^*/MgO vs SiO_2 for rocks of the Trail Canyon Volcanic Sequence. $\text{FeO}^* = 0.85\text{Fe}_2\text{O}_3$, and all data are normalized to 100% volatile free before plotting. Boundary between tholeiitic (TH) and calc-alkaline (CA) trends from Miyashiro [1974]. The Trail Canyon Volcanic Sequence samples are transitional between calc-alkaline and tholeiitic. AFM projections (not shown) would classify the series as more strongly calc-alkaline.

Figure 3. Major element variation of the Trail Canyon Volcanic Sequence samples. A. FeO^* and MgO versus SiO_2 , B. CaO and Na_2O , C. K_2O , and D. Al_2O_3 . Note the uniformly decreasing transition metal, soda, and alumina contents with increasing silica, and the inflection in most oxide trends at $\text{SiO}_2 = 72\%$

Figure 4. Trace element variation diagrams. A, B, and C; Sr and Rb, Ba, and Co and Sc versus SiO_2 . D. REE and ITE plots for the Trail Canyon Volcanic Sequence and Nova Basin samples.

Figure 5. Isotopic data. A. $^{87}\text{Sr}/^{86}\text{Sr}$ versus $^{87}\text{Rb}/^{86}\text{Sr}$. Note the expanded scale of the lower diagram. B. $^{207}\text{Pb}/^{204}\text{Pb}$ versus $^{206}\text{Pb}/^{204}\text{Pb}$ and $^{208}\text{Pb}/^{204}\text{Pb}$ versus $^{206}\text{Pb}/^{204}\text{Pb}$.

Figure 6. Results of fractional crystallization models for the genesis of the Trail Canyon Volcanic Sequence. Model results (solid line) are calculated from the fractionation assemblage given in the text. The inflection in the model results indicates the disappearance of olivine, and the appearance of biotite, on the liquidus.

Figure 7. Incompatible trace element concentrations of the Trail Canyon Volcanic Sequence versus the degree of liquid remaining in the fractional crystallization model. A value of F was assigned to each sample by comparing the silica content of the sample to that of the model. Totally incompatible elements should be partitioned completely into the remaining liquid during fractionation, and would follow the line marked "1/F expected". The majority of the samples follow linear trends suggesting that simple mixing, rather than fractional crystallization, was the primary agent responsible for the formation of the Trail Canyon Volcanic Sequence.

Figure 8. Regional trends in the isotopic compositions of syn-extensional volcanic rocks. Key for this and subsequent Figures: empty circles, Trail Canyon Volcanic Sequence [this report], filled circles, Nova Basin [Walker and Coleman, submitted]; diamonds, Death Valley-Pancake Range samples of Farmer et al [1989]. A. Epsilon Nd versus $^{208}\text{Pb}/^{204}\text{Pb}$, B. $^{208}\text{Pb}/^{204}\text{Pb}$ versus $^{87}\text{Sr}/^{86}\text{Sr}$, and C. eNd versus $^{87}\text{Sr}/^{86}\text{Sr}$. The fields are interpreted to represent the effects of three component mixing in the generation of the volcanic rocks. See Figure 9 for this interpretation.

Figure 9. Regional trends in the isotopic compositions of syn-extensional volcanic rocks overlain by contours showing the weight fraction of inferred crustal, enriched mantle (EM) and depleted mantle (DM) components involved in the genesis of the samples. The solid lines represent expected isotopic composition of binary mixes between the reservoirs. Each solid line (which represents 0% of the component on

the opposite vertex) is paralleled by two dashed lines. Upon addition of a third component, the mixing hyperbolae moves toward the vertex representing the newly added component. Two such hyperbolae are shown, for 33% of the third component (the dashed line farther from the vertex) and 66% of the third component (the dashed line closer to the vertex). The mixing model explains most, though not all, of the isotopic measurements from post-Oligocene volcanic rocks in the Death Valley Extended Area.

Figure 10. Regional trends in Pb isotope compositions, along with the field for the Pb composition of the "Great Basin Miogeoclinal Sediments" as defined by Zartman [1974]. Trail Canyon Volcanic Sequence samples are shown by empty circles, the fields for the other regional data sets are also shown. Both the Trail Canyon Volcanic Sequence and the Coso volcanic rocks shown Pb signature that plot within the field of the miogeoclinal sediments. The range of the Trail Canyon Volcanic Sequence is very large, reaching from the center of the GBMS field to the Nova Basin field. The 4.55 Ga geochron is shown for reference. Adapted from Farmer et al [1989].

Figure 11. Incompatible trace element plot of samples from the regional data set which, based upon their isotopic compositions, are derived primarily from one of the three components. Normalizing concentrations are given in Table 2, except for K and Ti, which are 100 and 436 ppm respectively. See Table 3 notes for references. The samples rich in DM and EM components are distinguished from each other by their relative LREE (eg, Sm/Nd) fractionation, while these mantle reservoirs are distinguished from crustal samples by the large Sr depletions and Rb enrichments in the latter.

Figure 12 A. Trace element fractionations (Rb/Sm versus Sm/Nd) of samples within the regional data set which have Sr, Pb and Nd isotopic analyses. These samples were fitted to the mixing model shown in Figure 9 to determine the relative contributions of each reservoir to a given samples. The lines (dotted, dashed, and solid) superimposed on the diagram represent contours of each component as determined from the results of the fitting procedure. Solid lines show 40 and 60% of the

Dm component, large dashed line shows 40 and 60% of the EM component, and the short dashed line shows 35% crustal component. B. Contours from A superimposed on the trace element data for the regional data set. More samples are plotted because more trace element data than isotopic data are available. Samples from the Trail Canyon Volcanic Sequence show roughly equal contributions of EM and DM components in their genesis

Figure 13. Comparison of the Zr/Ba ratios of the Trail Canyon Volcanic Sequence and Nova Basin samples with Rb/Sm and $^{87}\text{Sr}/^{86}\text{Sr}$. Ormerod et al [1989] discriminated between EM and DM derived magmas based on Zr/Ba, with samples having $\text{Zr/Ba} > 0.2$ representing DM-derived magmas. A. The Zr/Ba ratio versus Rb/Sm. The Trail Canyon Volcanic Sequence represents mixtures of crustal (plotting to the right of the diagram) and DM components, although none of the samples have Zr/Ba as high as the range of samples from the Geronimo field [Kempton et al, 1987] (representing "pure" DM component, Menzies [1989]). B. Zr/Ba versus $^{87}\text{Sr}/^{86}\text{Sr}$ shows very good agreement with the trends in 13A, demonstrating both the coherence of the trace element enrichments and the isotopic composition of the reservoirs, and the utility of the Rb/Sm index. The fields show the trend of data from Ormerod et al [1987]: ruled represents lithospheric values (accreted at low $^{87}\text{Sr}/^{86}\text{Sr}$ and continental at high $^{87}\text{Sr}/^{86}\text{Sr}$), while open field shows the limits of samples with $\text{Zr/Ba} > 0.20$. Note the five fold range of Zr/Ba within the Nova Basin samples, from 0.1 to 0.5.

Figure 14. A series of sketches representing the tectonic and magmatic evolution of the Basin and Range Province from 11 Ma to the present. See text for discussion.

Table 1: Major Element Concentrations

| | 1-87-12 | 2-87-15 | 2-87-16 | 2-87-19 | 2-87-21 | 3-87-5 | 3-87-6 | 3-87-11 | 3-87-12 |
|--------------------------------|---------|---------|---------|---------|---------|---------|---------|---------|---------|
| SiO ₂ | 66.4 | 74.6 | 73.1 | 53.8 | 65.7 | 67.4 | 74 | 67.3 | 75.3 |
| TiO ₂ | 0.55 | 0.32 | 0.28 | 1.46 | 0.76 | 0.55 | 0.14 | 0.6 | 0.13 |
| Al ₂ O ₃ | 16.1 | 13.4 | 14.1 | 17.5 | 17.0 | 15.6 | 12.7 | 15.4 | 12.5 |
| Fe ₂ O ₃ | 3.4 | 1.8 | 1.6 | 9.2 | 4.4 | 3.3 | 0.9 | 3.4 | 0.9 |
| MgO | 1.1 | 0.4 | 0.3 | 5.3 | 1.2 | 0.9 | 0.3 | 0.9 | 0.0 |
| CaO | 2.4 | 1.1 | 1.0 | 8.2 | 2.4 | 2.8 | 1.5 | 2.5 | 0.7 |
| Na ₂ O ₃ | 4.3 | 4.2 | 4.7 | 3.8 | 4.9 | 5.2 | 4.0 | 4.5 | 4.0 |
| K ₂ O | 5.4 | 4.8 | 4.3 | 1.5 | 4.2 | 2.2 | 4.8 | 4.6 | 4.0 |
| P ₂ O ₅ | 0.18 | 0.07 | 0.05 | 0.46 | 0.23 | 0.18 | 0.03 | 0.13 | 0.02 |
| LOI | 2.4 | 2.0 | 3.7 | 1.9 | 1.8 | 3.7 | 4.5 | 2.2 | 4.7 |
| Total | 102.1 | 102.6 | 103.1 | 103.1 | 102.4 | 101.8 | 102.9 | 101.5 | 102.1 |
| | 3-87-17 | 3-87-18 | 3-87-19 | 10-87-4 | 10-87-7 | 11-87-0 | 11-87-4 | 11-87-8 | 11-87-9 |
| SiO ₂ | 64.8 | 62.7 | 61.9 | 55.6 | 75.7 | 74.0 | 76.3 | 75.8 | 74.8 |
| TiO ₂ | 0.86 | 1.11 | 0.81 | 1.39 | 0.14 | 0.16 | 0.18 | 0.14 | 0.18 |
| Al ₂ O ₃ | 15.7 | 16.5 | 16.4 | 17.7 | 12.4 | 14.2 | 13.0 | 12.5 | 13.0 |
| Fe ₂ O ₃ | 5.9 | 6.1 | 5.2 | 8.1 | 0.9 | 1.1 | 1.2 | 0.9 | 1.2 |
| MgO | 1.7 | 1.9 | 1.6 | 4.4 | 0.0 | 0.4 | 0.1 | 0.1 | 0.0 |
| CaO | 3.0 | 3.4 | 4.4 | 7.7 | 0.7 | 1.3 | 0.7 | 0.7 | 0.5 |
| Na ₂ O ₃ | 5.2 | 5.0 | 5.0 | 3.9 | 3.4 | 1.7 | 4.0 | 3.5 | 3.9 |
| K ₂ O | 3.5 | 3.3 | 3.7 | 2.1 | 4.8 | 5.2 | 4.9 | 4.8 | 5.0 |
| P ₂ O ₅ | 0.22 | 0.33 | 0.23 | 0.41 | 0.02 | 0.04 | 0.03 | 0.03 | 0.02 |
| LOI | 1.2 | 1.4 | 2.3 | 0.1 | 4.0 | 4.7 | 0.4 | 3.4 | 3.7 |
| Total | 101.9 | 101.8 | 101.5 | 101.5 | 102 | 102.9 | 100.9 | 101.9 | 102.4 |

Table 2: Trace Element Concentrations

| | 1-87-12 | 2-87-15 | 2-87-16 | 2-87-19 | 2-87-21 | 3-87-5 | 3-87-6 | 3-87-11 | 3-87-12 |
|----|---------|---------|---------|---------|---------|--------|--------|---------|---------|
| Rb | 152.8 | 114.2 | 117.5 | 26 | 94.3 | 122.4 | 130.4 | 129.7 | 158 |
| Cs | 0.81 | 1.01 | 2.295 | 0.25 | 0.75 | | | 1.33 | 3.22 |
| Ba | 2040 | 981 | 948 | 758 | 1281 | | | 1300 | 1000 |
| Sr | 380.4 | 152.4 | 148.7 | 719.4 | 420.9 | 485.6 | 56.8 | 279.3 | 72.9 |
| Y | 22.4 | 13.7 | 14.9 | 22.4 | 27.7 | 20.1 | 18.3 | 27.2 | 17.5 |
| Zr | 247 | 205 | 209 | 170 | 268 | 211 | 94 | 339 | 87 |
| Nb | 17.6 | 15.6 | 16.9 | 14 | 20.5 | 16.2 | 15.3 | 20.4 | 15.3 |
| Ta | 1.22 | 1.274 | 1.415 | 0.91 | 1.44 | | | 1.29 | 1.356 |
| Hf | 6.72 | 5.75 | 5.57 | 4.18 | 6.77 | | | 8.65 | 3.29 |
| Cr | 11.5 | 2.8 | 2.3 | 44.2 | 3.9 | | | 4.8 | 2.6 |
| Ni | | | 0.65 | 20.8 | | | | | |
| Co | 3.27 | 1.62 | 1.04 | 25.47 | 3.09 | | | 3.4 | 0.27 |
| Sc | 5.94 | 2.53 | 2.1 | 20.07 | 6.6 | | | 6.74 | 1.97 |
| La | 52.8 | 36.46 | 37.915 | 35.41 | 54.7 | | | 54.4 | 31.5 |
| Ce | 107.9 | 66.6 | 67.9 | 73 | 113.1 | | | 115.3 | 61.9 |
| Nd | 38.5 | 19.9 | 19.3 | 35.6 | 42.7 | | | 43.3 | 21.4 |
| Sm | 6.71 | 3.1 | 3.16 | 6.17 | 7.44 | | | 7.45 | 3.88 |
| Eu | 1.242 | 0.616 | 0.561 | 1.81 | 1.671 | | | 1.427 | 0.36 |
| Tb | 0.69 | 0.35 | 0.35 | 0.65 | 0.85 | | | 0.79 | 0.47 |
| Tm | | 0.7 | 0.64 | 1.38 | | | | | |
| Yb | 2.56 | 1.49 | 1.64 | 2.02 | 2.79 | | | 2.9 | 1.87 |
| Lu | 0.343 | 0.232 | 0.255 | 0.284 | 0.417 | | | 0.42 | 0.258 |
| Pb | 22 | 15 | 17 | 8 | 15 | 19 | 24 | 19 | 22 |
| U | 7 | 3.5 | 4.4 | 0 | 4 | 0 | 0 | 4 | 5 |
| Th | 16.8 | 14.4 | 16.2 | 3.8 | 11.1 | 12.5 | 20.7 | 14.8 | 19.5 |

Table 2: Trace Element Concentrations (Continued)

| | 3-87-17 | 3-87-18 | 3-87-19 | 10-87-4 | 10-87-7 | 11-87-0 | 11-87-4 | 11-87-8 | 11-87-9 | 11-87-10 |
|----|---------|---------|---------|---------|---------|---------|---------|---------|---------|----------|
| Rb | 87.4 | 71.9 | 85.4 | 34.7 | 169 | 94.9 | 139.8 | 133.8 | 190 | 145.6 |
| Cs | 1.33 | | 1.62 | 0.86 | 4.05 | | 1.91 | | 3.13 | |
| Ba | 1000 | | 885 | 740 | 350 | | 190 | | 100 | |
| Sr | 330.5 | 442 | 409.6 | 682.2 | 69.9 | 678 | 16 | 84 | 34.7 | 542 |
| Y | 33.1 | 32.1 | 29.1 | 26.1 | 17.8 | 14 | 23.4 | 17.5 | 34.8 | 22.4 |
| Zr | 286 | 276 | 292 | 210 | 84 | 86 | 140 | 92 | 153 | 247 |
| Nb | 18.2 | 19.8 | 21.9 | 15.2 | 15.5 | 14.5 | 22.5 | 14.7 | 28 | 23.4 |
| Ta | 1.32 | | 1.47 | 0.94 | 1.423 | | 1.47 | | 1.98 | |
| Hf | 7.15 | | 7.3 | 4.92 | 3.06 | | 5.2 | | 5.88 | |
| Cr | 16.3 | | 9.2 | 77 | 0.5 | | 4.2 | | 3.8 | |
| Ni | | | | | | | | | | |
| Co | 6.35 | | 7.03 | 22.58 | 0.64 | | 0.28 | | 0.19 | |
| Sc | 10.58 | | 8.93 | 18.06 | 2.08 | | 3.2 | | 2.51 | |
| La | 45.8 | | 52.45 | 35.97 | 29.52 | | 47.8 | | 43.4 | |
| Ce | 97.3 | | 105.95 | 75 | 62.9 | | 104.4 | | 97.9 | |
| Nd | 38.3 | | 40.05 | 35.8 | 21.4 | | 38.7 | | 39.9 | |
| Sm | 7.39 | | 6.84 | 6.06 | 3.81 | | 7.1 | | 7.74 | |
| Eu | 1.661 | | 1.404 | 1.692 | 0.394 | | 0.671 | | 0.582 | |
| Tb | 0.93 | | 0.82 | 0.76 | 0.51 | | 0.79 | | 1.06 | |
| Tm | 0 | | 1.16 | 1.32 | 0.639 | | 0.67 | | 0.44 | |
| Yb | 3.36 | | 3.04 | 2.29 | 1.96 | | 2.39 | | 3.8 | |
| Lu | 0.494 | | 0.447 | 0.451 | 0.304 | | 0.361 | | 0.544 | |
| Pb | 15 | 13 | 15 | 11 | 22 | 15 | 14 | 19 | 30 | 27 |
| U | 4 | 0 | 3.6 | 1.3 | 3.7 | 0 | 0 | 0 | 4.6 | 0 |
| Th | 11.4 | 11.4 | 10.9 | 5.1 | 21.2 | 14.8 | 15.4 | 19.3 | 18.3 | 18.6 |

Table 3: Isotopic Results

| | 1-87-12 | 2-87-15 | 2-87-16 | 2-87-19 | 2-87-21 | 3-87-5 | 3-87-6 | 3-87-11 | 3-87-12 | |
|-----------------------------------|-------------|------------|-------------|------------|------------|------------|------------|------------|------------|----------|
| $^{87}\text{Sr}/^{86}\text{Sr}_0$ | 0.70958(6) | 0.70878(6) | | | 0.70721(6) | 0.70912(6) | 0.71164(6) | 0.70921(6) | | |
| $^{143}\text{Nd}/^{144}\text{Nd}$ | | | | | 0.51241(5) | | | | | |
| $^{206}\text{Pb}/^{204}\text{Pb}$ | 18.80(2) | | 18.80(2) | 19.08(2) | 19.06(2) | | 18.69(2) | | | |
| $^{207}\text{Pb}/^{204}\text{Pb}$ | 15.64(2) | | 15.62(2) | 15.71(2) | 15.72(2) | | 15.66(2) | | | |
| $^{208}\text{Pb}/^{204}\text{Pb}$ | 39.6(1) | | 39.1(1) | 39.2(1) | 39.5(1) | | 39.7(1) | | | |
| | 3-87-17 | 3-87-18 | 3-87-19 | 10-87-4 | 10-87-7 | 11-87-0 | 11-87-4 | 11-87-8 | 11-87-9 | 11-87-10 |
| $^{87}\text{Sr}/^{86}\text{Sr}_0$ | 0.70773(6) | 0.70717(6) | 0.70708(6) | 0.70603(6) | 0.70976(6) | 0.71281(6) | 0.70969(6) | | 0.71335(6) | |
| $^{143}\text{Nd}/^{144}\text{Nd}$ | 0.512498(5) | | 0.512455(5) | | | | | | | |
| $^{206}\text{Pb}/^{204}\text{Pb}$ | 19.38(2) | | 19.39(2) | | | | | | | |
| $^{207}\text{Pb}/^{204}\text{Pb}$ | 15.75(2) | | 15.70(2) | | | | | | | |
| $^{208}\text{Pb}/^{204}\text{Pb}$ | 39.7(1) | | 39.4(1) | | | | | | | |

Table 4. Model Characteristics

| | A Crust | B Enriched Mantle | C Depleted Mantle |
|-----------------------------------|------------|-------------------------|-------------------------|
| Sr (ppm) | 500 | 700 | 800 |
| $^{87}\text{Sr}/^{86}\text{Sr}$ | 0.715 | 0.707 | 0.703 |
| Nd (ppm) | 20 | 20 | 20 |
| ϵ Nd | -15 | -10 | +10 |
| Pb | 15 | 7 | 3 |
| $^{208}\text{Pb}/^{204}\text{Pb}$ | 40 | 38.1 | 38.7 |

Table 5. Regional Model Fits

| Sample Group | χ^2 residual | Wt. Percent A | Wt. Percent B | Wt. Percent C |
|--------------------------------------|-------------------|---------------|---------------|---------------|
| <u>Coso Range</u> | | | | |
| 106-5† | 47 | 18 | 63 | 19 |
| 84-1† | 120 | 9 | 70 | 21 |
| 104-13† | | 4 | 21 | 75 |
| 12-8† | 1 | 11 | 19 | 70 |
| <u>DVPR</u> | | | | |
| CF-12-6-10† | 5.9 | 23 | 70 | 7 |
| TS9-22-1† | 0.75 | 17 | 72 | 11 |
| TS6-14-7†A | 2.6 | -2 | 40 | 62 |
| TS6-15-2† | 7.0 | 19 | 36 | 45 |
| FB785† | 3.1 | 17 | 72 | 11 |
| NE 5205 | 0.44 | 17 | 67 | 16 |
| TS 6-136 | 0.7 | 2 | 97 | 1 |
| TS 61-41-2 | 1.6 | 4 | 27 | 69 |
| DV | | | | |
| <u>Nova Basin</u> | | | | |
| PP-1 | 10 | 1 | 46 | 54 |
| PP-2 | 8.3 | 6 | 51 | 43 |
| PP-4† | 0.14 | 5 | 50 | 45 |
| PP-5 | 0.05 | 3 | 18 | 79 |
| PP-6 | 0.44 | 9 | 27 | 64 |
| PP-7 | 0.01 | 10 | 25 | 65 |
| PP-8 | 430 | 75 | 30 | -5 |
| PP-10 | 0.4 | 0 | 46 | 54 |
| PP-11 | 0.17 | 11 | 43 | 46 |
| PP-12† | 2.0 | 36 | 62 | 62 |
| PP-13 | 43 | 0 | 56 | 44 |
| PP-15 | 0.0 | 11 | 32 | 57 |
| PP-20† | 0.54 | 3 | 44 | 53 |
| PP-23† | 2.1 | 20 | 49 | 31 |
| PP-24 | 0.6 | 17 | 55 | 28 |
| PP-26 | 0.01 | 7 | 55 | 38 |
| PP-28 | 1.2 | 1 | 49 | 50 |
| PP-32 | 0.44 | 7 | 43 | 50 |
| PP-41 | 6.5 | 17 | 63 | 20 |
| PP-48 | 4.4 | 1 | 39 | 60 |
| PP-49 | 7.2 | 4 | 23 | 73 |
| <u>Tail Canyon Volcanic Sequence</u> | | | | |
| 2-87-21† | 7.0 | 35 | 23 | 42 |
| 3-87-17† | 1.25 | 39 | 23 | 38 |
| 3-87-19† | 0.42 | 47 | 5 | 48 |

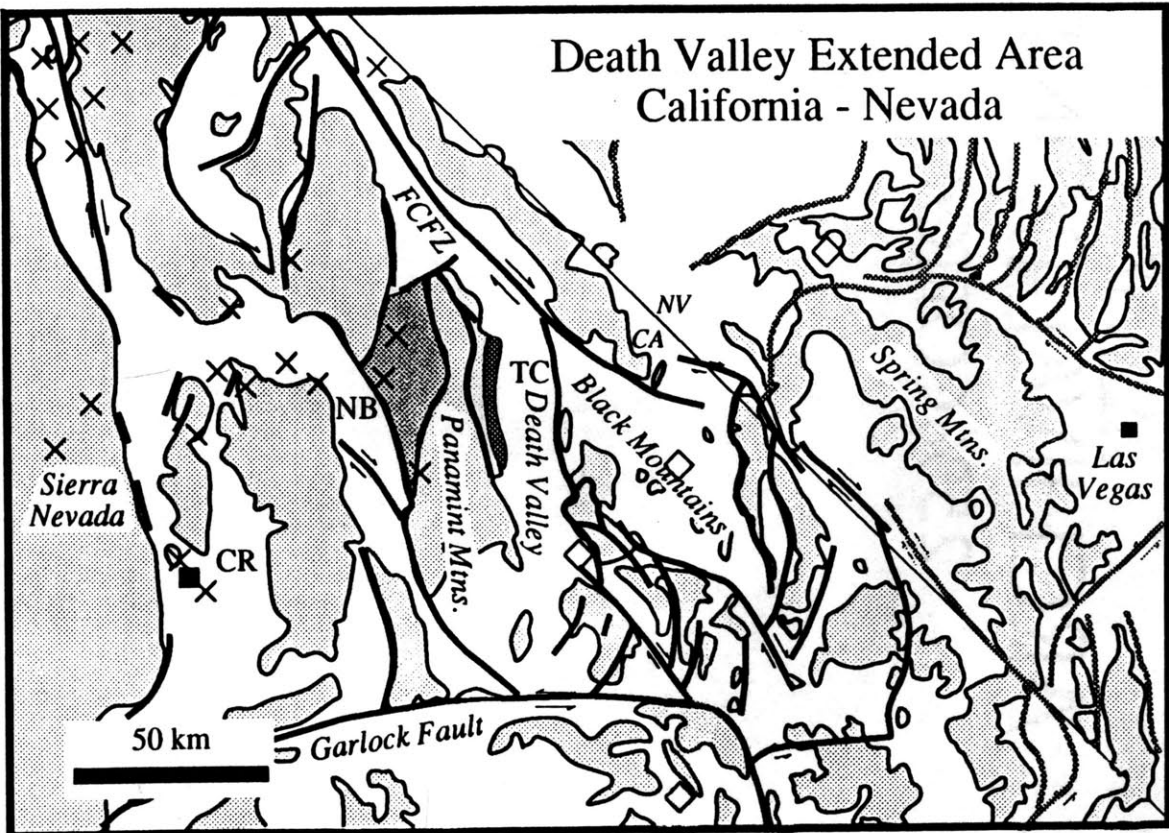


Figure 1

Figure 2

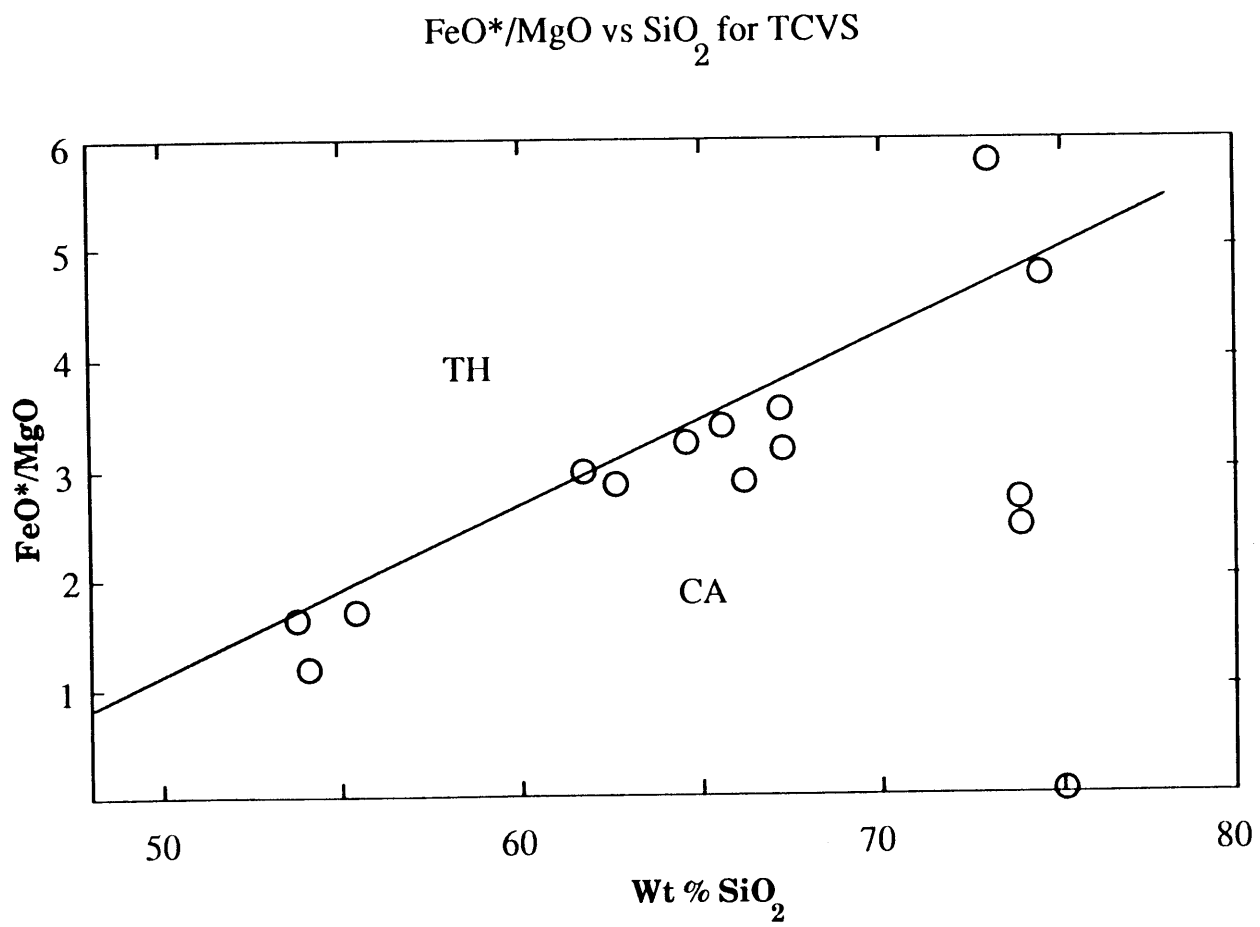


Figure 3 A, B

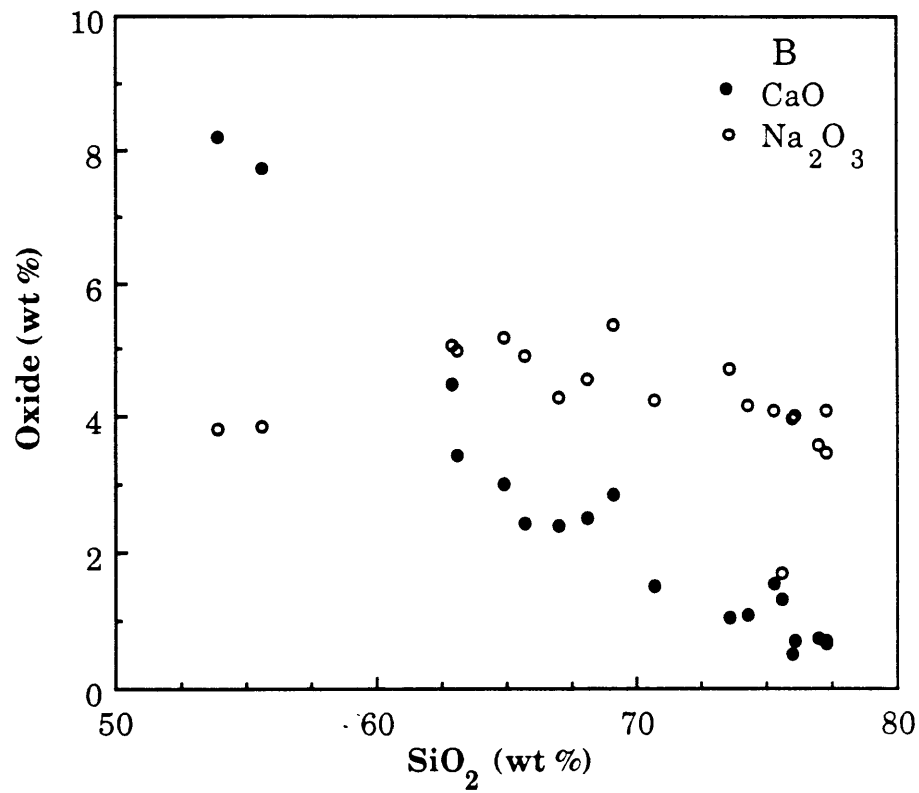
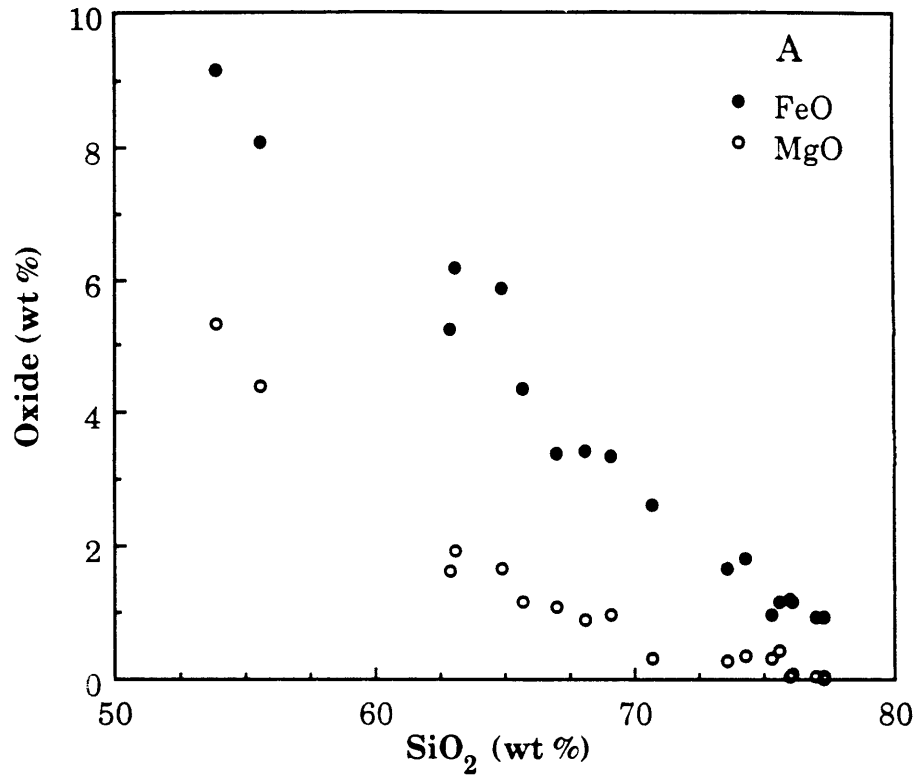


Figure 3 C, D

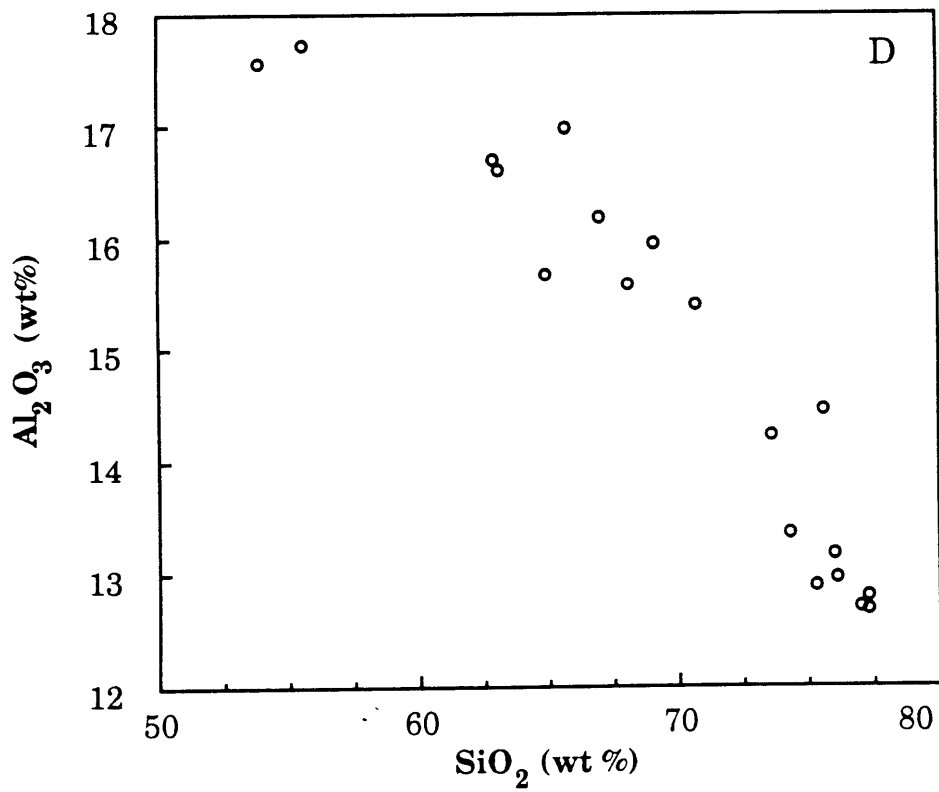
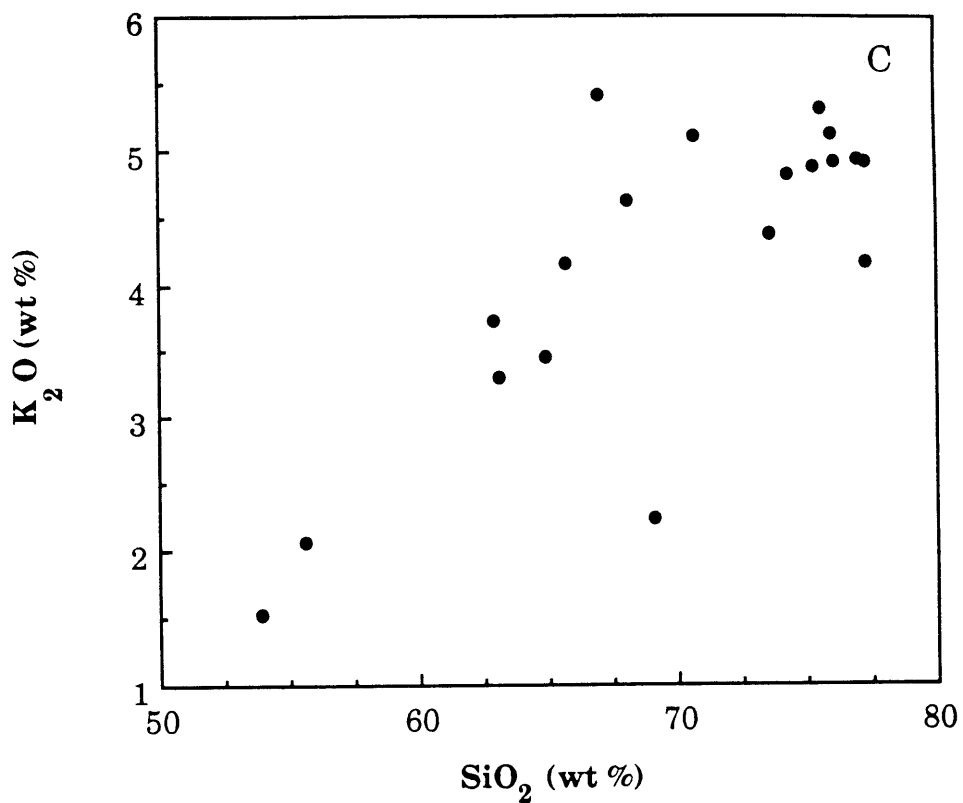


Figure 4.1 A, B

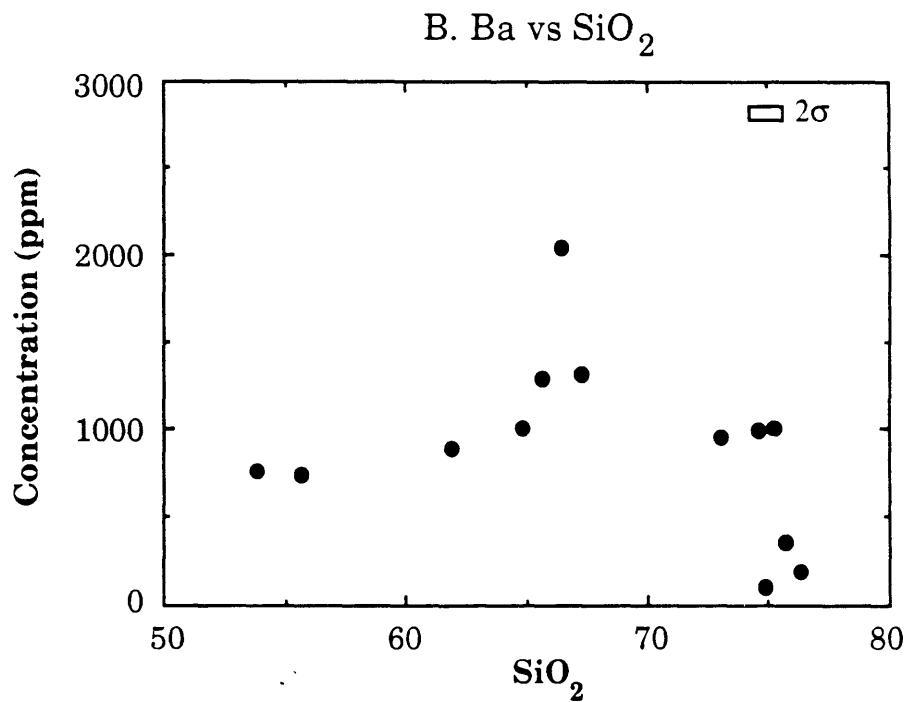
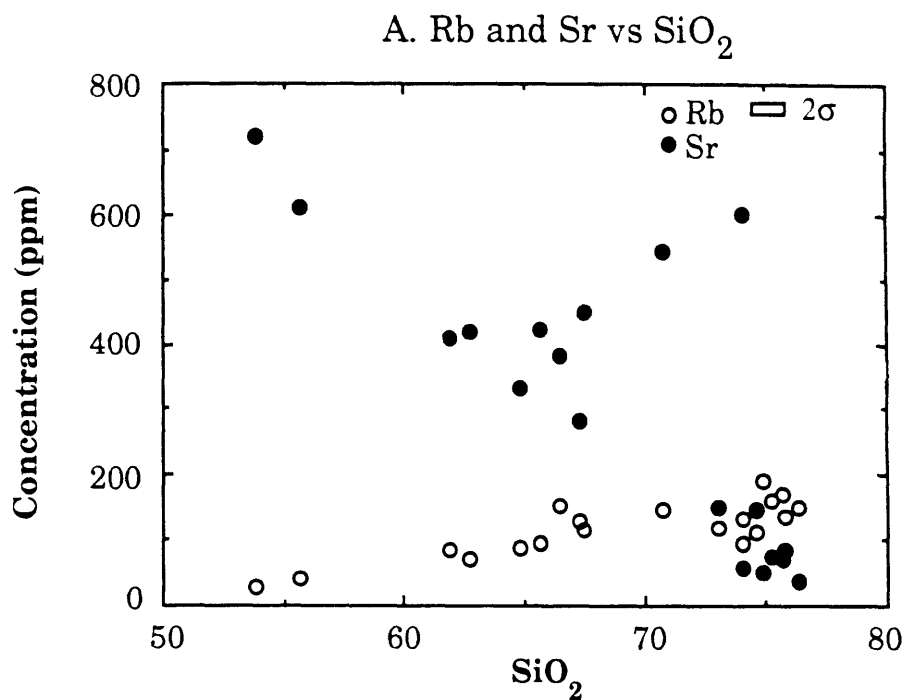


Figure 4.1 C

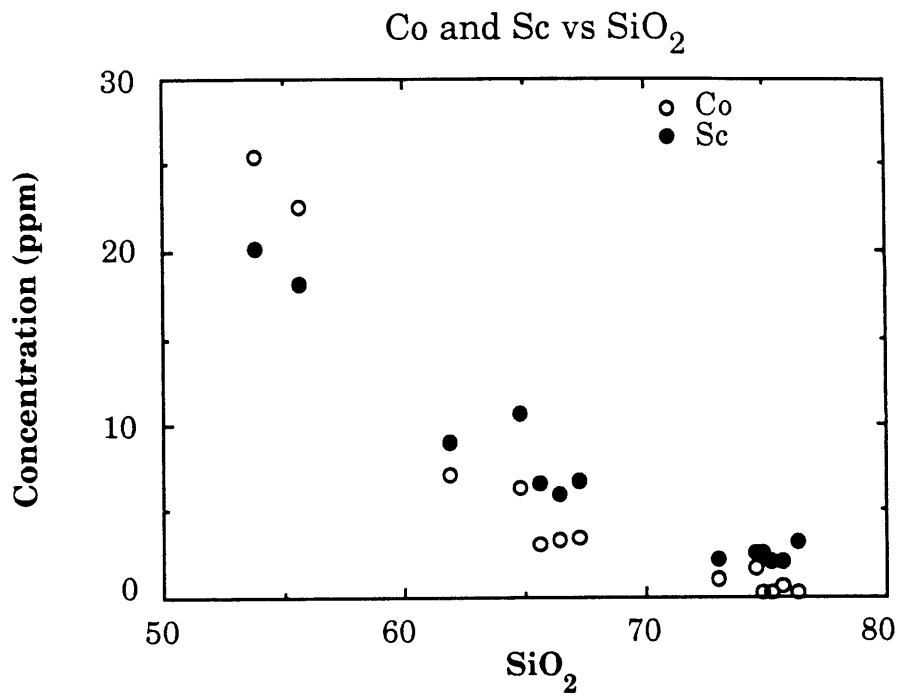


Figure 4.2 A, B

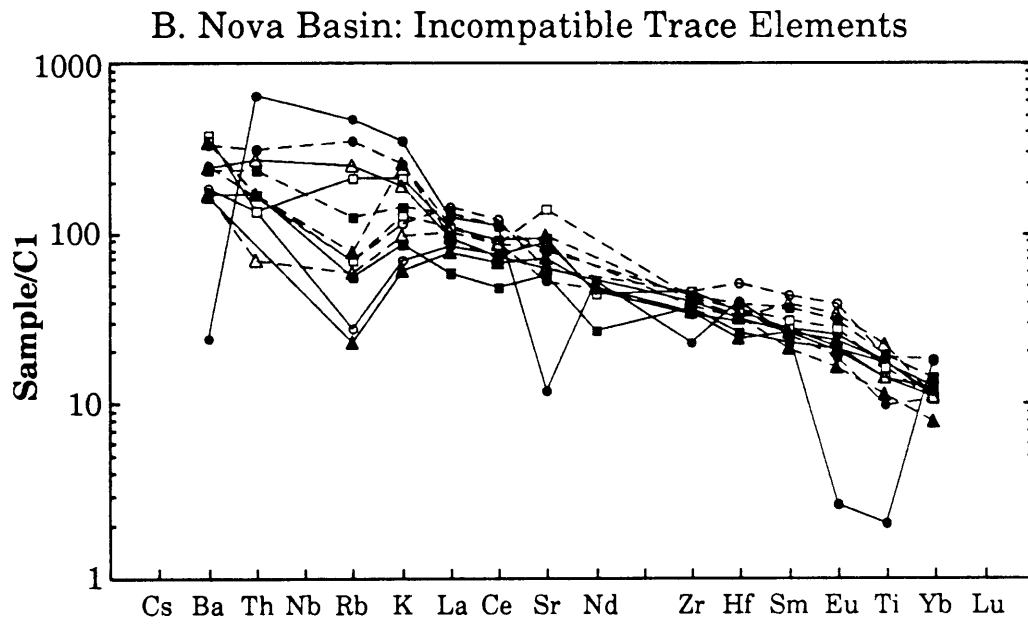
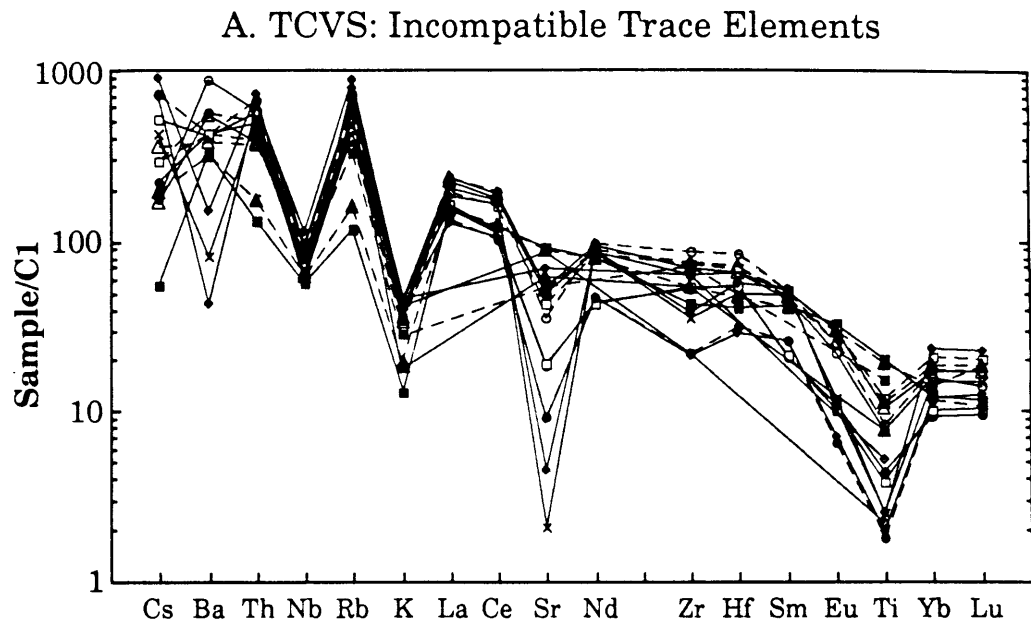


Figure 4.2 C, D

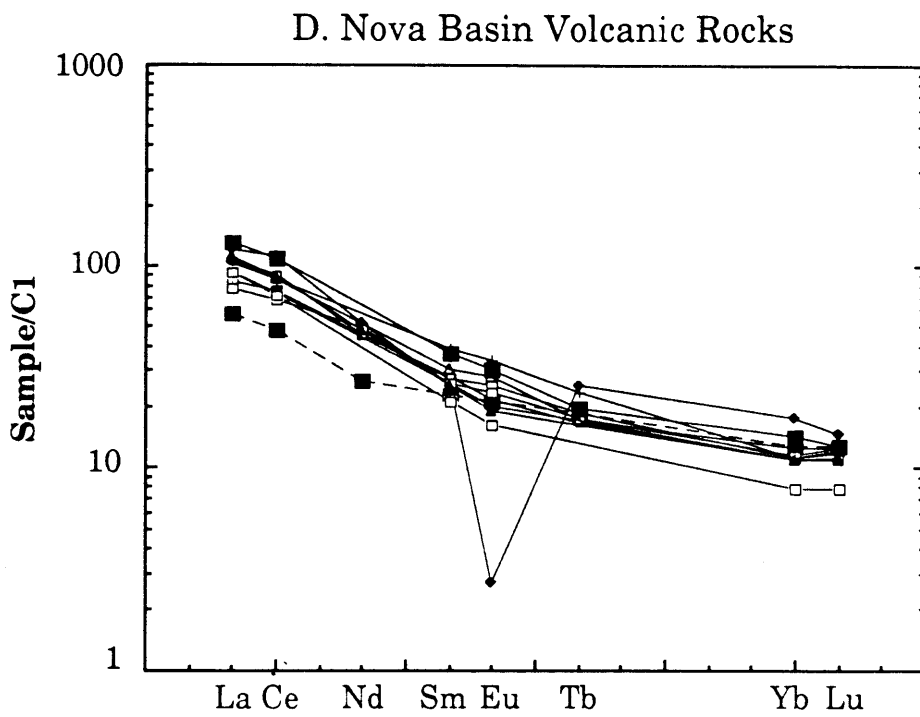
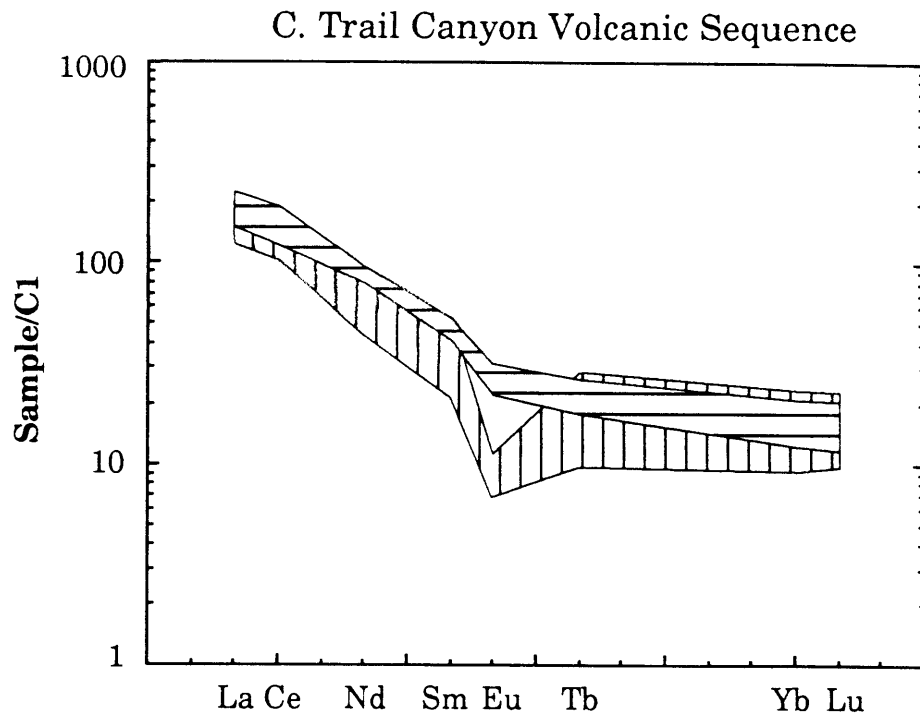


Figure 5.1 A, B

Sr isotopic correlations

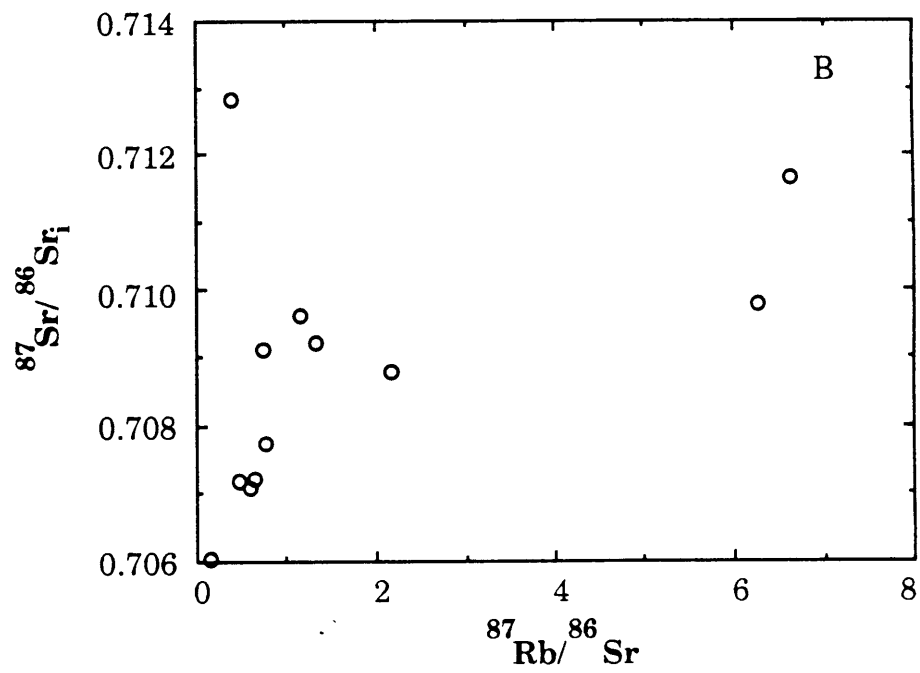
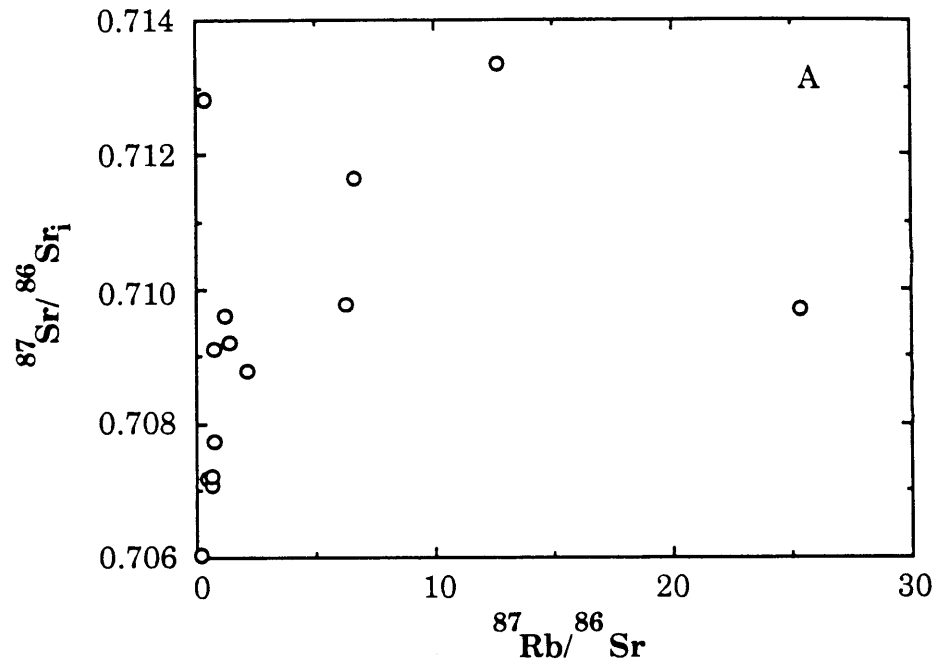


Figure 5.2 A, B

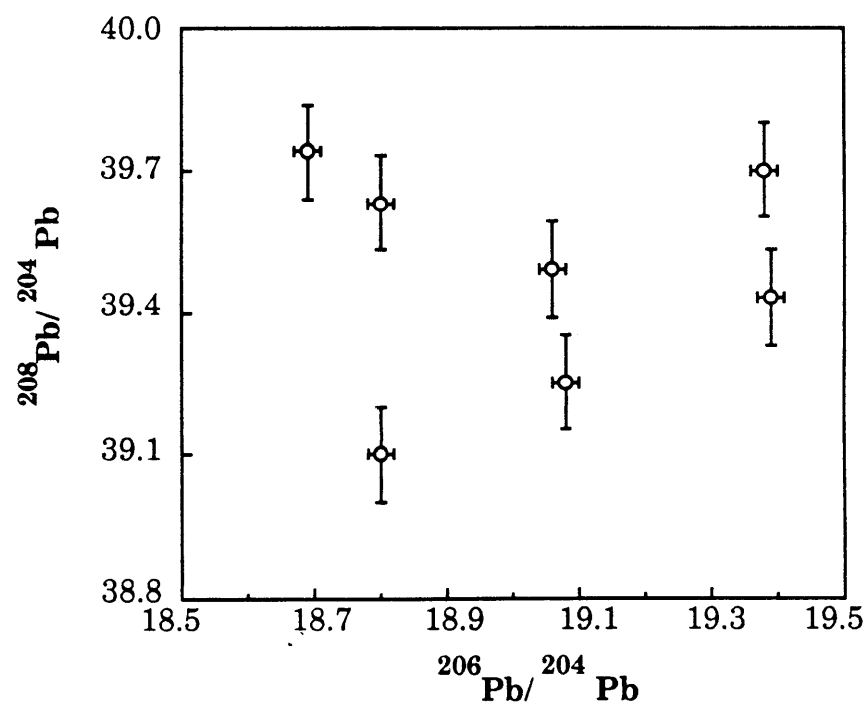
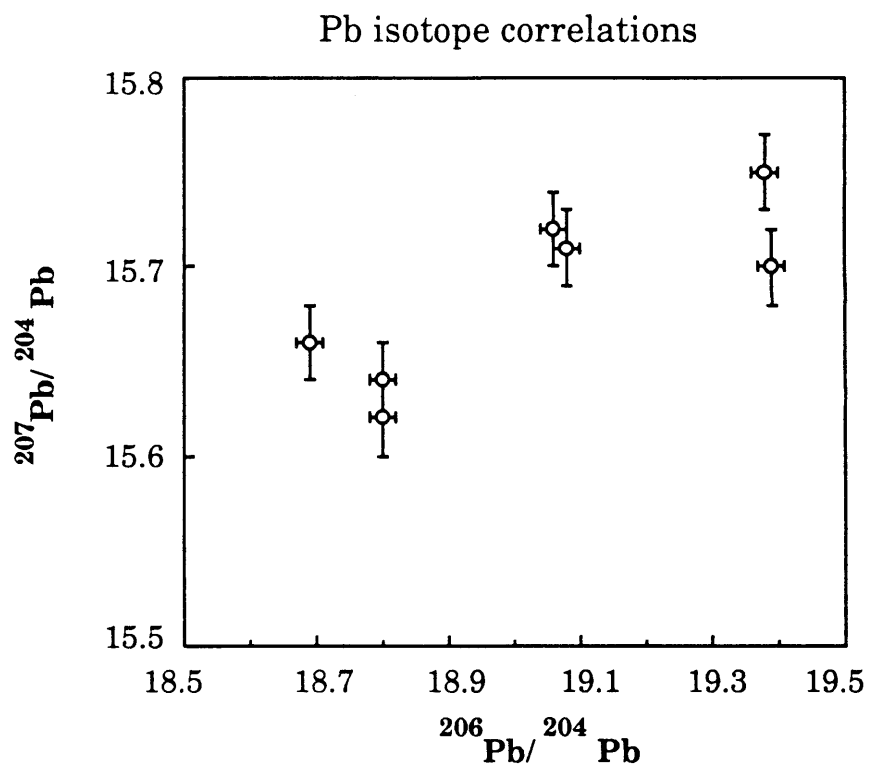


Figure 6 A, B

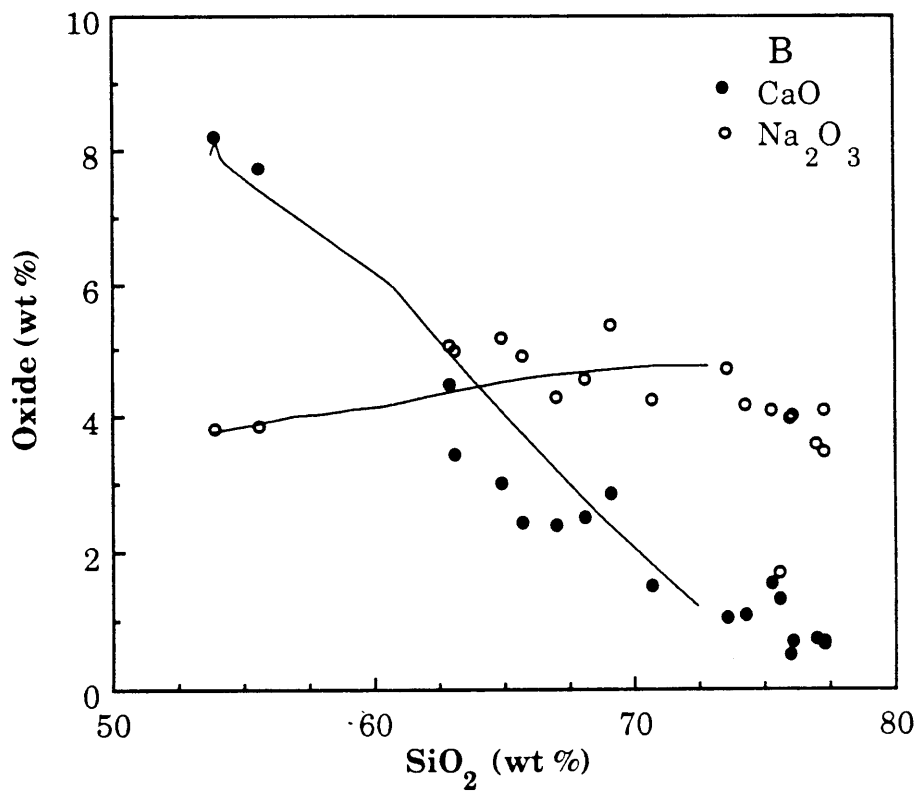
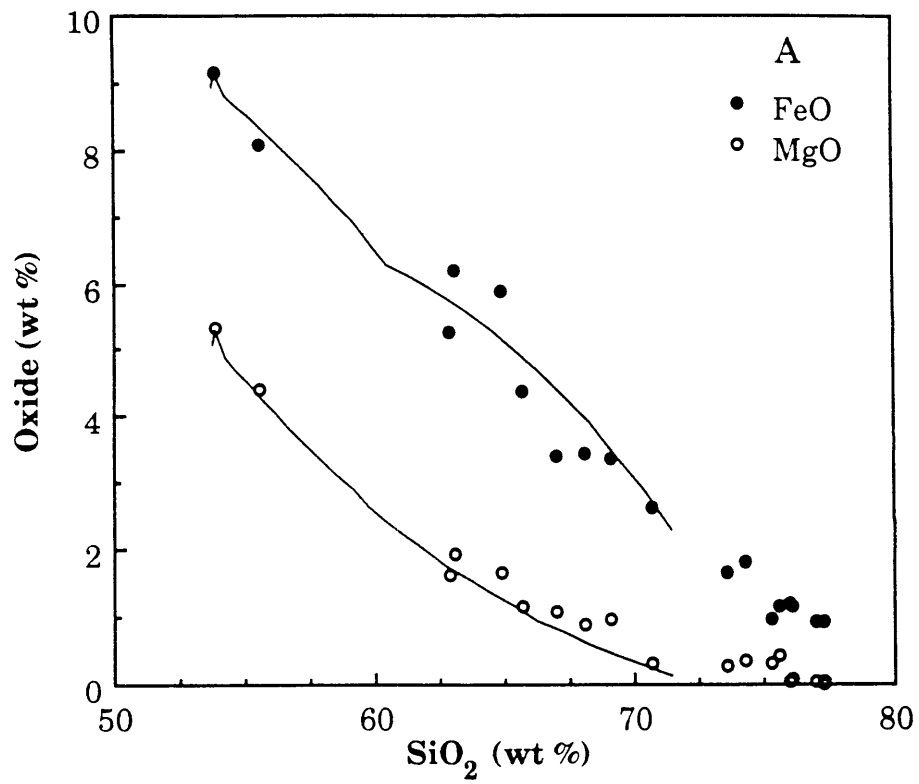


Figure 6 C, D

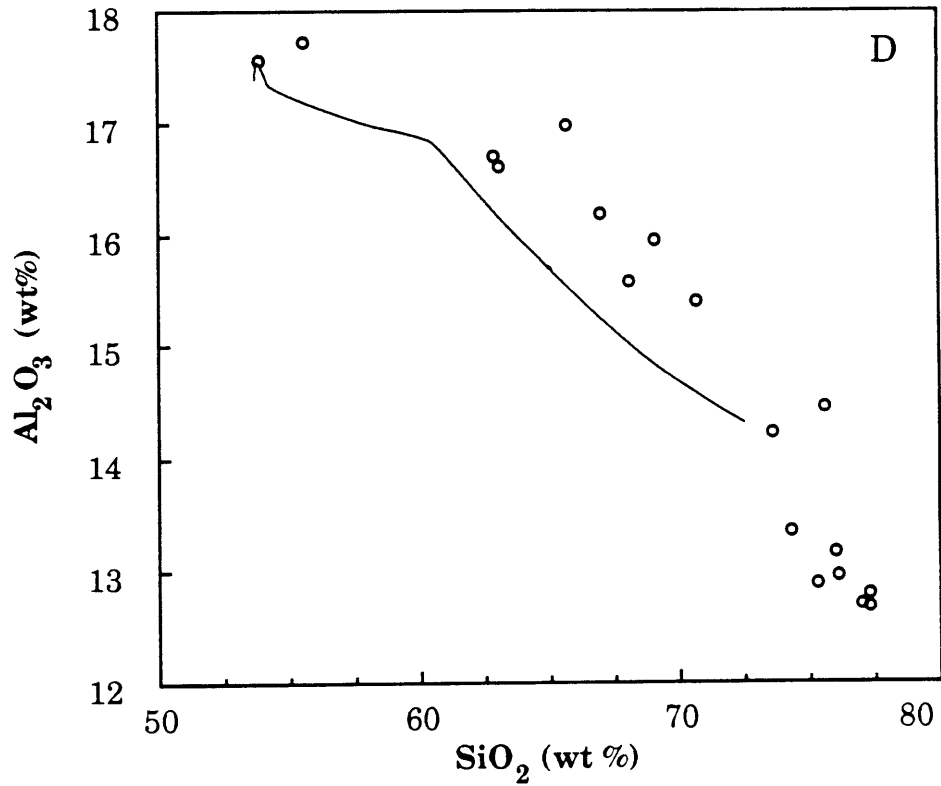
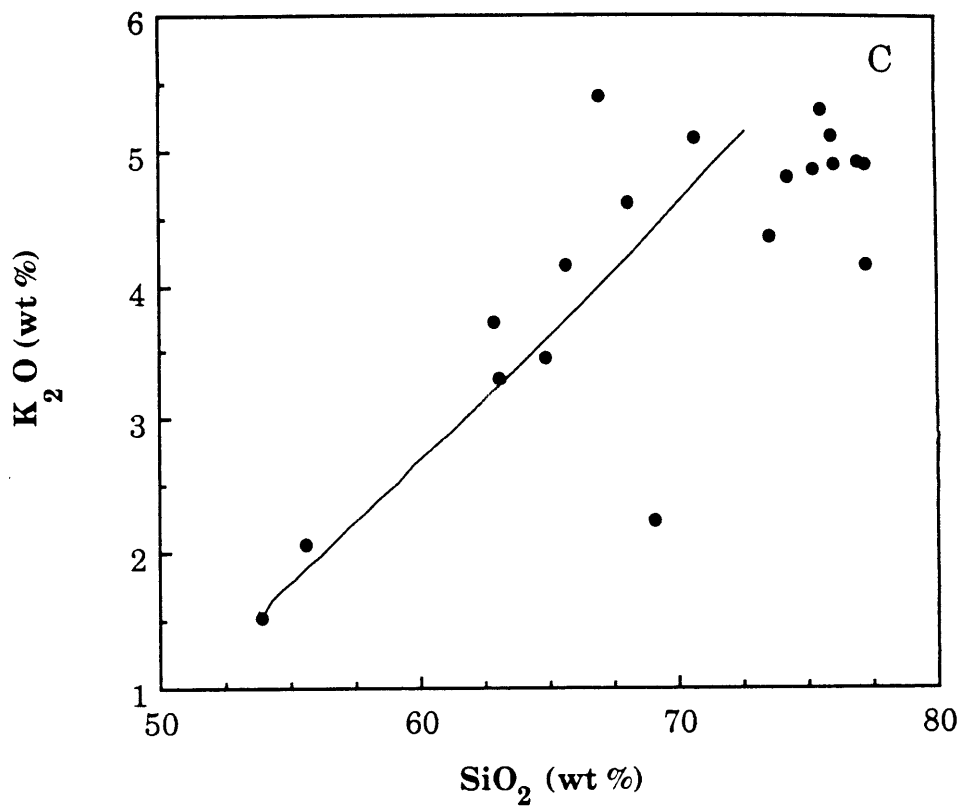


Figure 7

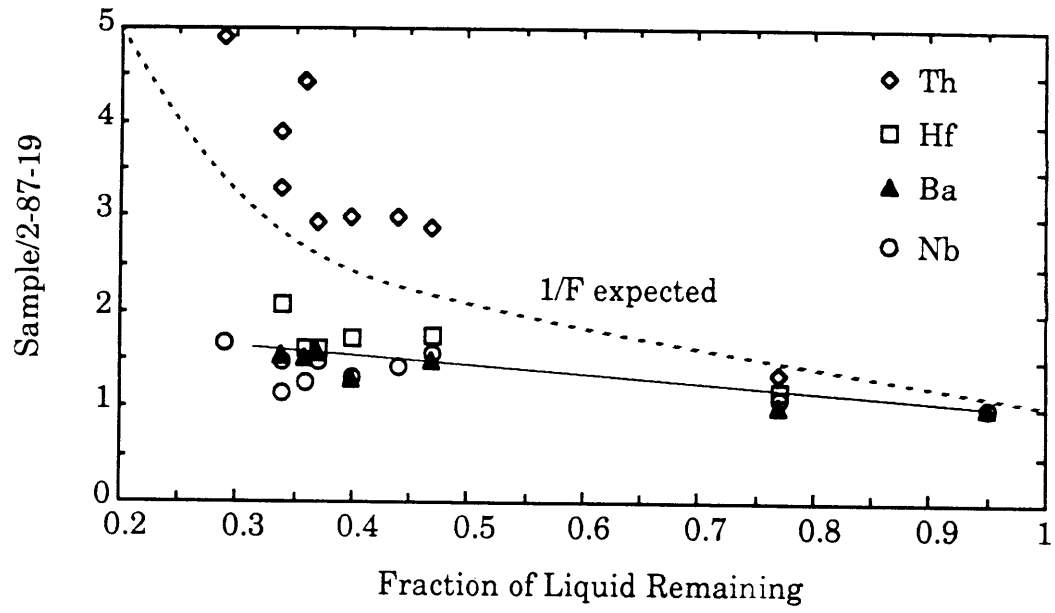


Figure 8 A, B

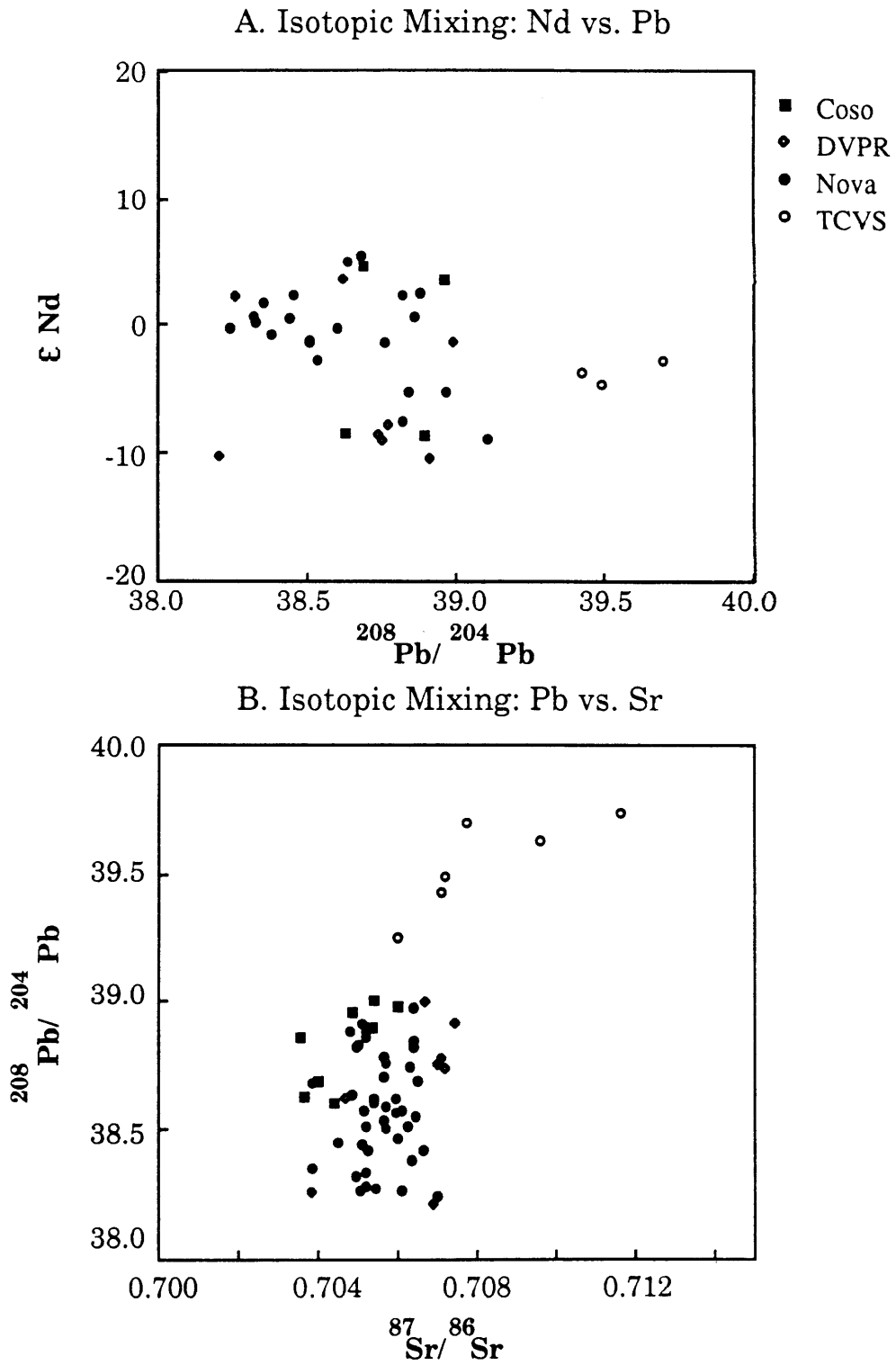


Figure 8 C

C. Isotopic Mixing: Nd vs. Sr

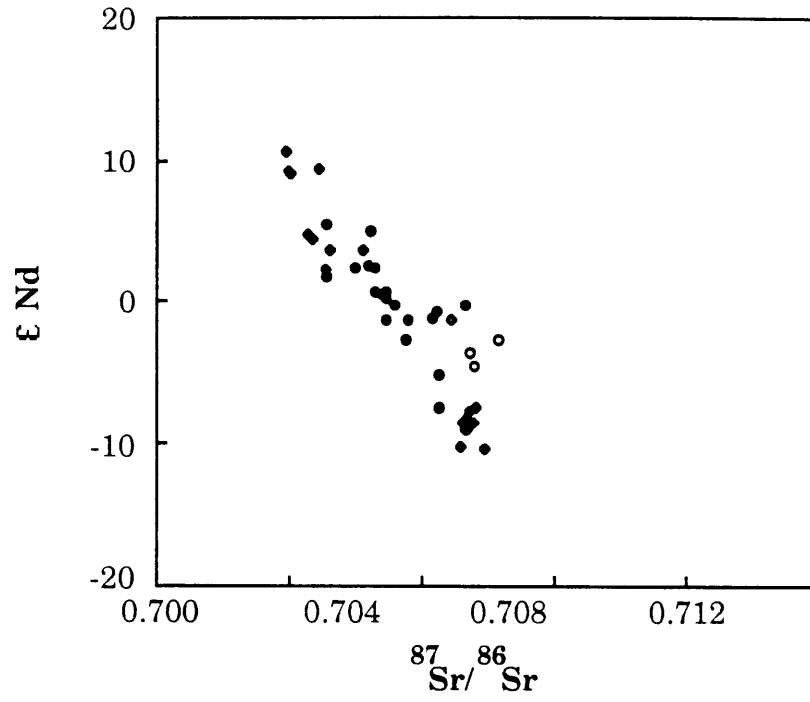


Figure 9 A, B

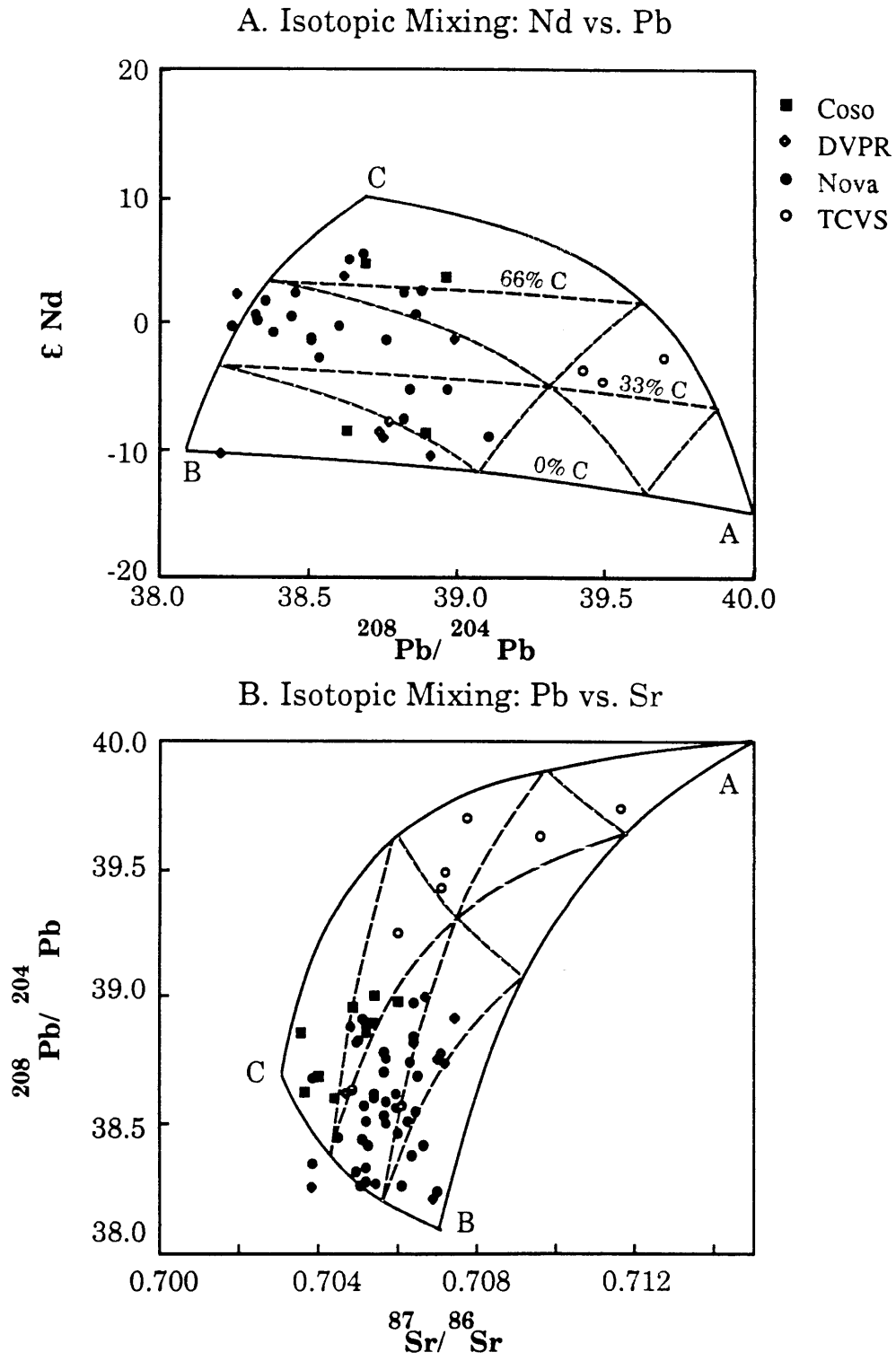


Figure 9 C

C. Isotopic Mixing: Nd vs. Sr

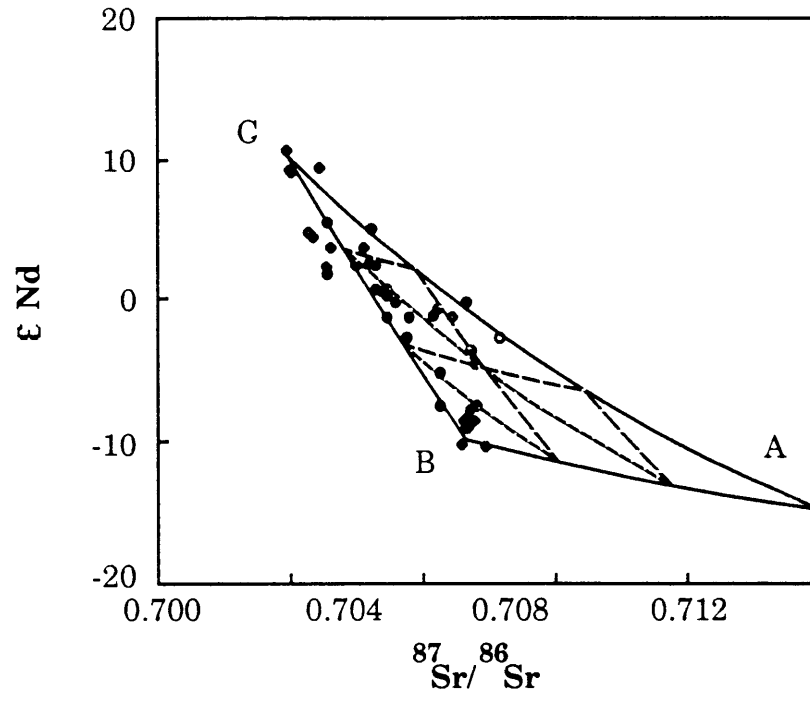


Figure 10

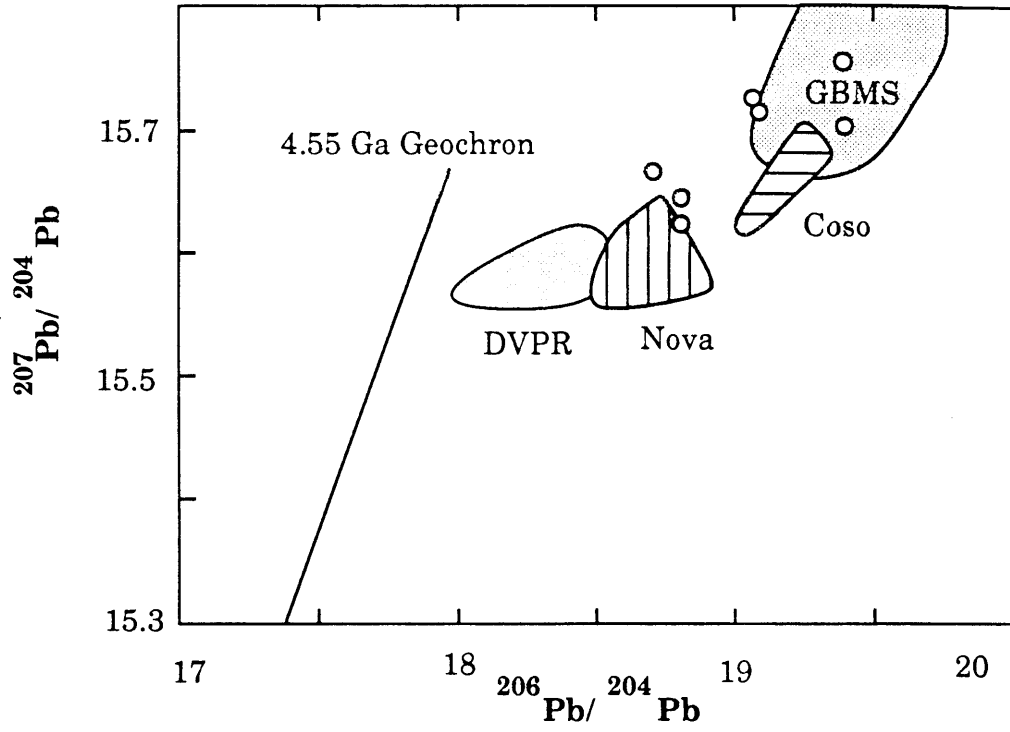


Figure 11

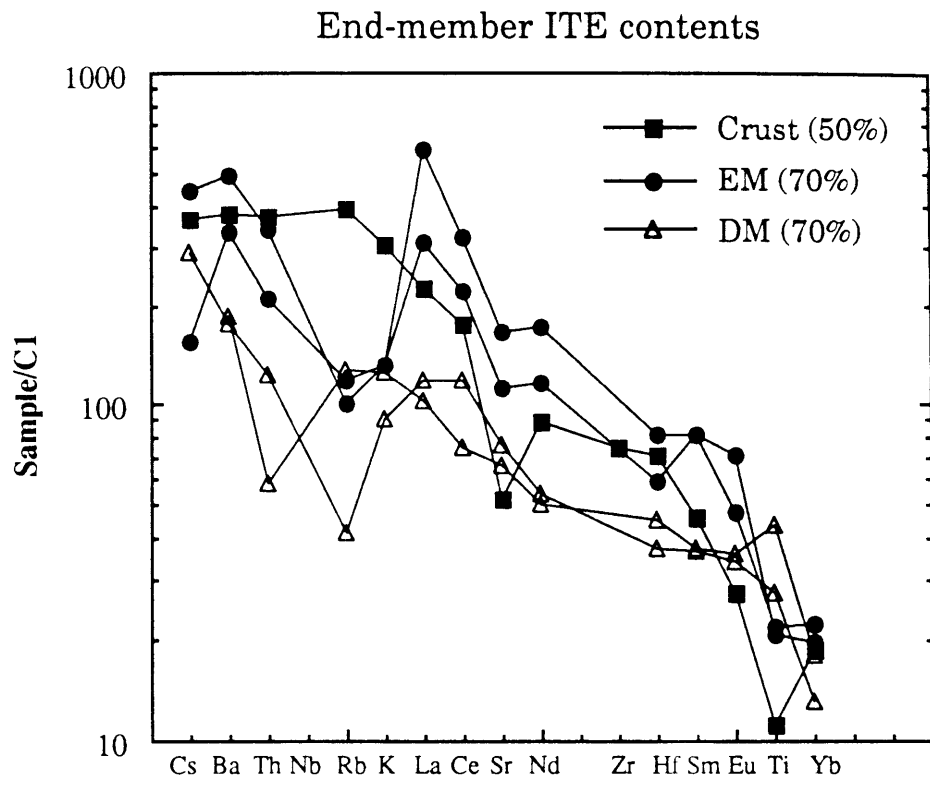
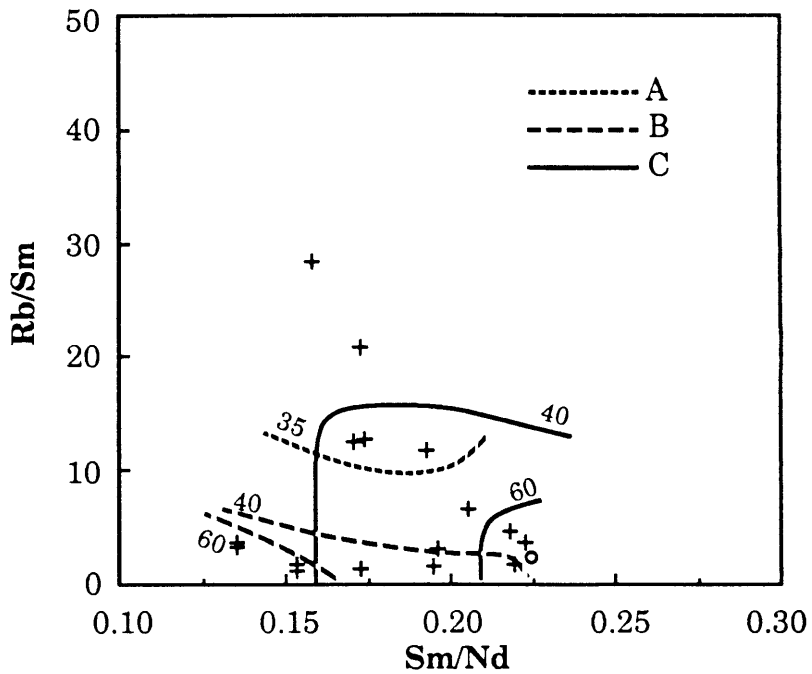


Figure 12 A, B

A. Enrichments vs. Isotopic Provenance



B. Volcanic rocks from the Death Valley Area

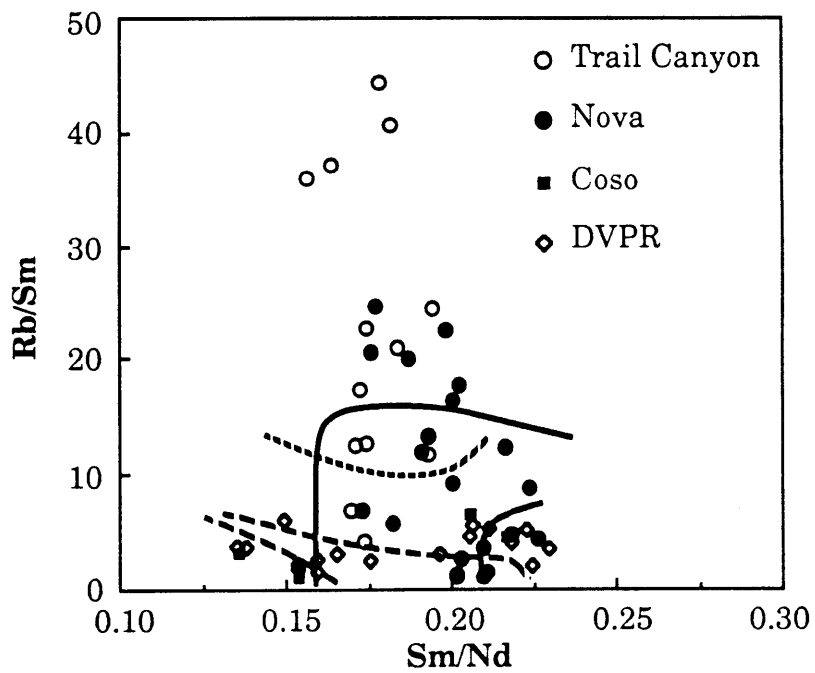
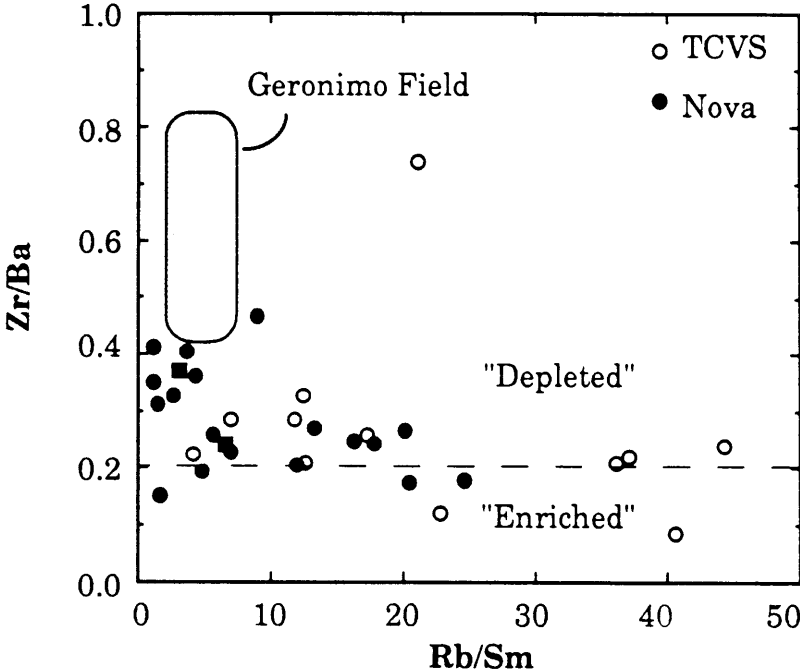


Figure 13 A, B

A: Zr/Ba vs. Rb/Sm



B: Mantle Provenance, Basin and Range Basalts

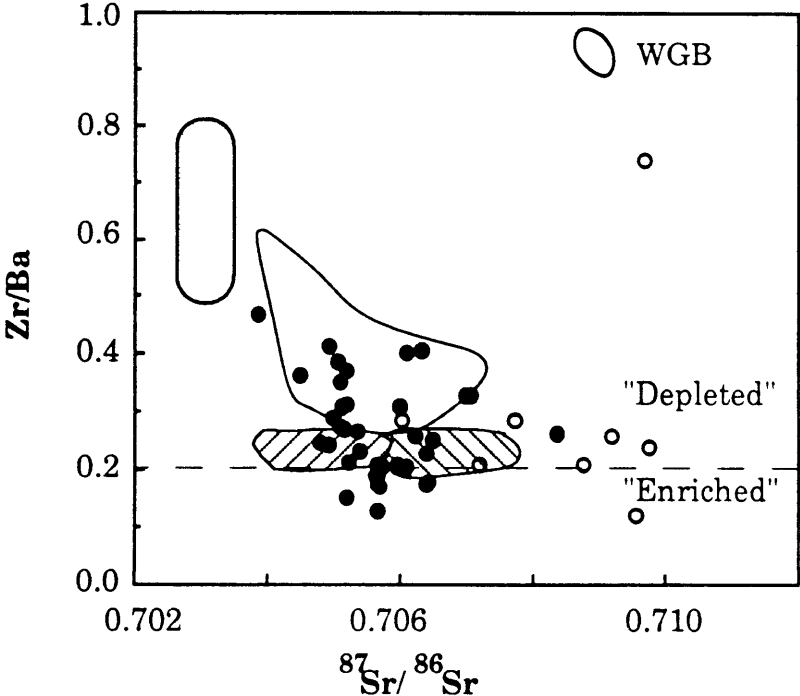


Figure 14

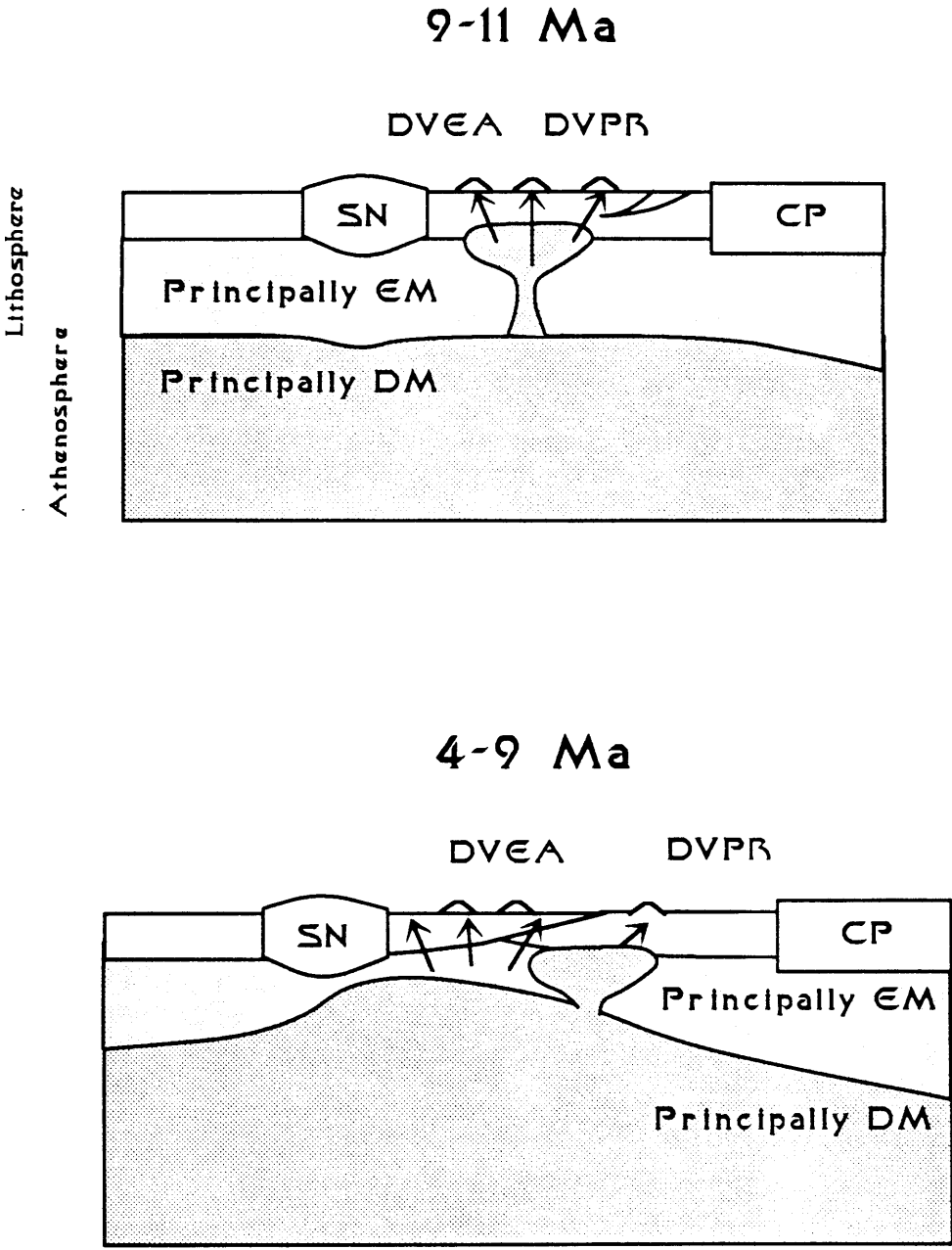
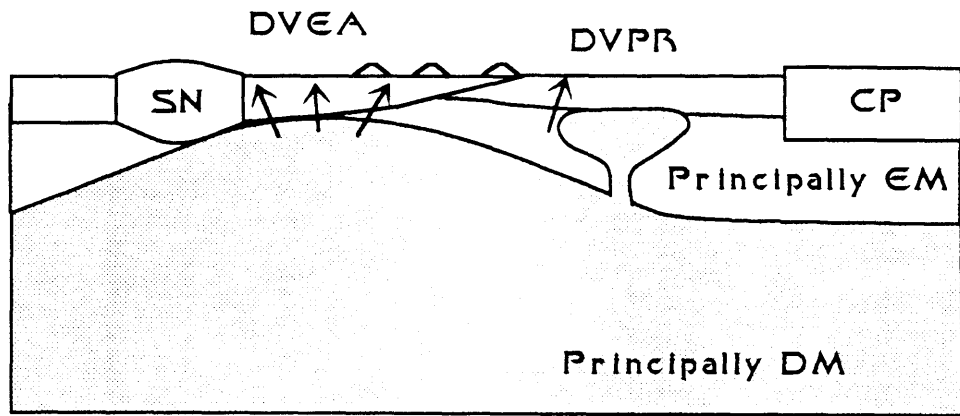


Figure 14

0-4 Ma



CHAPTER 4

VOLCANOTECTONIC RELATIONSHIPS IN
THE DEATH VALLEY AND COLORADO
RIVER EXTENDED AREAS

ABSTRACT

Extension within the Basin and Range was accompanied by significant volcanism, ranging from alkalic basalts to high silica rhyolites. In this chapter, the mantle sources involved in the volcanism, and the spatial progression of the locus of volcanism, are used to test various models for active versus passive upwelling of asthenospheric material during extension. This is done by combining the existing data for the isotopic and trace element compositions of volcanic rocks within the greater Death Valley Area [Farmer et al., 1989; Ormerod et al., 1988; Walker and Coleman, submitted; McKenna, Chapter 3] with the compilations by Luedke and Smith [1978] of the age and composition of volcanic rocks within the southern Basin and Range, and placing these data on a palinspastically restored base map. In effect, this removes the apparent spatial variability in the composition of volcanic rocks caused by different amounts of post-eruption extension within the Death Valley Extended Area. With these data in hand, a number of models for the large-scale structural formation of the Basin and Range are tested, and a hybrid simple shear-active upwelling model is proposed to integrate the observations.

MODELS

The tectonic models being tested are shown in Figure 2. The presence of numerous low angle normal faults in the Death Valley Extended Area, and the uniform extension directions within the area suggests that pure shear models [McKenzie, 1978] are not applicable to this area [Lister et al., 1986]. Two models for the lithosphere-scale description of continental extension are shown, the whole-crust shear zone and delamination models of Wernicke [1981] and Lister et al. [1986]. Bosworth [1987] invoked the delamination model of Lister et al. [1986] to explain continental extension within the Gregory rift system of Kenya, and discussed the implications of the simple shear model for the locus of synextensional volcanism. In this model, he explained the large lateral offset (100-150 km) between the locus of extension as seen in the crust (the 'axis' of extension) and the location of major volcanic centers as being due to the offset between the location of crustal and lithospheric extension (Figure 2). He suggested that this offset of volcanism from the axis of extension may be characteristic of continental rifts experiencing simple shear.

For a simple-shear system, the definition of what constitutes "off-axis" is dependent upon the lateral extent of the crust undergoing active extension and the lateral distance from the breakaway zone of a fault to the area of melt generation. For a planar shear zone, the distance from the breakaway zone to the intersection of the shear zone with the mantle lithosphere (termed here the "ramp-length" for brevity) is a function of the dip of the shear zone and thickness of the crust. For dips of 15° – 30° , and crustal thicknesses of 25–50 km, the ramp-length is <90 km. In the Death Valley area, Prodehl [1979] suggested a crustal thickness of approximately 30 km. Thus the width of the upper crust currently undergoing extension (≥ 100 km) is of the same scale as the ramp-length. This allows the possibility that volcanism may occur in what appears to be the axis of extension.

Menzies [1989] has recently presented a review of the chemical and physical structure of the mantle below the Western United States, and identified a number of distinct chemical reservoirs within the lithosphere and asthenosphere, analogs to the sub-oceanic crust reservoirs discussed

by Zindler and Hart [1986]. Two reservoirs of particular importance for this paper are: (1) a source with $^{87}\text{Sr}/^{86}\text{Sr}=0.703$, $\epsilon\text{Nd}=+10$, $^{208}\text{Pb}/^{204}\text{Pb}=38.1$, which is generally identified with a depleted or MORB-like mantle (referred to as 'DM' here), and (2) a source with $^{87}\text{Sr}/^{86}\text{Sr}=0.707$, $\epsilon\text{Nd}=-10$, $^{208}\text{Pb}/^{204}\text{Pb}=38.7$, generally referred to as an enriched mantle (EM) reservoir. Many authors [including Menzies, 1989; Perry et al., 1987] correlate these chemical reservoirs with physical reservoirs: the DM with asthenospheric mantle and the EM component with the sub-crustal lithospheric mantle. Menzies [1989] also describes an enriched reservoir he correlates with recycled, Proterozoic age, sub-continental crust (his EM2); it is differentiated from the EM introduced above by the higher Rb/Sr and $^{87}\text{Sr}/^{86}\text{Sr}$, and less negative ϵNd , than the EM reservoir. Farmer et al. [1989] and Menzies [1989] are in some disagreement about the age and distribution of the EM domain, and their presence or absence below specific areas within the Basin and Range. Most importantly, Menzies [1989] suggests the presence of EM2, and not EM, in the mantle lithosphere below the Sierra Nevada and Colorado Plateau. Three parameters are crucial to differentiating the two models using the chemical composition of volcanic rocks: the depth of melting, the location of melting (and by assumption, extrusion) relative to the axis of extension, and the distribution, laterally and vertically, of chemical heterogeneities within the mantle.

TECHNIQUES

A study which attempts to probe the composition of the mantle using volcanic rocks must account for the possibility that different samples have equilibrated at different depths within the mantle. Perry et al. [1987] examined the heterogeneity of the mantle beneath the Rio Grande Rift using both alkali basalts derived at depths of greater than 65 km, and tholeiitic rocks, which equilibrated at depths of less than 65 km. Because of the potential for this vertical heterogeneity masking the lateral heterogeneity, this study utilizes only non-alkaline volcanic rocks.

The second parameter, location of melting, can be difficult to ascertain in highly extended terrains such as the Basin and Range. Because post-eruption extension within this area has changed (drastically, in some cases) both the relative and absolute positions of volcanic centers, the

geometric distributions can be understood only from a palinspastically corrected reference frame. This chapter uses the reconstructions for the southern Basin and Range published by Levy and Christie-Blick [1989]. Finally, the third parameter, the mantle provenance of a sample, is determined according to the criteria discussed in Chapter 3 for distinguishing EM and DM sources for the syn-extensional volcanic rocks.

SETTING

As noted in Chapters 1 and 2, the Basin and Range Province is composed of domains which appear to act as coherent systems undergoing diachronous extension in uniform directions [Bohannon, 1984; Burchfiel et al., in preparation; Howard and John, 1987]. It is not surprising then that within the Basin and Range Province as a whole, and even within the single extensional domains, the axis of extension migrated with time. This was one of the major conclusions derived from the research presented in Chapters 1 and 2.

Thus, unlike the East African rift systems [Bosworth, 1987], one cannot define a single axis for the continental extension within the Basin and Range, or even for the Death Valley Extended Area. Additionally, more than one locus of extension was active at a given time within the Death Valley Extended Area; these loci were separated by from 10 to perhaps 100 km (Chapter 1 and 2; Figure 4D). As extension within the Death Valley Extended Area continued, the western limit of faulting migrated uniformly westward (Figure 9 of Chapter 1; Figure 9 of Chapter 2). However, extension continued (and continues today) east of these western-most faults. In effect, the width of the area within the crust undergoing active extension increased with time, and the "axis" of extension evolved into a "zone" of extension which may have been half as wide as the extended area itself. The regional tilt direction of miogeoclinal units within the exposed ranges of the Death Valley Extended Area is primarily eastward, suggesting the majority of the faults which accommodated extension dipped westward [Stewart, 1978].

DATA

Farmer et al. [1989], Ormerod et al. [1988], Walker and Coleman [submitted] and McKenna [Chapter 3] have collected isotopic and trace element compositions of syn-extensional volcanic rocks within the Death Valley Extended Area. We utilize these data to identify the prevalent mantle components within the samples (Figure 3). Ormerod et al [1988] and Farmer et al [1989] measured individual samples over a wide geographic area, while McKenna [Chapter 3] and Walker and Coleman [in press] measured a number of samples from single volcanic fields. In the latter case, a field is identified as EM or DM based on the most prevalent signal in the data, or mixed if the components are present in roughly equal proportions. This is a somewhat subjective classification scheme, but the results of Chapter 3 suggests that the discrimination criteria are valid. For the Farmer et al and Ormerod et al sets, we utilize the identification (EM or DM) the authors used. A few samples from Hedge and Noble [1970] have $^{87}\text{Sr}/^{86}\text{Sr}$ ratios which are diagnostic of DM sources, and these are also included in Figures 3 and 4. As experience with oceanic basalts has shown (for example, Zindler and Hart [1986]), very large data sets are needed to ensure adequate sampling of the mantle to deduce its heterogeneities, and the small number of data on Figures 3 and 4 emphasizes the preliminary nature of the models discussed below.

Figure 4 shows the reconstructed locations of all volcanic rocks exposed within the Death Valley Extended Area included in the compilation of Luedke and Smith [1978], and includes its mantle provenance type if available. Four figures are shown, for the periods 18-11 Ma (early extensional), 11-9 Ma, 9-4 Ma, and 4-0 Ma. In each case, the Colorado Plateau is considered to be a stable reference point for the relative positioning of the western boundary of extension, the Sierra Nevada. The light gray shading reflects the reconstructed locus of extension within the Death Valley Extended Area during the period indicated, based on the work in Chapters 1 2 and the sources of data quoted therein. Also shown is the locus for extension within the Colorado River Extensional Corridor [Bartley and Glazner, 1989], a middle Miocene age extensional Province which includes the Whipple Mountain-Chemenheuvi Mountain core complex

terrain in Arizona. Syn-extensional volcanic rocks erupted within this terrain are also shown.

Figure 4A shows the disposition of volcanism and volcanics for the early extensional period. While many of these early volcanic rocks were principally rhyolitic in composition, important mafic and andesitic flows within the Kingston Range and the McColloch Range (the areas west and east of the shaded areas respectively) have not been analyzed. Nonetheless, the pattern noted by Wernicke et al [1987] is well displayed: the locus of extension is much narrower than the locus of volcanism, although the degree of this is less than Wernicke et al [1987] suggested. Note also the presence of basalt flows along (what is now) the southwestern rim of the Colorado Plateau [Luedke and Smith, 1978]. These flows appear to be roughly synchronous with the initiation (in the late Miocene) of extension within the Colorado River Corridor [Bartley and Glazner, 1989], and are also located near the axis of extension. Some data are available for these early flows, and the magmas appear to represent derivation from a mixed EM-DM source.

More data are available for the period from 11-9 Ma, both from the work of Chapters 2 and 3, and from the data of Farmer et al., [1989]. As shown on Figure 4B, the locus of extension is still within the center of the extensional area, but relative to the (stable) Colorado Plateau, the extensional locus has migrated westward. Note also that the majority of the volcanic rocks of this age are aligned with the locus of extension and consist primarily of DM components. The only EM components seen in the 11-9 Ma volcanic rocks are from the Nevada Test Site, and, as will be seen below, appear to originate from a persistent EM source. In the Colorado River Corridor, the overlap of extension and magmatism continues, now with a strong DM component. The locus of magmatism within the Colorado River Corridor begins to migrate northeastward [Luedke and Smith, 1978], a trend that strengthens after approximately 4 Ma [Tanaka et al., 1986].

During the period 9-4 Ma (Figure 4C), the zone of extension within the Death Valley Extended Area includes an area over 50 km wide (Chapter 1, 2) and magmatism is active over an even wider area, in both actively

extending and previously extended areas. The affinities of the active volcanic centers (DM, EM, or mixed) are, relative to the stable Colorado Plateau, similar to the affinity of volcanics erupted previously. The area of EM volcanism (open arrow) is located approximately the same distance from the Colorado Plateau as the EM area was in the previous Figure. In a similar sense, the mixed EM-DM center (closed arrow) is located approximately the same distance from the Colorado Plateau as the DM center in the previous Figure. The only "new" center is in the area of active extension in the west, these are the Nova-Funeral-Saline Range Basins, discussed in Chapter 3. These centers are located farther from the Colorado Plateau than the Sierra Nevada was prior to extension, and the EM component here may indicate the presence of a sub-Sierra Nevada enriched reservoir below the crust of the Death Valley Extended Area at this time [Walker and Coleman, submitted]. However, the chemical and isotopic composition of this component seems very different from the EM2 component discussed by Menzies [1989], and the centers are considered to be of EM affinity. By this time magmatism within the Colorado River Corridor has migrated onto the margin of the Colorado Plateau.

By the time shown on Figure 4D, (4-0 Ma), extension within the Death Valley Extended Area has widened to a zone 100 km wide, and magmatism has developed throughout (and outside of) the area of active extension. In the area of the Nevada Test Site (open arrow), the area of persistent EM magmatism continues, and the appearance of new DM and EM sources along the Sierra Nevada documents the wide spread presence of new magma sources. Within the Colorado River Corridor, the locus of magmatism has migrated into the Colorado Plateau, and active volcanism (of DM affinity) is present within the Cima Dome area of the Mojave Desert (filled arrow). Within the Colorado Plateau, two areas of alkaline basalts, the Hopi Buttes (at 5 Ma) and the Western Grand Canyon (<5 Ma) were emplaced during this period.

DISCUSSION

The general progression of extension and magmatism within the paired Death Valley Extended Area and Colorado River Corridor extensional domains can be summarized by the migration of magmatism across the

hanging wall of the system in the direction of upper plate extension-roughly eastward in the Colorado River Corridor and westward in the Death Valley Extended Area. This progression is easily seen in the Colorado River Corridor volcanic rocks, because later extension has not significantly penetrated the Plateau relative to the area overlain by volcanic rocks. However, the profound extension within the Death Valley Extended Area does obscure this relationship within there. This progression is summarized in Figure 5, which shows the eruptive position of all Cenozoic fields shown on the compilation of Luedke and Smith [1978], palinspastically reconstructed. The general westward migration of the volcanic rocks, with some overlap at 9-4 Ma, is well displayed.

The similar progression of volcanism within the two extensional domains suggests that it may be an integral part of the extensional process. The prevalence of a DM component in the recent volcanics, a component probably derived from asthenospheric mantle, suggests that this mechanism driving the migration is active removal of the mantle lithosphere by asthenosphere. The migration of the locus of volcanism across the hanging wall of the system requires modifications to the simple-shear models shown in Figure 2. Specifically, these models predict that the locus of volcanism should migrate in the opposite direction of hanging wall transport, as the area of magma generation is successively over-ridden by the hanging wall. Figure 6 illustrates three models which predict the observed migration pattern and DM-rich chemistry of the volcanic rocks. In the upper diagram, the volcanism migrates in the transport direction because the mantle lithosphere is eroded by upwelling asthenosphere. This is essentially the lithospheric erosion model of Perry et al. [1987]. In the middle diagram of Figure 6, the migration of volcanism is explained via delamination of the mantle lithosphere [Houseman et al., 1981]. Magma is generated by upwelling asthenosphere replacing the sinking lithosphere. In the lower diagram, the migration of volcanism is due to rightward stepping crustal shear zones, each of which is associated with an area of magma genesis. This model seems inapplicable to the Colorado River Corridor, because no substantial extension has migrated into the Colorado Plateau during the period magmatism has migrated across the Plateau.

The remaining models, lithospheric erosion and delamination, both explain a diverse collection of observations from the Death Valley Extended Area. Both models allow production of mixed EM-DM melts because the EM-rich lithosphere is heated by the upwelling DM-rich asthenosphere during its replacement. Melts generated during this heating could range from EM dominated to mixed EM-DM, depending upon the scale of the melting area, even though the EM component might be considered more fertile [Richter and Daly, 1989]. Both models predict the rapid reconstruction of a Moho following extension, as is suggested by deep reflection profiles from the Basin and Range [de Voogd, 1988]. As new, perhaps more "fertile" asthenosphere upwells at the area of active replacement, the locus of magmatism would migrate in the direction of hanging wall transport.

The two models are difficult to distinguish from their chemical signals alone. Instead, the most direct way to distinguish these models would be to test for the presence of a cold, dense slab (the delaminating lithosphere) below the western boundary of the Death Valley Extended Area: the Sierra Nevada. Jones [1988] reported a summary of the geophysical observations from the southern Sierra Nevada that would be underlain by a delaminating slab. Because the lithosphere is denser than the ambient asthenosphere, one would expect a gravity high in the area underlain by the slab. The Eastern Sierras are in fact characterized by a gravity low, only in the western foothills does there a gravity high. Additional work needs to be done to fully differentiate between these models.

Regardless of the mechanism by which it occurs, the data in Figure 4 clearly indicate the regional replacement of an a EM component by a DM-enriched component in the western Death Valley Extended Area since 4 Ma. Ormerod et al [1988] noted that this transition was time transgressive, initiating in the north end of the Sierra Nevada and migrating southward. They hypothesized that this trend was due to a "slab-window" in the subducting Farallon Plate, allowing DM mantle to rise through the EM lithosphere. Instead, I interpret this to represent the erosion of the EM layer by upwelling DM, as discussed above. The presence of similar patterns of magmatism beneath the Colorado Plateau, where no slab

window was present, suggests that one of the erosion models discussed above was responsible.

A "translating" DM source is seen in the San Francisco Field in the hanging wall of the Colorado River Corridor extensional area. Tanaka [1986] estimated that the locus of volcanism (and the source, in their model) moved at a rate of approximately 1 to 3 cm/a to the north east in the interval 4-0 Ma. I interpret this to be the rate of erosion of DM component into the EM component beneath the plateau. The rate of translation of the magma source on the Death Valley side of the Garlock Fault can be estimated from Figure 5, and suggests a rate of 400 km in 10-15 Ma or 3-4 cm/a, in good agreement with the values derived by Tanaka et al [1986] for the San Francisco Field. The presence of persistent EM components in the Death Valley Area suggests that large parts of the lithospheric mantle are preserved during the replacement by DM component.

The paired extensional system involved in these two area, the similar timing, composition, and evolution of these sources all indicate that a process inherent to the extension is controlling the locus of volcanism in the Colorado River Corridor and the Death Valley Extended Area. Figure 7 shows the model that was developed in Chapter 3 to explain the pattern of volcanism for the Death Valley Extended Area, and the comparison done here suggests that the key feature of this model, the upwelling DM component in the latter part of extension, is either caused by the extension, or is in fact driving the extension. The key to discriminating between these possibilities lies obtaining the chemical signature of early syn-extensional basalts. Within the Colorado River Corridor, the early basalts have a mixed EM-DM composition, suggesting that active upwelling of a DM component may be present at the initiation of extension. The causal relationship between this upwelling and the extension is not clear. The fact that the Colorado Plateau is not actively extending suggests that this mechanism alone is insufficient to drive extension. Finally, the close spatial relationship between the locus of extension and magmatism seen in the Death Valley and Colorado River Corridors suggests that Bosworth's observations of continental extension do not apply to all continental areas undergoing extension through simple shear

REFERENCES

- Bartley, J. and Glazner, A., A hypothesis for the link between Miocene extension in the Colorado River Trough and Mojave Desert, *Geol. Soc. Amer. Abs. Prog.*, 21, A354, 1989.
- Bohannon, R.G., *Nonmarine sedimentary rocks of Tertiary Age in the Lake Meade region, southeastern Nevada and northwestern Arizona*, pp. 72, 1984.
- Bosworth, R., Off-axis volcanism in the Gregory Rift, east Africa: Implications for models of continental rifting, *Geology*, 15, 397-400, 1987.
- Burchfiel, B.C., Hodges, K.V. and Walker, J.D., Geology of the Kingston Range Detachment, in preparation.
- de Voogd, B.L.d., Serpa, L. and Brown, L., Crustal extension and magmatic processes: COCORP profiles from Death Valley and Rio Grande rift, *Geol. Soc. Amer. Bull.*, 100, 1550-1567, 1988.
- Eaton, G.P., The Basin and Range province: origin and tectonic significance, *Ann. Rev. E. Planet. Sci.*, 10, 409-440, 1982.
- Farmer, G.L., Perry, F.V., Semken, S., Crowe, B., Curtis, D. and De Paolo, D.J., Isotopic evidence on the structure and origin of subcontinental lithospheric mantle in southern Nevada, *J. Geophys. Res.*, 94, 7885-7898, 1989.
- Houseman, G.A., McKenzie, D.P. and Molnar, P., Convective instability of a thickened boundary layer and its relevance for the thermal evolution of continental convergent belts, *J. Geophysic. Res.*, 86, 6115-6132, 1981.
- Howard, K.A. and John, B.E., Crustal extension along a rooted system of imbricate low angle faults: Colorado River extensional corridor, California and Arizona, in *Continental Extension Tectonics*, pp. 299-311, Geological Society of London, London, 1987.

- Levy, M. and Christie-Blick, N., Pre-Mesozoic palinspastic reconstruction of the Eastern Great Basin (Western United States), *Science*, 245, 1454-1463, 1989.
- Lister, G.S., Etheridge, M.A. and Symonds, P.A., Detachment faulting and the evolution of passive continental margins, *Geology*, 14, 246-250, 1986.
- Luedke, R.G. and Smith, R.L., *Map showing distribution, composition, and age of Late Cenozoic volcanic centers in Arizona and New Mexico*, pp. United States Geological Survey, Reston, VA, 1978.
- McKenzie, D.P., Some remarks on the development of sedimentary basins, *Earth Planet. Sci. Lett.*, 40, 25-32, 1978.
- Menzies, M.A., Cratonic, circumcratonic and oceanic mantle domains beneath the Western United States, *J. Geophys. Res.*, 94, 7899-7915, 1989.
- Menzies, M.A., Leeman, W.P. and Hawkesworth, C.J., Isotope geochemistry of Cenozoic volcanic rocks reveals mantle heterogeneity below western United States, *Nature*, 303, 205-209, 1983.
- Ormerod, D.S., Hawkesworth, C.J., Rogers, N.W., Leeman, W.P. and Menzies, M.A., Tectonic and magmatic transitions in the Western Great Basin, USA, *Nature*, 333, 349-353, 1988.
- Perry, F.V., Baldrige, W.S. and De Paolo, D.J., Role of asthenosphere and lithosphere in the genesis of Late Cenozoic basaltic rocks from the Rio Grande Rift and adjacent regions of the Southwestern United States, *J. Geophys. Res.*, 92, 9193-9213, 1987.
- Prodehl, C., Crustal Structure of the Western United States, in *United States Geological Survey Prof. Pap. 1034*, pp. 1-74, 1979.
- Richter, F.M. and Daly, S.F., Dynamical and chemical effects of melting a heterogeneous source, *J. Geophys. Res.*, 94, 12499-12510, 1989.
- Stewart, J.H., Basin-range structure in western North America: A review, in *Cenozoic Tectonics and Regional Geophysics of the Western*

Cordillera, edited by Smith, R.B. and Eaton, G.P., pp. Geological Society of America, Boulder, CO, 1978.

Tanaka, K.L., Shoemaker, E.M., Ulrich, G.E. and Wolfe, E.W., Migration of magmatism in the San Francisco Volcanic Field, Arizona, *Geol. Soc. Amer. Bull.*, 97, 129-141, 1986.

Walker, J.D. and Coleman, D.S., Crustal-scale kinematics of extensional deformation in the Death Valley extended area revealed by geochemistry of volcanic rocks, *Geology*, submitted.

Wernicke, B., Axen, G.J. and Snow, J.K., Basin and Range extensional tectonics at the latitude of Las Vegas, Nevada, *Geol. Soc. Amer. Bull.*, 100, 1738-1757, 1988.

Wernicke, B.P., Christiansen, R.L., England, P.C. and Sonder, L.J., Tectonomagmatic evolution of Cenozoic extension in the North American Cordillera., in *Continental Extensional Tectonics*, edited by Coward, M.P., Dewey, J.F. and Hancock, P.L., pp. 203-221, Geological Society of London, Oxford, 1987.

Wernicke, B.P., Low-angle faults in the Basin and Range Province—Nappe tectonics in an extending orogen, *Nature*, 291, 645-648, 1981.

Zindler, A. and Hart, S.R., Chemical Geodynamics, *Annu. Rev. Earth Planet. Sci.*, 14, 493-571, 1986.

FIGURE CAPTIONS

Figure 1. Location map and tectonic setting of the study area. Abbreviations: CP, Colorado Plateau; SN, Sierra Nevada; TZ, Transition Zone; GF, Garlock Fault; SF, San Andreas Fault. Small lined areas indicate metamorphic core complexes. The Death Valley Extended Area lies north of the Garlock fault, and south of the Furnace Creek Fault Zone, the Colorado River Extended Area is south of the Garlock Fault.

Figure 2. Modes of continental extension, from Lister et al [1986].

Figure 3. Current location and provenance of Cenozoic basaltic volcanic rocks studied by Ormerod et al [1988], Farmer et al [1990], Walker and Coleman [submitted] and McKenna [Chapter 3].

Figure 4. Palinspastically reconstructed positions of the fields shown in Figure 3, along with all the Cenozoic volcanic centers shown by Luedke and Smith [1978] (light lines). Reconstructions are shown for four periods, in which the position of the Sierra Nevada (SN) relative to the stable Colorado Plateau (CP) is shown for the end of the period indicated. Grey shading represents the area of active crustal extension. A. Pre-extension to 11 Ma, B. 11 to 9 Ma, C. 9 to 4 Ma, D. 4-0 Ma. See text for discussion.

Figure 5. Palinspastically restored position of major Cenozoic volcanic centers, with age indicated by line type (see Key).

Figure 6. Model for the development of volcanism in extensional systems. See text for discussion.

Figure 1

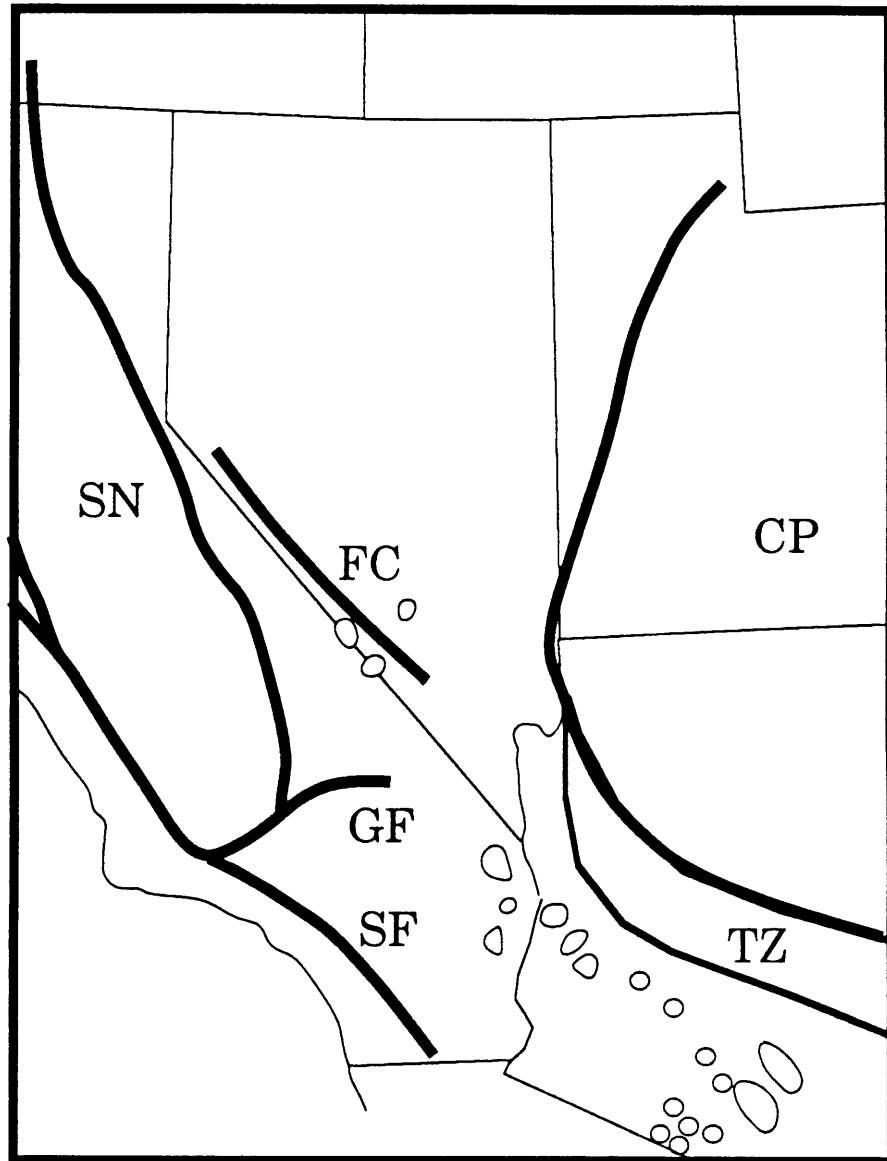


Figure 2

Modes of Continental Extension

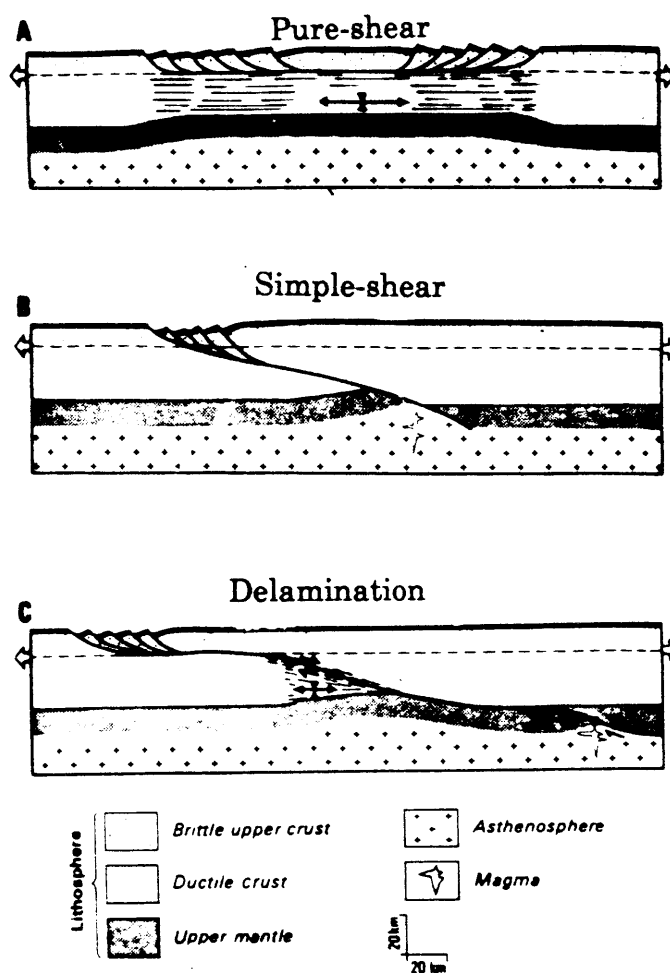


Figure 4A

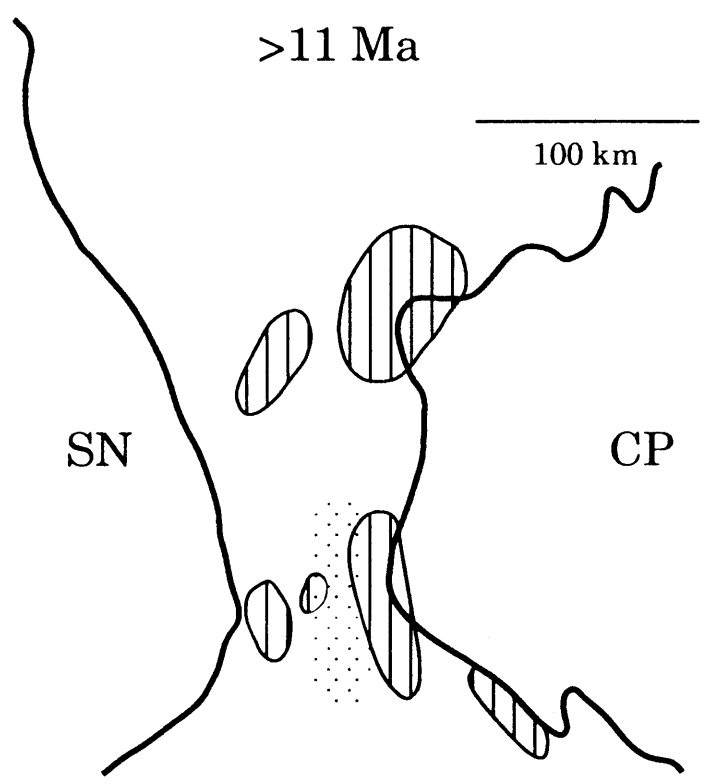


Figure 4B

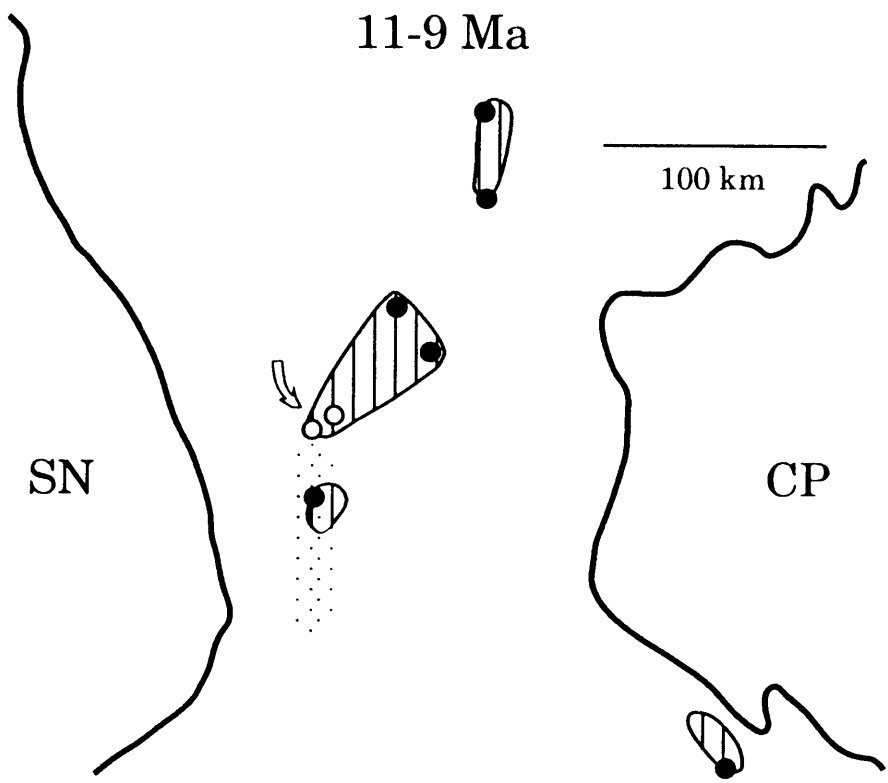


Figure 4 C

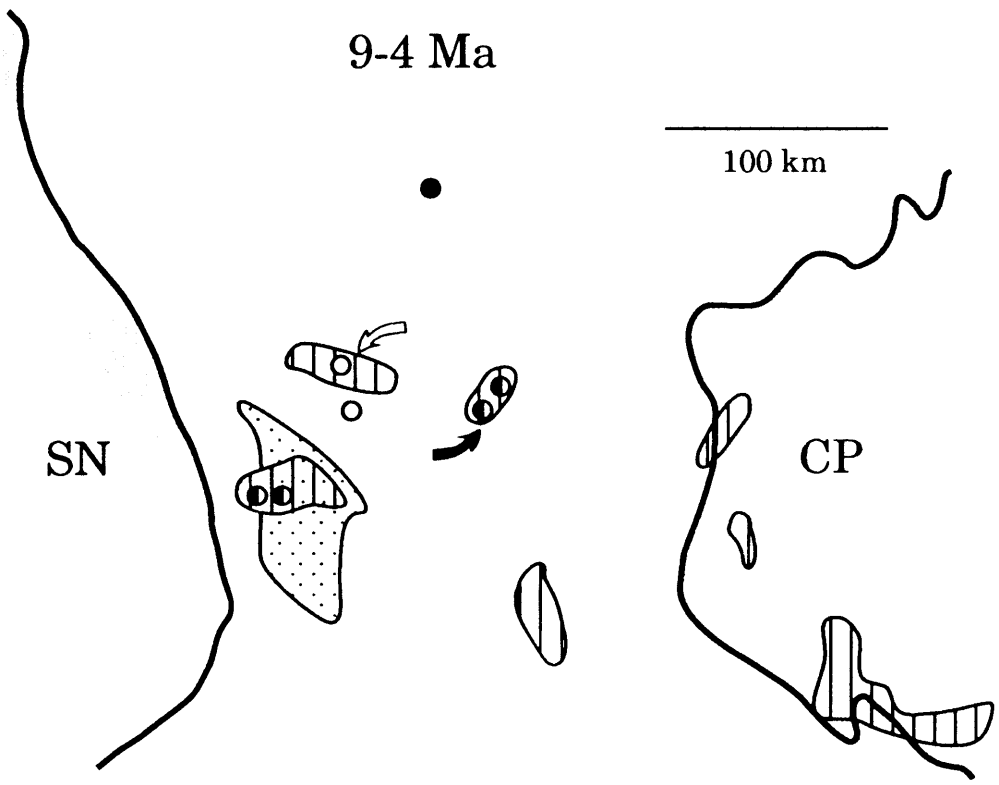


Figure 4D

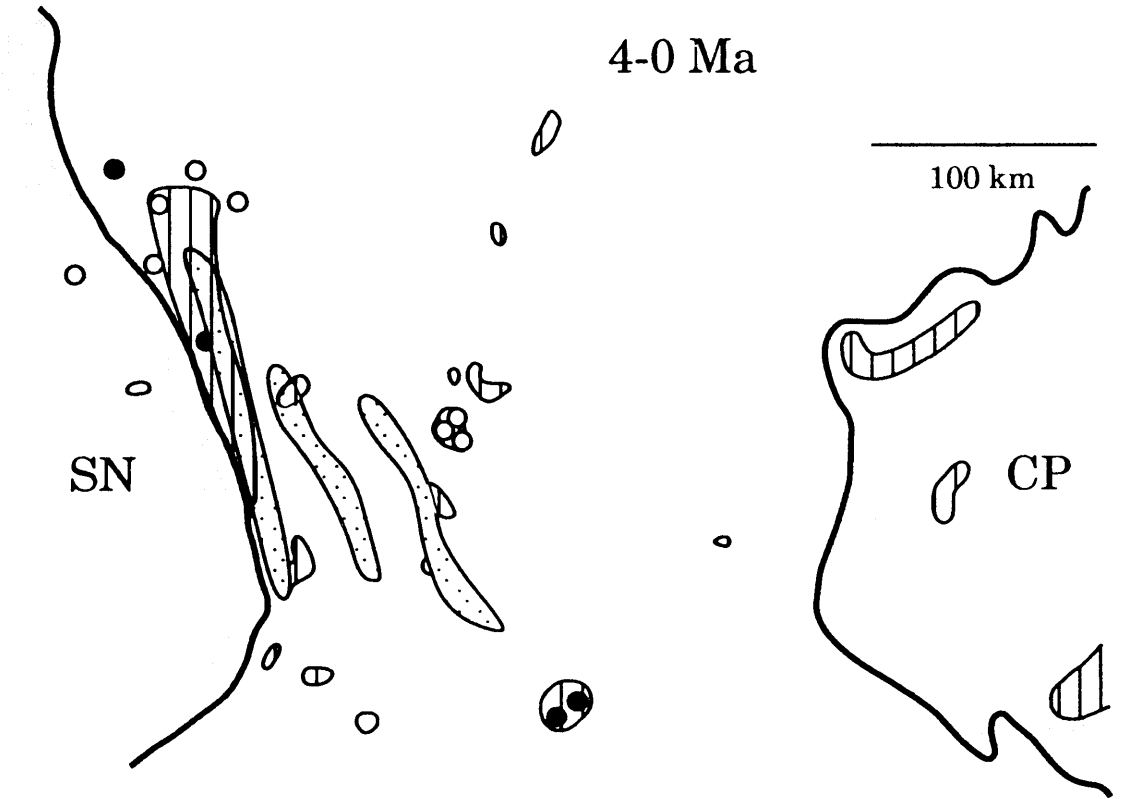


Figure 5



Ages of Volcanic Rocks



>15 Ma



10-5 Ma



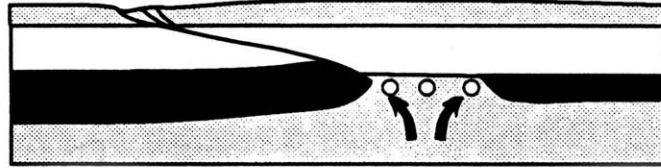
15-10 Ma



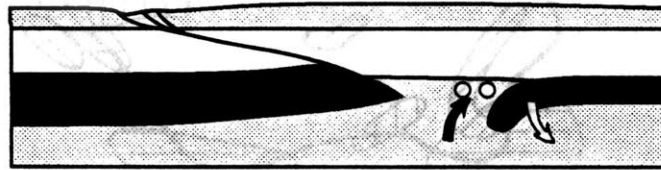
<5 Ma

Figure 6

Lithospheric Erosion via Asthenospheric Upwelling





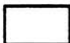




Lithospheric Delamination



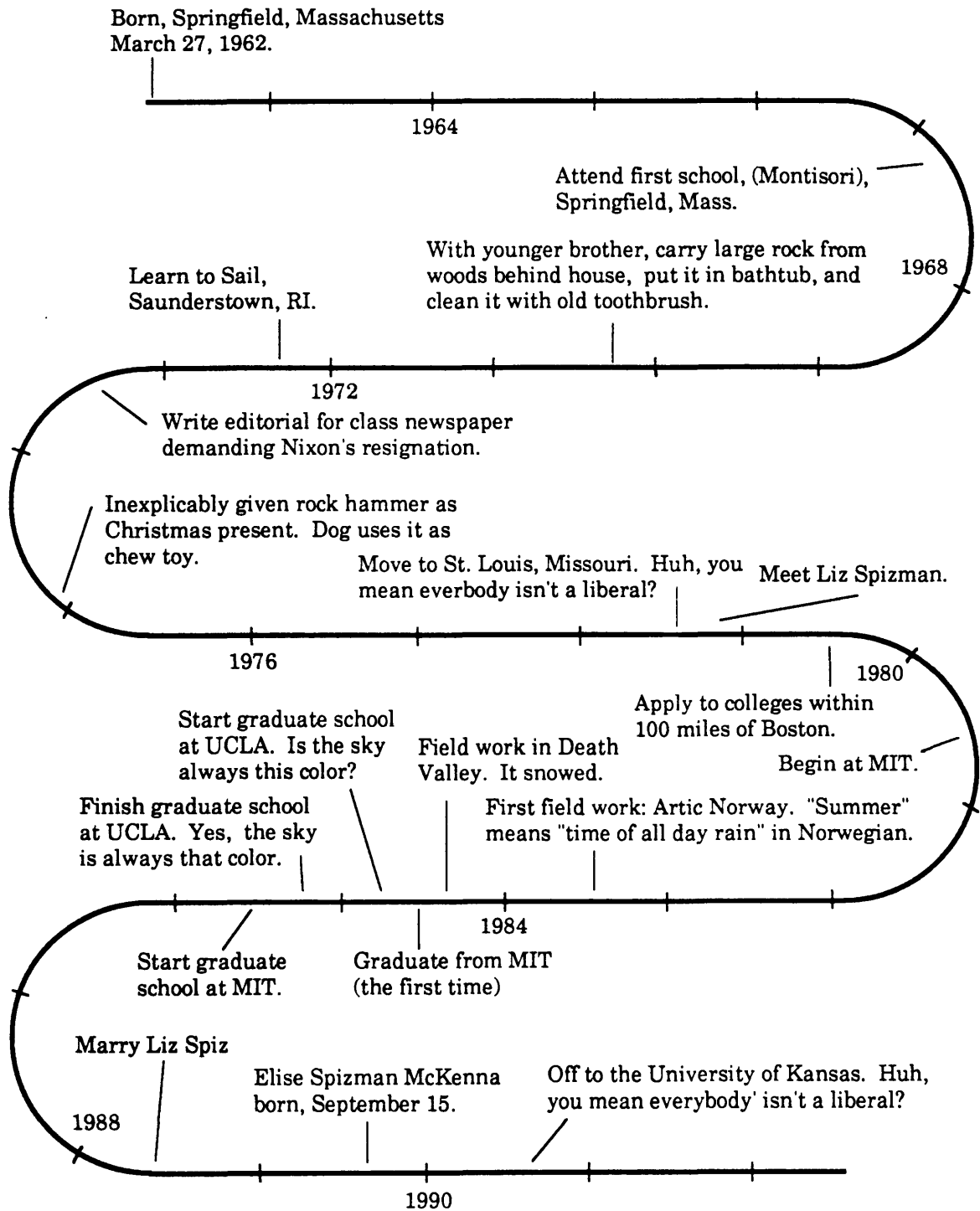
Multiple Shear Zones



100 km

- | | | | |
|---|-------------------------------------|--|-------------------------------------|
|  | Upper Crust |  | Mantle Lithosphere (EM-enriched) |
|  | Middle and Lower Crust |  | Asthenosphere (DM-enriched) |
|  | Locus of Melt Generation | | |
|  | Translating DM-enriched material |  | Translating EM-enriched material |

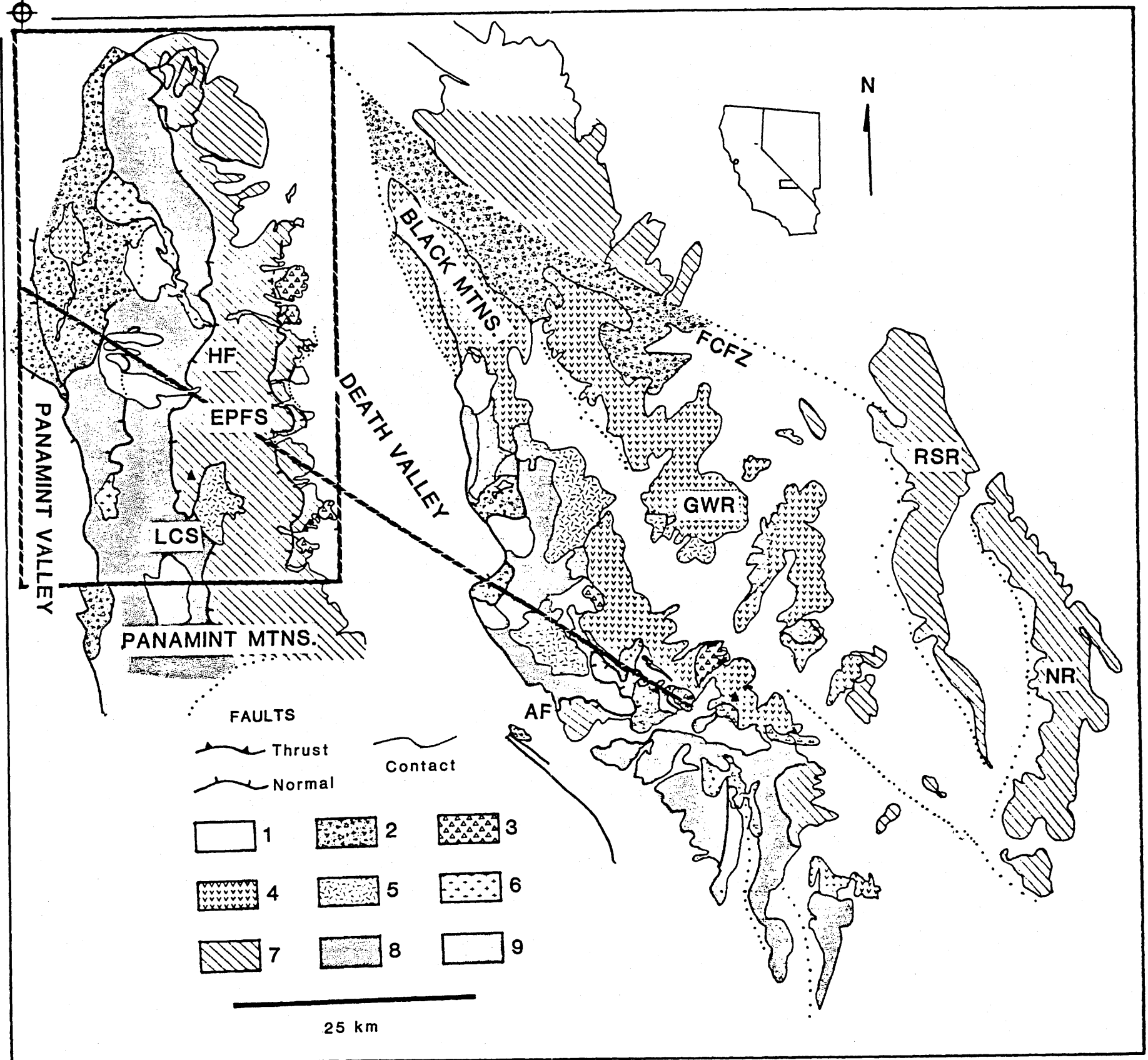
BIOGRAPHICAL SKETCH



The text, tables and majority of figures for this work were composed on the Macintosh® II and Plus computers. Text and tables were written with Microsoft® Word, while the figures were drafted in Deneba's Canvas®. The text, tables, and majority of the figure text were set in New Century Schoolbook (12 point), except for Table 3 of Chapter 2, which was set in Times (12 point) to conserve space. The thesis was printed on acid-free paper using a LaserWriter® IINT.

7459-72
3254-16

Figure 2, Chapter 1
 McKenna, Lawrence William III
 Processes of Crustal Extension as
 Viewed from the Death Valley
 Area, California
 Ph. D., MIT, 1990



VOLCANIC STRATIGRAPHY OF THE TRAIL CANYON VOLCANIC SEQUENCE

Panamint Range, Inyo County, California

Figure 3, Chapter 1
McKenna, Lawrence William III
Processes of Crustal Extension as
Viewed from the Death Valley
Area, California
Ph. D., MIT, 1990

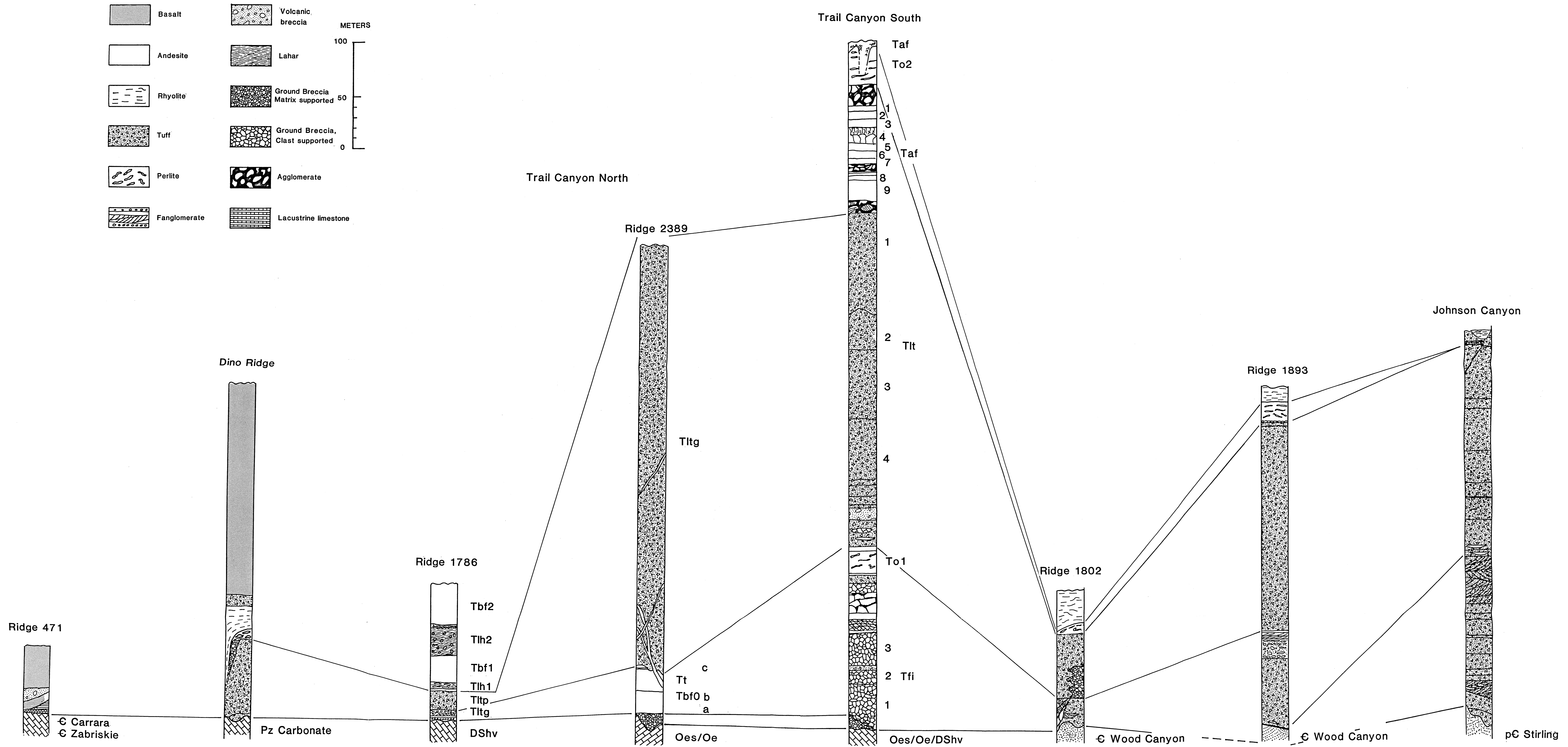
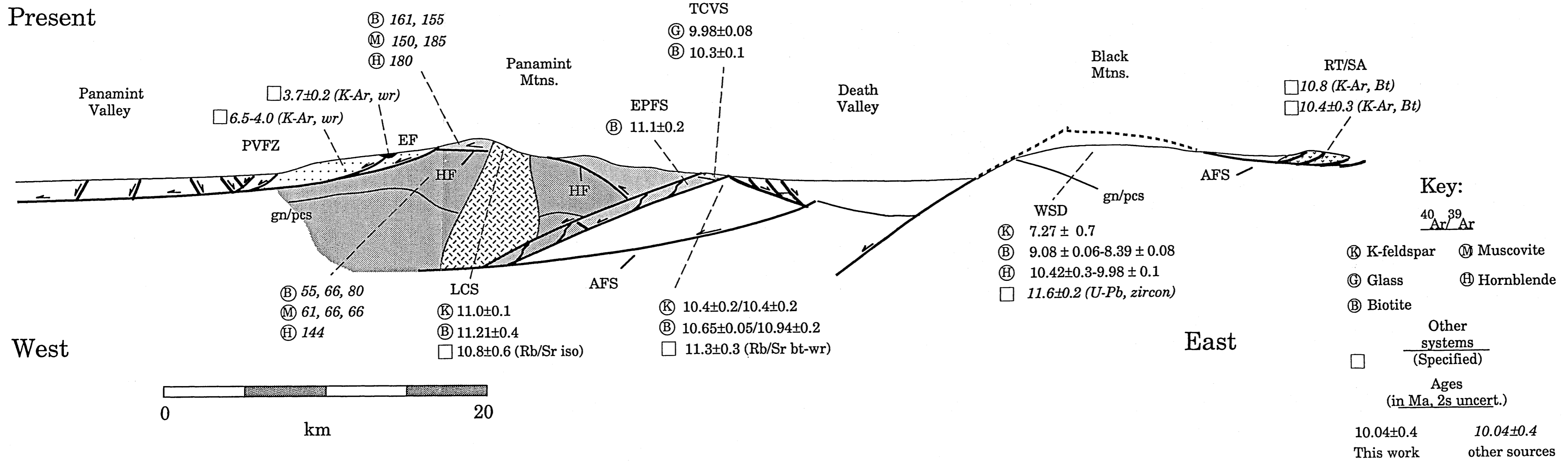


Figure 3, Chapter 2
 McKenna, Lawrence William III
 Processes of Crustal Extension as
 Viewed from the Death Valley
 Area, California
 Ph. D., MIT, 1990

Present



Cross-section A-A' reconstructed

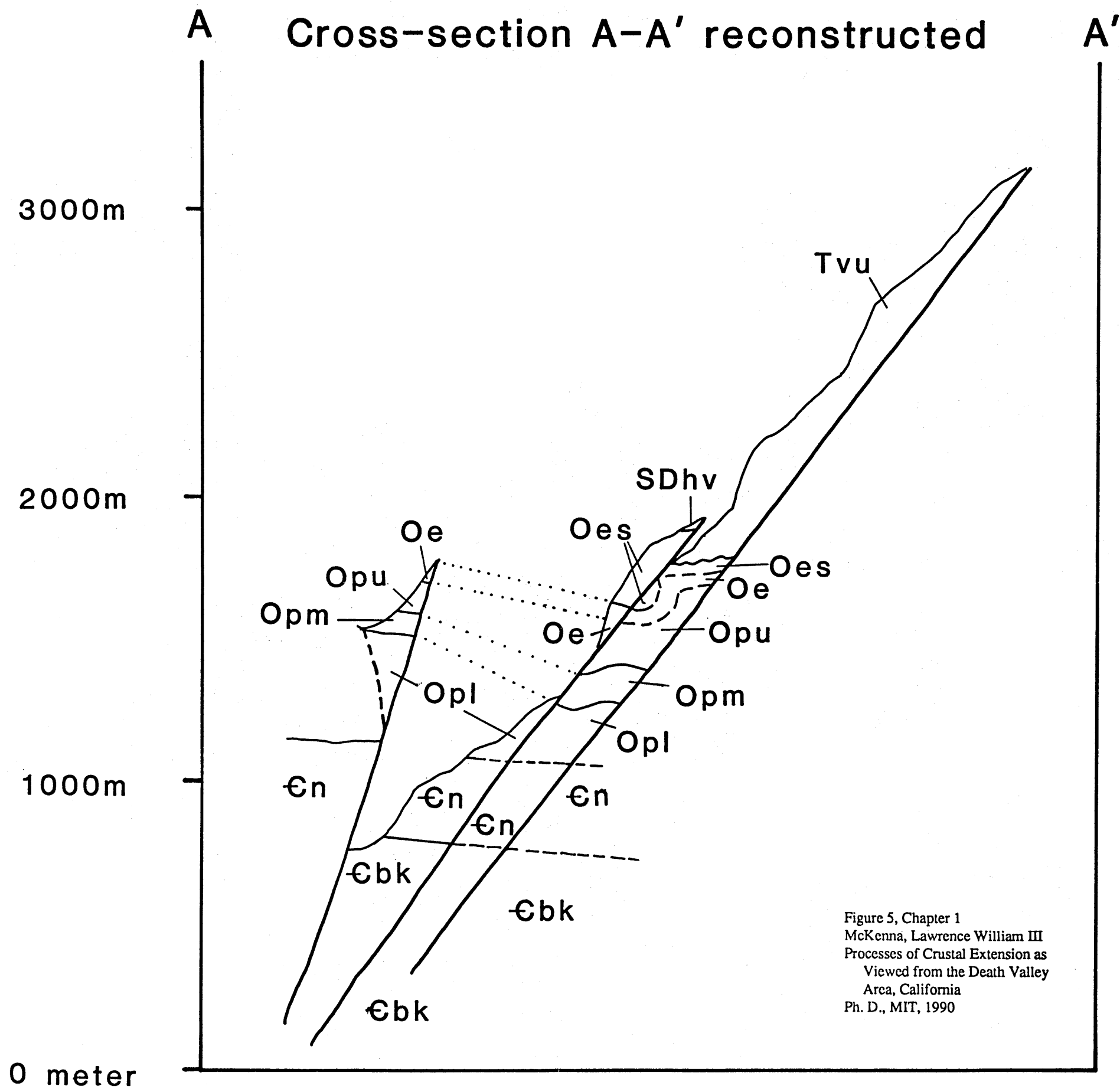
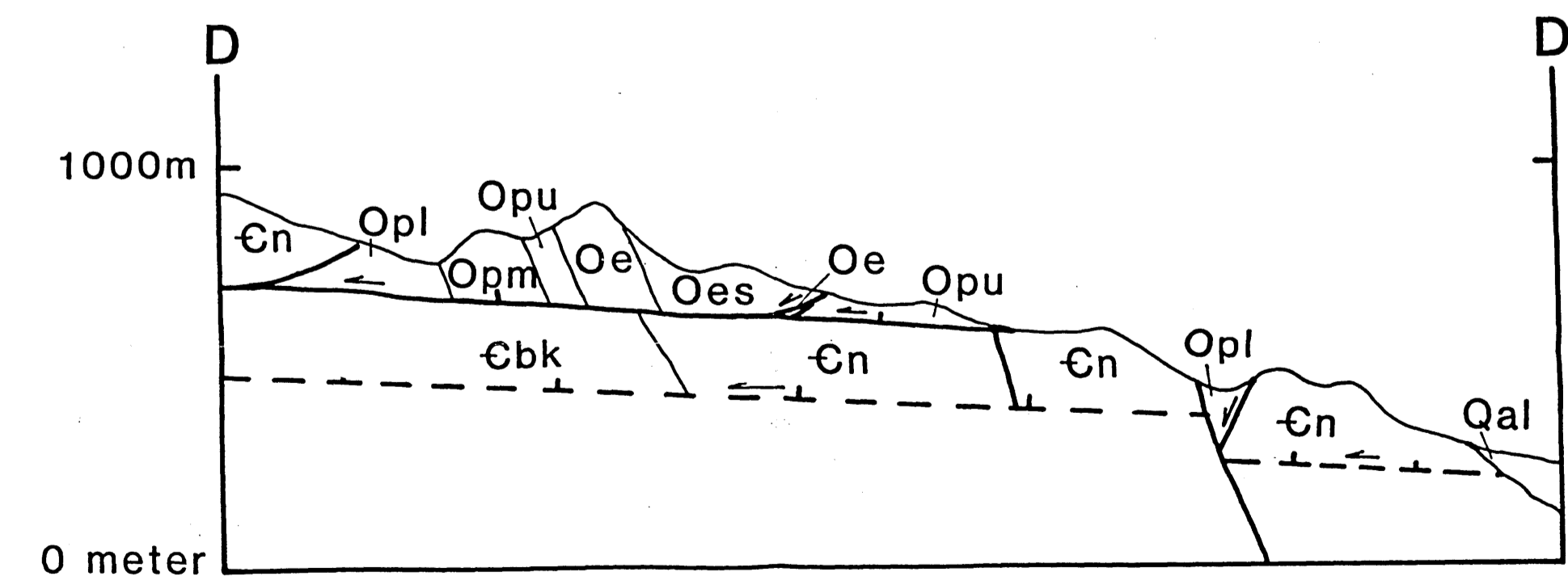
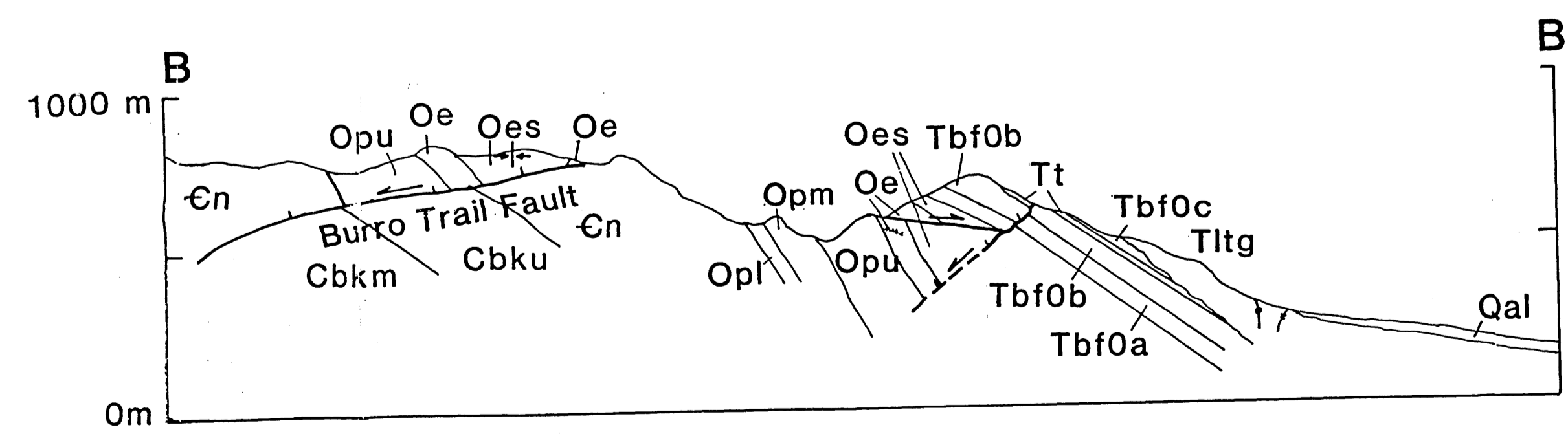
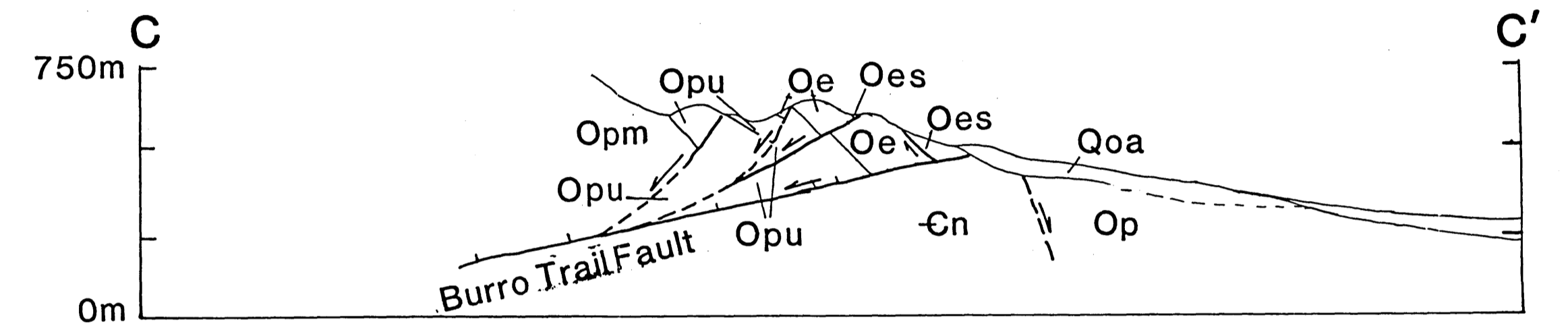
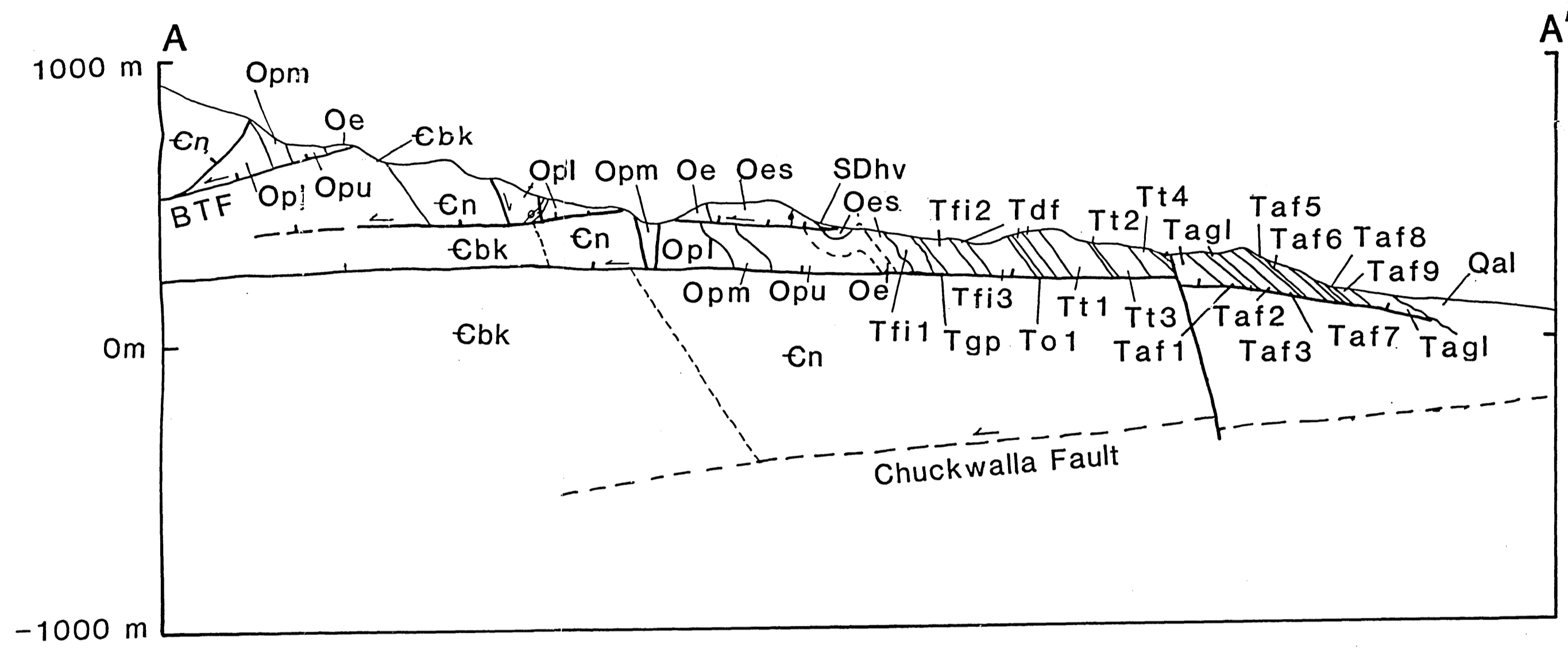
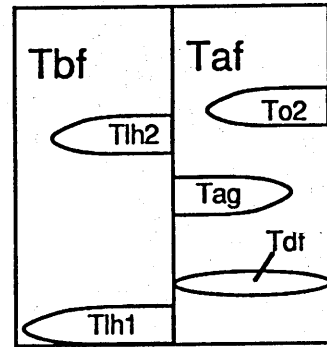
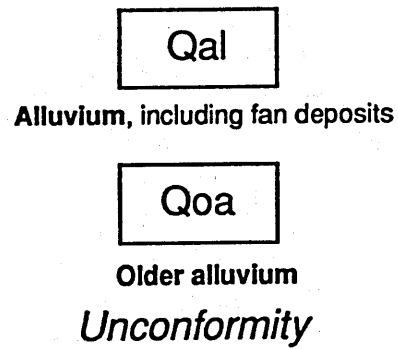
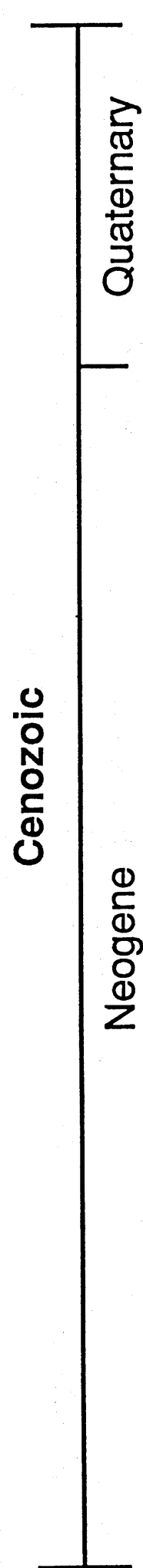


Figure 5, Chapter 1
McKenna, Lawrence William III
Processes of Crustal Extension as
Viewed from the Death Valley
Area, California
Ph. D., MIT, 1990

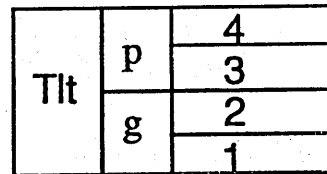
Geologic Cross Sections Trail Canyon Area, Death Valley, CA

No vertical exaggeration



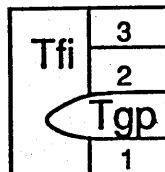
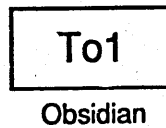


Taf, Andesite flows, numbered sequentially from bottom to top; Tbf, Andesite flows stratigraphically equivalent to flows in Taf; To2 obsidian; Tag, Agglomerate; Tdf, debris flows and landslide breccias containing oligomictic layers of Oes and Oe; Tlh, Lahar.



Lapilli tuff. White (units 1-4) to pale green (unit g) to pale pink (unit p) lapilli tuff containing 10-30% lithic fragments.

Unconformity

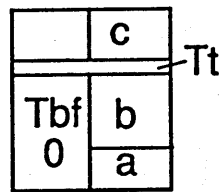


Tfi, Ground breccia. Clasts of porphyritic rhyolite in a matrix of fine grained to porphyritic rhyolite; Tgp, granophyric intrusive.

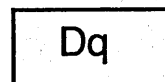
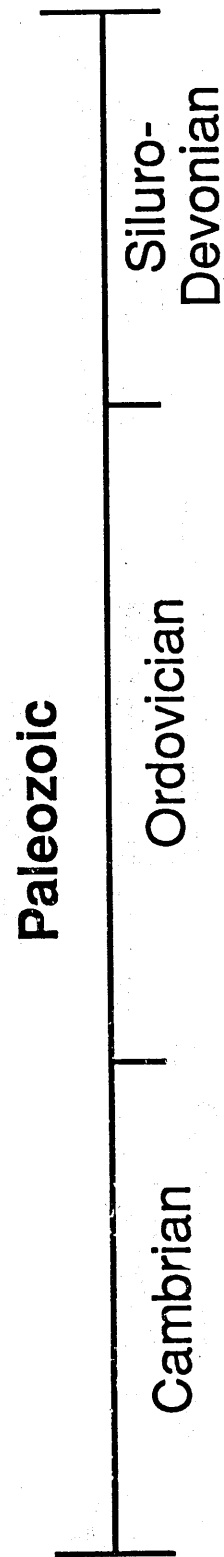


Volcaniclastic conglomerate. Rounded, ellipsoidal clasts of porphyritic rhyolite cemented by detrital material.

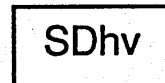
Unconformity



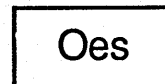
Aphyric basalt flows with interbedded lapilli-fall tuff



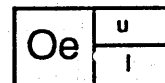
Devonian Quartzite. Thickbedded, dark brown weathering quartzite



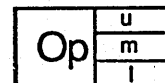
Hidden Valley Dolomite. Gray to light gray dolomite above a basal quartzite.



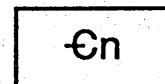
Ely, Spring Dolomite. Thickly-bedded dolomite.



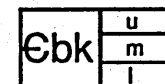
Eureka Quartzite. White to very-light gray vitreous quartzite. Lower part is bedded and stained brown.



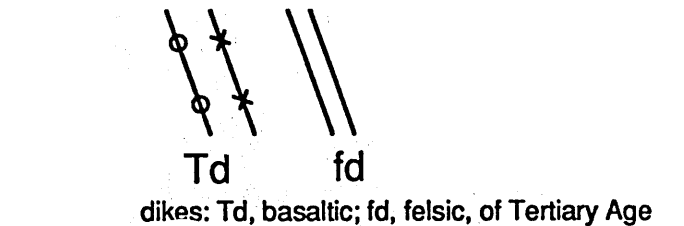
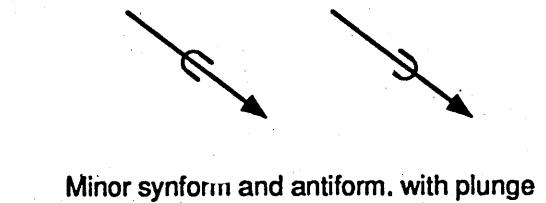
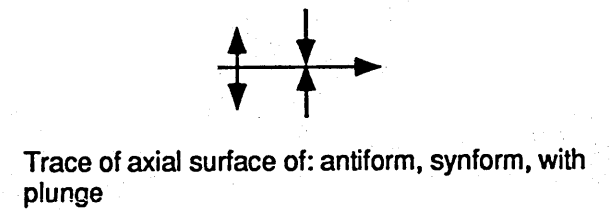
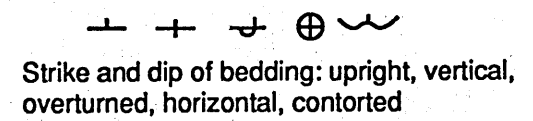
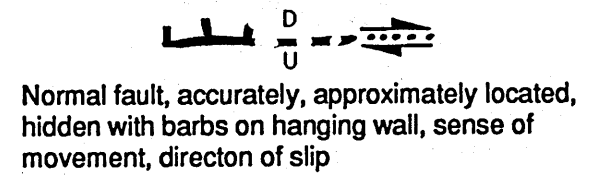
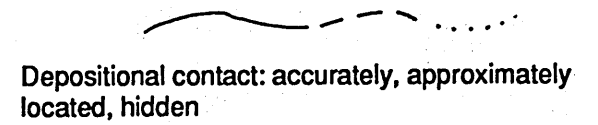
Pogonip Group. Upper part is dark gray, well-bedded limestone, middle is interbedded limestone and shale, while lower is dark dolomite and limestone



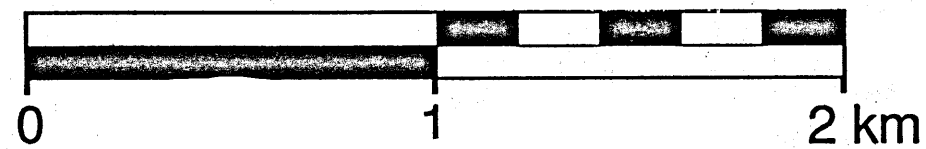
Nopah Formation. Mostly brown sandy dolomite alternating with black and cream colored limestone.



Bonanza King Formation. Upper part is thick-bedded dolomite, middle part consists of light-tan shale interbedded with platy limestone and sandstone, while lower part consists of interbedded dark limestone and light-colored dolomite.



Location marker



Scale: 1:15840

Key to Plate 1, Chapter 1
McKenna, Lawrence William III
Processes of Crustal Extension as
Viewed from the Death Valley
Area, California
Ph. D., MIT, 1990

GEOLOGIC MAP OF THE TRAIL CANYON AREA, DEATH VALLEY, INYO COUNTY, CA

